

# URS-755-3

B-1

URS 755-3

- 1) ~~Levy~~
- 2) ~~Mr. Jones~~
- 3) ~~Mr. Kuhn~~
- 4) ~~Mr. Fletcher ERF~~
- 5) Mr. Babb
- 6) ~~Mr. White ERF~~

THE AIR-BLAST-INDUCED ENVIRONMENT  
WITHIN CIVIL DEFENSE BLAST-SLANTED SHELTERS

Final Report  
November 1969

Reproduced From  
Best Available Copy

Contract No. DAHC20-67-C-0136  
OCD Work Unit 1123F

URS RESEARCH COMPANY



LOVELACE FOUNDATION  
DOCUMENT LIBRARY

This document has been approved for public release  
and sale; its distribution is unlimited.

20011030 049

THE AIR-BLAST-INDUCED ENVIRONMENT  
WITHIN CIVIL DEFENSE BLAST-SLANTED SHELTERS

Final Report

November 1969

by

Joseph F. Melichar

URS RESEARCH COMPANY  
1811 Trousdale Drive  
Burlingame, California

for

Office of Civil Defense  
Office of the Secretary of the Army  
Washington, D.C. 20310

Contract No. DAHC20-67-C-0136  
OCD Work Unit 1123F

OCD REVIEW NOTICE

This report has been reviewed in the Office of Civil Defense and approved for publication. Approval does not signify that the contents necessarily reflect the views and policies of the Office of Civil Defense.

This document has been approved for public release and sale;  
its distribution is unlimited.

## ACKNOWLEDGMENTS

The author would like to express his appreciation to Miss Jane E. Northall for the computational, programming, and graphic support she provided this project. The inclusion of a significant portion of the data and computations presented are the direct result of her diligent efforts. The running and reprogramming of the FLIC program was undertaken by Dr. Clifford Colvin. Dr. Peter Strom's comments and suggestions on the derivations presented in Appendixes B and C were most helpful. The author would also like to express his appreciation to the Ballistic Research Laboratories for allowing him to use past notes to develop Appendix B. The comments by J. Rempel and C.K. Wiehle of SRI on the final draft of this report were most helpful. Finally, the author would like to express his appreciation to Mrs. Patty Wiscavage for her editorial assistance and for the management of the compilation, typing, and production of the report.

THE AIR-BLAST-INDUCED ENVIRONMENT  
WITHIN CIVIL DEFENSE BLAST-SLANTED SHELTERS

Final Report

November 1969

by

Joseph F. Melichar

URS RESEARCH COMPANY  
1811 Trousdale Drive  
Burlingame, California

for

Office of Civil Defense  
Office of the Secretary of the Army  
Washington, D.C. 20310

Contract No. DAHC20-67-C-0136  
OCD Work Unit 1123F

OCD REVIEW NOTICE

This report has been reviewed in the Office of Civil Defense and approved for publication. Approval does not signify that the contents necessarily reflect the views and policies of the Office of Civil Defense.

This document has been approved for public release and sale;  
its distribution is unlimited.

Summary Report  
of  
THE AIR-BLAST-INDUCED ENVIRONMENT  
WITHIN CIVIL DEFENSE BLAST-SLANTED SHELTERS

The objective of this work unit was to review and discuss the application of hydrodynamic codes in the Office of Civil Defense (OCD) shelter research program, and then consider the development of a conceptual model of the flow into and through blast-slanted basement shelters. The review selected a two-dimensional Eulerian code which numerically simulated inviscid, compressible flow without heat transfer. This form of code was shown to be the most suitable form of code for OCD needs on a cost-effectiveness basis.

The Eulerian equations were discussed, linked to their numerical form, and a complete set of numerical equations was appended for the reader's convenience. To provide the basis for the evaluation of this approach to future OCD problems a brief review of the internal workings of this form of code was undertaken. A bibliography was provided which will allow the reader to expand the brief review provided by this work unit.

To test the accuracy of numerical simulation the code was applied to several situations which represented conditions that would have to be reproduced in the shelter research program. These situations had been simulated experimentally so that a direct comparison between simulation procedures could be undertaken. The first cases reviewed the code's ability to reproduce a shock wave profile, and then surveyed the difficulties of correctly matching the time frames of rapidly decaying waves between experimental and numerical simulations. An appended section discusses some of these difficulties based on a geometric representation of the pressure-time profiles.

The first comparisons of experimental and numerical simulations of shelter situations used small scale model shelters. Shelter models used in scaled experiments (referenced in text) were reproduced in the numerical

simulations to allow direct comparisons. Some difficulties in matching pressure-time profiles were noted, but an agreement of better than 90 percent between the simulations was noted for the extremely short term transients of the filling process. The short term transients were also shown not to affect the long term fill history of the shelter.

Trajectories of points formed by a smoke grid in the same scaled experiments were used to test the accuracy of the numerically simulated flow field. The difficulty of precisely aligning the space-intensity profiles in time between simulations was again found. Procedures were developed to improve the comparison techniques. In the evolution of these procedures it was established that the problem of timing comparisons was partly due to experimental error. An error analysis of the experiments was undertaken and pinpointed some errors in the experimental simulations. In general the numerical simulations were concluded to produce flow velocities that were about 10 percent higher along the inflow axis and about 5 to 10 percent lower in the other regions of the shelter.

Further evaluations were made against full scale shelters. Data were gathered from a full-scale field test using high explosives and from some preliminary URS shock tunnel tests. The numerical simulations reproduced the average pressure-time profiles within the simulated chambers to within 90 percent of the experimental value. The evolution of an error range for the experimental data proved to be the limiting factor in developing a more precise estimate of variation between simulations.

The pressure data from URS shock tunnel tests, its evaluation, and data and analysis of flow visualization experiments were developed in an appended section. The presentation of the flow experiments included a consideration for the movement of spheres in the inflow. The flow data generated by the experimental and numerical simulations varied on the average less than 10 percent (within the limits of experimental accuracy). The conclusion reached was that the numerical simulation procedures were sufficiently accurate to be used in the shelter research program. Some potential problem areas were outlined for future study.

A section on cost and utilization of numerical simulations was included. Comparisons of the costs of numerical versus experimental simulations showed numerical simulations to be less costly. A common difficulty with data display for both simulation techniques was noted. The numerical simulations were shown to have the advantage of better output and monitoring control. The credibility and reliability of results were considered. The possibility of using a simple coarse grid code for general use on a small computer was discussed.

A review of the transient inflow process was undertaken. A review of incompressible flow studies provided some insight into the dynamics of jet formation. This review was followed by the evolvement of an analytic model of the transition flow of a compressible gas into the chamber. The model used a quasi-one-dimensional representation of the inflow which was analytically defined by the method of characteristics. The method showed how imbalances in the flow occurred due to the high inflow velocity of the adiabatic expansion. The result was in effect a piston which drove the gas in the chamber ahead of it. The implications were discussed and verified from the experimental data presented in the report.

A review of the turbulence and jet spreading problem was undertaken and a bibliography on it and associated flow problems was developed. Many estimation procedures for growth and spread of turbulence were noted. The discussion used a simple boundary layer model to represent the spread of the flow. The model indicated that the boundary layer and turbulence effects were much more pronounced in the scaled experiments than would be expected in the prototype situation. The work indicated that the spread and growth of turbulence and boundary layers would probably not be of major proportions in full scale shelters.

A general view of associated flow problems was undertaken. The most significant of these problems was the effect of the inflow into the shelter on the reservoir conditions. The inability of the reservoir to completely

replace the effluent mass and energy was shown to reduce the driving pressure and also to decrease the driven flow. The comments were related to experimental results.

A series of numerical simulations were undertaken in support of this study. The problem of effective and economic data display arose, hence the results of these simulations were verbally described. The simulations treated a variety of geometric situations and included multiple room geometries. Implications of the observed results were discussed.

The last section summarized the review of the shelter flow in terms of a conceptual model of the flow. The use of a systems representation of the flow was used to show that a conceptual model on any general scale was probably not a reasonable goal. Some suggestions on how to circumvent this difficulty, and what areas of the flow problem might yield the most gains in future studies were outlined.



## CONTENTS

<u>Section</u>		<u>Page</u>
	ACKNOWLEDGMENTS . . . . .	ii
	ILLUSTRATIONS . . . . .	v
	TABLES . . . . .	vii
	SUMMARY . . . . .	ix
1	INTRODUCTION . . . . .	1-1
	Study Outline . . . . .	1-3
2	COMPUTER FLOW CODE EVALUATION . . . . .	2-1
	The Eulerian Method . . . . .	2-3
	Difference Equations . . . . .	2-9
3	CODE APPLICATION . . . . .	3-1
	Accuracy Considerations . . . . .	3-1
	Comparison of Numerical Simulation with Full Scale Experimental Results . . . . .	3-31
	Utilization, Cost, and Display of Numerical Simulations . .	3-36
	Utilization . . . . .	3-38
	Cost . . . . .	3-41
	Display . . . . .	3-43
4	FLOW PROCESSES . . . . .	4-1
	The Transient Inflow Process . . . . .	4-1
	General Comments . . . . .	4-33
5	REVIEW OF NUMERICAL SIMULATIONS . . . . .	5-1
	Chamber Length Variation Simulations . . . . .	5-1
	Entrance Location Effects . . . . .	5-2
	Multiple Chamber Simulations . . . . .	5-4
	Comments . . . . .	5-6
6	DISCUSSION . . . . .	6-1
7	REFERENCES AND BIBLIOGRAPHY . . . . .	7-1

## CONTENTS (Continued)

<u>Appendix</u>		<u>Page</u>
A	REPRESENTATIVE FINITE-DIFFERENCE EQUATIONS . . . . .	A-1
B	A DISCUSSION OF THE GEOMETRIC ASPECTS OF PRESSURE MEASUREMENT . . . . .	B-1
	Introduction . . . . .	B-1
	Discussion . . . . .	B-4
	Conclusions . . . . .	B-18
C	PRESENTATION OF PRELIMINARY URS SHOCK TUNNEL TEST DATA . .	C-1

## LIST OF ILLUSTRATIONS

Figure		Page
1	An Example of Two-Dimensional Eulerian Mesh . . . . .	2-5
2	BRL Smoke Grid Model . . . . .	3-2
3	Pressure Profile Across a Shock Wave . . . . .	3-3
4	Velocity Profile Across a Shock Wave . . . . .	3-4
5	Pressure Profile Across a Reflecting Shock Wave . . . . .	3-6
6	Comparison of Numerical and Model Experimental Simulations . . .	3-9
7	Particle Velocity Comparison . . . . .	3-12
8	Velocity Time Profiles for Fixed Positions in the BRL Model. . .	3-13
9	Dimensions of Simulation Field . . . . .	3-14
10	Velocity-Time Profiles . . . . .	3-15
11	Experimental Flow Contours at Time = 215 $\mu$ sec . . . . .	3-22
12	Experimental Flow Contours at Time = 405 $\mu$ sec . . . . .	3-23
13	Experimental Flow Contours at Time = 713 $\mu$ sec . . . . .	3-24
14	Comparison of Model Configurations . . . . .	3-29
15	Comparison of Numerical and Experimental Full Scale Pressure Histories . . . . .	3-32
16	A Two Dimensional Simulation of a Free Field Test Case . . . . .	3-33
17	Orientation of Shelter Models with Respect to the Incident Shock Waves for Tests in Ref. 43 . . . . .	3-39
18	Grid for Comparison of Variable-Cell-Size Procedure . . . . .	3-46
19	Grid for Comparison of Variable-Cell-Size Procedure . . . . .	3-49
20	Cumulative Mass Influx as a Function of Time . . . . .	3-52

Figure		Page
21	Cumulative Total Energy Influx as a Function of Time . . . . .	3-53
22	Cumulative Potential Energy Influx as a Function of Time . . . . .	3-54
23	Cumulative Kinetic Energy Influx as a Function of Time . . . . .	3-55
24	Mass Influx as a Function of Computation Intervals . . . . .	3-57
25	Total Energy Influx as a Function of Computation Intervals . . . . .	3-58
26	Potential Energy Influx as a Function of Computation Intervals . . . . .	3-59
27	Kinetic Energy Influx as a Function of Computation Intervals . . . . .	3-60
28	Vena Contracta and Cell Size Geometry . . . . .	3-62
29	Curle's Representations of Early Inflow Process . . . . .	4-4
30	Blast Transmission into a Narrow Entrance and the Equivalent Process in a Long Entry . . . . .	4-7
31	A Simple Diagram of a Quasi-One-Dimensional Process . . . . .	4-8
32	Preliminary Wave Diagram of One-Dimensional Model . . . . .	4-11
33	Wave Diagram Approximation for Quasi-One-Dimensional Inflow Simulation . . . . .	4-14
34	Schematic of Jet Flow . . . . .	4-19
35	Centerline Velocity Distribution . . . . .	4-21
36	The Velocity Profiles for a Plane Jet . . . . .	4-22
37	Transient Boundary Layer Transformation to Steady Flow Analogy . . . . .	4-27
38	Approximated Boundary Layer Thickness Parameters for a Free-Flow Jet . . . . .	4-31
39	Average Entry Dynamic Pressure . . . . .	5-7
40	A Simple Graphic Representation of Flow Field Boundary Conditions . . . . .	6-2

## LIST OF TABLES

<u>Table</u>		<u>Page</u>
1	Flow Vector Comparison at Time = 214 $\mu$ sec . . . . .	3-18
2	Flow Vector Comparison at Time = 406 $\mu$ sec . . . . .	3-19
3	Flow Vector Comparison at Time = 713 $\mu$ sec . . . . .	3-20
4	An Outline of Numerical and Experimental Simulation Procedures . . . . .	3-42
5	Comparison of Multiply Variable Cells with Non-variable Cell Size . . . . .	3-47
6	Comparison of the Effect of Grid Coarseness on the Output of Numerical Simulations . . . . .	3-50
7	Comparison of Flow Particle Velocities . . . . .	4-10
8	Flow Field Parameters for Fig. 33 . . . . .	4-16

# NOTATION

$\mathbf{v}$	is the vector velocity
$\nabla$	is the vector operator
grad	is the vector operator
div	is the vector operator
$\rho$	is density
$t$	is time
$E$	is total energy
$e$	is internal energy
$p$	is pressure
$V$	is the control volume of an element
$A$	is surface area of the control volume
$\bar{A}$	is the area including the local normal unit vector orienting the surface
$a$	sound speed
$\gamma$	ratio of specific heats
$S$	is entropy

## SUMMARY

The objective of this work unit was to review and discuss the application of hydrodynamic codes in the Office of Civil Defense (OCD) shelter research program, and then consider the development of a conceptual model of the flow into and through blast-slanted basement shelters. The review selected a two-dimensional Eulerian code which numerically simulated inviscid, compressible flow without heat transfer. This form of code was shown to be the most suitable form of code for OCD needs on a cost-effectiveness basis.

The Eulerian equations were discussed, linked to their numerical form, and a complete set of numerical equations was appended for the reader's convenience. To provide the basis for the evaluation of this approach to future OCD problems a brief review of the internal workings of this form of code was undertaken. A bibliography was provided which will allow the reader to expand the brief review provided by this work unit.

To test the accuracy of numerical simulation the code was applied to several situations which represented conditions that would have to be reproduced in the shelter research program. These situations had been simulated experimentally so that a direct comparison between simulation procedures could be undertaken. The first cases reviewed the code's ability to reproduce a shock wave profile, and then surveyed the difficulties of correctly matching the time frames of rapidly decaying waves between experimental and numerical simulations. An appended section discusses some of these difficulties based on a geometric representation of the pressure—time profiles.

The first comparisons of experimental and numerical simulations of shelter situations used small scale model shelters. Shelter models used in scaled experiments (referenced in text) were reproduced in the numerical simulations to allow direct comparisons. Some difficulties in matching pressure—time profiles were noted, but an agreement of better than 90 percent between

the simulations was noted for the extremely short term transients of the filling process. The short term transients were also shown not to affect the long term fill history of the shelter.

Trajectories of points formed by a smoke grid in the same scaled experiments were used to test the accuracy of the numerically simulated flow field. The difficulty of precisely aligning the space-intensity profiles in time between simulations was again found. Procedures were developed to improve the comparison techniques. In the evolvement of these procedures it was established that the problem of timing comparisons was partly due to experimental error. An error analysis of the experiments was undertaken and pinpointed some errors in the experimental simulations. In general the numerical simulations were concluded to produce flow velocities that were about 10 percent higher along the inflow axis and about 5 to 10 percent lower in the other regions of the shelter.

Further evaluations were made against full scale shelters. Data were gathered from a full-scale field test using high explosives and from some preliminary URS shock tunnel tests. The numerical simulations reproduced the average pressure-time profiles within the simulated chambers to within 90 percent of the experimental value. The evolvement of an error range for the experimental data proved to be the limiting factor in developing a more precise estimate of variation between simulations.

The pressure data from URS shock tunnel tests, its evaluation, and data and analysis of flow visualization experiments were developed in an appended section. The presentation of the flow experiments included a consideration for the movement of spheres in the inflow. The flow data generated by the experimental and numerical simulations varied on the average less than 10 percent (within the limits of experimental accuracy). The conclusion reached was that the numerical simulation procedures were sufficiently accurate to be used in the shelter research program. Some potential problem areas were outlined for future study.



A section on cost and utilization of numerical simulations was included. Comparisons of the costs of numerical versus experimental simulations showed numerical simulations to be less costly. A common difficulty with data display for both simulation techniques was noted. The numerical simulations were shown to have the advantage of better output and monitoring control. The credibility and reliability of results were considered. The possibility of using a simple coarse grid code for general use on a small computer was discussed.

A review of the transient inflow process was undertaken. A review of incompressible flow studies provided some insight into the dynamics of jet formation. This review was followed by the evolution of an analytic model of the transition flow of a compressible gas into the chamber. The model used a quasi-one-dimensional representation of the inflow which was analytically defined by the method of characteristics. The method showed how imbalances in the flow occurred due to the high inflow velocity of the adiabatic expansion. The result was in effect a piston which drove the gas in the chamber ahead of it. The implications were discussed and verified from the experimental data presented in the report.

A review of the turbulence and jet spreading problem was undertaken and a bibliography on it and associated flow problems was developed. Many estimation procedures for growth and spread of turbulence were noted. The discussion used a simple boundary layer model to represent the spread of the flow. The model indicated that the boundary layer and turbulence effects were much more pronounced in the scaled experiments than would be expected in the prototype situation. The work indicated that the spread and growth of turbulence and boundary layers would probably not be of major proportions in full scale shelters.

A general view of associated flow problems was undertaken. The most significant of these problems was the effect of the inflow into the shelter on the reservoir conditions. The inability of the reservoir to completely

replace the effluent mass and energy was shown to reduce the driving pressure and also to decrease the driven flow. The comments were related to experimental results.

A series of numerical simulations were undertaken in support of this study. The problem of effective and economic data display arose, hence the results of these simulations were verbally described. The simulations treated a variety of geometric situations and included multiple room geometries. Implications of the observed results were discussed.

The last section summarized the review of the shelter flow in terms of a conceptual model of the flow. The use of a systems representation of the flow was used to show that a conceptual model on any general scale was probably not a reasonable goal. Some suggestions on how to circumvent this difficulty, and what areas of the flow problem might yield the most gains in future studies were outlined.

## Section 1 INTRODUCTION

One option being investigated for the future design and utilization of civil defense shelters is to keep the shelter open during an attack situation. The open entrances allow the blast environment to be transmitted into the shelter in the form of potentially hazardous high-velocity flows. These flows are of interest to the designer because of the structural loads that they form and their potential for causing injury to the shelter occupants.

The damage potential of the inflow into shelters for incident overpressures below 15 psi was documented in Refs. 1 and 2. These studies further showed that the induced flow field could be the major cause of human injury. The basis for the work in Ref. 2 was two earlier studies (Refs. 3 and 4) which first continued previous work on the prediction methods for chamber filling, and then the flow field within the chambers. These definitions illustrated the intensity of the inflow, provided some upper bounds on the magnitude of the flow-field parameters, and established where additional work was required to better define the inflows.

The second generation of experimental and analytical studies (Refs. 2 and 5) better defined the flow field and evaluated the effectiveness of flow-limiting devices. Within these OCD work units, some better estimates of inflow parameters were determined. Some of the previous problem areas did recur, namely, the description of the flow field during the early part of the filling process, the establishment of a model for the spreading of the inflow, and the development of circulating flows within the shelters.

To provide the shelter designer with more accurate information, all of these studies had to be linked together. The concept of the open-door, blast-slanted basement shelter (Ref. 6) requires the flow to be defined in greater detail since the feasibility of the concept is dependent upon the casualty expectations from all causes including the high velocity flows. The preceding

studies bounded the problems but did not provide the complete definition of the flows required to ascertain the feasibility of the concept. This study undertook to meet this specific need of the Office of Civil Defense planners by providing improved understanding of the flow as well as linking all the existing information into a conceptual model of engineering accuracy.

The study of these flows is complicated by the wide range of geometries encountered in basements, and by the transiencies of the flows. The component flows which make up the total flow field also change and interact. This complexity precludes an explicit analytic solution. The problem has been classically approached either through experimental studies, through analytical descriptions of the component flows (usually using quasi-steady-state approximations), or through numerical simulations. The final engineering solution to these qualitative and quantitative descriptions of the flows will be made through a synthesis of all three approaches.

Experimental studies will provide the data against which the analytically based techniques must prove themselves. The limitations of experimental procedures in the greatly space-time-dependent flows preclude an empirical solution, if any reasonable cost-effectiveness-benefit ratios are to be maintained. The variation in potential geometries would increase the necessary testing to unreasonable levels.

The use of numerical simulations poses similar problems, i.e., an excessive number of simulations is required to provide an empirical solution from the data. The numerical simulations do provide considerably more information on the space-time variable flows, in terms of both the flow and thermodynamic variables, at a lower cost per unit of information than the experimental methods. Even so, the numerical simulations will still not provide the overall solution required.

The use of the individual flow types presents analytic expressions for the flows. These can be approached as quasi-steady-state solutions and then pieced together. The quasi-steady solutions are not quite precise in the

formative stages of the flows; hence analytic models to describe the variations must be developed.

The numerical simulations are useful in this context because they provide a review of the formative flows and describe how they relate to form the entire flow field. The experimental data can then be used to review and check the accuracy of the simulations and of the conceptual flow model. The last stage is to relate quantitative prediction schemes to the qualitative model of the flow. The work to be described in this report used the above approach as described by the following statement of objectives and scope from the OCD work unit outline:

#### OBJECTIVE

The objective of the proposed work is to define (relative to the potential hazard to shelter occupants) the characteristics and intensity of the flows formed within civil defense basement shelters by the transmission of an air blast environment into the shelter.

#### SCOPE

The study will develop a conceptual model for the description of air blast phenomena inside an open shelter. The form of the conceptual model will allow its use in defining engineering equations and empirical relationships to describe the environment within the shelter during blast loading. In addition to analytical inputs, the study will use hydrodynamic computer code calculations to develop the conceptual model. As part of the work unit task, a brief review of existing codes will be made and a suitable code will be selected to perform the computer calculations and evaluated.

#### STUDY OUTLINE

The initial emphasis of the work unit was to consider the selection of the computer code and provide a brief description of code formulation and function. The selected code work was then applied to problems delineated in past work to determine the accuracy of numerical simulations relative to the shelter flows being studied. Concurrent with this effort, analytical studies were undertaken to begin developing the conceptual model. The computer code was used to support these studies as needed.

Because of funding constraints, the study had to rely strongly on development of bounds on the magnitudes of the flows. Primary emphasis was placed on attempts to develop a conceptual model and the computer code as outlined in the scope. The studies of particular facets of the flow were limited in scope and depth to a large degree by the funds available after the primary objectives had been met. These limitations affected the breadth and depth of the conceptual model, though the model presented is valid for engineering estimates.

The attempt to develop a conceptual model was undertaken as much as possible from a total systems viewpoint and, therefore, attempted to consider parameters such as blast wave-structure orientation, architectural/engineering constraints, and shelter management procedures. The inclusion of these other parameters forced the flow model into the proper perspective, that of being but one part of a larger system which controlled the flow's boundary conditions. The application of this technique was somewhat restricted under the above-mentioned funding constraint, but its use was felt to be necessary in the development of the most practical and realistic conceptual model of the flow in the shelter.

## Section 2

### COMPUTER FLOW CODE EVALUATION

In order to select a code to simulate the transmission of the air blast environment into the basement shelters, the constraints developed by flow-shelter environment must be considered. The incident and transmission flows are compressible flows with shock waves. The range of incident shock overpressure for open blast-slanted shelter design extends to about 15 psi; hence, heat transfer can be neglected. The flows into the shelters form jets, and turbulent momentum transport does occur in the transmission flow.

The shelter doors extend nearly the full height of the room, making flow in the shelter approximately two-dimensional. The various entrance configurations are in reality three-dimensional; but, by careful selection of geometries, the entries can be represented in two dimensions. The viscous interaction of the flow with the bounding walls is neglected. The lack of functional three-dimensional computer codes precludes their application to shelter research; therefore, the disadvantages of the two-dimensional approach will have to be accepted and evaluated to determine the range of deviations they create.

The techniques available to compute the properties of compressible flow into chamber, including shock waves, for two-dimensional space-time coordinates are limited. One of the most direct methods uses numerical step-wise procedures to compute the flows through zones or cells in the flow field by means of finite-difference representations of the equations of motion in either a Lagrangian or Eulerian mesh. The zones of the Lagrangian system move and distort with the flow. This feature allows particles to be followed in space and time, but significant inaccuracies are developed when large fluid distortions occur. The Eulerian mesh is a fixed grid in space and time through which this fluid flows. This representation allows greater fluid distortion without loss of accuracy, but it cannot distinguish between gases and particles within the flow field. Some codes, such as the PIC code,

combine the two systems, using the best features of each; but they require a large computer memory and have long running times.

The strongly space-time-dependent flows found in the basement shelters introduce considerable fluid distortion. The Lagrangian system of representation is therefore not a good coordinate system for these problems. The disadvantage entailed by the Eulerian system's not being able to distinguish between gases within the flow is not significant. Air is the sole gas involved, and since the shock strengths are relatively low, entropy increases are minor and differences across contact surfaces are minimized. Knowledge of particle location is unnecessary in shelter research; hence, use can be made of a strict Eulerian system, with its reduced computer memory and running time requirements.

URS had previously undertaken a similar review process of available codes and had established that the Eulerian system would best meet the requirements of general two-dimensional shock-wave interaction problems. The selection process not only considered the preceding factors, but also took into account the machine time and storage required to execute any given problem. In that these parameters represent costs to be incurred by the project, it was necessary to consider cost-effectiveness parameters in the selection process.

The specific code URS selected was the Fluid-In Cell (FLIC) technique developed by Gentry, Martin, and Daly (Ref. 7) of Los Alamos Scientific Laboratory to compute two-dimensional time-dependent compressible flows. The FLIC code uses a Eulerian mesh of cells in which improved (with respect to earlier Eulerian codes) energy, mass, and momentum transport calculations are used to reduce the computer memory requirements and to increase the computational speed. The flexibility of the FLIC code is enhanced by allowing boundary and initial conditions to be input for each specific problem without code modifications.

The development of the FORTRAN IV version of the FLIC code was undertaken by URS as an in-house project during recent years. It had been utilized in a



previous OCD work unit and shown to provide considerable information within engineering accuracy (approximately accurate to  $\pm 0.9$  of the actual value). Within the spectrum of Eulerian codes there seems little significant variation as to their properties. The review of the available Eulerian codes undertaken by this study reconsidered the selection process relative to OCD shelter problem needs and also included a review of more recently developed hydrodynamic computer codes.

The review did not find another method that would provide any significant advantages over the FLIC technique. The evaluation also weighed the cost of developing a new code against the cost of the already operational FLIC code for use in this project. Based on the review and the cost constraints, the FLIC code was selected for use in order to conserve funds. A description of general code capabilities and availability relative to Office of Civil Defense needs will be presented to shorten the review process for future problems.

#### THE EULERIAN METHOD

The problem of simulating a general compressible flow is complicated by several factors, as pointed out by J. Von Neuman and R. D. Richtmyer in their pioneer work on hydrodynamic codes (Refs. 8 and 9):

- The presence of shock waves across which the thermodynamic variables are discontinuous
- The difficulty of relating boundary conditions across these discontinuities
- The space-time variation of the shock waves and of the flow field itself
- The motion of the waves and the flow-field composition are not known in advance; hence the boundary conditions on the shock waves are space-time dependent

Von Neuman and Richtmyer proposed a method of introducing an artificial viscosity term into the difference equations of motion to smooth out the

discontinuity and make the equations stable. This procedure is the basis upon which succeeding codes were developed.

By means of the smoothing factor, the equations of motion can be written in a general form. A given flow field can be divided into sections called zones or cells and a set of initial and boundary conditions specified. The generalized equations can then be applied sequentially and the flow field computed in monotonically increasing time. The modern high-speed digital computer reduces to practical limits the computation times and intricate bookkeeping required.

The following discussion of the Eulerian computation sequence for a planar two-dimensional isentropic compressible flow will use a mesh of equal spacing. The programmer defines the mesh size, the geometry of the field, and the boundary and initial conditions. The boundary conditions include the boundaries of the field as well as the boundaries of objects within the field (see Fig. 1).

A mesh generation and bookkeeping process must be evolved to control the computational procedure. Once the mesh is established and the field boundary defined, the process of defining objects within the field must be undertaken. The bookkeeping must insure flow is stopped at all solid boundaries and must keep the order of the cells. When this is done, the computation of the flows can be undertaken.

Euler's equations of motion, which form the basis for the computational sequence to be described, must fulfill the following set of conditions everywhere in the flow field (Ref. 10). Every particle in the fluid must obey Newton's Second Law at all times. The boundary conditions must be fulfilled at the boundaries of each cell. The continuity equations must be satisfied at all points in the fluid except at singular points. The importance of these conditions will be noted in the later description of the computational phases of the Eulerian codes.

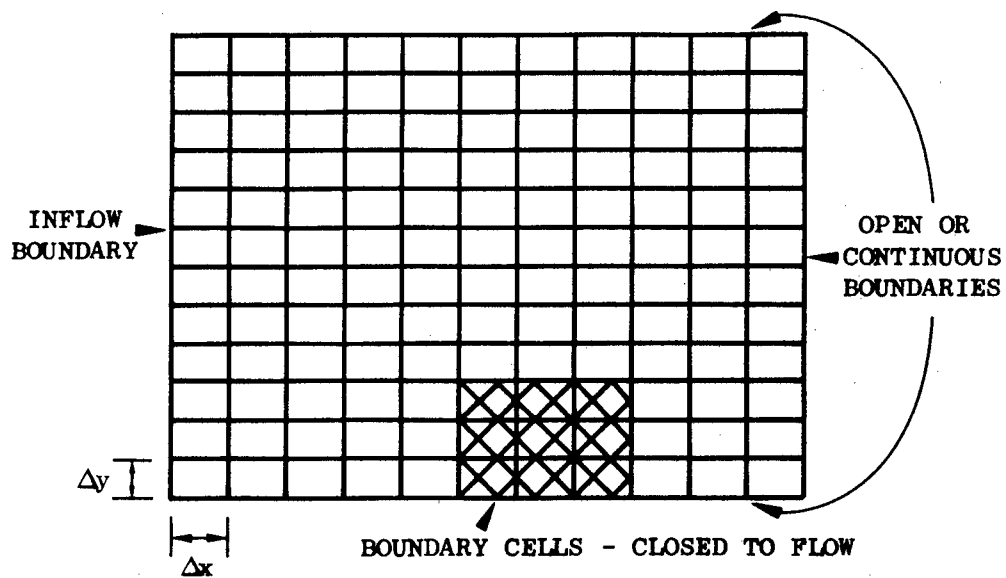


Fig. 1. An Example of Two-Dimensional Eulerian Mesh

The basic equations of motion are those stemming from the equation of state and the conservation of momentum, energy, and mass. There are five fundamental parameters described as a function of two spatial coordinates at any instant of time (Ref. 11).

$$\frac{\partial \rho}{\partial t} + \text{div } \rho \mathbf{v} = 0 \quad \text{Mass} \quad (1)$$

$$\frac{\partial \mathbf{v}}{\partial t} + \mathbf{v} \cdot \nabla \mathbf{v} + \frac{1}{\rho} \text{grad } p = 0 \quad \text{Momentum} \quad (2)$$

$$\frac{\partial S}{\partial t} + \mathbf{v} \cdot \text{grad } S = 0 \quad \text{Energy} \quad (3)$$

$$p = p(\rho, S) \quad \text{State} \quad (4)$$

where  $S$  is the entropy, and  $E$ , the total energy per unit mass, would be defined by  $E = e + 1/2 (\mathbf{v})^2$ . The use of the d'Alembert-Euler acceleration formula (Ref. 12) in Eq. (2) should be noted, i.e.,

$$\text{acceleration} = \frac{\partial \mathbf{v}}{\partial t} + \mathbf{v} \cdot \nabla \mathbf{v} \quad (5)$$

where  $\frac{\partial \mathbf{v}}{\partial t}$  is the local acceleration and  $\mathbf{v} \cdot \nabla \mathbf{v}$  is the convective acceleration. This representation shows both the spatial and temporal variations of acceleration with the flow field and is useful for interpreting the flow field characteristics to be discussed later in the report.

There is a more convenient method than the spatial presentation above for developing the difference equations for the Eulerian codes. The corresponding hydrodynamic equations in Eulerian coordinates for compressible isentropic flow in the integral form as defined by Rich (Ref. 13) are:

$$\int_V \frac{\partial}{\partial t} \rho \, dV = - \oint_A \rho \mathbf{v} \cdot d\bar{\mathbf{A}} \quad (\text{conservation of mass}) \quad (6)$$

$$\frac{\partial}{\partial t} \int_V \rho \mathbf{v} \, dV = - \oint_A p \, d\bar{\mathbf{A}} \quad (\text{conservation of momentum}) \quad (7)$$

$$\frac{\partial}{\partial t} \int_V e \, dV = - \oint_A p \mathbf{v} \cdot d\bar{\mathbf{A}} \quad \text{(conservation of energy)} \quad (8)$$

$$p = p(\rho, E) \quad \text{(equation of state)} \quad (9)$$

The integrals are evaluated over the volume  $V$  of an element of surface  $A$ . These equations are commonly referred to as the conservation or divergence equations.

A brief review of the properties of the equations will be presented since they form the basis for the computational scheme used. Equation (6), the conservation of mass (or in this form sometimes called the "Reynolds transport theorem," states that the time rate at which mass increases within the volume is equal to the net rate of mass flux across the surface of the volume. In terms of the Eulerian calculation grid, each cell becomes a volume of unit depth with the surface which must meet the above conservation of mass condition.

Equation (7), the integral expression for the conservation of momentum, indicates the condition that at any given time the rate of change of momentum in the control volume must equal the resulting force on the volume. The resulting force is the net stress or pressure acting on the surface area. The last conservation condition, the energy equation as given by Eq. (8), expresses the similar conditions for energy that the Reynolds transport theorem expressed for mass. The conservation of energy for a control volume at any given instant requires that rate of accumulation of energy in the form of heat is equal to the rate of energy increase within the control volume and the rate work is done by the boundaries on the surroundings. The direct relationship between the integral form and its control volume representation to the mesh of cells is helpful in understanding the computational basis of the Eulerian codes.

The preceding basic equations are transformed into difference equations which correspond to the flow field grid. The transformation occurs in relation to a prescribed calculation sequence, which will be described in the following paragraphs. The relationship of the sequence to the conditions for

an Eulerian system of equations described above should be noted. The sequence will be considered, but the difference equations will not be presented in the body of this report. For the reader's convenience a full set of Eulerian Difference Equations for two-dimensional flow, from the work of Rich (Ref. 13), is presented in Appendix A. A brief discussion of the differencing and stability criteria for the equations will be presented after the computational sequence is considered.

The first phase of the calculation procedure fixes the fluid within the cell, i.e., there is no movement of fluid across the boundaries of the cell. The conditions of the preceding step are applied to the fluid element as boundary and initial conditions. By applying the equations of motion and state, a new set of values (termed intermediate values and defined by the tilde symbol) for the velocities and internal energy within the cell can be calculated. The procedure is applied to every cell in the mesh.

The second phase of the calculation procedure allows flow to occur across cell boundaries based on the intermediate values calculated in phase one. The mass and energy flow out of each cell is tabulated. During this phase energy, mass, and momentum are conserved, but no change in the flow or state variables is calculated.

The third phase of the computation sequence sums the mass and energy interchange carried out in phase two. The first step of the calculation determines a new value of density for each cell in the mesh. By applying conservation of energy and momentum to the new flow and state variables, values of the flow velocity and specific energy in the cell can be calculated.

The sequence of operations must occur at all cells within the mesh that have open boundaries on all sides. For cells which do not have four open sides, a series of new conditions exists. One of the two types of these cells uses completely closed boundaries, i.e., the cell is an obstacle through which no flow occurs. The other type of cell is a partial cell, in which a portion of it allows flow to occur and the remainder is a closed cell. These three types of cells establish the flow field and its boundary

conditions. The control portion of the code program insures that these boundary conditions are adhered to during the computational sequences. The only remaining information required to begin the computational sequence is the initial conditions of the flow field. Use of the code thus permits one to ascertain (in monotonically increasing temporal sequence) the flow field properties.

To better understand the validity and meaning of the computed results, the following items will be considered.

- Differencing techniques
- Expansions and errors
- Stability
- Internal dissipation
- Cumulative errors

The first three items are problems which must be controlled if the code is to work at all. The latter two items may exist at undesired levels even if a stable difference scheme exists.

#### DIFFERENCE EQUATIONS

There are many different approaches to the difference equations which can be applied to the general hydrodynamic internal equations. The various differencing techniques and their advantages and shortcomings can be found in discussions in Refs. 13 through 35 and will not be considered here. The following discussion will, however, review those techniques commonly used in the two-dimensional hydrodynamic codes and, in particular, those of the FLIC code employed in this study. The review will be based on the work in Refs. 13 through 17 and will present only that material needed to provide a background for the later discussion of code applicability to the OCD type of aerodynamic problem.

It was shown earlier that the conservation equations could easily be applied to the individual cells of a finite-difference mesh. The equations presented are used in the hydrodynamic codes in their equivalent numerical

difference expressions which are obtained by numerical forms at a given time. The numerical forms of the equations are then applied with respect to the calculational sequence discussed earlier.

The final phase of the calculation sequence closes the cell boundaries to inflow; hence the mass and average density of the fluid in the cell must remain constant. The density term can be removed from the time derivative in the control volume integration of the conservation of momentum and energy equations. By using simple linear averages for the pressure and velocities at the boundaries between cells, difference expressions for the time derivatives can be written and the resultant expressions for the intermediate velocities and specific energies can be written.

The FLIC code used in this review was developed to allow the use of either planar or cylindrical coordinates. To allow for the divergence of the cylindrical field in the radial direction, the FLIC equations resemble those of the Eulerian portions of the PIC codes (Ref. 14). The differencing technique selected for FLIC also varies slightly from the equations presented in Appendix A, particularly for the energy equation which follows the Zip-type differencing format described by Harlow (Ref. 14).

The authors of the FLIC code point out that the difference between the FLIC format and that presented in Appendix A is the use of forward-backward time averages for velocity values, i.e.,  $\bar{u}_{ij}^n = \frac{1}{2} (u_{ij}^n + \tilde{u}_{ij}^n)$ . The use of this differencing format limits the occurrence of negative internal energies in the computational procedure and also reduces the tendency to destroy entropy. The occurrence of negative internal energies results from computational instabilities and fluctuations, which tend to decrease the internal energies in individual cells. Harlow (Ref. 14) presents the condition

$$\left| \frac{\tilde{e}^{(n)} - e^{(n)}}{e^{(n)}} \right| \leq 2(\gamma-1) u_{\max} \Delta t \left( \frac{1}{\Delta x} + \frac{1}{\Delta y} \right) \quad (10)$$

as the criterion for limiting the occurrence of negative internal energies for a polytropic equation of state,  $p = (\gamma-1) \rho e$ .



In comparing the equations presented in Appendix A with those of Gentry, Martin, and Daly in their presentation of the FLIC code (Ref. 7), the appearance of the artificial viscosity term in the pressure term of the equations can be noted. The use of the artificial viscosity term enhances the stability of the equations in the presence of shock waves in the flow field. The value of the term is controlled by the conditions at the boundary interfaces and by an arbitrary constant. A more thorough discussion of the application procedure can be found in Ref. 7.

The form of the artificial viscosity, or damping factor, in the equation varies quite widely. The methods that can be used are discussed and compared by Emery in considerable detail in Ref. 18. The von Neuman-Richtmyer form of the damping factor need not be used. For example, the equations presented in Appendix A do not include the use of the specific external damping term, but rather use a term inherent to the Taylor series expansion terms. The FLIC code on the other hand does use the von Neuman-Richtmyer artificial viscosity term as modified by Landshoff (Ref. 15).

The artificial viscosity term normally is needed in regions where the gradients of flow field properties are steep. The strength of the dissipative mechanism is a function of the velocity and the mesh size. However, neither of these conditions is an absolute guide. For example, the effect of artificial damping must be reduced in rarefaction regions and enhanced in stagnation regions. To meet all these conditions, various dissipative terms are used. The application of the proper term is accomplished by the computational controls through a series of test conditions.

The use of the artificial viscosity term enhances the stability of the difference equations, but it does not fully eliminate the oscillations behind the shock. Landshoff's method does provide fairly accurate representation of steep gradients. Relative to the needs of the OCD studies of chamber filling, the steepness of the gradients is a useful feature, and the small oscillations are a minor disturbance or perturbation in the presentation of data.

The use of this procedure does introduce the bound on the computational time step discussed above, i.e., the maximum allowable time step is a function of the cell size and the maximum flow velocity. To insure stability, the following further conditions are necessary (Ref. 7):

$$\frac{|u|}{\Delta x} \Delta t < 0.4 \quad (11)$$

$$\frac{c \Delta t}{\Delta x} < \lambda_{\min} \quad (12)$$

$$\text{where } \lambda_{\min} = \text{Min}[1 < B, -\gamma B + (\gamma^2 B^2 + 4\gamma)^{\frac{1}{2}}, \gamma B/(\gamma-1)] \quad (13)$$

and B is a constant used to determine the magnitude of the viscous pressure term and c is sound speed. The inequality expressed in Eq. (11) was found to cause some minor difficulties in some instances, and a 0.3 value on the right-hand side was found to be a more reliable condition. This equation sets the condition that a mass point in a cell cannot flow more than 0.3  $\Delta x$  in one time step ( $\Delta t$ ), thus insuring that a cell cannot empty itself. These conditions are of practical interest for shelter research since they provide one of the main limits on the computational speed of the codes.

Variation of the FLIC equations, as presented in Ref. 7, from the equations presented in Appendix A occurs in phase 2 of the computational sequence. The main difference is found in the determination of the flow-parameter values at the boundaries of the cells. The FLIC code uses the donor-cell method of differencing, in which the transport properties are proportional to the properties of the donor cell. The authors indicate an increased stability when used in conjunction with the artificial viscosity terms. The preceding factors are also used in the last computational phase.

The preceding discussion has shown dissimilarities exist between the various types of differencing techniques. Of primary interest to the OCD shelter program is the effect these dissimilarities have on the computational accuracy of the blast-induced flows into and through the shelters. Further review of the numerical equations will not be undertaken, only a brief outline of their related characteristics. Similarly, the development of

equations for boundary cells and partial cells will not be reviewed. The attached bibliography provides a full description for the reader who wants a more thorough coverage and more recent innovations.

The Eulerian difference equations, as used in the more common numerical techniques, have been shown to conserve mass, energy, and momentum (Ref. 13). Non-conservative conditions could result due to computational errors, which may simply be cumulative errors in the large number of calculations made. These errors are easily checked by keeping a running tabulation of the total mass, energy, and momentum in the system. If the tabulation remains consistent with the accuracy of the computing machine, one check on the computational accuracy has been made.

Even if exact conservation is maintained, errors can exist in the numerical solutions. Local perturbations, mathematical instabilities, spreading of discontinuities, expansion and internal dissipation, mathematical errors, and exclusion of some non-ideal effects can cause temporal deviations from the simulation's real world counterparts. It is this type of variation that is of most significance in the consideration of shelter flows.

In the initial discussion of the FLIC equations (Ref. 7), the authors discussed the errors in the finite-difference equations by expanding them in a Taylor series. In reviewing the expansions, the error terms were considered to cause artificial diffusion of mass, momentum, and energy where sharp gradients in flow properties occur. The physical effect is to cause the gradients to spread out spatially.

The distention of the gradients is a function of the cell size. For example, the thickness of a shock wave is usually spread over 3 to 5 cells by the dissipative factors. The spread factor for the von Neuman Richtmyer artificial viscosity is given by  $[8B/(\gamma + 1)]^{\frac{1}{2}}$ , where B is a critical constant in the damping, ranging in value between 0.2 and 0.4. To get the best resolution, the cell mesh must be kept small. The smaller the spatial

or time differences, the smaller the error in the finite-difference approximations. By following this argument, infinitely small cells could be used, but a limit in available computer memory and computational time is soon reached.

Another source of error is violation of the principle of Galilean invariance (the relative motions of particles are the same irrespective of the frame of reference). This principle is particularly important when a shock wave moves into a flow field, as opposed to a stationary gas. At equal Mach numbers, the profiles of the flow parameters across the shock wave should be identical. Reference 7 has shown Galilean invariance is violated for a shock wave propagating into a fluid moving at one-half the shock wave's velocity. A greater spatial diffusion occurred due to increased velocity relative to the computing mesh. In the general case, the diffusion is a function of the value of the parameters involved (Mach number, cell size, gas properties, etc.). In shelter studies, these variations must be considered because strong gradients do exist within counterflows.

Other regions in which the diffusion terms can cause deviations are stagnation and rarefaction regions. In stagnation regions, there is no flow; hence the artificial viscosity which is proportional to flow velocities is of negligible strength. It has been shown (Ref. 7) that if the conditions expressed by Eqs. (12) and (13) are met, then a stable solution is possible. The condition is generally the same for all small-magnitude flows. Similarly, adjustments for the artificial viscosity must be used in rarefaction regions.

### Section 3

#### CODE APPLICATION

The discussion in Section 2 reviewed some of the general background, limitations, and structure of the Eulerian codes. The usefulness of the codes in shelter applications depends on a number of factors: the ability to accurately reproduce the blast-induced flow environment in the shelter, the cost of reproducing the environment, and the ability to display and utilize the generated data. The accuracy of the code is the most important of the factors, because if it does not exist, cost and utilization are only academically interesting. Hence the discussion of application will begin with a consideration of accuracy.

#### ACCURACY CONSIDERATIONS

Since accuracy is related to a comparison of the numerical simulations with prototype conditions, a group of experiments was numerically simulated. The first series of these simulation-to-experiment comparisons was made using scaled data gathered at the Ballistic Research Laboratories (Ref. 4) for OCD. These experimental data relate to the model shown in Fig. 2. Both pressure-time histories and smoke grids to measure particle velocities were recorded for the model.

The evaluation will begin by reviewing the code's simulation of a classical step shock wave. The pressure and velocity spatial profiles for a 1/8-in. mesh size are shown in Figs. 3 and 4. Since the profile is a function of the number of cells, finer mesh would provide a correspondingly reduced spatial profile. The overshoot and damping characteristics of the code can also be observed.

The steepness of the change of pressure and velocity variables in these profiles approaches 1/4 in. for the cells shown. This rise is directly comparable to the rise-time associated with the pressure sensors used by

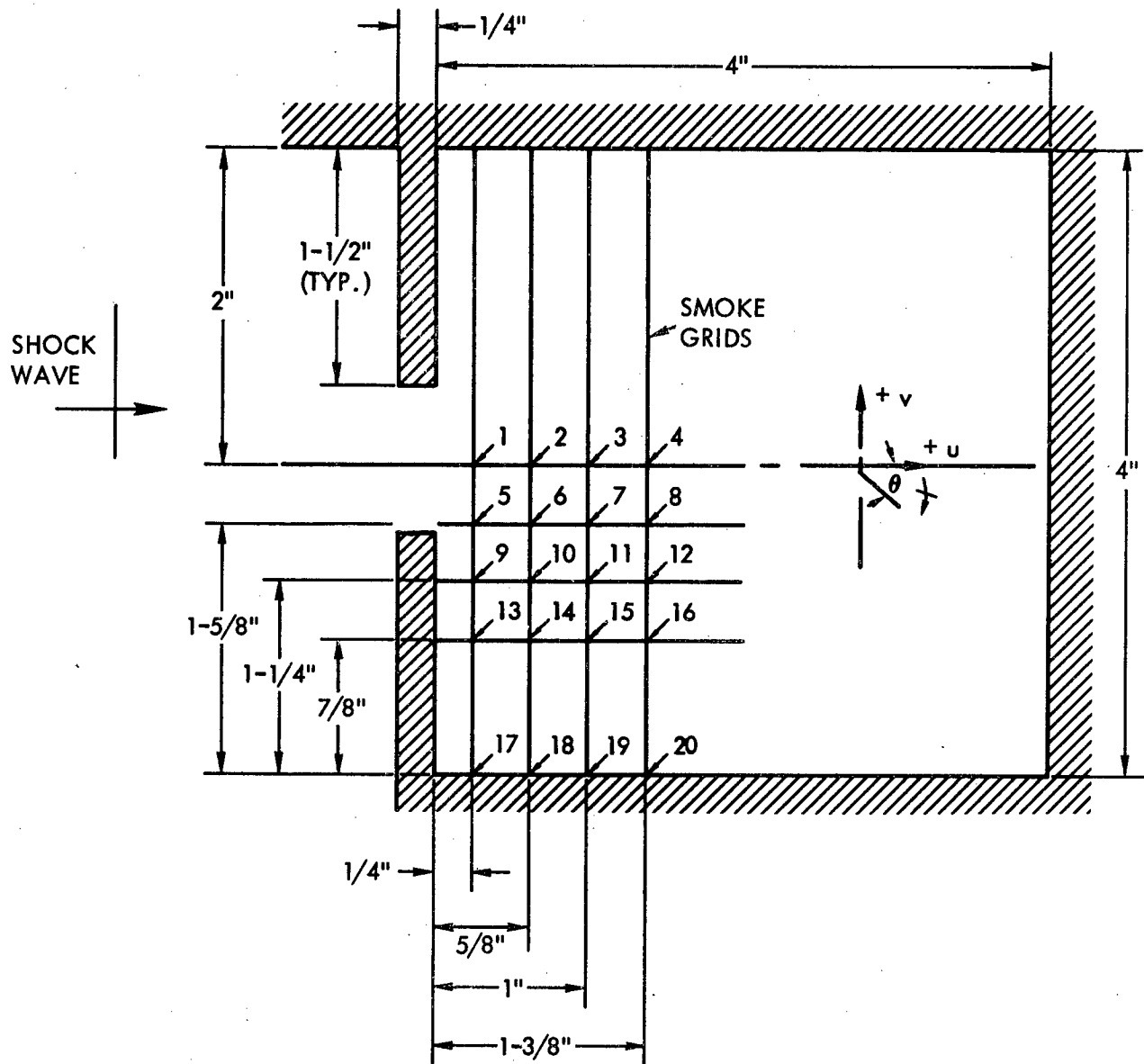


Fig. 2. BRL Smoke Grid Model

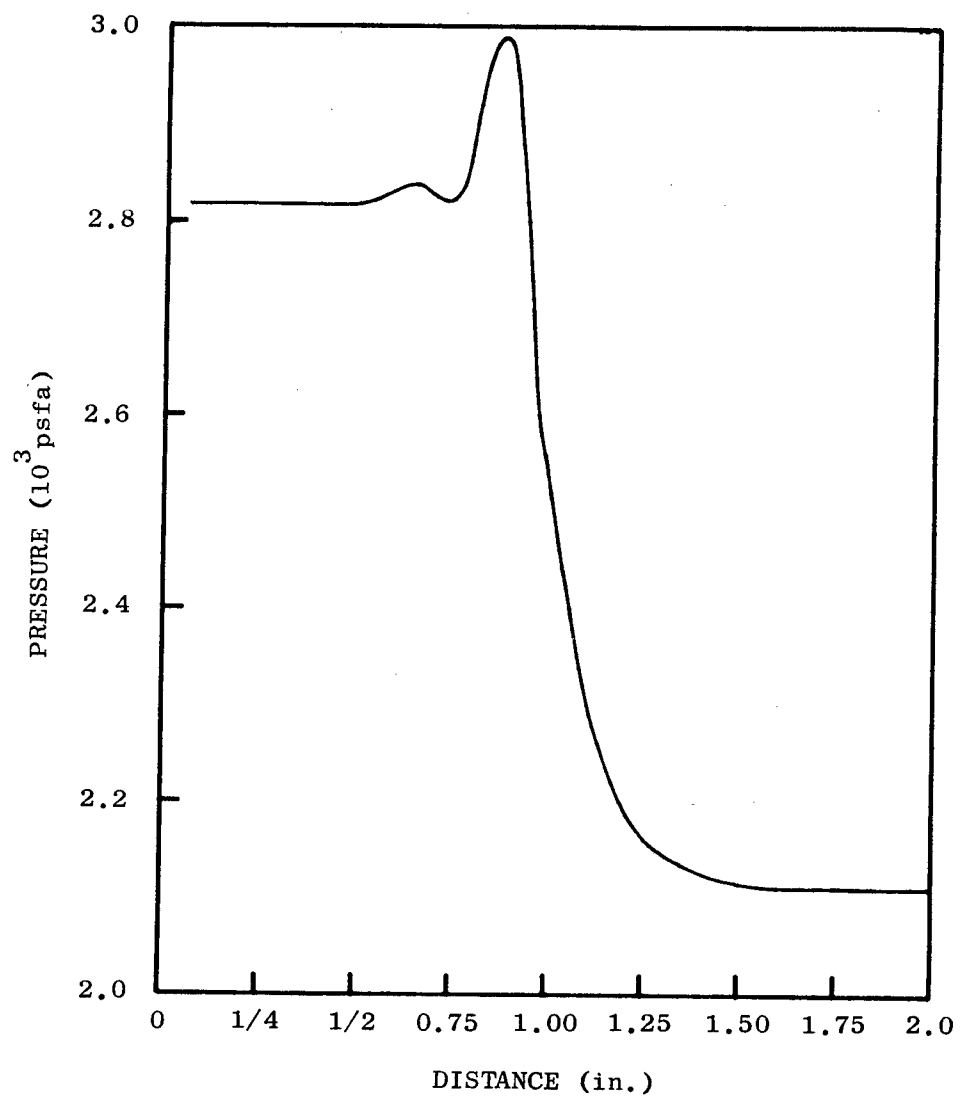


Fig. 3. Pressure Profile Across a Shock Wave

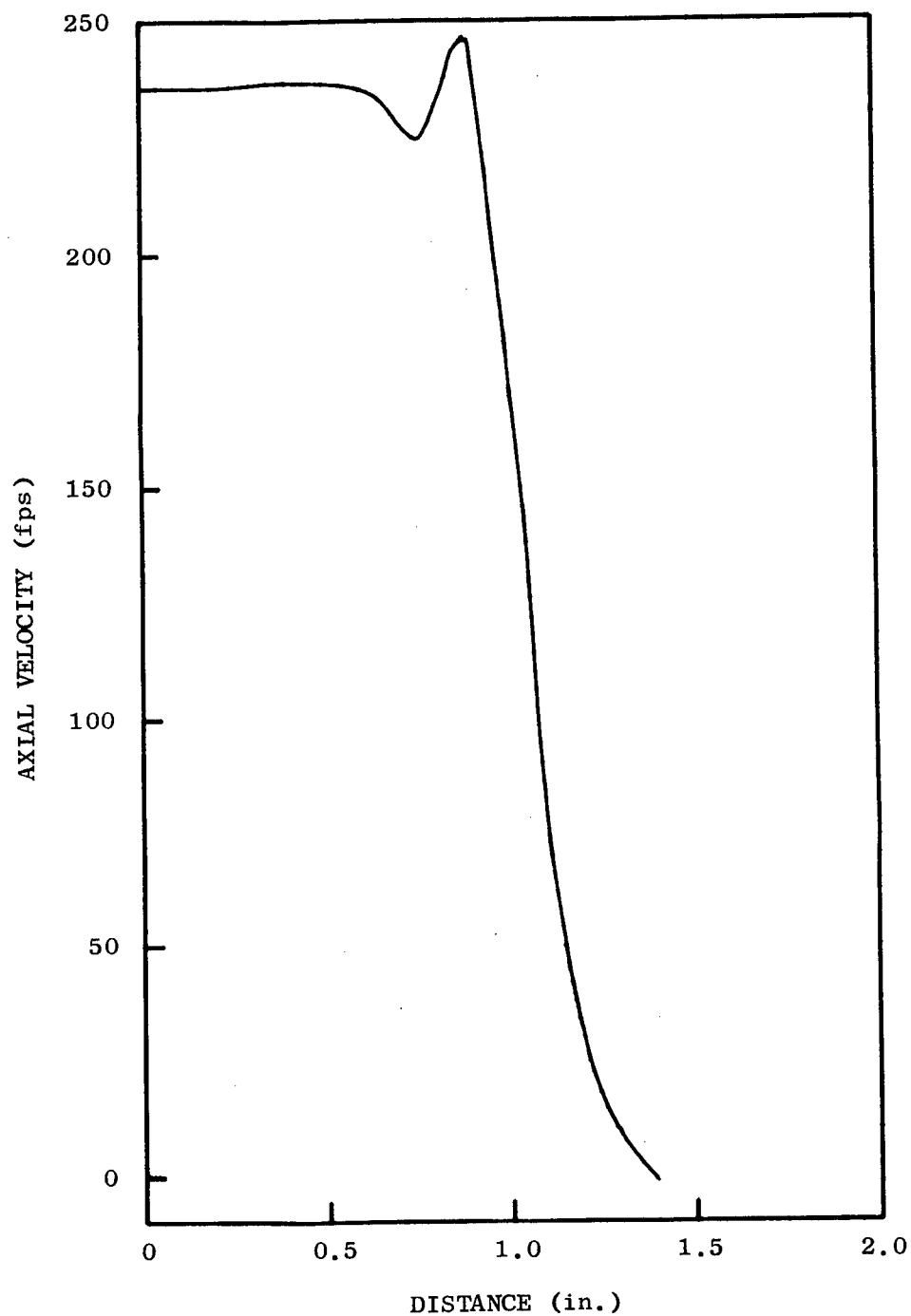


Fig. 4. Particle Velocity Profile Across A Shock Wave



BRL in the experiments. The overshoot added another 1/8 in. to the profiles before the "step" condition was reached. The earlier work (Ref. 2) in this area showed this to be of negligible importance to the shelter studies because short-term pressure transients did not play a major role in damage predictions.

Another advantage gained by the steep profiles is that they allow the use of coarser grids in the simulation procedure without degrading resolution. During the period between these reports, the FLIC code was modified to accommodate variable cell sizes to increase local resolution without increasing memory requirements (to be discussed more fully in a later section). The ability to use finer grids where resolution was required put still less of a premium on profile steepness.

A stability analysis was undertaken by independently varying the coefficients of the artificial viscosity terms, the cell size, and the computational time step increments. From this analysis a smoother, though slightly less steep (about 3 to 4 cells), rise was selected. A pressure-distance-time profile series is presented in Fig. 5 for a regular reflection process in a mesh incorporating two cell sizes.

The test shown in Fig. 5 is also useful in evaluating the effect of mesh size changes, the Galilean invariance, the code properties at reflective boundaries, and the stability of the code in low-flow regions. With the exception of the Galilean invariance, the test was favorable. The spatial spreading of the shock front, although present, is not of unusual proportions in comparison to similar results presented in the literature.

Although the preceding provides some insight into the general accuracy of the codes, there are specific questions that must be considered concerning the accuracy of the codes relative to the reproduction of flows in basement shelters. Attention is being directed to the main damage mechanism (the flow) rather than to the pressure profiles of transient shock waves. One source of

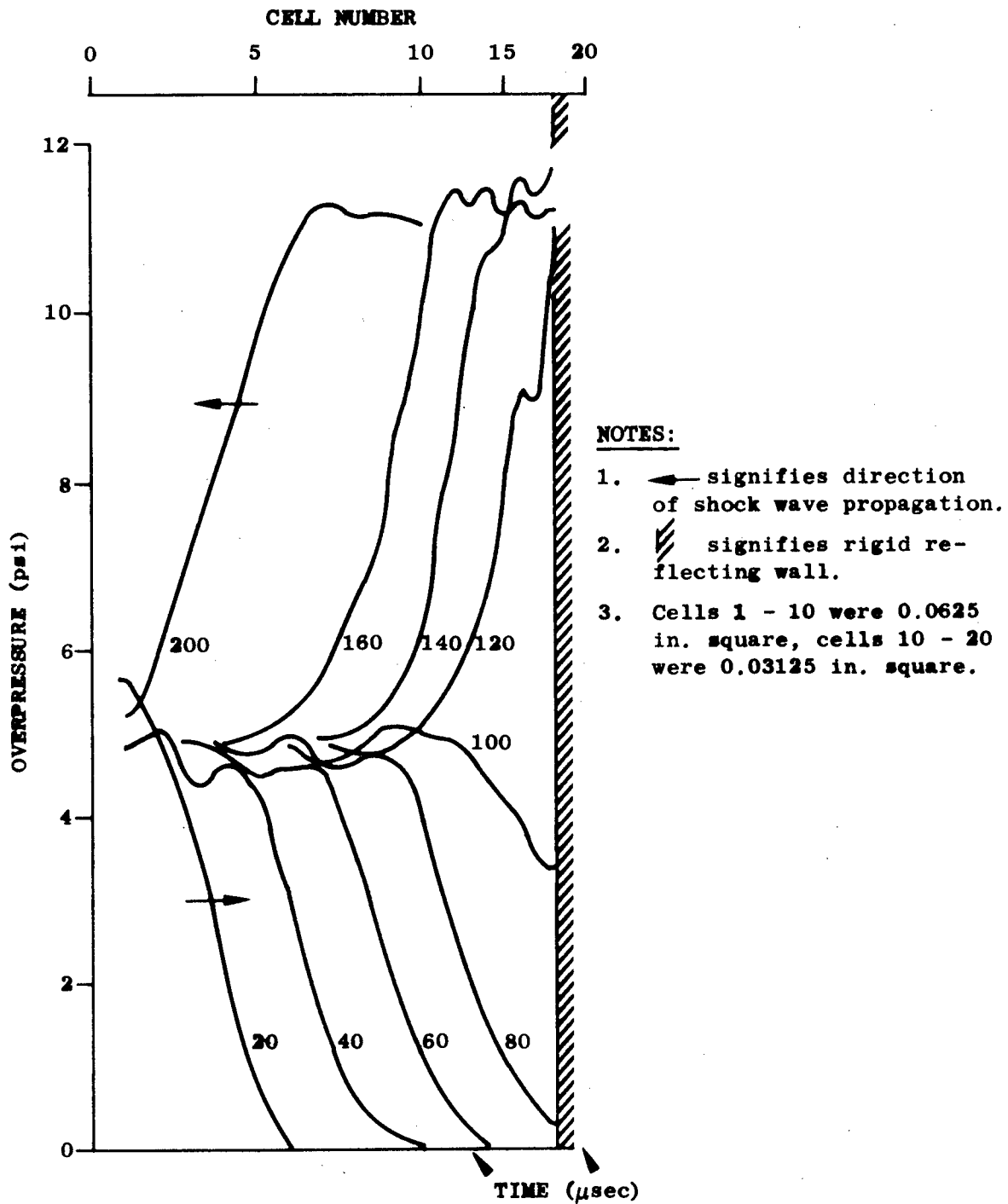


Fig. 5. Pressure Profile Across a Reflecting Shock Wave

information available from the BRL experiments is the individual pressure histories within the chamber, which provide an indirect measure of one of the flow-field parameters.

These pressure histories were compared with the numerical simulations on a preliminary basis in Ref. 2 and reasonably good agreement was noted. A more thorough review was undertaken and will be presented in the following pages. The difficulty in using the data is caused by the shortness of the histories presented and the rapid transients included in them. Although not of direct interest to the flow problems being considered, the inclusion of the transients provides a severe test for the code.

The spatial dispersion of the steep gradients in the flow must be interpreted to coincide with a point in space. The arrival of the shock wave at a point will be measured from the center of the dispersion and not from its leading edge. Similarly, if we are to compare space-time points, the pressure records must be adjusted to a point, rather than the average pressure they monitor.

The paucity of information on how to approach the interpretation of the averaging of the applied pressure by transducers led to the inclusion of the analysis in Appendix B. This appendix is based on some referenced notes and should be useful to the reader in considering the averaging process in more detail. Using these techniques, a comparison of pressure monitored at the center of the gage versus the center of a comparably located cell could be undertaken.

In the earlier comparison (Ref. 2), the gage-sensing element was 0.218 in. in diameter and the cells used were 0.125 in. square. As mentioned earlier, this geometric ratio gave identical "rise times." This term is used to refer to the time it takes the sensed or calculated pressure (or other flow variables) to reach a step value in response to the incidence of a classical step shock wave, i.e., the time it took the shock front to cross the sensing element.

Although matched on a rise time basis, the pressure gage monitored an area 2.3 times greater than the cell of the numerical simulation. The implications of the use of the averaging process involved for both simulations is described in Appendix B. Another consideration related to the use of experimental data for the evaluation of the numerous simulations is the measurement accuracy of the monitoring and recording systems. The systems had a 5 percent error in amplitude measurement and could respond in the range of 230 kHz without resonance (about a 3  $\mu$ sec rise-time capability in response to a step pulse).

The present comparison is for the same problem, but 1/8- by 1/4-in. cells were used. The cells were positioned with their long sides parallel to the center line of the entry. The new cell size increases the resolution of the numerical simulations and represents about the coarsest grid employed in the numerical simulations for development of the conceptual model. The comparison of pressure histories for two gage positions is given in Fig. 6.

Some deviations in the profiles can be noted in regions where sharp gradients occur. The experimental data were taken from reproductions in Ref. 4 and are estimated to be accurate to about 7 percent. Some of the resolution in the code was lost in using large printout intervals; however, the primary cause of the loss of the high-frequency components of the traces is the large cell size.

In addition to losing some of the finer characteristics, there was also a phase shift (10 to 50  $\mu$ sec) in some regions of the histories. The phase shifts are due to the spatial dispersion of the wave in combination with the coarse grid sizes. Comparisons of the calculated data at selected other locations show equal or improved resolution. Since the original data were not available, further comparative work was not undertaken. The relatively good agreement for the coarse grid used provides sufficient confidence in the reliability of the code to reproduce the pressure distributions that correspond to the flow fields of interest.

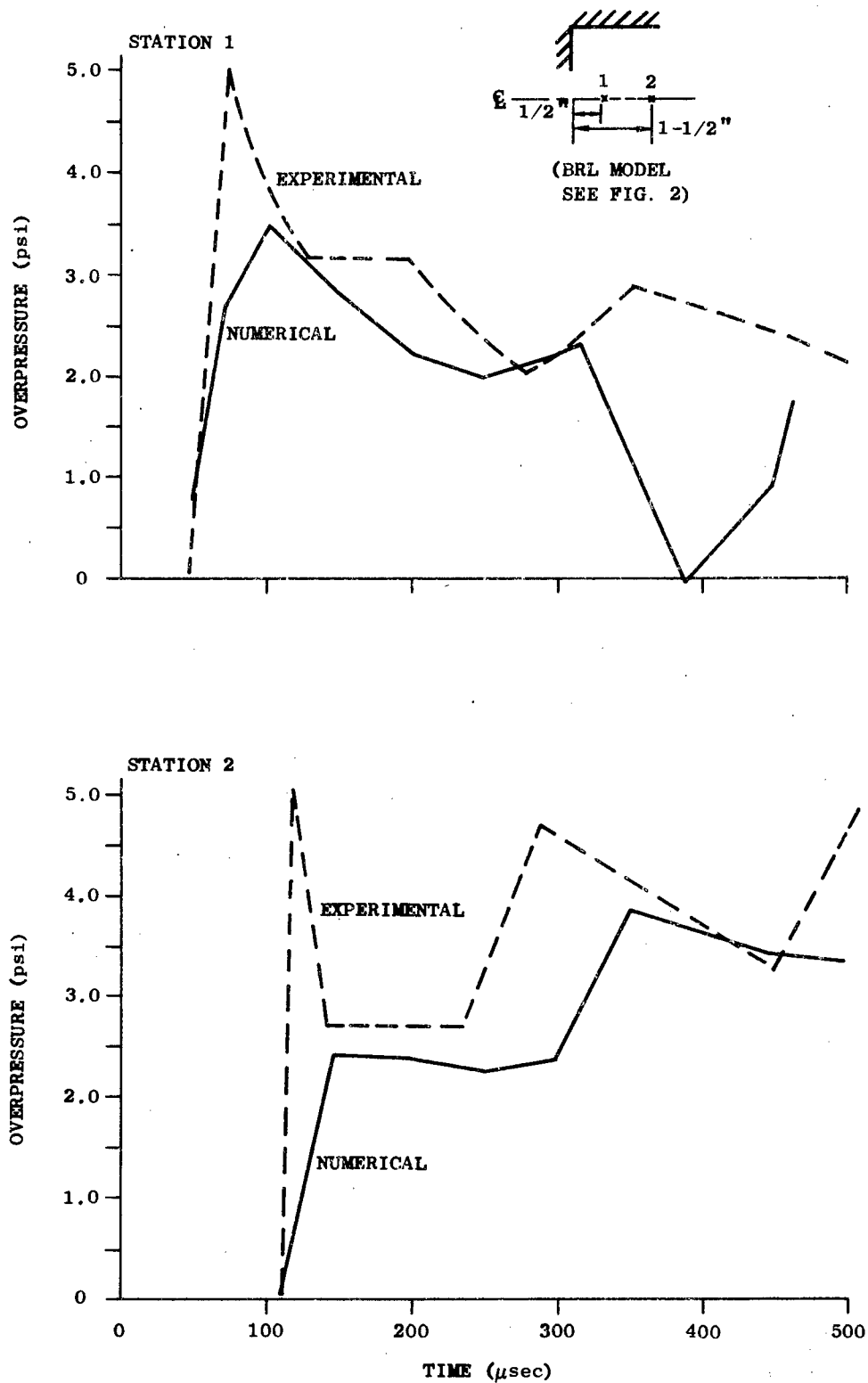


Fig. 6. Comparison of Numerical and Model Experimental Simulations

A similar test comparison using the FLIC code was made for an entrance-way in Ref. 7. The results were similar — a good long-term pressure contour but a poor resolution of extremely short-term transients. The result is of interest to the shelter problem, because it supports the argument that the local pressure transients developed by shock waves moving through chambers with small orifices ( $\leq 10$  percent) are in effect really transients and do not substantially affect the "filling" process. If they were important, it would be difficult to explain why the long-term pressure contour of the numerical simulation compared favorably with the experimental data.

A further review of the predictive accuracy of pressure histories determined by codes as compared with test data from scale models will not be undertaken. Full-scale data will, however, be used in a later section. The remaining comments on the BRL model experimental data will relate to the smoke-grid experiments (Ref. 5). The geometry of the grid was given in Fig. 2.

In the numerical simulation process, the shock wave's discontinuity is spread over 3 to 4 cells ahead of the front. A "marked" particle placed in the flow will have a false path traced in Lagrangian coordinates. The spreading of the discontinuity establishes a flow in the simulation ahead of the shock wave. The comparison of the path of marked particles in the simulation would not, therefore, correspond to the counterpart particles in the experimental flow.

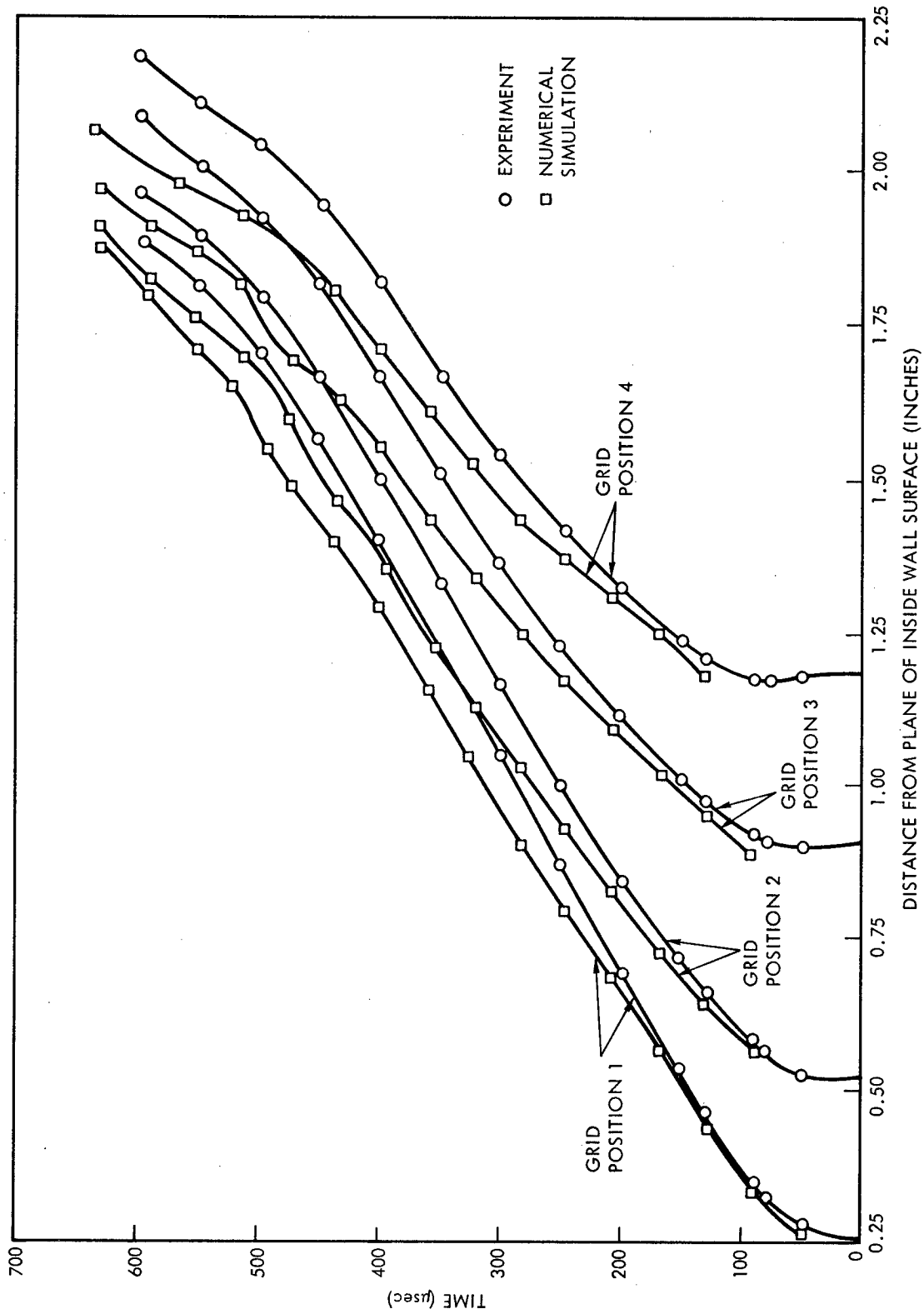
For example, Particle 1 in the simulation moved sooner and more rapidly, and at approximately 320  $\mu\text{sec}$  overtook the position of experimental Particle 2. From this point in time, Particle 1 of the experiment had the x,y,t path corresponding to simulated Particle 2. A method of comparing the experimental and numerical simulations under this set of conditions is to plot the velocity-time histories of each point. By establishing the x,y position of the particle as a function of time, the corresponding velocities of the experimental and numerical simulations can be compared. This procedure was

undertaken for the data presented in Fig. 7 and the results are plotted in Fig. 8. The plots provide velocity-time profiles for fixed points within the model chamber. The plotting method combined the spatial and velocity-time histories of each particle in the experiments and the simulation in order to determine the velocity-time distribution for fixed spatial points.

This representation (Fig. 8) shows a better correlation between experimental and numerical data than the simple plots of the particle paths. The improved accuracy results from comparing velocities at like space-time points. The direct comparisons of particle trajectories included large leverages which magnified small errors. The magnification or leverage was caused by the strong spatiotemporal variations in the flow fields. Once a particle's location was slightly in error relative to a fixed time, a very different history resulted because the flow-field gradients were so steep.

The accuracy of the comparisons between experimental and numerical simulations ranged between 3 and 10 percent for most data points. This result is considerably smaller than the 10-to-15-percent error range estimated from the raw data in Ref. 2. The grid used in that simulation was fairly coarse (four cells were used to represent one-half the entrance opening). Therefore, as a test of whether or not the accuracy of the simulation could be improved, the simulation was rerun using the grid shown in Fig. 9. Lagrangian marked particles were placed in the simulation, but the early motion of particles caused by the spreading of the shock wave again made comparisons difficult.

To avoid the complex cross-plotting undertaken in the preceding work, the absolute velocities (the magnitude of the velocity vector) of two particles in the experiments were compared to those developed by the numerical simulations. The spatial position of each particle at a given time was determined from the experimental data (Ref. 4). An interpolation for the absolute velocity at an equal position in space-time was made for the numerical simulation. The results are presented for two particles in Fig. 10.



(Reproduced from Ref. 2)

Fig. 7. Particle Velocity Comparison



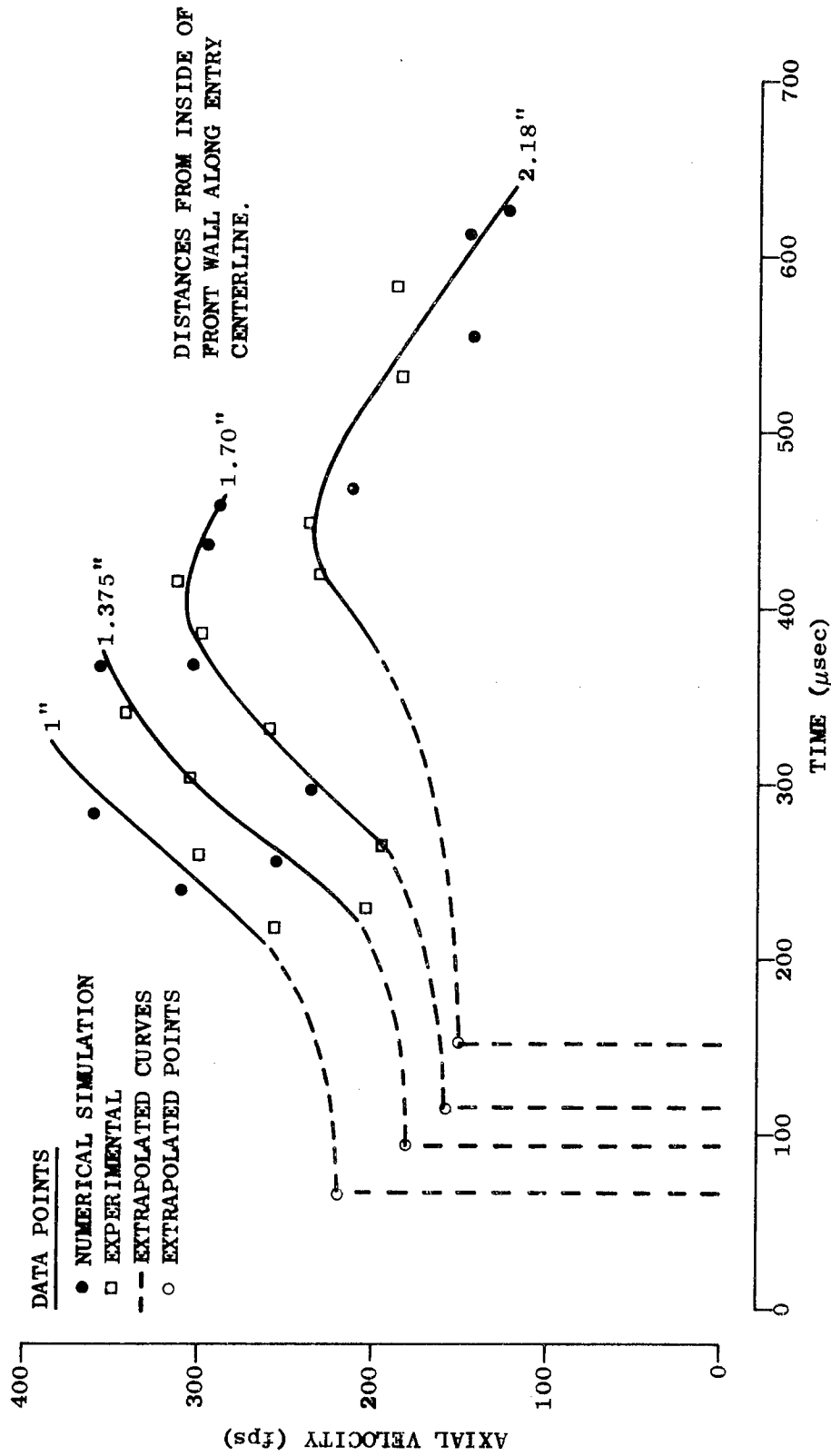


Fig. 8. Velocity Time Profiles for Fixed Positions in the BRL Model

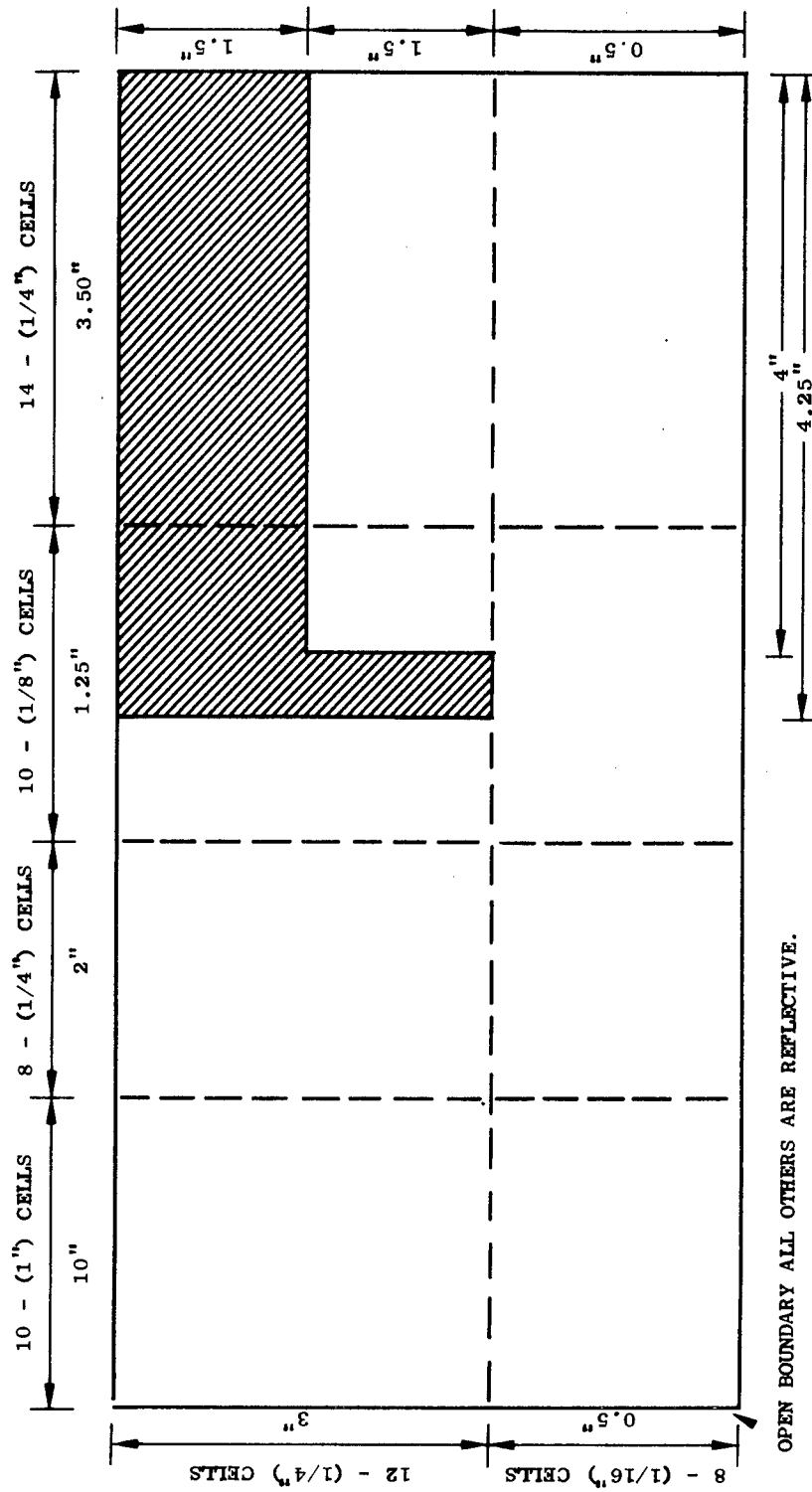


Fig. 9. Dimensions of Simulation Field

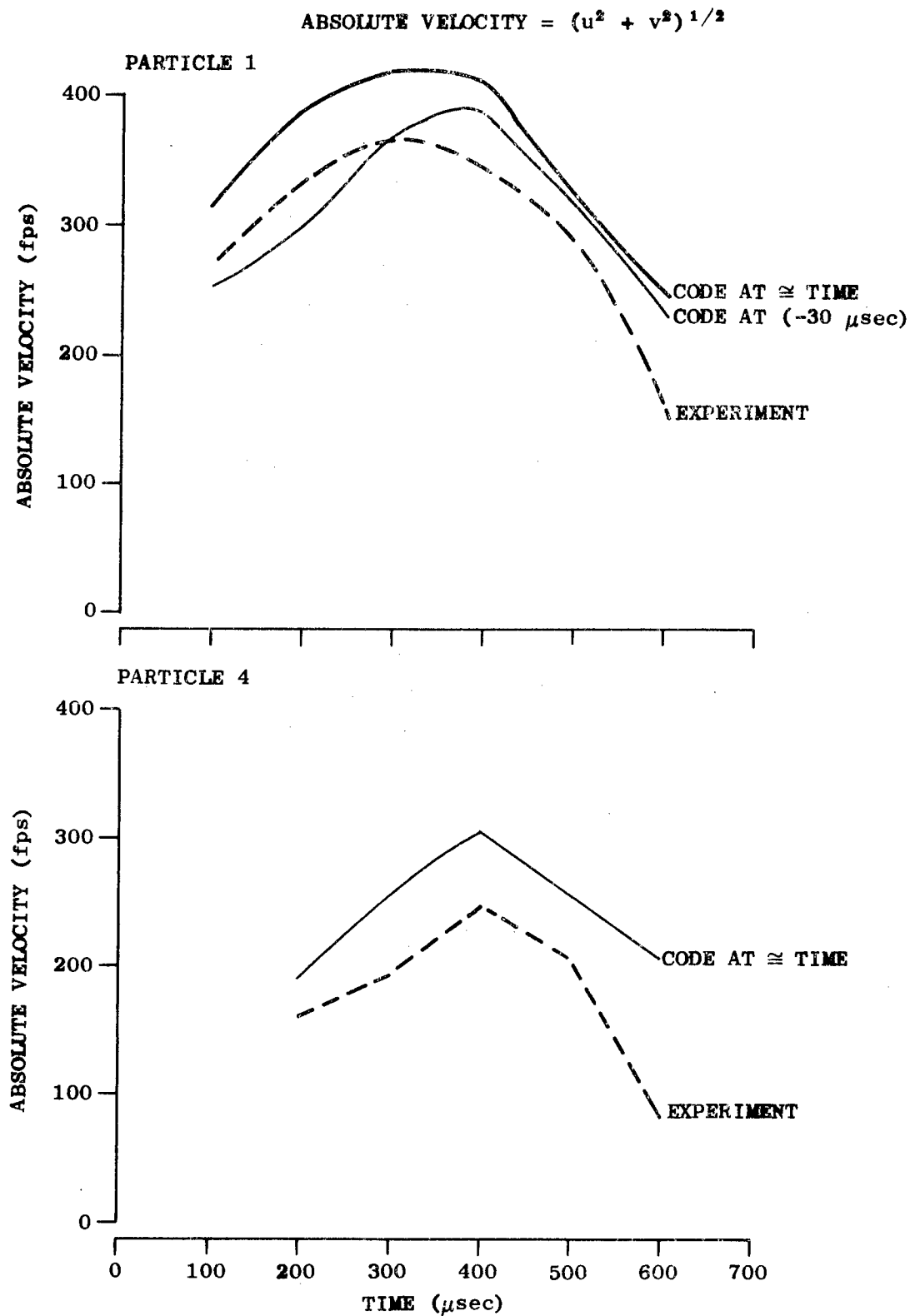


Fig. 10. Velocity-Time Profiles

An increase in the deviation between numerical and experimental data is evident. The time grid did pose some problems in the interpolations in location and time. A 30- $\mu$ sec variation in the profile is plotted in the upper portion of Fig. 10, and a large change in the deviations between the experimental and numerical curves can be observed. Linear interpolations were used to determine the axial and radial velocities at a space-time point in the numerical simulations from which the absolute velocity was calculated. A more sophisticated and accurate interpolation procedure would have been preferable, but the time involved in establishing the procedure and introducing the data could not be justified under the limited scope guidelines of the project.

The presentation of the techniques for interpreting pressure-time histories outlined in Appendix B discussed some of the problems associated with determining the values of variables at specific space-time points. A direct quantitative application cannot be made because the assumptions made regarding the relationship of wave shape and cell size do not hold for the general cases of the simulations. The simulations, in addition, present data for specific points and not areas, as was the basis for the methods presented. The interpolation could use the general guidelines established; but, more importantly, the material did provide some insight into the problems of interpreting spatially and temporally varying data.

A simpler procedure than plotting the velocity-time histories was used for further comparisons of the data. The vector values of velocity (magnitude and direction) were established from the experimental and numerical data for the experimental space points at three times. Time was measured from incidence of the shock wave at the inner surface of the entrance. Time interpolation was avoided by selection of the points of time comparisons, and a variation of under 7  $\mu$ sec between comparisons was achieved. Linear spatial interpolation was still used to provide correlations between corresponding points. Linear interpolations were also used by Coulter to develop the experimental velocity vectors from the particle trajectory data.

Tables 1, 2, and 3 present the data for the 20 grid points shown in Fig. 2. The experimental values used in the evaluations were the corrected values from the errata for Ref. 4. In Table 1 (213  $\mu$ sec) the deviations between numerical and experimental data range from 1 to 30 percent. The numerical simulation showed higher velocities along the centerline of the doorway and lower velocities away from the entrance. The vectors had a deviation range of 0 to 18 deg, with 85 percent being within 8 deg of each other and 95 percent within 11 deg.

At 450  $\mu$ sec (Table 2), the variation in the values of vector angles increased slightly, as did the variations in flow magnitudes. The trend continued and increased at 750  $\mu$ sec (Table 3). For the full time range, the centerline and boundary flow vector angles agreed fairly well. The centerline numerically simulated flows remained above the experimental values and the off-axis flows continued below the experimental values.

The first inclination is to fault the numerical simulations; however, a closer examination of the experimental data shows some inconsistencies. Point 5 in Table 2 has an unrealistic magnitude, and the variations in vector angle for points 9 and 10 are inconsistent with the flow field geometry. In Table 3, the flow magnitudes at experimental points 6, 19 and 20 appear unrealistically large. The vectors at experimental points 10, 14 and 20 are inconsistent with the flow-field geometry. These inconsistencies, coupled with the errors caused by small temporal and spatial variations, prompted a brief investigation of the accuracy of the experimental data.

The first area investigated was the data collection and reduction process. The camera framed a picture of 1- $\mu$ sec duration every 38  $\mu$ sec. The zero time had to be computed as the shock wave passed the reference plane between frames. Due to the relative invariance of shock front velocity (1282 fps incident and 1132 fps at sound speed) an error of only a few microseconds should have resulted. More error would be attributed to the reading process, since grid

Table 1  
FLOW VECTOR COMPARISON AT TIME = 214  $\mu$ sec

Point (a)	EXPERIMENTAL (Ref. 4)		NUMERICAL				COMPARISON	
	$\bar{u}^{(b)}$ (fps)	$\theta^{(c)}$ (deg)	$u^{(c)}$ (fps)	$v^{(c)}$ (fps)	$\bar{u}^{(b)}$ (fps)	$\bar{\theta}$ (deg)	$R_{ne} = \bar{v}/\bar{u}$	$\Delta\bar{\theta} =  \bar{\theta} - \theta $
1	292	1	371	7	371	-1	1.27	2
2	258	-1	335	3	335	-1	1.30	0
3	198	-1	253	4	253	-1	1.28	0
4	164	-2	210	3	210	-1	1.28	1
5	257	-43	129	146	195	-46	0.76	3
6	239	-26	223	118	252	-27	1.05	1
7	193	-15	187	82	204	-23	1.06	6
8	161	-11	192	57	200	-16	1.24	5
9	131	-108	0	104	104	-90	0.80	18
10	181	-53	78	102	128	-53	0.71	0
11	162	-35	111	90	143	-39	0.88	4
12	150	-24	96	62	114	-32	0.76	8
13	66	-94	8	65	66	-83	0.99	11
14	103	-47	55	76	94	-54	0.91	11
15	131	-29	87	60	106	-34	0.81	5
16	135	-24	96	62	114	32	0.84	8
17	18	0	-2	---	2	---	0.11	0
18	56	0	52	---	52	---	0.93	0
19	104	0	90	---	90	---	0.87	0
20	112	0	100	---	100	---	0.89	0

(a) Corresponds to smoke grid intersections as defined in Fig. 2.

(b) Magnitude of the velocity vector of angle  $\theta$  and x component u and y component v.

(c) Sign conventions shown in Fig. 2.

Table 2  
FLOW VECTOR COMPARISON AT TIME = 406  $\mu$ sec

Point (a)	EXPERIMENTAL (Ref. 4)		NUMERICAL			COMPARISON	
	$\bar{u}^{(b)}$ (fps)	$\theta^{(c)}$ (deg)	$u^{(c)}$ (fps)	$v^{(c)}$ (fps)	$\bar{u}^{(b)}$ (fps)	$R_{ne} = \bar{v}/\bar{u}$	$\Delta\bar{\theta} =  \bar{\theta} - \theta $
1	330	-4	430	6	430	1.3	4
2	297	-3	400	5	400	1.35	2
3	244	0	350	---	350	1.43	0
4	218	-2	295	---	295	1.35	2
5	831 <sup>(d)</sup>	166	-8	84	84	---	-
6	252	-38	81	112	138	.55	3
7	243	-22	187	100	212	.87	6
8	209	-11	245	91	261	1.25	9
9	138	114	-10	150	150	1.09	163
10	165	-128	70	54	88	.54	168
11	197	-46	70	99	121	.61	11
12	190	-28	100	90	135	.71	14
13	74	137	-21	-62	65	.89	26
14	74	-133	-14	40	42	.58	24
15	141	-61	36	60	70	.50	1
16	161	-32	65	66	93	.58	13
17	40	180	-22	0	22	.55	0
18	40	-180	-6	0	6	.15	0
19	86	0	35	0	35	.41	0
20	144	0	52	0	52	.36	0

(a) Corresponds to smoke grid intersection as defined in Fig. 2.

(b) Magnitude of the velocity vector of angle  $\theta$  and x component u and y component v.

(c) Sign conventions shown in Fig. 2.

(d) Error

Table 3  
FLOW VECTOR COMPARISON AT TIME = 713  $\mu$ sec

Point (a)	EXPERIMENTAL (Ref. 4)		NUMERICAL				COMPARISON	
	$\bar{u}^{(b)}$ (fps)	$\theta^{(c)}$ (deg)	$u^{(c)}$ (fps)	$v^{(c)}$ (fps)	$\bar{u}^{(b)}$ (fps)	$\bar{\theta}$ (deg)	$R_{ne} = \bar{v}/\bar{u}$	$\Delta\theta =  \bar{\theta} - \theta $
1		-	- - -	N O D A T A	- - -			
2	215	-12	308	7	308	---	1.44	0
3	164	4	298	7	298	---	1.81	0
4	144	9	272	6	272	---	1.89	0
5	84	75	91	117	148	51	1.76	26
6	911 (d)	17	-112	90	206	-129	----	--
7	166	-78	-128	105	166	-129	1.0	59
8	188	-68	-25	103	106	-104	.57	34
9	46	90	23	-7	24	72	.52	18
10	188	-107	-64	-101	120	112	.64	161
11	247	158	-165	-33	168	169	.68	11
12		-	- - -	N O D A T A	- - -			
13	122	180	-10	-187	187	177	1.53	3
14	158	-114	-76	-79	110	133	.70	123
15		-	- - -	N O D A T A	- - -			
16		-	- - -	N O D A T A	- - -			
17	20	180	-17	0	17	180	.85	0
18	78	-179	-74	0	74	180	.95	1
19	276 (d)	-180	-131	0	131	180	.48	1
20	446 (d)	0	-167	0	167	180	.37	180

- (a) Corresponds to smoke grid intersections as defined in Fig. 2.  
 (b) Magnitude of the velocity vector of angle  $\theta$  and x component u and y component v.  
 (c) Sign conventions shown in Fig. 2.  
 (d) Error.



intersections must be read. The intersections are formed by finite-width grids which distend in time and space. The grid intersections are small blocks similar to the blocks formed by the grids from which the densities were calculated.

The edges become more diffuse with time, hence each intersection point may not represent the same particle over a period of time. The extensiveness of the turbulent flows and the boundary layer growth along the viewing windows in the later portions of the flow field would add to the diffusion process. The local, as well as the regional, momentum transfers will also affect the experimental grid locations.

The averaging interpolation process in evolving the numerically simulated data was found to be a highly sensitive factor. The linear method chosen did not always present the most accurate result, but it did provide a consistent, simple and unbiased value. It is expected that the averaging process for evolving the experimental velocities and vectors would have encountered similar difficulties. An error analysis of the averaging processes would be a fruitful exercise if further evaluations are undertaken.

Because of constraints on the scope of the project, a less exacting and simpler method was chosen. The front and rear smoke grids experiments for the same model at equal incident conditions were collated as shown in Figs. 11, 12, and 13. The data at equal times should be consistent for both experiments (a small time bias of 18  $\mu$ sec exists in the presented data and the timing difference between the data presented in Ref. 2). The velocity magnitudes and vectors are presented as a function of location in the flow field.

In Fig. 11, the region in the x direction (labeled A) shows an inversion of velocities at the interface between the front and rear model data. Some small variations between the vector directions and the normal to isovelocity contours can be observed. A variation of 20 to 30 fps at 150 fps and a vector variation of 10 to 20 deg appear to be reasonable estimates for average values. The flows in Region B are greater than those expected from other flow data. For example, the 257-fps value exceeds the flow velocity of the incident shock wave and is off axis from the axially directed inflow.

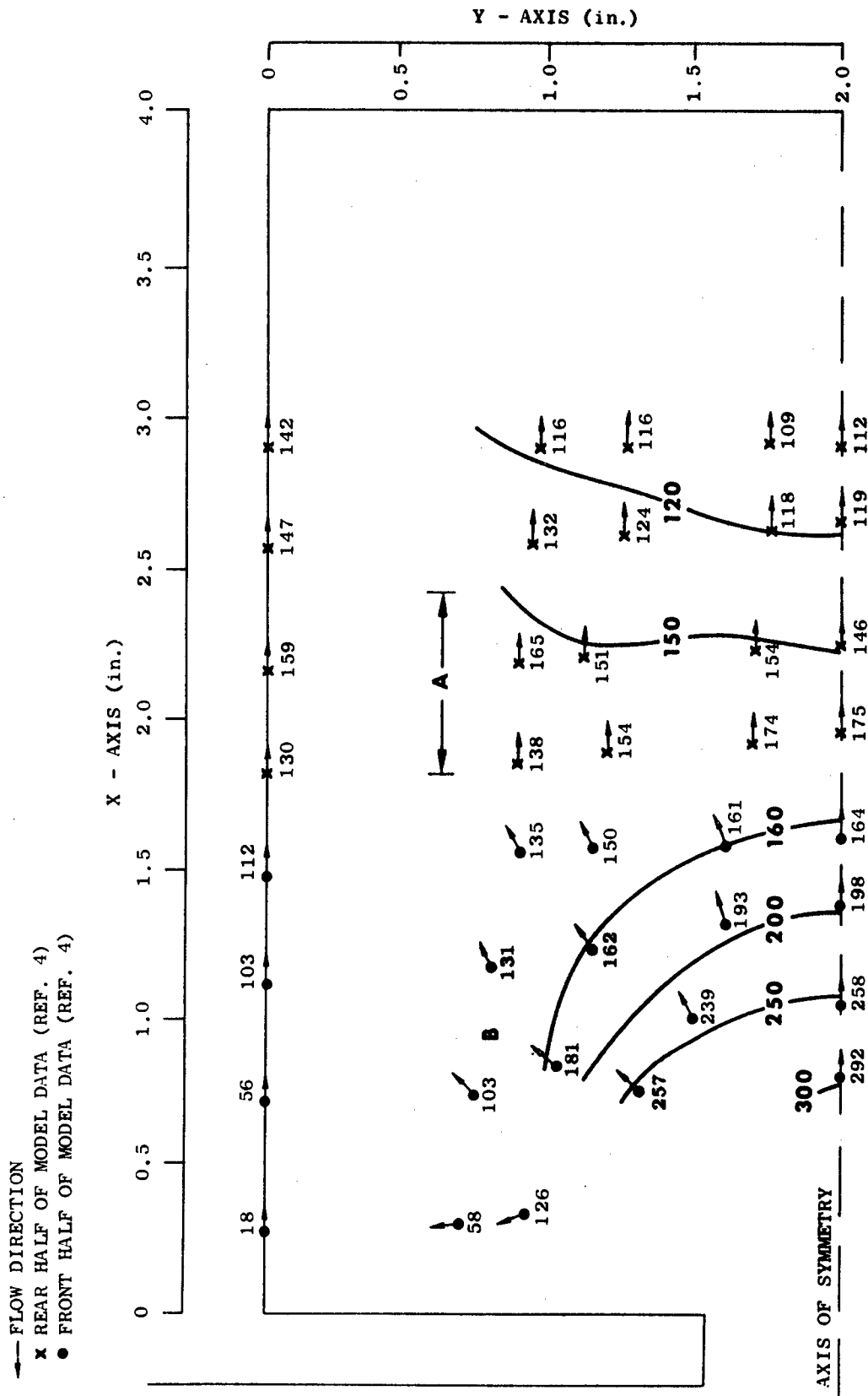


Fig. 11. Experimental Flow Contours at Time = 215  $\mu$ sec

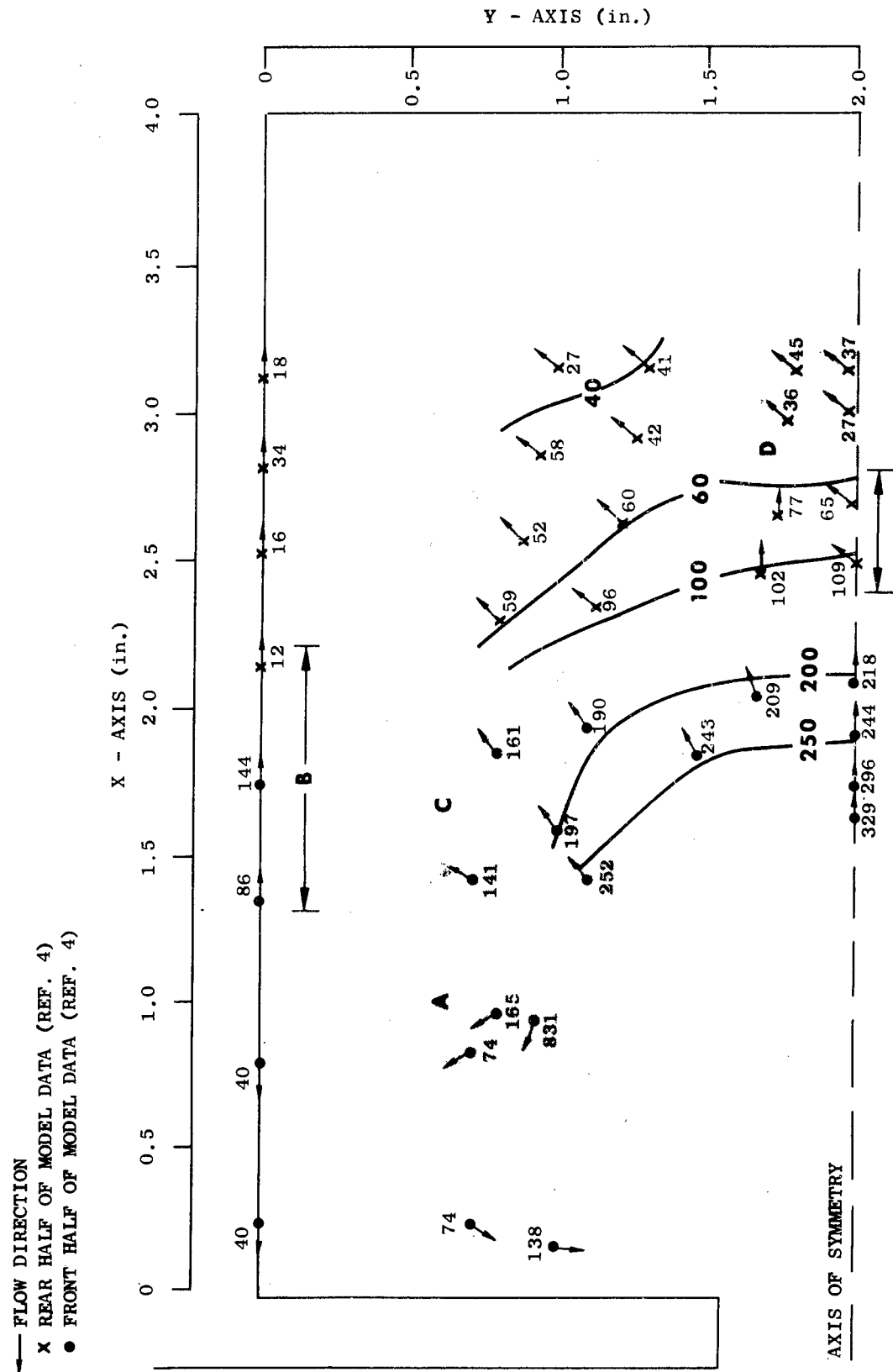


Fig. 12. Experimental Flow Contours at Time = 405 μsec

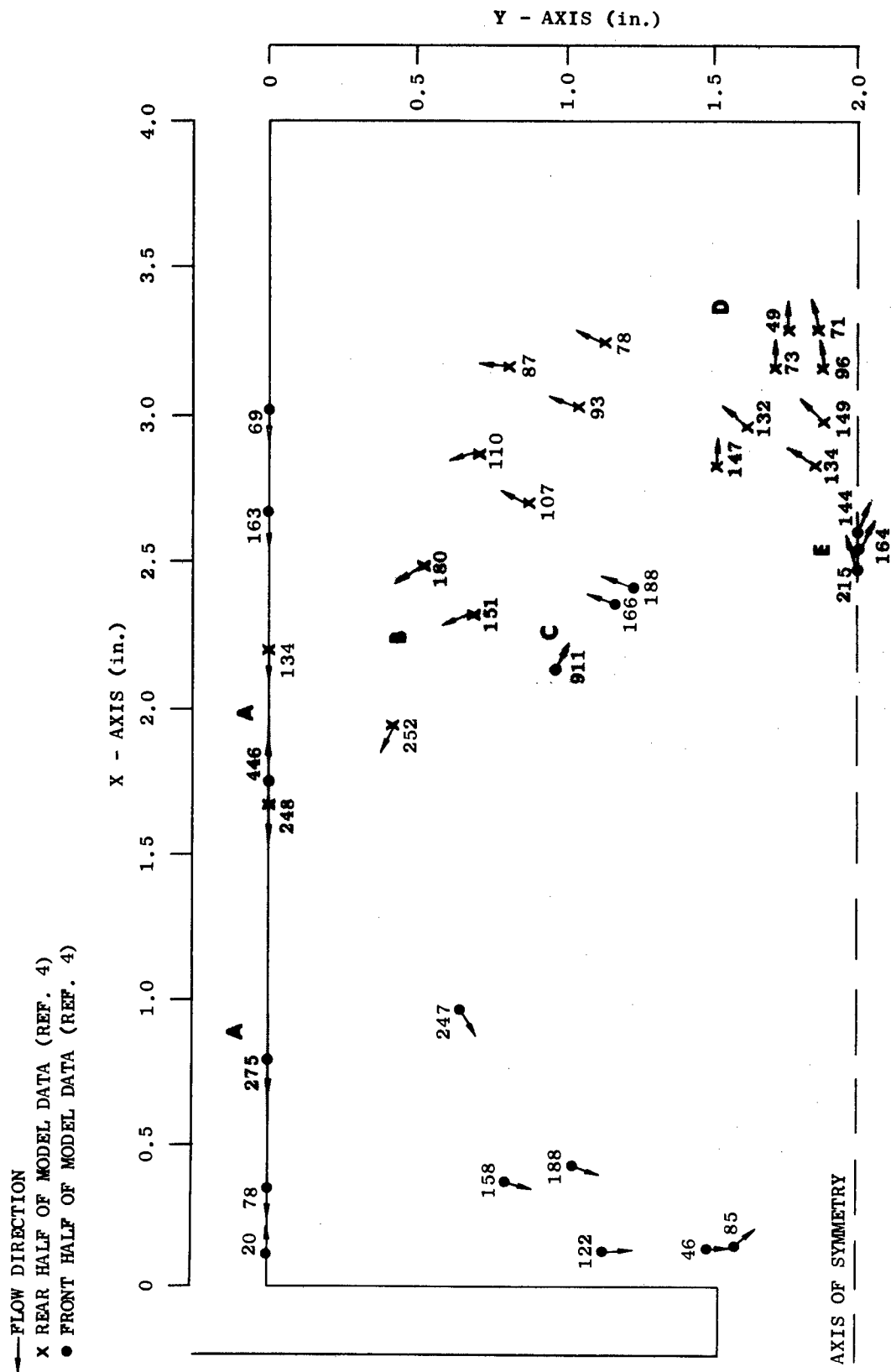


Fig. 13. Experimental Flow Contours at Time = 713  $\mu$ sec

In Fig. 12, Regions A, B, C, and D show some unusual variations in either flow magnitude, direction, or both. The data show a slightly smaller variation between front and rear flow magnitudes (relative to Fig. 11), but indicate equal or slightly increased angular variations. Region A shows a wide range of variation in flow velocity magnitude and, to a lesser degree, direction. Region B shows some rather unusual changes in flow magnitude. The flow magnitudes in Region C appear considerably higher than the surrounding regions. In Region D the flow vectors appear to have some inconsistencies in direction.

Figure 13 shows an even greater increase in the variation between front and rear data of the BRL experiments. Region A in Fig. 13 indicates flows inconsistent both in magnitude and in direction. The flow vectors shown in Region B have reversed flow magnitudes compared to surrounding regions. Region C contains a flow vector with a magnitude and direction which is inconsistent with the flow field. Region D includes a wide range of variations, which may indicate a pronounced turbulence or the limits of experimental accuracy at this time in the flow history. Region E indicates a gradient in the flow magnitude that appears inconsistent with the flow field at this point in its history. The range of variations appears to be 15 to 35 percent in magnitude and 10 to 40 deg in direction.

A comprehensive statistical analysis of the data was not within the project scope; hence a simpler approach was taken to provide some quantitative estimate of the variations. The method selected plots the angular deviations ( $\Delta\theta$ ) and the ratio of vector velocities ( $R_{ne}$ ), numerical to experimental, presented in Tables 1, 2, and 3 on normal and log-normal probability graph paper. Assuming the errors occur randomly about some mean value, the data points should form straight-line segments. Each segment would represent an error distribution in a region of the flow.

The data plotted from Table 1 indicated three distinct distributions for the ratio of the magnitudes of velocity vectors ( $R_{ne}$ ): one for the inflow region (points 1, 2, 3, 4, and 8), and a limited one for points 13, 6, 7 and the common distribution for the remainder of the points. The mean for the velocity ratio first set was 1.28; for the second set (points 6, 7, 13) the mean was 1.02; and for the third set the mean was 0.82. The vector direction variations ( $\Delta\theta$ ) showed two regions, one containing points 1, 2, 3, 4, 5, 6, 10, 11, 17, 18, 19, 20 and the other the remainder of the points. For the flow direction deviations the means were 3 deg and 8 deg, respectively.

The least variation in flow direction between numerical and experimental data was in regions where the flow was the strongest, or where the flow was along a wall. The values of the  $R_{ne}$  (numerical-to-experimental flow-magnitude ratios) showed two distinct flow areas, with an increase in variation between the inflow region and the bounding wall. To help understand why the error increased, iso- $R_{ne}$ , iso- $\Delta\theta$ , and isovelocity contours were plotted.

The plots reduced the indicated variation between numerical and experimental simulations in the central region of the off-axis flow. If corrections of the flow variables were developed from the  $R_{ne}$  contour values, the average velocity ratio variation rose to about 0.93 for the off-axis region. The inflow ratio was not altered. The distributions in both zones appeared to be random.

The same procedure was repeated for the data in Table 2. A similar two-segment distribution for the angular deviations was acquired. The mean of the variations increased for the distributions from 2 deg to 4 deg and from 8 deg to 20 deg.

The velocity ratio distribution changed slightly. The inflow zone mean increased to 1.33, as did the variance. The second zone consisted of points 12, 7, 13, 9, with points 8, 3, 11 forming its lower bound. The variance in this zone increased, and the mean was 0.92. The third segment of the plotted

velocity data contained points 6, 10, 11, 14, 16, 17, with a mean of 0.55, and the fourth segment contained points 15, 18, 19, 20, with a mean of 0.30. Each set of points was roughly related to zones of flow in the chamber, but a strongly decreased consistency in the relationships was noted.

If adjustments of purported inconsistencies in Fig. 12 were made, a complete alteration in the above results was noted. Mean values of the  $R_{ne}$  ratios began to approach 0.80 to 0.85, but a change in the values along the inflow axis was again absent. A gradient did occur between the inflow value and the flow parallel to the entrance axis that corresponded to the turbulent region of the jet.

The data from Table 3 shows a continued decrease in correlation between experimental and numerical simulations. The distributions of velocity ratios increased, as did the variations in flow direction. The mean values were all higher, with the value of the inflow ratio  $R_{ne}$  approaching 1.90 at particle position 4. A marked increase in variance occurred in this region.

The distribution of the data plotted from Table 3 was completely random in character. Particle position did not seem to be correlated with the resultant distributions. The isovelocity and isoratio contours did not provide additional insight into the nature of the distributions. The distributions formed into approximately the same two zones as did the data from Table 1, but with means of 1.65 and 0.75. If adjustments for the inconsistencies noted for Fig. 13 are made, the mean of 0.75 cited above for the off axis flows increases to a value in the range of 0.85 to 0.95.

The following conclusions were drawn from investigations. The experimental flow measurements increased in error with time, with strong gradients in flow magnitude and direction, and with decreased velocity. Errors of 20 percent in magnitude and 20 deg in direction are not uncommon and can be significantly greater at late periods in the flow history. An exhaustive error analysis is needed to fully interpret the data.

Relative to the numerical simulations, some observations on their accuracy can be made. The code does introduce some error in the turbulent inflows of the models tested. These turbulent regions have velocities 5 to 15 percent less than predicted by the numerical simulations. The overall flow patterns, both long and short term, are similar in character and magnitude for both simulation techniques.

The code produced higher inflows in the second simulation discussed. This deviation is attributed to the difference in entrance conditions between the two numerical simulations and the experiment. The earlier simulation, in which excellent agreement of centerline velocity profiles was reached, more closely resembled the upper portion of the BRL model; the second simulation more closely resembled the lower half (see Fig. 14). These variations in the two simulations were the result of using axial symmetry to save on computer time and memory and to increase resolution. Upstream pressures were not available from the model experiments, but a large-scale test (see Appendix C) similar to the first simulation showed a decrease in reservoir pressure of 3 psi.

The magnitude of the flow variation caused by the difference in reservoir pressure would constitute a portion of the variation noted. The increases in pressures on large reflecting surfaces and reservoirs of larger volume were noted and discussed for chambers in Ref. 42. This effect could be responsible for the higher inflows noted in the second numerical simulation, but it does not fully explain the higher velocity flows along the entrance axis later in the flow cycle.

Viscous and turbulent losses during the inflow and the filling cycle are to be expected, particularly in the smaller scale models. The comparison of numerical and experimental data supports this argument. The flow magnitudes of the simulations were about 10 percent higher along the inflow axis and 5 to 10 percent lower in the remainder of the chamber.



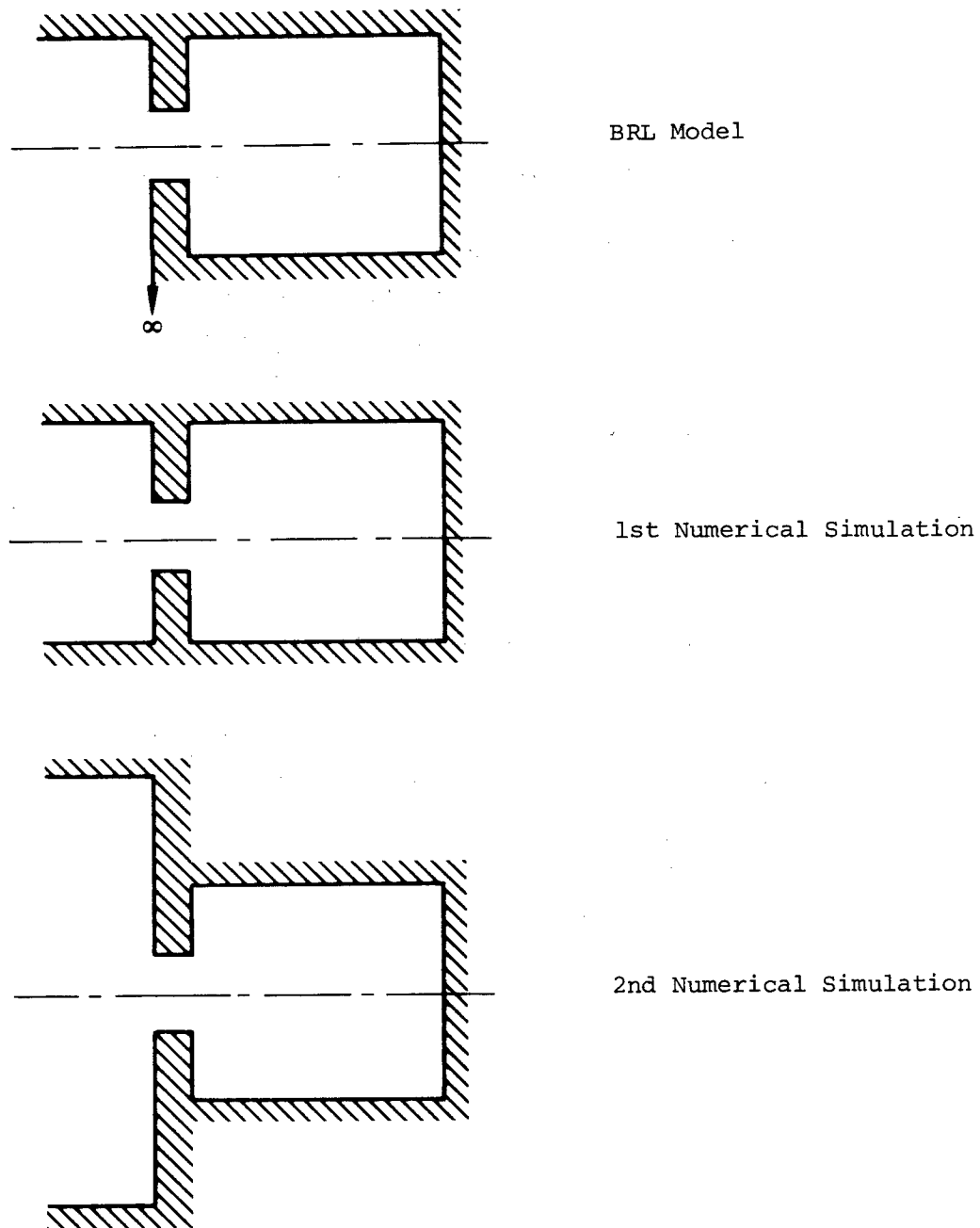


Fig. 14. Comparison of Model Configurations

Although these estimates of numerical simulation accuracies are not as precise as desired, further evaluations do not seem warranted. There is difficulty in providing precise comparisons between the parameters monitored in small-scale models and the numerical simulations. Small errors become significant. It is difficult to ascertain the absolute accuracy of experimental data.

The intent of the original work plan had been to secure the experimental digitized data from the original cards or tape used to develop the appendices of Refs. 4 and 5. This plan proved infeasible; hence the experimental data used in the comparisons either had to be reproduced in a format compatible with the Office of Civil Defense's CDC 3604 computer or had to be worked with manually. Either approach was severely limiting to the evaluation and comparison procedure.\*

For these reasons, further evaluations of the code using experimental data from scaled experiments were not undertaken. The shelter program's interest in large-scale data also suggested that more emphasis be placed on evaluation of the large-scale situation. Two sources of data were used: field test data and URS shock tunnel tests. The full-scale field test data used for evaluation were those presented by G. Coulter in Ref. 5. Though not precisely two-dimensional, the data were considered to adequately approximate the two-dimensional case in sufficient detail to test the numerical simulation.

---

\* Investigations under this study indicated magnetic tape conversion or the development of punch cards from published tables to be too costly an undertaking for studies such as this work unit. Future OCD requirements would be best met if all new digitized experimental data is in a format compatible with the OCD computer.

## COMPARISON OF NUMERICAL SIMULATION WITH FULL SCALE EXPERIMENTAL RESULTS

The chamber geometry for the large-scale test is presented in Fig. 15 and the geometry of the numerical simulation in Fig. 16. The short clearing time of the structure and the entrance near the side of the building (and away from the stagnation region in the center of the front wall) reduced effects of the three-dimensional flows. In the two-dimensional case, the reservoir pressure would be slightly greater due to the absence of the upward expansion of flow over the roof of the structure. The higher reservoir pressure would result in higher inflow velocities and a higher internal pressure.

The monitored free-field pressure was used as an input to the numerically modeled situation. The input took the form of a calculated pressure-distance-time profile whose propagation over the measurement point which would correspond to the experimentally monitored pressure-time history. The results of the simulation are plotted in Fig. 15, as were the experimental data as taken from Ref. 5. To save computer time, the numerical simulations were only carried out to 60 msec, which is well into the outflow stage. No significant alteration in accuracy between the numerical-to-experimental profiles would be expected after this point.

The numerical simulations provided excellent agreement (better than 20 percent) for the first 20 to 25 msec. At this time, the three-dimensional effects began to be sensed at the internal gage locations, and the error increased 10 to 20 percent. An alternate view of the error is to consider it to be a 5- to 10-msec lag in the decay of the pressure. This agreement is better than that with the small-scale models discussed earlier and is well within the needs of this study, which is primarily interested in the more nearly two-dimensional basement shelters. Based on this comparison, the accuracy of the code in predicting pressure distributions in shelters would appear to be well above 90 percent.

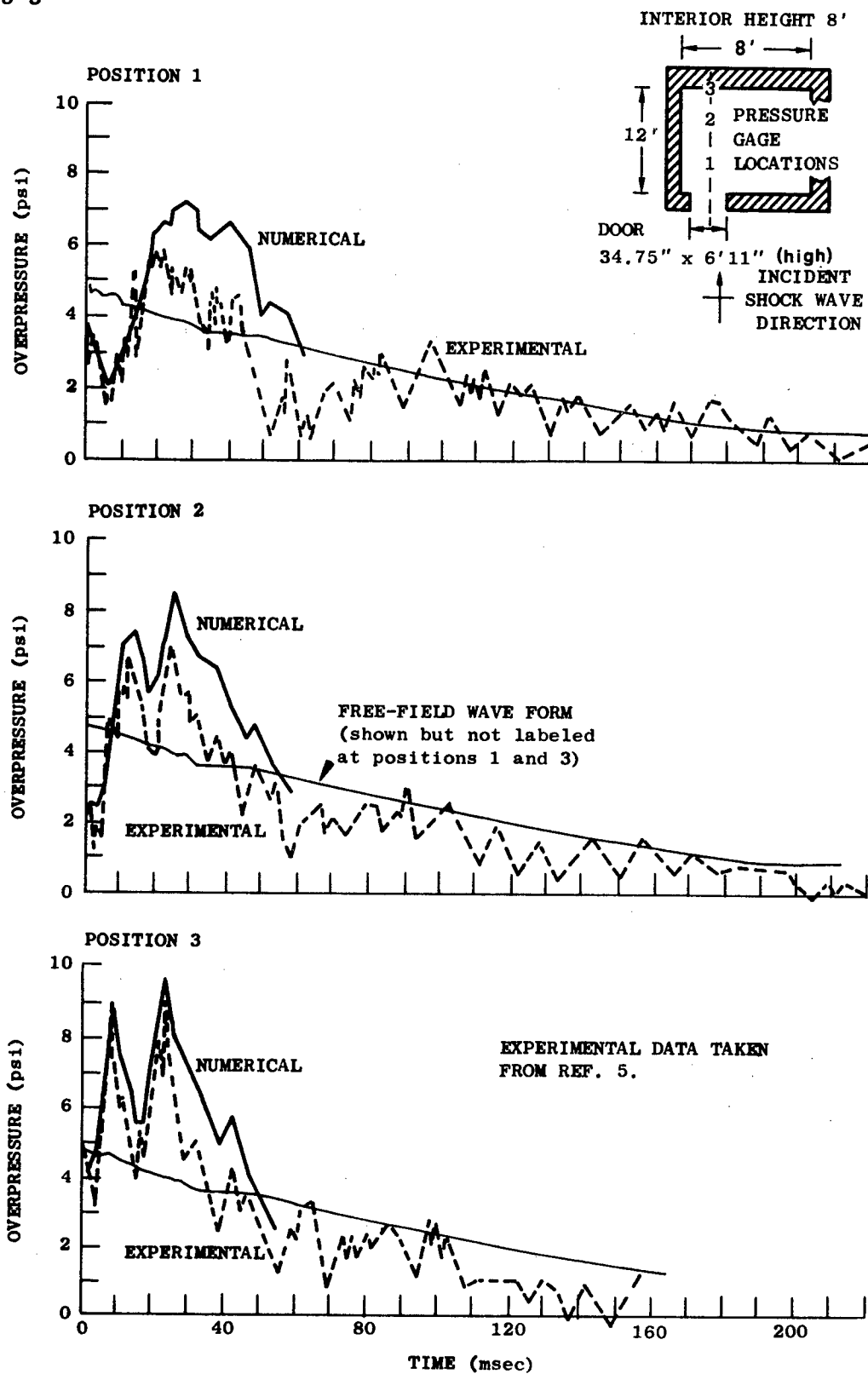
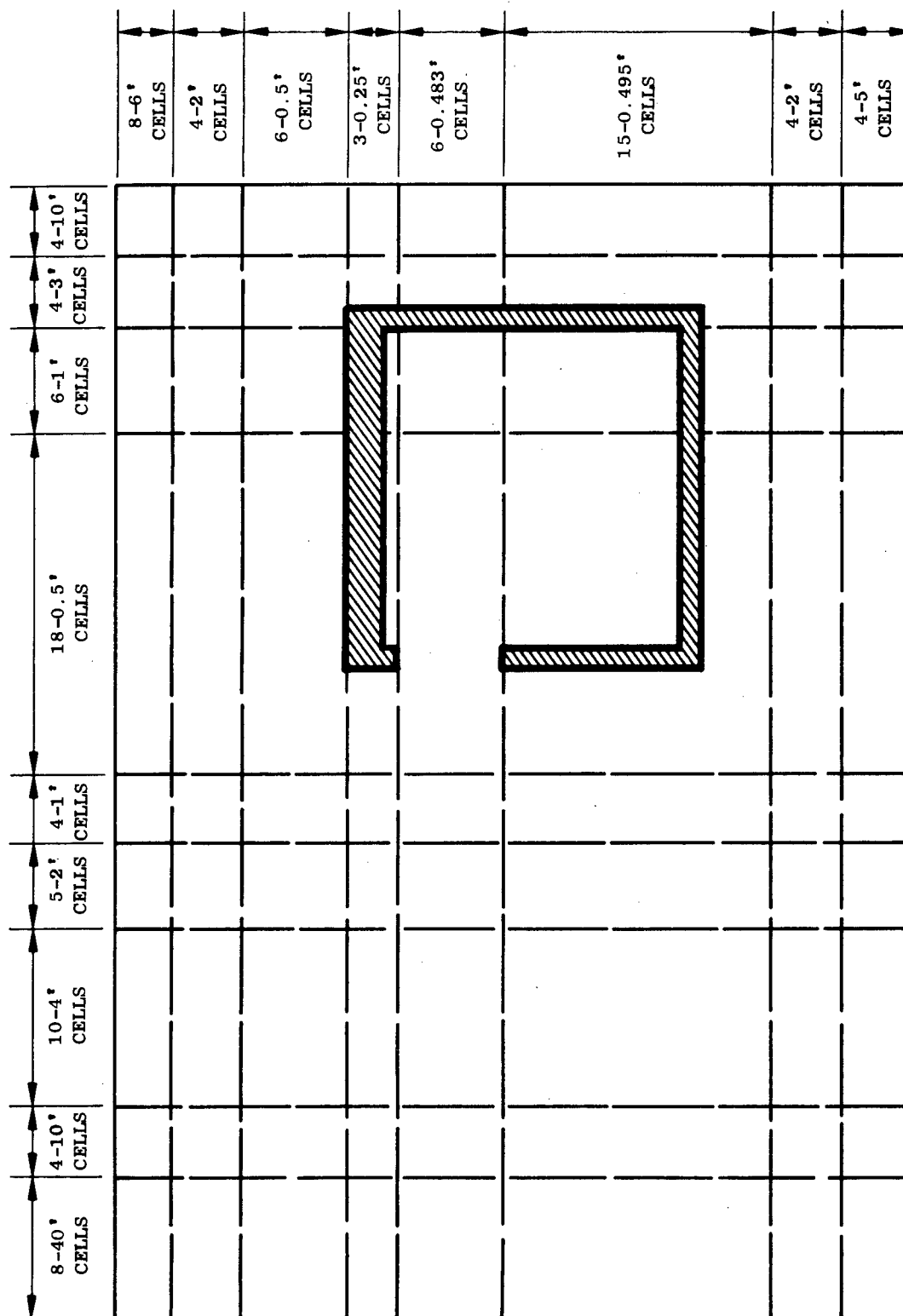


Fig. 15. Comparison of Numerical and Experimental Full Scale Pressure Histories



(Interior and exterior dimensions are the same as the experimental plan view as shown in Fig. 15)

Fig. 16. A Two Dimensional Simulation of a Free Field Test Case

An evaluation of full-scale test is presented in Appendix C. Due to the lack of other good full-scale data, it was decided to make use of the data in this study. The URS version of the FLIC code was used to numerically simulate the tests. Because of the length of the presentations and comparison of the results, the material was placed in Appendix C. The comparisons of test results support the conclusion that full-scale numerical and experimental simulations seem to agree to within a 90-percent absolute accuracy on both overpressure and dynamic pressure predictions.

The main difficulty encountered in comparing the numerical and experimental simulations was the manipulation of the available experimental data into a useful format. The accuracy of the distributions of two parameters were of prime interest: pressure for structural loading and dynamic pressure for human injury considerations. Pressure correlations are direct measurements and, if a common time base for comparisons can be established, comparisons are simple. As was noted earlier, the small model data did provide some difficulties in matching time scales. The problem did not reappear in the full-scale experimental-to-numerical comparisons. It was found that, in general, the experimentalists did not provide sufficient error analyses with their pressure data to allow precise comparisons to be made. As the variation between experiment and numerical simulation dropped below 10 percent, it was difficult to fault the numerical simulations, inasmuch as exact pressure-amplitude and time-scale error values and their distributions were not available.

The flow measurements underscored the problem more clearly. The measurements in the smoke grid experiments were presented to the thousandth of an inch (Ref. 5) and the time scale to the 100 nanoseconds. Even if this precision really did occur, two views of the same process did not overlay accurately. The preliminary error analysis accompanying the URS preliminary shock tunnel test data showed where large errors could be produced from basically accurate data. The question repeatedly arose as to how accurate were the data against which the numerical simulations were being compared.

Several factors noted in these comparisons will be presented here; other factors will be covered in later portions of the report. Although the experimental model data showed a pronounced spreading of the inflow through turbulence, this was not observed in the large-scale tests. The scale-model tests also showed an increase in turbulence with decrease in entrance size. The tests of the 1/8-in. entry showed an interference between opposite sides of the inflow pattern and the establishment of a Von Karman vortex street. These combined factors indicate that perhaps a scale effect may exist.

A marked effect on the inflow is exhibited by the reservoir conditions. As the entry cross section becomes of appreciable size (10 to 15 percent) in relation to the reservoir cross section, an appreciable change in reservoir pressure occurs. For a 19-percent opening in the URS shock tunnel tests, approximately a 29-percent decrease in reservoir pressure was monitored. This change in reservoir pressure was more rapid than the time normally ascribed to clearing phenomena.

Questions as to the distribution of kinetic and potential energy in the inflow were raised. Significant flows were monitored in the chambers after the filling process (as evidenced by the pressure increase) had terminated. The momentum generated by the inflow process was sufficient to maintain the flow, and form the circulation referred to in preceding work units. The review indicated the phenomenon was strongly associated with the redistribution of energy, and it appeared to be a critical factor in understanding the flow process.

The evaluations could not establish any significant evidence that the numerical simulation of full-scale situations would have errors over 10 percent in either overpressure or dynamic pressure. The evaluations did seem to indicate that if any errors did occur in the simulations, they tended to produce greater values of both variables. As to the predictive validity of the numerical simulations, some doubt remains regarding their possible overemphasis of the long-term flow in the chambers. This overemphasis would be expected in the absence of turbulent or viscous dissipation in the numerical simulations.

The remaining inconsistency of concern to this evaluation was the higher inflow velocities developed by the numerical simulations in the central and aft regions of the chamber particularly where the inflow turned and moved along the rear wall. The variation could be due to Galilean invariance of the numerical techniques, as discussed earlier; however, the pressure histories monitored on the rear walls of the full-scale tests (field and URS shock tunnel) did not indicate similar variation. The gages on these tests were exposed to stagnation pressures for the turning flow. The indication is that if an error does occur in this region, it is highly localized. The experimental data from the scaled models were slightly inconsistent at this point in time. Therefore it is hard to pinpoint where the error lies. With the agreement of the simulation with large-scale data, there appears to be no reason not to use the results of the simulations in these regions.

The investigation undertaken could not establish a reason for not using the two-dimensional hydrodynamic code in the OCD shelter research program. As new data are developed, this conclusion should be reviewed, particularly with respect to long-term flows. The predictive accuracy of the numerical simulations with respect to pressure distributions were particularly good. No evidence could be developed that indicated any significant variations between code and experiment relative to the information on structural loading required by the OCD shelter research program. The overall usefulness of the codes to the shelter research program appears to be more a function of the factors of utilization, cost, and data display.

#### UTILIZATION, COST, AND DISPLAY OF NUMERICAL SIMULATIONS

The term "numerical simulation" has been used to discuss the code outputs. The choice was selected to indicate the close resemblance, in terms of the data acquired, between using the codes and undertaking experimental studies. The process of planning and executing a simulation follows a procedure identical to establishing and executing an experimental test plan. The main exception is that the data reduction process entailed in experimental work is absent.



Under this assumption, it would be useful to compare the features of both approaches to simulating the shelter environment during a nuclear attack. One of the main features favoring the experimental approach is credibility. Where numerical and analytical studies suffer from a credibility gap, the experimental results tend to be unquestioned. In the preceding review some difficulties were noted in both techniques. These difficulties will be reviewed to form a background for the discussion of the usefulness of the numerical simulation techniques.

One of the problems noted in the preceding discussion was the absence of error analysis on, and verification of, experimental results in the flow studies as was underscored by the comparisons against the numerical simulations and their unbiased consistency. The numerical simulations covered a broad spectrum of geometric scale, which underscored the fact that the shelter research program is interested in what happens in the full-scale prototype situation and not in the simulations. The simulations, both numerical and experimental, are the means to the end, not the end itself.

Once stated, the above is so obvious that it appears too elementary to merit consideration. However, reviewing the available material, most studies did not appear to have a strong problem-oriented focus. This situation appears to have been caused by having to use small-scale experiments to study the physical process due to the expense and large yields resulting from full-scale testing. An example of the potential conflict can be found in the chamber-filling process. The chamber-filling process, based on the volume-to-area ratio model of Ref. 42, is nonlinear; yet the validity of linear scaling of the flow processes has not been questioned.

The difficulty of acquiring valid and comprehensive flow data must also be reviewed. The experimentalist selects monitoring locations which he feels will provide a true picture of the phenomena being investigated. Constraints governed by cost, available instrumentation, and size (in scaled experiments) limit his choice in varying degrees. The combination of the above factors can produce some misleading results.

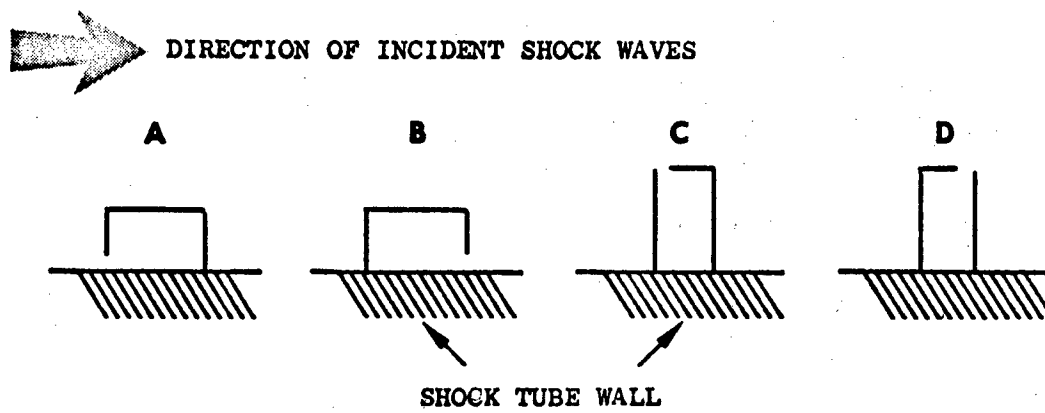
An example of these misleading results can be found in Ref. 43, in which smoke-paricle experiments were used to visualize flow in chambers. These experiments observed the motion of a single smoke grid initially positioned across the door entrance of the models shown in Fig. 17. The trajectory of the grid was used to establish the "maximum flow" in the chamber. These experiments are similar to those in Refs. 4 and 5, which used a grid of smoke particles (Fig. 2) to establish a more general flow pattern.

The maximum velocities reported are not consistent with either the data presented in this report or in Ref. 2, or from considering the mass influx necessary to fill the chamber in the correct "fill time." The velocities presented in Ref. 43 are considerably lower than those indicated in the other sources. The variation is caused by the time required for the inflow to accelerate to its maximum velocity. During this period, the smoke particles move away from the high-flow zone. The conclusion in Ref. 43 (on the spatial flow distribution) is drawn from observations of the particles traversing the inflow zone, but does not account for the strong temporal variations which exist in the flow field.

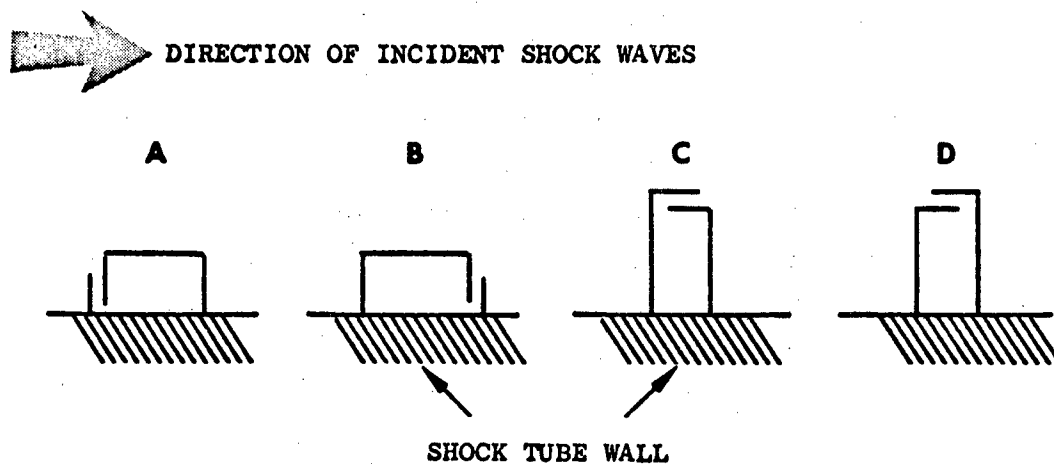
Both sets of experimental work reviewed above were extremely well done and produced good and consistent information within the experimental limitations. These limitations precluded long-term observations of the spatial distribution of the flow field. This limitation, in turn, did not provide the needed overview to develop an entire review of the flow fields generated. These comments are not presented as an argument against experimentation, but rather as reminder that the data may not be complete or infallible, particularly in cases where strong temporal and spatial variations of multiple parameters exist.

#### Utilization

The numerical simulation technique does provide an advantage which circumvents the problem of having to define monitoring locations. The code must calculate the complete set of parameters needed to define the flow field at



SHELTER WITH UNPROTECTED DOOR



SHELTER WITH PROTECTED DOOR

(Reproduced from Ref. 43)

Fig. 17. Orientation of Shelter Models with Respect to the Incident Shock Waves for Tests in Ref. 43

every cell. The complete set of data for all cells in any form desired can be provided in the output. The cost of the procedure is dependent on the exact output procedure, whether output is taken from all the cells or just some portion of them, and on the particular computer involved; but in general the cost range is about 5 to 30 percent of the total program running time.

The second advantage of numerical simulation is that the output is in the form of final data, not raw data which must be reduced to a useful form. The absence of the data reduction step has extremely attractive economic aspects. By placing the output of the code onto magnetic tape, data searches, data ordering, and data plotting can be done quite simply and economically. The overall effect is a flexibility, thoroughness, and rapidity which experimental techniques cannot often approach.

Two basic arguments can be presented against numerical simulations. These concern the credibility of results, since the simulation is not "physically real," and consideration of cost. The credibility objection can often be valid, but the code can be checked against limited experimental data for verification. The difficulties of a complete verification of numerical with experimental simulation were discussed earlier in considering code accuracy. Part of the difficulty is that the experimental data relating to flow parameters is not complete. However, since data are now available for study that were not obtainable from preceding studies, some estimate of the relationship of numerical simulation to experimental data can be inferred.

Another aspect of credibility must also be probed, i.e., the fact that experiment, like the code, is still a simulation of the prototype (full-scale) situation. The situation could exist in which the small-scale experiment could not be simulated with the accuracy required for a simulation of the prototype situation. The comparison of code to experiment made earlier in this section did indicate the code was slightly more accurate in the large-scale case than in the modeled cases (although in both cases the accuracy was sufficient for the purposes of the shelter research program). Based on this reasoning, the credibility argument against numerical simulation, as applied to this OCD shelter research program, is weak.

Cost

The second argument often used against the utilization of numerical simulation concerns cost. The only objective evaluation of cost available is to compare it to the other form of simulation—experiment. A comparison of the procedures involved in acquiring data through each of the simulation procedures is presented in Table 4. The assumption is made that the experimental facility, the data acquisition system, the experimental data reduction system (including the computer programs for data reduction), the computer, and the numerical code are available for project use on a per-hour basis. The table indicates that the first and final steps are similar for both simulation procedures, and it will be assumed that they represent equal costs.

Under these rules the comparison lies in the intermediate stages. These stages (as outlined in Table 4) are formed by experimental steps 2, 3, and 4, which correspond to numerical step 2. From past experience, step 2 in either simulation procedure costs approximately the same on either project. The experimental costs would be greater than the costs of the numerical simulation by an amount equal to the cost of experimental steps 3 and 4. The exact dollar cost would depend upon experimental conditions, such as size, data acquisition needs, number of times the model will be tested, and the complexity of the experimental design.

The next stage in the comparison is the actual performance of either simulation. Each of the shelter chambers numerically simulated for OCD by URS have cost in the range of \$30.00 to \$120.00 at standard commercial rates. If the pretest cost of the experimental facility and data acquisition system is neglected, the per-test cost is the project charge of the experimentalist and his test crew. On the basis of standard overhead and salary rates, the project cost of a senior experimentalist would be \$20/hr and a senior technician \$12/hr for a combined rate of \$32/hr. Depending on the size of the facility, more technicians might be used, thus raising the per-hour cost further. The cost per experiment for either size test group would be comparable or greater than the cost of numerical simulation without the overhead costs of the experimental facility being involved.

Table 4

## AN OUTLINE OF NUMERICAL AND EXPERIMENTAL SIMULATION PROCEDURES

<u>Experiment</u>	<u>Numerical Simulation</u>
1. Design the experiment	1. Design the experiment
2. Design the data model	2. Develop the input data
3. Fabricate the model	3. Perform the simulation
4. Design and set up the data acquisition system	4. Review the output for errors or inconsistencies
5. Perform the experiment	5. Data presentation
6. Reduce the data	
7. Perform an error analysis of the experiment	
8. Data presentation	

Another pertinent comparison would be the use of the OCD Olney Computer Facility for the numerical simulation. This facility is provided to projects on a time-available basis. The cost to the project of each simulation, including sending a person from the most distant location in the country, ranges between \$5 and \$20 for batch runs, depending on the number of simulations in each batch. The cost of the performance stage of the simulation will, in either situation, be equal to or less than the cost of experiment.

The last items listed in Table 4 compare experimental steps 6 and 7 with numerical simulation step 4. The data reduction process is not necessary in the numerical simulations; thus, the added cost of the error analyses and consistency checks are equal in both simulations. The computer costs of adequate data reduction is similar to the computer costs of the numerical simulation; hence a significant difference would exist between simulations. If all these cost factors are summed, numerical simulation has an intrinsically favorable cost-benefit ratio. If we further define the ratio to account for the amount of information per simulation, the more complete data from the numerical simulations still further increases the cost-benefit ratio in favor of numerical simulation.

Another, more powerful, approach would combine numerical and experimental simulation. In this case the greater portion of the simulation would be performed numerically, reinforced by experiments to substantiate the numerical results. The combination provides the credibility of experiment with the thoroughness and cost-saving features of the numerical simulation.

#### Display

The combined approach still contains the data display difficulty found in both simulation techniques. Both simulation techniques simply provide data, not mathematical and physical understanding of the flows, which reduces both simulation techniques to the status of tools for the researcher, i.e., they are means to an end rather than end product. The inability of many studies on shelter flows to display and use available data stresses the lack of understanding of the basic processes involved. The code, like experiment, provides data for theoretical or empirical analysis, which is the basis of the shelter research program.

The problem with data display is primarily due to the wide variety of shelter geometries and input conditions possible, to the strong spatio-temporal variations, and the many flow variables needed to describe the chamber flows. In the chamber-filling studies (Refs. 2 through 5, 42, and 44), the methods for predicting a gross pressure-time history in a chamber became complex and the authors finally resorted to a series of simple computer codes. At present this is still the major shortcoming of both simulation techniques.

The cost-benefit ratios of the numerical simulations were further improved. The computer codes allow flow out of three of the four sides of the computational mesh. The fourth side, the input flow boundary, can only have inflow and cannot accept the incidence of a change in the flow moving upstream. The reflected shock wave from the chamber in the simulation, upon reaching the input boundary, terminates the calculation period. To provide acceptable test durations, a long distance between the chamber and the input boundary must exist.

If equal cell sizes are used, then large computational meshes must be used. To reduce this requirement, variable cell lengths can be instituted. The cells become increasingly elongated in moving from the flow shelter interaction area toward the input boundary. Since the upstream region of the grid is not of interest, the coarseness of the grid is not of importance. The use of this technique effectively minimizes computer memory requirements.

The use of variable cell size can be extended further. In regions of steep gradients and intense flow, the need for high resolution exists; but, if an adequate grid representation is used, computer memory requirements become excessive. To circumvent this difficulty, a doubly variable cell geometry can be used. With this approach, a 3000-cell mesh can provide quite high local resolution and still avoid long computation times. A 3000-cell grid is compatible with the 53-K bit storage available on the OCD Olney computer.

The difference between the effect of a doubly variable grid size and a simulation with a fixed grid must be negligible if the technique is to be useful. The profile in Fig. 5 indicates the transmission of a shock wave is



not significantly perturbed by the variation in grid size; hence a test was run to show that long-term effects were similarly unaffected. An existing test of constant grid size run on the OCD computer in late 1968 was selected and rezoned as shown in Fig. 18. The rezoned shelter was run on a CDC 6600. The results of both tests are presented in Table 5. No significant variation was noted, and the data provide a good indication of the repeatability of results. It should be noted the runs were on different machines and at different facilities (commercial and government), which also indicates the small variability of running on different equipment.

The main drawback of the above approach is that the computational time step is a direct function of cell size. The smallest zones then tend to control the time step for the entire grid, which results in long running times. The code could be rewritten to allow calculations in small time steps. At certain integer steps, the next set of large zones would be included. Then, after a series of these computational sequences, the next larger set of zones included, and so on. For the immediate needs of the shelter research program, this approach is an unattractive choice because of the potential reprogramming, debugging, and proofing costs.

Still another procedure might be considered for future use—that of rezoning. The flow pattern in later flows in the filling of the shelter by the air blast environment does not require the high resolution of the earlier flows. The grid could be rezoned to coarser zones to take advantage of this feature of the flow. The rezoning of the computational grid would reduce the number of cells and would also increase the computational time step, since the cells would be larger and the flows lower, all of which would reduce the running time. After reviewing this procedure, it was also discarded since no significant addition to the project's objectives would have resulted.

The last item to be considered under the computer code evaluation is the effect of the grid size on the predictive accuracy of the numerical simulation. Of importance to the shelter research program is the cost saving coarser grids would provide in reducing computer running time. A possible

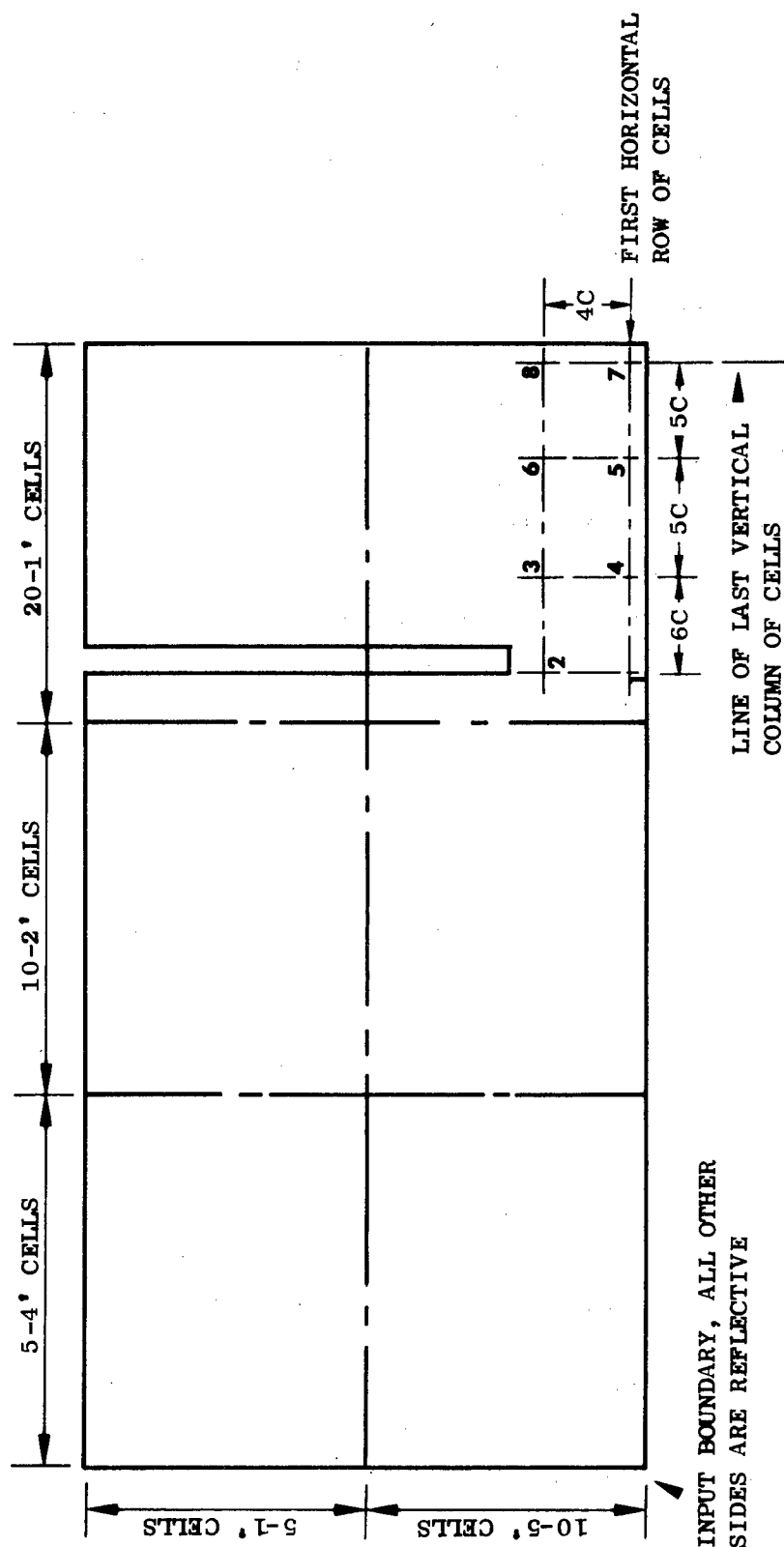


Fig. 18. Grid for Comparison of Variable-Cell-Size Procedure

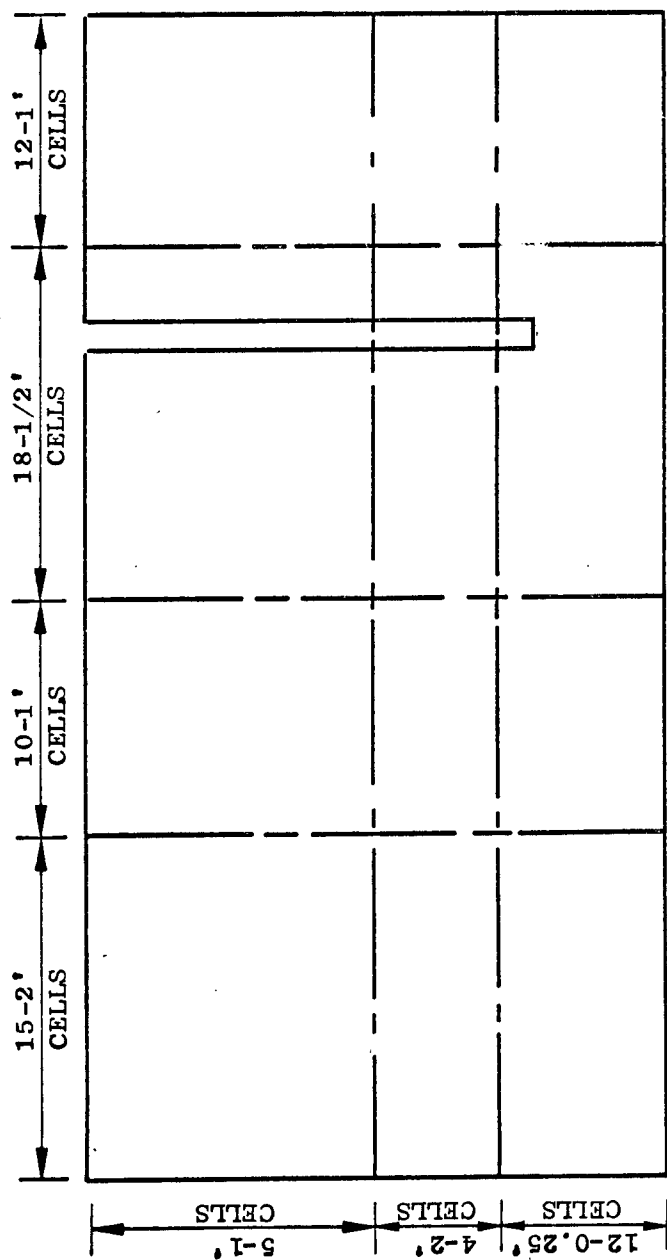
Table 5  
COMPARISON OF MULTIPLY VARIABLE CELLS  
WITH NON VARIABLE CELL SIZE

Point	Time (msec)	Axial Velocity (fps)		Radial Velocity (fps)		Overpressure (Psi)	
		5 cell	10 cell	5 cell	10 cell	5 cell	10 cell
1	10	459	464	-10.6	-11.5	4.86	4.95
	20	613	610	16.6	13.3	3.08	3.11
	30	613	608	16.7	17.8	3.92	3.91
	40	430	432	10.5	13.2	7.52	7.45
2	10	480	484	-41.8	-46.3	3.33	3.42
	20	538	541	-85.0	-83.5	1.53	1.68
	30	501	503	-83.0	-83.9	2.54	2.46
	40	233	239	-39.4	-44.7	7.10	7.03
3	10	242	243	14.8	14.4	2.56	2.53
	20	517	514	21.3	22.5	2.67	2.61
	30	583	574	16.2	16.0	3.92	4.03
	40	609	602		3.40	6.77	6.82
4	10	231	232	74.2	73.4	2.55	2.54
	20	449	448	84.8	87.3	2.59	2.61
	30	453	449	66.0	66.8	3.89	4.00
	40	419	418	5.63	4.08	6.45	6.54
5	10	60.3	62.6	3.42	3.53	1.01	1.05
	20	173.	176.	29.2	3.18	3.49	3.64
	30	129.	128.	11.7	12.0	7.57	7.56
	40	294.	292.	13.0	11.5	7.79	7.88
6	10	51.	52.9	9.8	10.1	.89	.93
	20	171.	170.	17.48	19.6	3.76	3.77
	30	100.	102.	75.7	74.1	7.41	7.42
	40	219.	223.	81.6	71.6	7.84	7.83
7	10	-.98	1.0	-.006	-.0065	0	0
	20	9.8	10.4	5.4	4.85	3.83	3.96
	30	21.1	22.3	8.78	7.0	7.65	7.60
	40	43.2	45.1	15.1	10.6	8.98	8.85
8	10	-.69	-.71	-.188	-.153	0	0
	20	9.4	10.3	31.35	30.6	3.87	4.02
	30	18.7	19.0	52.8	53.4	7.53	7.58
	40	31.4	32.3	45.6	66.5	8.22	8.34

additional feature is that they may provide some insight into the feasibility of writing a small coarse-grid code to provide the general shelter research program and the practicing architectural engineer with a way of establishing load and flow information. This approach is attractive in that it limits the data display problem, provides for a wide range in geometric and input variation, and offers potential simplicity for the user. The key to its feasibility is the coarseness of the grid that can be tolerated. The following discussion will consider some of the aspects of the effect of grid size on the computer output, after noting some pertinent functional aspects revealed in the course of solving the problem.

Figure 19 presents the geometry of a test case used to determine the effect of grid size on the results of the numerical simulations. The simulation was performed on UNIVAC to determine if a significant cost differential existed between it and the CDC series of machines. None was established, but differences in peripheral equipment were found to give each an advantage in different situations. This observation does underscore one feature that should be noted with regard to the use of machines from several different manufacturers. The best way to handle the computer output is on magnetic tape. The problem arises with the variation in tape format and number of bytes per word. If differences do occur, conversion of the tape to the new machine format is required. This procedure is costly and, hence should be avoided by careful planning of computer usage.

The main purpose of the simulation (Fig. 19) was to compare the effect of cell size variation on the basis of the situation presented in Fig. 18. A 5-cell-wide entrance was used in the simulation presented in Fig. 18 and a 10-cell-wide entrance in the other simulation presented in Fig. 19. The axial and radial velocities and the pressures at 10-msec time intervals at the locations noted in Fig. 18 are presented for both simulations in Table 6.



BOUNDARY AND INPUT CONDITIONS AND THE MONITORING POSITIONS ARE THE SAME AS FOR FIG. 18.

Fig. 19. Grid for Comparison of Variable-Cell-Size Procedure

Table 6  
COMPARISON OF THE EFFECT OF GRID COARSENESS  
ON THE OUTPUT OF NUMERICAL SIMULATIONS

Pt	Time (msec)	Axial Velocity (fps)			Radial Velocity (fps)			Overpressure (Psi)		
		5 cell	10 cell	5c/10c	5 cell	10 cell	5c/10c	5 cell	10 cell	5c/10c
1	10	464	463	1.002	-11.5	- 7.4	1.554	4.95	4.98	.993
	20	610	642	.950	13.3	- 21.4	-.621	3.11	3.31	.940
	30	608	616	.987	17.8	- 22.6	-.7876	3.91	4.41	.887
	40	432	394	1.0964	13.2	- 18.2	-.7253	7.45	8.79	.848
2	10	484	515	.940	-46.3	- 47.4	.977	3.42	3.42	1.000
	20	541	590	.917	-83.5	-118.	.708	1.88	2.00	.803
	30	503	509	.988	-83.9	-112.7	.744	2.46	3.05	.807
	40	239	184	1.2989	-44.7	- 53.8	.831	7.03	8.27	.850
3	10	243	235	1.034	19.4	11.8	1.644	2.53	2.71	.934
	20	514	491	1.047	22.5	17.6	1.278	2.61	3.97	.657
	30	574	601	.955	16.0	17.2	.930	4.03	3.98	1.013
	40	602	676	.891	3.4	6.01	.566	6.82	6.48	1.052
4	10	232	219	1.059	73.4	72.5	1.012	2.54	2.63	.966
	20	448	441	1.016	87.3	105	.831	2.61	2.79	.935
	30	449	482	.932	66.8	112	.596	4.00	3.79	1.055
	40	418	439	.952	4.08	12.8	.3188	6.54	6.12	1.069
5	10	62.6	58.9	1.063	3.53	1.5	-	1.05	.93	1.129
	20	176	177	.994	3.68	2.38	-	3.64	3.79	.960
	30	128	123	1.041	12.	10.4	1.154	7.56	7.88	.959
	40	292	284	1.028	11.5	13.5	.852	7.88	7.92	.995
6	10	52.9	51.9	1.019	10.1	9.6	1.256	.93	.84	1.107
	20	170	171	.994	19.6	17.1	1.146	3.77	3.87	.974
	30	102	105	.971	74.1	70.8	1.0466	7.42	7.65	.970
	40	223	230	.970	71.6	86.1	.832	7.83	7.83	1.000
7	10	10	9.47		- .0065		1.000	0	0	1.000
	20	10.4	11.7		4.85	4.06	1.195	3.96	4.19	.945
	30	22.3	18.1		7.	7.03	.996	7.60	7.82	.972
	40	45.1	39.		10.6	10.	1.06	8.85	8.67	1.021
8	10	- .71	.755		- 1.53			0	0	1.000
	20	10.3	11.8		30.6	26.3	1.163	4.02	4.11	.978
	30	19.0	15.2		53.4	53.3	1.002	7.58	7.77	.976
	40	32.3	33.0		66.5	66.8	.996	8.34	8.28	1.007

A review of the data presented in Table 6 indicates some regions in which deviations do exist between the 5- and 10-cell-wide entrances. In the entrance region (points 1, 2, 3) the inflow in the 5-cell-wide entrance persists for a slightly longer period than for the 10-cell case. One explanation for the longer flow is the poor representation of rarefaction waves by the coarser grids.

A more comprehensive method of reviewing the data would be to consider the mass and energy influxes into the chamber. These basic parameters determine the chamber conditions; hence by comparing the influx across the entry at comparable times, a comparison of the effects of the variation in coarseness of the mesh in the entrance can be made. The values of these parameters can be determined from the thermodynamic and flow parameters in the code output by summing the values determined for each cell.

The values of mass and energy influx determined for any time step are, in effect, instantaneous values. Accordingly, the computed influxes are mass and energy rates at that instant, as opposed to quantitative values. Quantitative values were determined by combining the mean influx rate over the interval with the influx area and the time increment between intervals. This gross averaging process was sufficiently accurate, because the influx curves could be accurately approximated by linear segments for each computational interval.

The values of mass rate were computed using the product of the vector velocity and the density. The energy influx was computed using the energy equation in the form of kinetic and potential energies (as discussed in Ref. 2). The results of these computations are plotted in Figs. 20, 21, 22, and 23. The cumulative influxes defined in these curves are then the total influx of mass or energy to that instant in time.

The simulation with the 10-cell entry produced higher influxes of mass and energy. The influxes of mass and total energy and potential energy had a maximum variation of approximately 3.5 percent between the two simulations, whereas the variation in kinetic energy influx was approximately 20 percent.

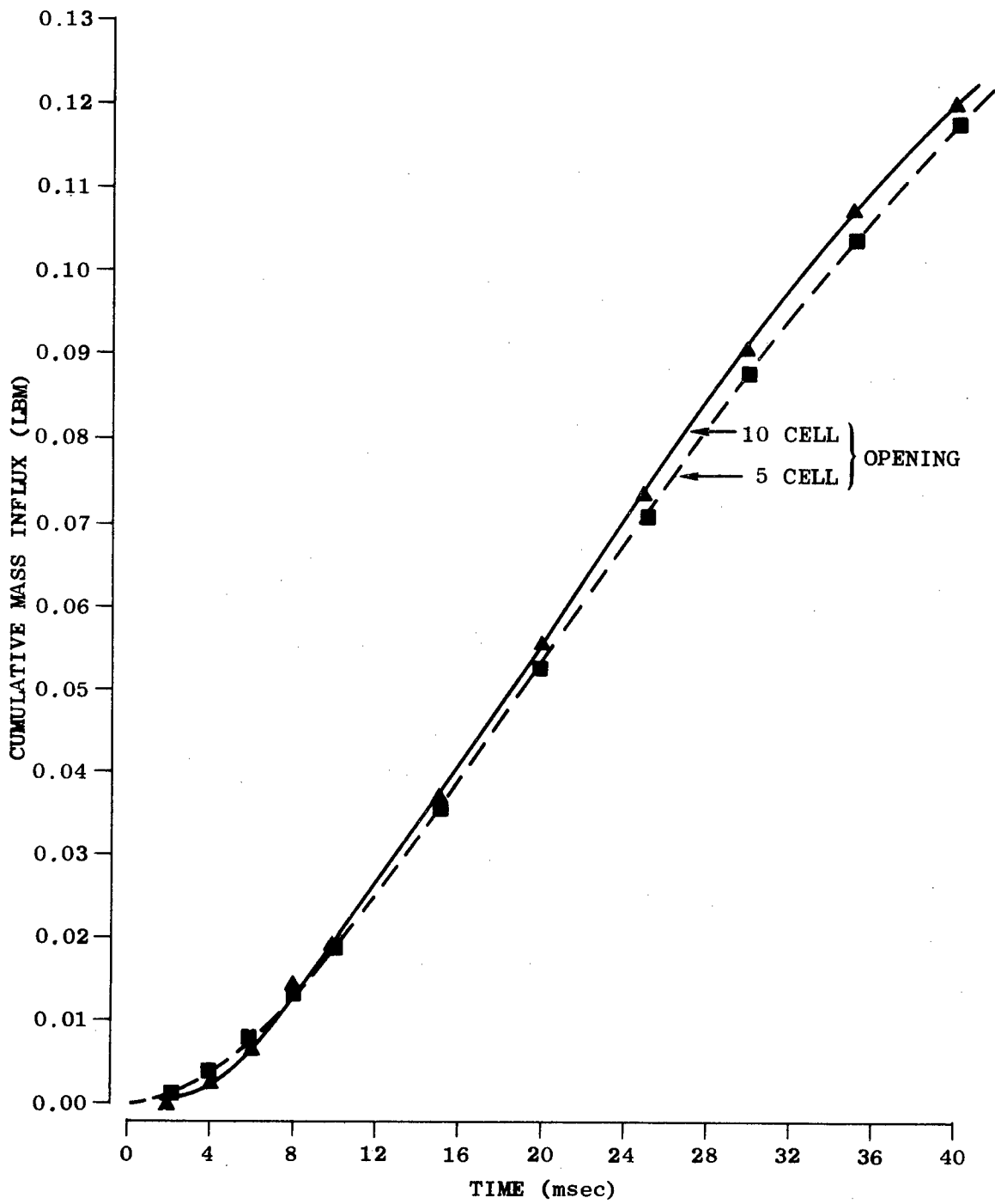


Fig. 20. Cumulative Mass Influx as a Function of Time



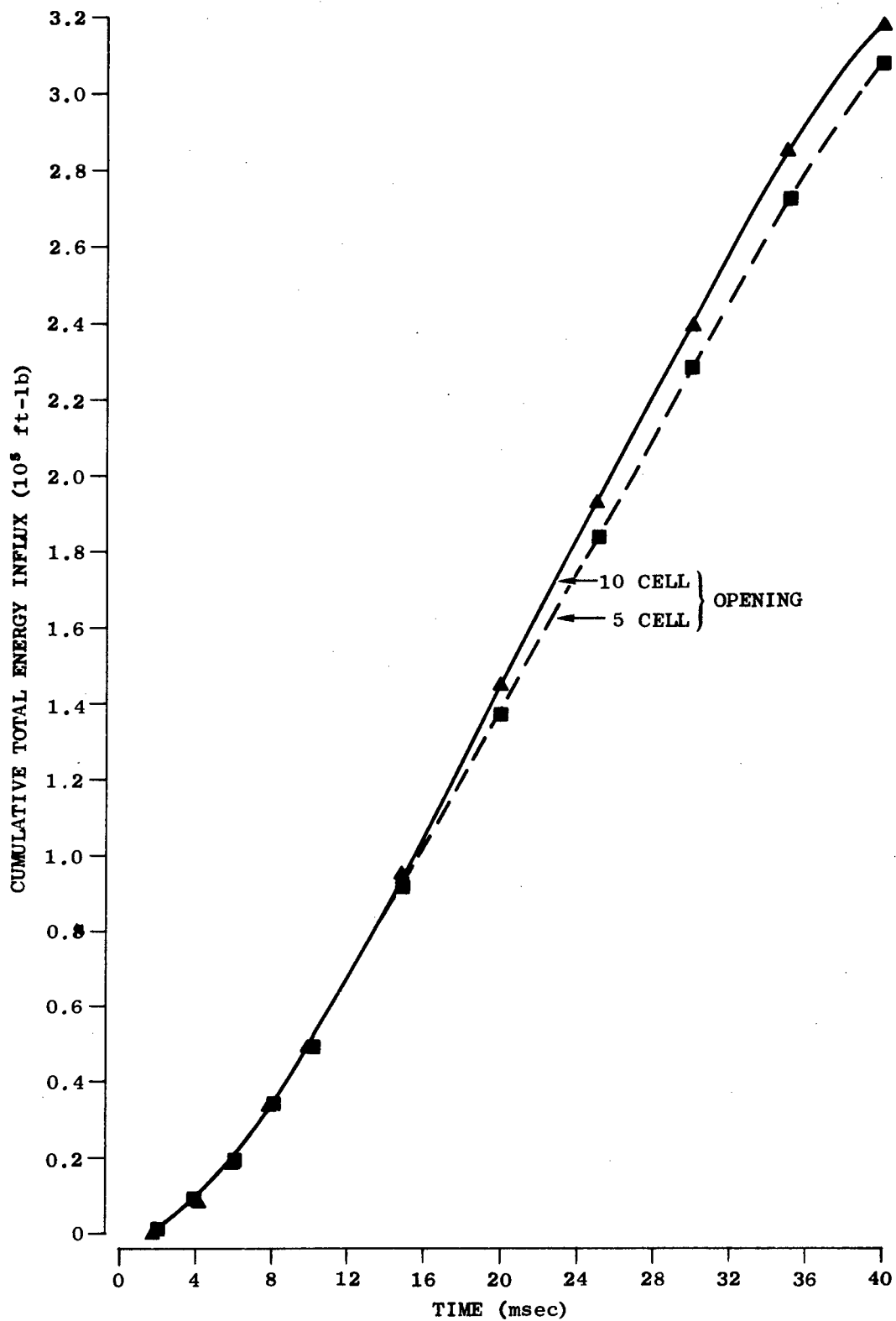


Fig. 21. Cumulative Total Energy Influx as a Function of Time

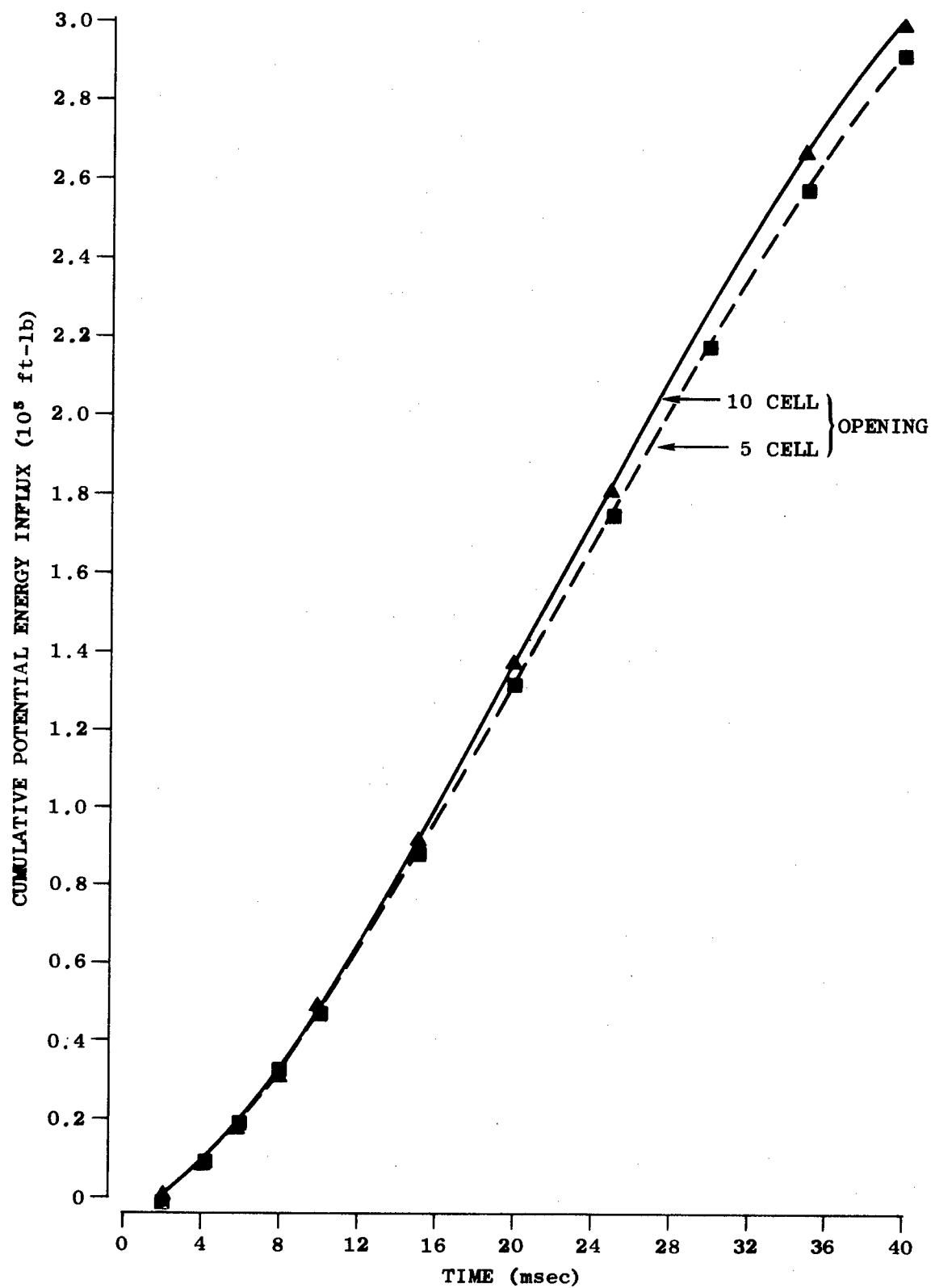


Fig. 22. Cumulative Potential Energy Influx as a Function of Time

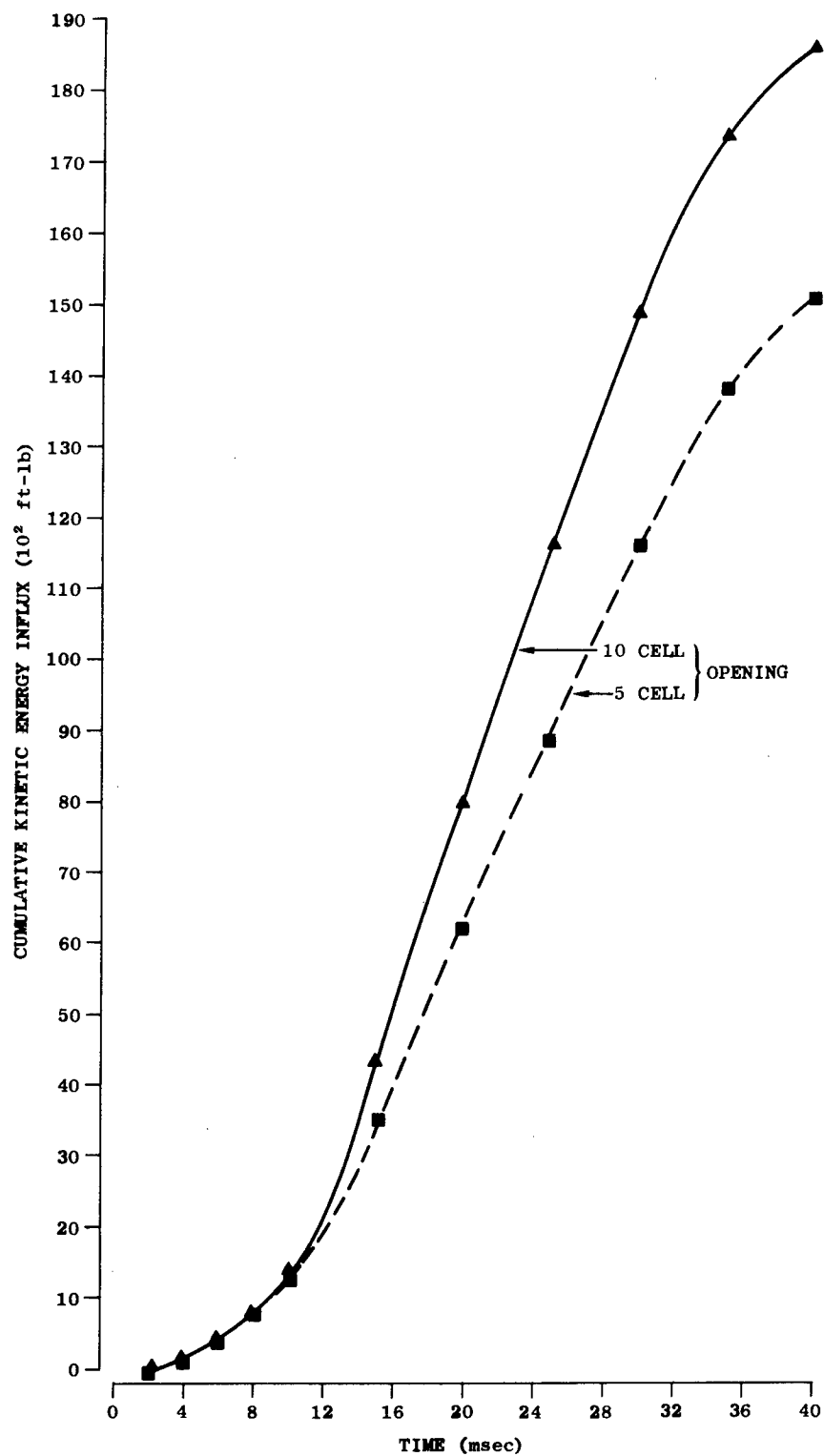


Fig. 23. Cumulative Kinetic Energy Influx as a Function of Time

The percentages would indicate that the variation in predicted pressure profiles in the simulated room were not drastically affected by the number of entry cells. The kinetic energy variation was more pronounced, and velocity distributions and profiles would accordingly be expected to vary.

Figures 20 to 23 provide cumulative influxes as a function of time. Variations in the influxes of energy and mass can occur in large steps in short time intervals making it difficult to establish the error source. The dilemma is caused by the errors being carried forward cumulatively. To provide a better insight into the process, the mass and energy influxes in specific computation time intervals are presented in Figs. 24 through 27.

The largest deviations in the plotted data occurred in the kinetic energy influxes in the 15 to 20 msec time interval. The 10-cell simulation had a  $37.7 \times 10^2$  ft-lb kinetic energy influx and a 0.0189 lbm mass influx, as compared to  $26.7 \times 10^2$  ft-lb and 0.0175 lbm influxes for the 5-cell simulation. These influxes correspond to average inflow velocities of 632 fps and 552 fps, respectively, with corresponding dynamic pressures of 3.32 psi and 2.68 psi. The variation in dynamic pressure corresponds to about 20 percent at this peak interval. The variation for most of the time range would be considerably lower.

One interesting feature is that the kinetic energy, although a small portion of the total energy involved, does play a large role in determining the drag forces of the flow. A brief review of why the discrepancy occurred is accordingly appropriate. The basic reason for the variation is the inability of the coarser grid to accurately reproduce gradients in the flow.

These gradients of interest are the entering shock wave and its subsequent reflections, the rarefaction waves propagating around the entry and through the chamber, and the rapidly curving streamlines of the inflow. The first two factors cause delays in the changes in the flow variables, but should not form long-term variations. The problems cannot, however, be completely isolated because the inflow is dependent upon the movement of these waves. The waves initiate the strong inflow that develops the strong gradients in the streamline curvature.

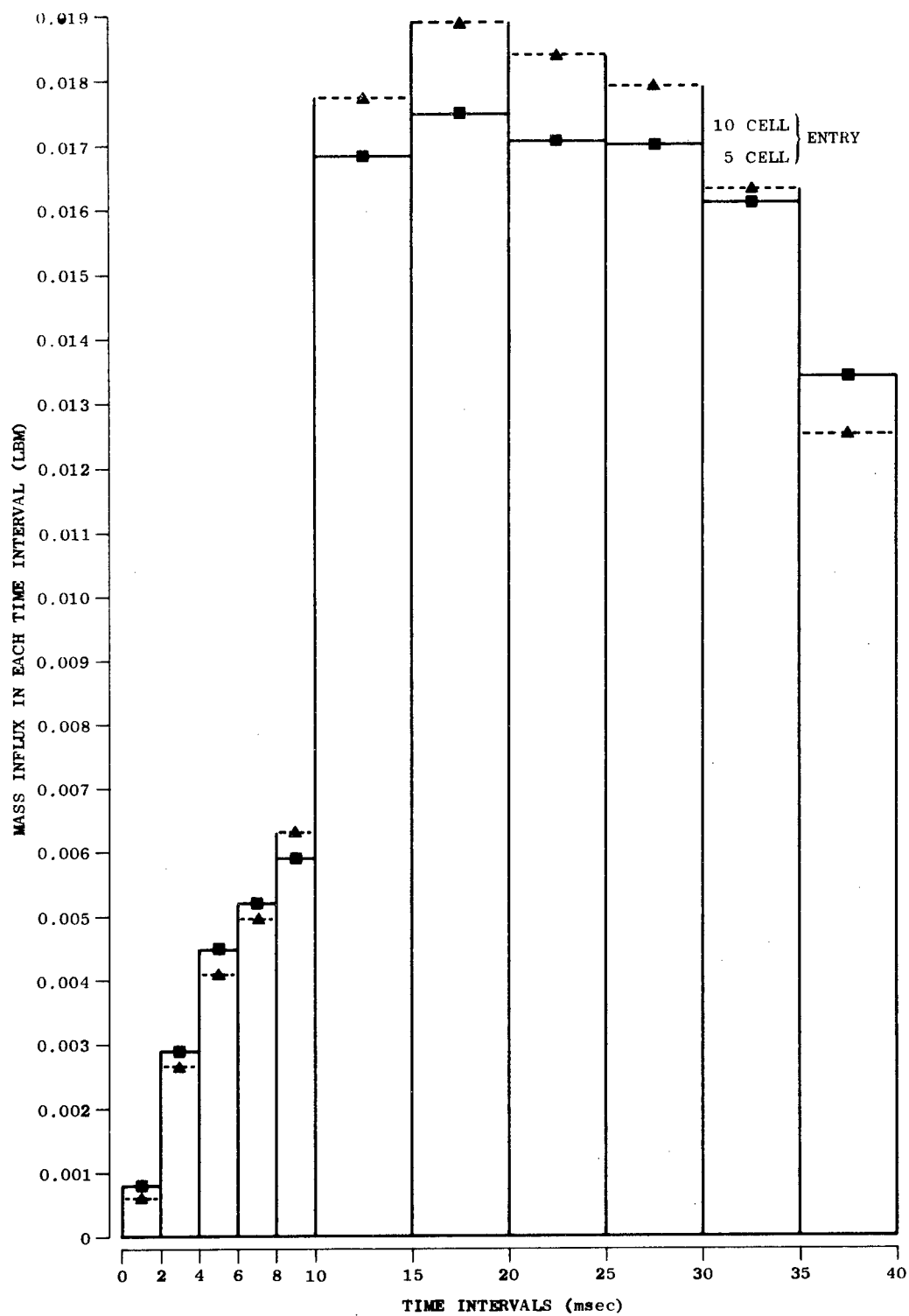


Fig. 24. Mass Influx as a Function of Computation Intervals

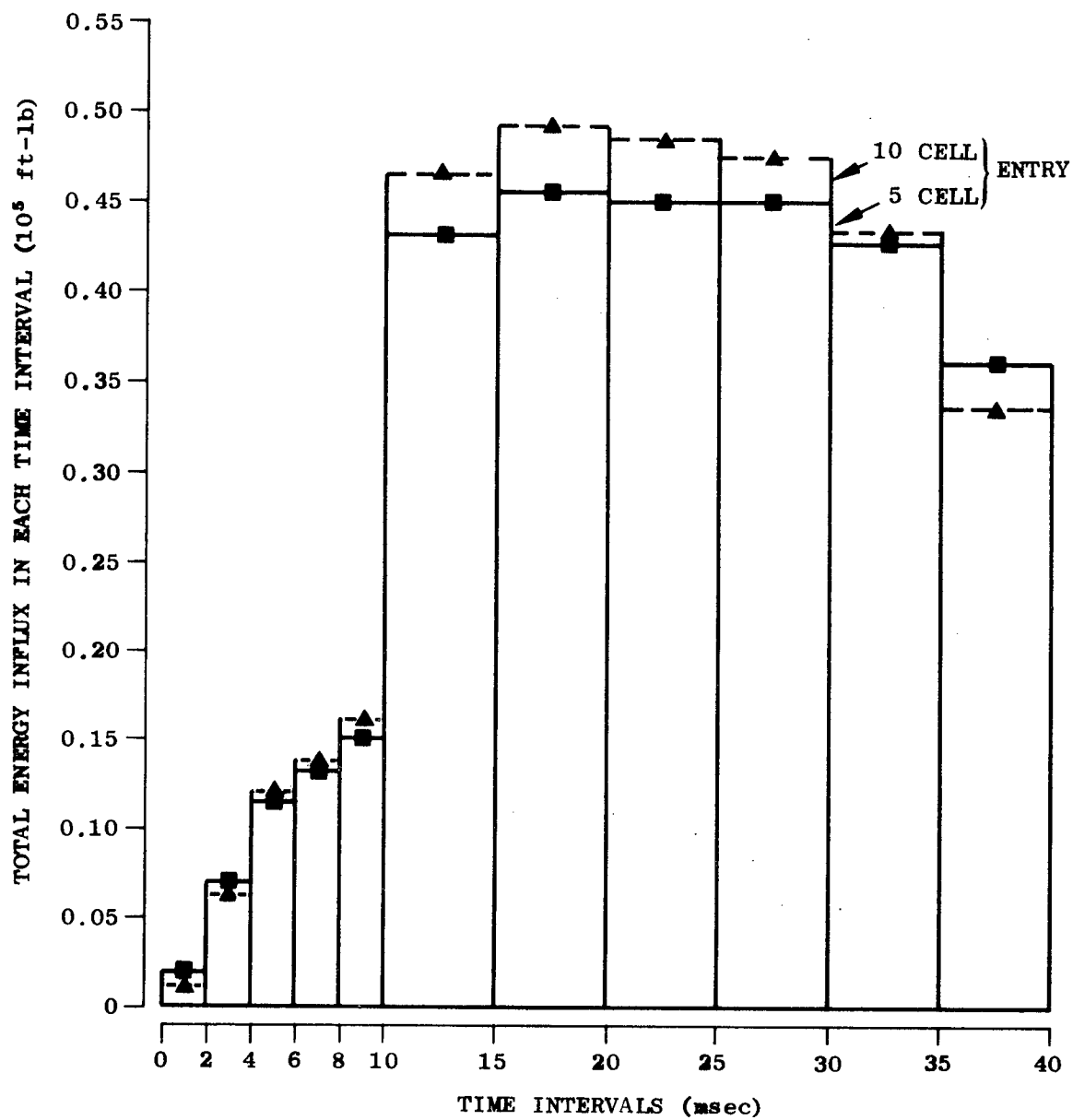


Fig. 25. Total Energy Influx as a Function of Computation Intervals

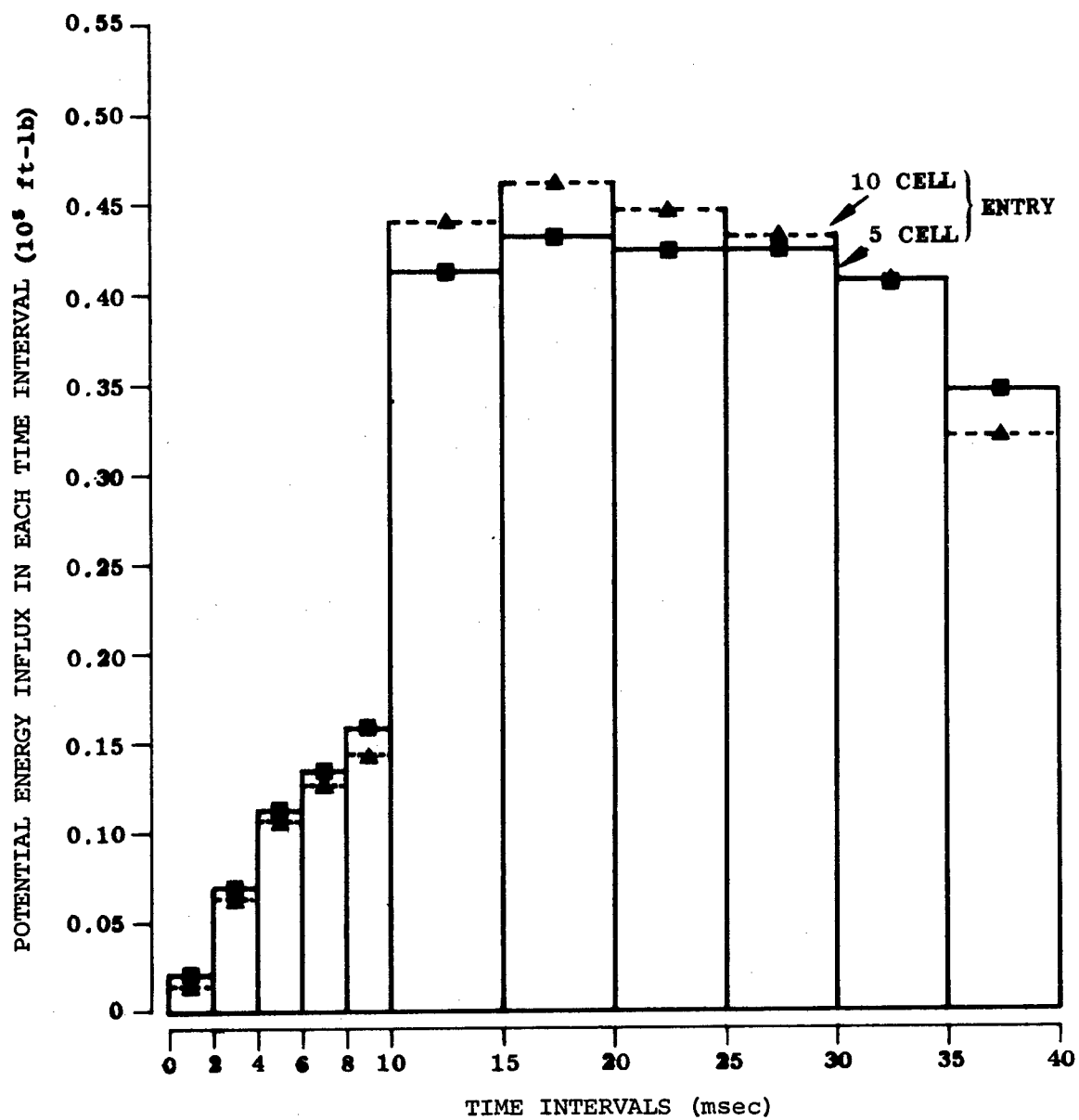


Fig. 26. Potential Energy Influx as a Function of Computation Intervals

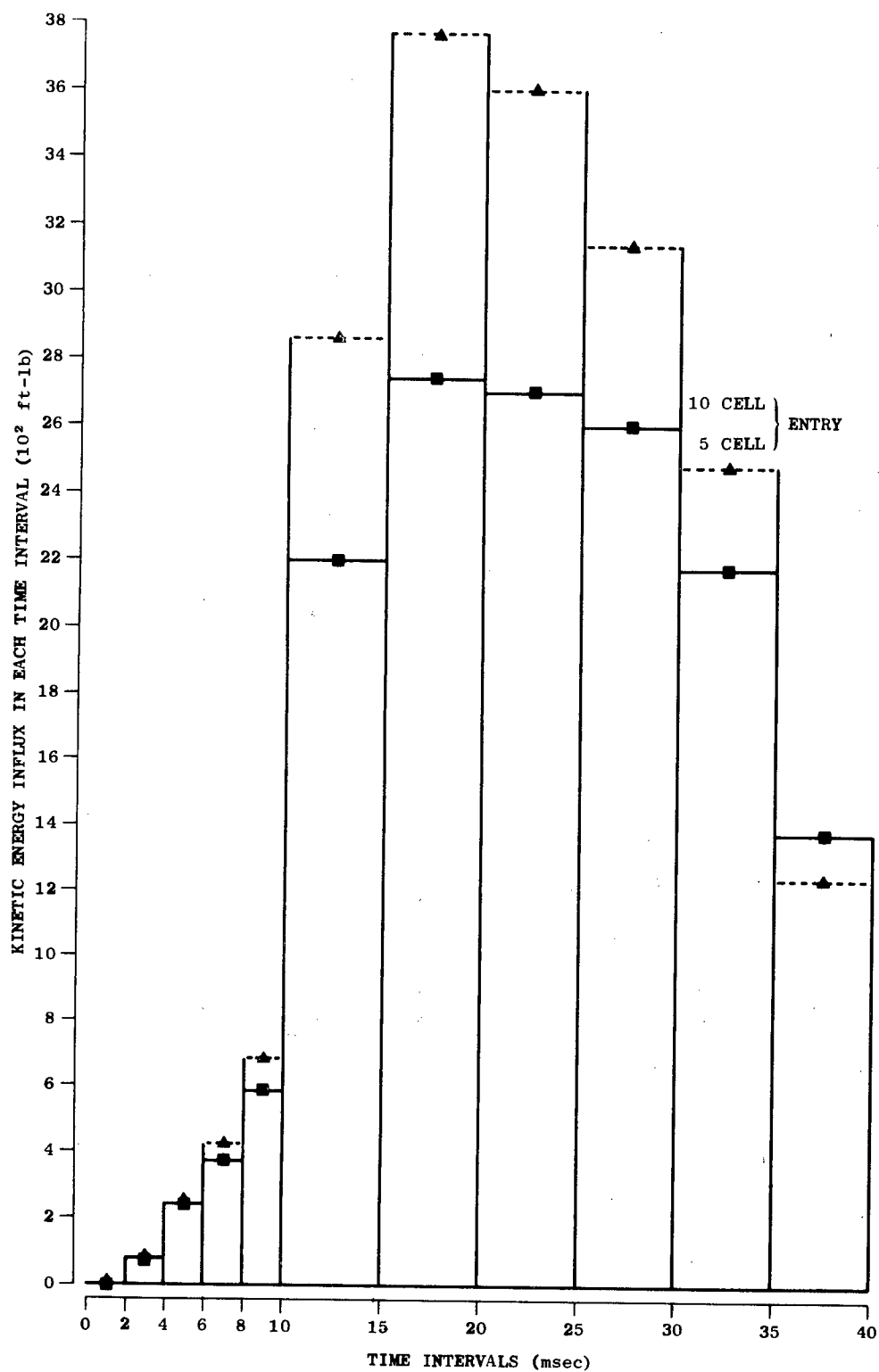


Fig. 27. Kinetic Energy Influx as a Function of Computation Intervals



The problem of the rapid change in curvature can be considered by reviewing the contraction equations for a vena contracta. To arrive at an estimate of the curvature of a streamline, the maximum curvature for a free jet of incompressible fluid is selected. The maximum curvature would occur on the free streamline. Conformal mapping via the Schwarz-Christofel theorem as applied by Chaplygin will provide a functional form for the streamline. Discussions of these methods can be found in Refs. 45 to 53.

The parametric equations of the steady free surface, first developed by Lamb, are given by Ref. 45 as

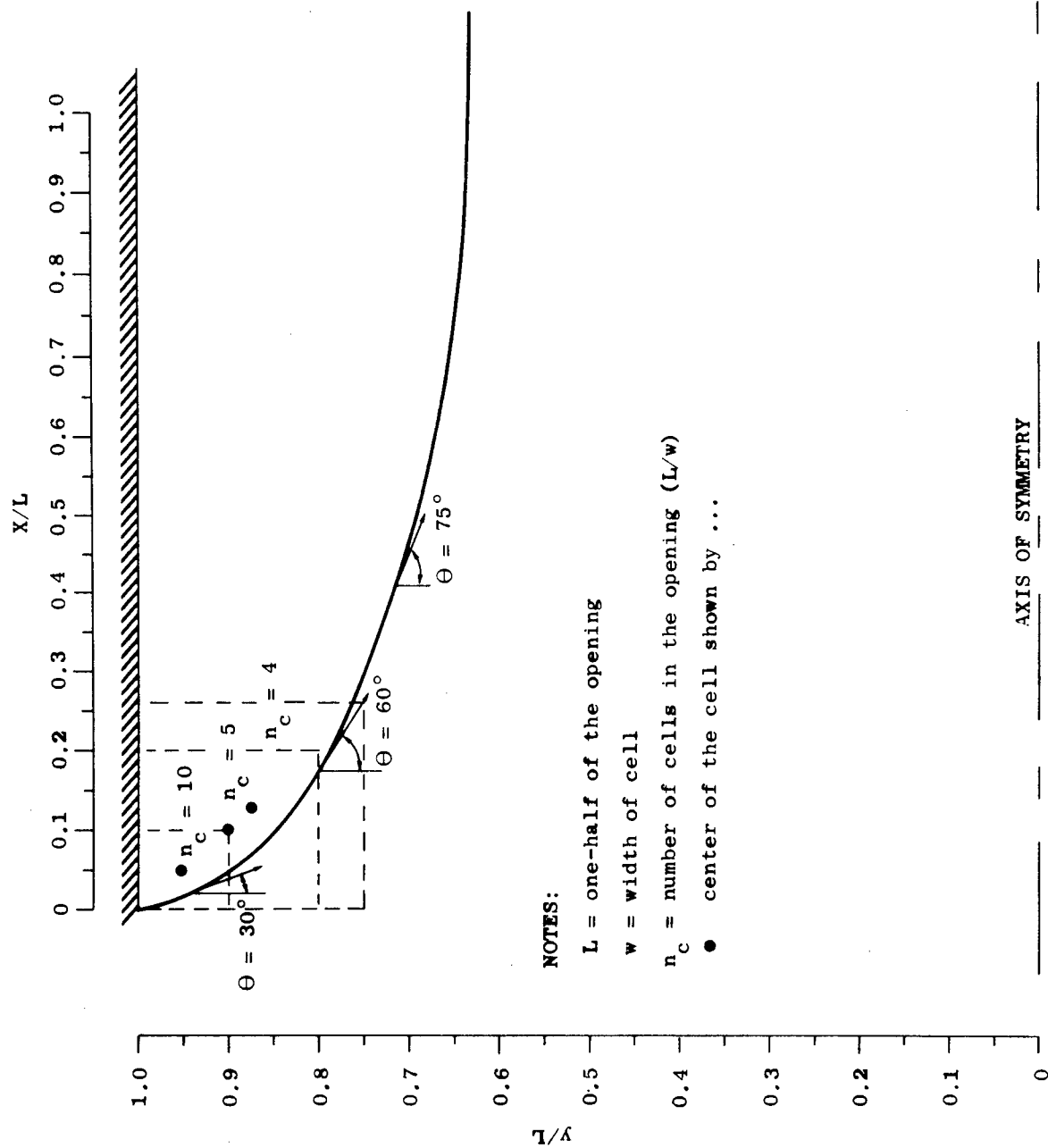
$$\frac{x}{L} = \frac{\pi}{2 + \pi} - \frac{2}{2 + \pi} \cos \theta \quad (14)$$

$$\frac{y}{L} = \frac{2}{2 + \pi} \left[ \ln (\sec \theta + \tan \theta) - \sin \theta \right] \quad (15)$$

where the terms in the equations are defined in Fig. 28. Define a cell width  $w$  equal to  $L/n_c$ , where  $n_c$  equals the number of cells in distance  $L$ , and assume the cells are square. Since these equations cannot be worked with easily, a graphic approach to the interacting effects of vena contracta and cell size will be used.

The variation in the cell size as shown in Fig. 28 affects the coverage in the first cells. For the three cases shown,  $w = 0.1x/L$ ,  $0.2x/L$ , and  $0.25x/L$ , i.e., corresponding to 10, 5 and 4 cells per half-width of entry, none of the cases provided a capability to adequately represent the flow. The value of the flow calculated for each cell is at the center of the cell. In the cases shown in Fig. 28, the centers of all the cells are outside of the vena contracta, in a zone in which there is no flow.

The averaging process by which the conditions of the cell boundaries are calculated (see discussion in Section II and Appendix A) can provide a method for accounting for this type of variation. Due to the rapid change in flow



NOTES:

- $L$  = one-half of the opening
- $w$  = width of cell
- $n_c$  = number of cells in the opening ( $L/w$ )
- center of the cell shown by ...

Fig. 28. Vena Contracta and Cell Size Geometry

properties and the rapid curvature of the streamline, the flow field cannot be accurately represented by the cells shown. The reason for the greater flows in the 10-cell case can be deduced from Fig. 28.

In the smaller cell size ( $n_c = 10$ ), the first cell against the barrier does not contain the free streamline; but a cell below it would contain 85 percent of the corresponding flow field for that zone. The first cell area contained 25 percent of the flow inside the vena contracta in that cell. For the case of  $n_c = 5$ , approximately 30 percent of the first cell's area is in the flow zone of the vena contracta. This small percentage corresponds to an inability of the larger single cell to represent the flow accurately. In the comparisons of energy and mass influx, the result was a higher influx of mass and energy for the 10-cell case, which could more accurately represent the inflow. The 5-cell case represented a greater spreading of the inflow to lower values.

The reduced influx in the 5-cell case appears to correlate more closely to experiment. The reduced influx corresponds to some of the energy-dissipation mechanisms internal to the flow fields which the numerical simulations do not account for. The dissipation mechanisms appear to be lessened in larger scale shelters, but sufficient experimental evidence is not available to completely document this observation.

In that the deviation between 5- and 10-cell data seems to favor use of the smaller number of zones, it would seem possible for a coarse-grid code to be used to predict flows in shelters. Additional analytical and experimental work should be undertaken to fully ascertain the implications. If the present indications are supported, a fairly simple and very general two-dimensional code could be developed as a general prediction tool for the shelter designer.

## Section 4

### FLOW PROCESSES

This section will review several aspects of the general flow process prior to discussing a qualitative model of the flow. Based on prior work (Ref. 2), the following general model of the total inflow process is presented as preliminary groundwork for the individual flow processes. The qualitative or conceptual model will then be formulated using these results, the numerical simulations, and implications drawn from experimental studies.

The airblast wave, on reaching the exterior of the shelter chamber, establishes a high pressure reservoir which provides the energy for driving the inflow of gas into the shelter. The airblast initially enters as a shock wave which propagates and expands through the chamber. This transient process is seen as a perturbation on the long term filling process of the chamber.

The inflow is formed by an adiabatic expansion from the reservoir to the chamber conditions. The influent gas is a high-velocity, highly directed flow which is in effect a transient jet. The inflow is the driving force for a long term circulatory flow field. The pattern is altered if the chamber is long relative to the side in which the entrance exists. For this case the flow approaches that found in a tunnel in which the circulatory flows are replaced by axial flows.

#### THE TRANSIENT INFLOW PROCESS

The initial expansion of gas into the room is a two-part phenomenon. The first is the transmission of the incident shock wave into the room and its subsequent expansion. The second part is the evolution of the flow field behind the shock wave. In early times (in the range of  $t = 0$  to  $t = d/a_2$  where  $d$  is the slit width and  $a_2$  is the sound velocity behind the incident shock wave) the transmission process governs, but with time decreases in effect until the flow expansion behind the shock wave governs the flow. In this section some of the characteristics of the formation process will be reviewed.

A specific precise mathematical solution for the unsteady flow of a jet of compressible fluid could not be found in the literature. The closest approximation to the process was found in a presentation by Curle (Refs. 52 and 53) on the expansion of an inviscid incompressible fluid from a vessel. Although an error occurs for the compressible flows being considered, this work will be reviewed and used to provide further inputs to the conceptual model being developed.

The unsteady flow representation is based on the classical Helmholtz conformal mapping procedures found in Refs. 45 through 51. These works are the outgrowth of Lamb's now classical solution (Ref. 51) to the problem of defining the free flow of an inviscid and incompressible flow through a slit from a large reservoir into free space. Although the flows are incompressible, the close correlation of the incompressible flows to compressible flows can be found in the work based on Chaplygin's techniques (Ref. 50). The steady state representation, such as the one shown in the preceding section, is not directly applicable to the transient portion of the compressible flows encountered in shelter flows.

The unsteady flow analysis developed by Curle (Refs. 52 and 53) does provide some interesting, though limited, insight into the transient flow definition problem. A brief review of his work will accordingly be undertaken and its significance relative to the conceptual model will be discussed.

The basic analytical procedure in conformal mapping is the transformation of the physical plane to the hodograph plane using a complex velocity. The rationale for this procedure is that  $\theta$  (the flow vector direction) is then a constant along all solid boundaries and  $q$  (the magnitude of the flow vector) is constant on free streamlines. The procedure, a further description of the mapping process, and examples of applications of the theory can be found in the references.

Curle's contribution extends the steady state analysis of jets to include their transient formation. The solutions apply to the expansion of an incompressible fluid into free space. Since the purpose of this study is to gain insight into the processes, the use of the incompressible approach seems justified because analytical work on compressible flows is not available. It must be stressed that the approach will only provide analytical approximations, very much qualitative as opposed to quantitative.

Curle's method is to expand the velocity potential  $\phi$  in powers of  $e^{-\lambda t}$  in the form

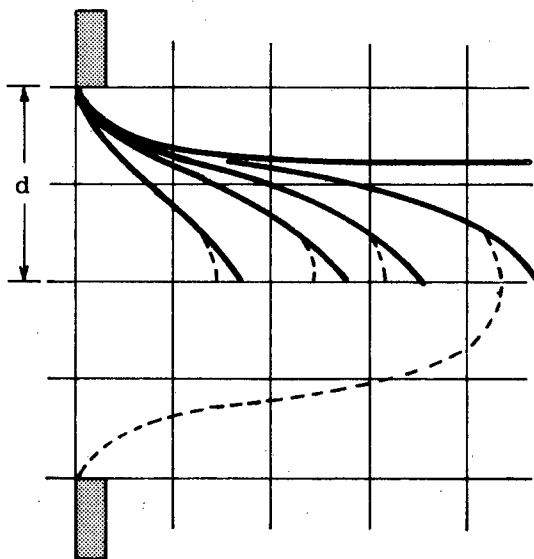
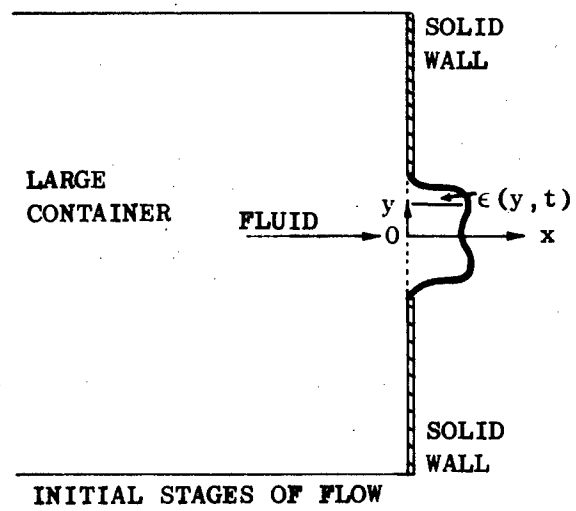
$$\phi(x,y,t) = \phi_0(x,y) + e^{-\lambda t} \phi_1(x,y) + O(e^{-2\lambda t}) \quad (16)$$

Equation (16) is basically the perturbation of the steady state solution  $(x,y)$  by time-dependent terms including an Eigenvalue  $\lambda$  which is determined by the boundary condition at infinity. Curle also defined the spatial variation of the unsteady flow  $[\phi(s,t)]$  from the steady state boundary by the expression

$$\phi(s,t) = \phi(s) e^{-\lambda t} + O(e^{-2\lambda t}) \quad (17)$$

Through these expressions Curle has altered the physical boundaries of the flow to correspond to the transient situation. The mathematics involved in the process can be found in Refs. 52 and 53.

The first result Curle predicts in his work is the existence of an M-shaped discharge in the jet, shown in the upper portion of Fig. 29. The strong influx along the edges of the entry provides the reverse effects of the vena contracta which eventually forms with its strong flow in the central region. Curle points out that extension of this analysis would require a more detailed knowledge of the upstream conditions.



SHAPE OF JET AT TIMES  $t = (d/U)\{1.08, 1.81, 2.28, 3.08\}$

(Reproduced from Ref. 53)

Fig. 29. Curle's Representations of Early Inflow Process

The lower portion of Fig. 29 shows the outline of the jet shape at varying times after inception of the flow into the downstream region. The dashed curves show improved estimates of the curvature of the nose of the jet which Curle points out is inversely proportional to the square of its velocity and that the limiting radius of curvature approaches four tenths of one-half the slit width. The lower dashed curve in the bottom portion of Fig. 29 represents the shape of the jet when the nose has propagated more than a slit width downstream.

The conditions of the transient compressible flow situation negate many of the results reached in the preceding analysis. The initiation of the flow by the propagation of a shock provides a downstream flow field for the jet to flow into. Similarly, the reflection processes in the upstream region also contribute to the formation of the inflow process. Unlike the incompressible solution in which free space was assumed, the downstream region contains mass which must be moved by the influent gas.

The above, although negating the possibility of a direct application of Curle's work to the shelter inflow situation, does indicate features in the flow which may be of interest. These features are the result of the flow dynamics and should occur in some form in the compressible flow. Of particular interest is the profile of the influx as it moves into the chamber. The narrowing of the inflow in these early stages corresponds to the lack of spread of the jet observed in the large scale experimental studies discussed in Appendix C. The profiles of the flows in the numerical simulations resemble the described phenomena, but superpositioned on the shock induced flow field.

Further work in this area was not undertaken. Future studies should review this area, for if the effect predicted by Curle does exist in shelter flows, a limitation in the spreading of the inflow would result during the transient flows of the filling process. The following review of the transition processes considers the compressible gas effects via a one-dimensional approximation.

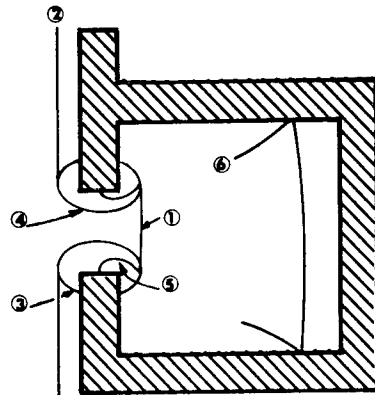


The inflow process in its initial stages for a compressible gas is comprised of a complex system of interacting waves. The process was described in Ref. 2 for a simple two dimensional geometry using the wave systems which form upon the incidence of the shock wave at the tunnel entrance. Figure 30 presents the wave configurations for both a narrow and a long entry. To gain further insight into the transient inflow process, the two-dimensional system will be transformed into a one-dimensional system which approximates the described wave systems.

For the purpose of this discussion, the entry will be extended through the chamber in the form of a long tunnel. The extension is in effect a model of the jet that forms without any components interacting with the remainder of the chamber. The reservoir conditions will also be developed on a one-dimensional basis with constant pressure conditions imposed to form the source. The resultant geometric and wave diagram schematics are presented in Fig. 31.

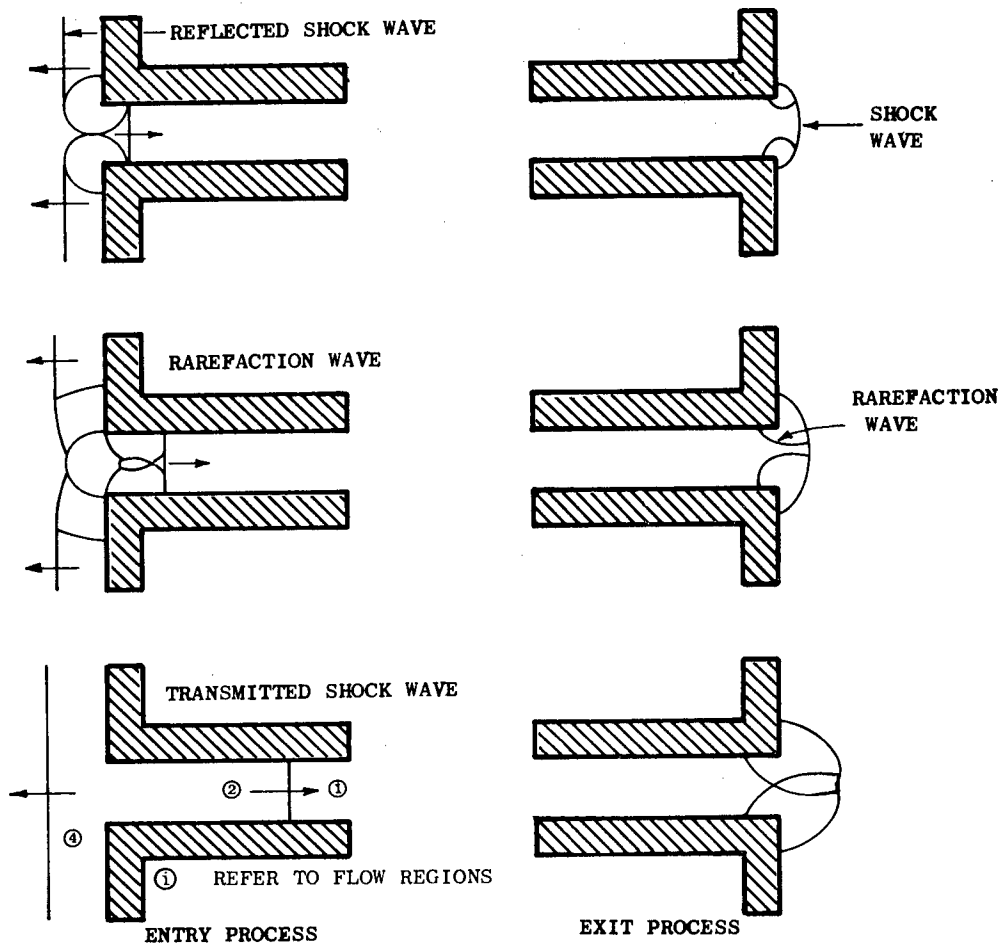
The increase in the velocity of the reflected shock wave at early times corresponds to the closure of the reflected wave and the gradual approach to equilibrium conditions. The wave diagram shown in Fig. 31 is for an infinite reservoir. For a finite reservoir, the rarefaction fan shown would have a continuing interaction with the reflected wave until equilibrium conditions were reached. The equilibrium conditions would result when the upstream mass influx into the system was balanced with the mass influx into the chamber through the entry.

A decrease in the velocity of the transmitted shock wave begins early in the transmission process. The decrease corresponds to the interaction of the rarefaction wave with the transmitted shock wave (labeled 1 and 5 in Fig. 30, respectively). The rarefaction fan shown in the wave diagram of Fig. 31 represents the acceleration of the fluid from the reservoir into the jet corresponding to the pressure differential between the two regions.



- (1) Transmitted incident shock wave
- (2) Reflected incident shock wave
- (3) Rarefaction wave from exterior corner
- (4) Reflected wave of Mach configuration
- (5) Rarefaction wave from interior corner
- (6) Regular reflection wave from wall interaction

(Abstracted from Ref. 3)



(Abstracted from Ref. 2)

Fig. 30. Blast Transmission into a Narrow Entrance and the Equivalent Process in a Long Entry

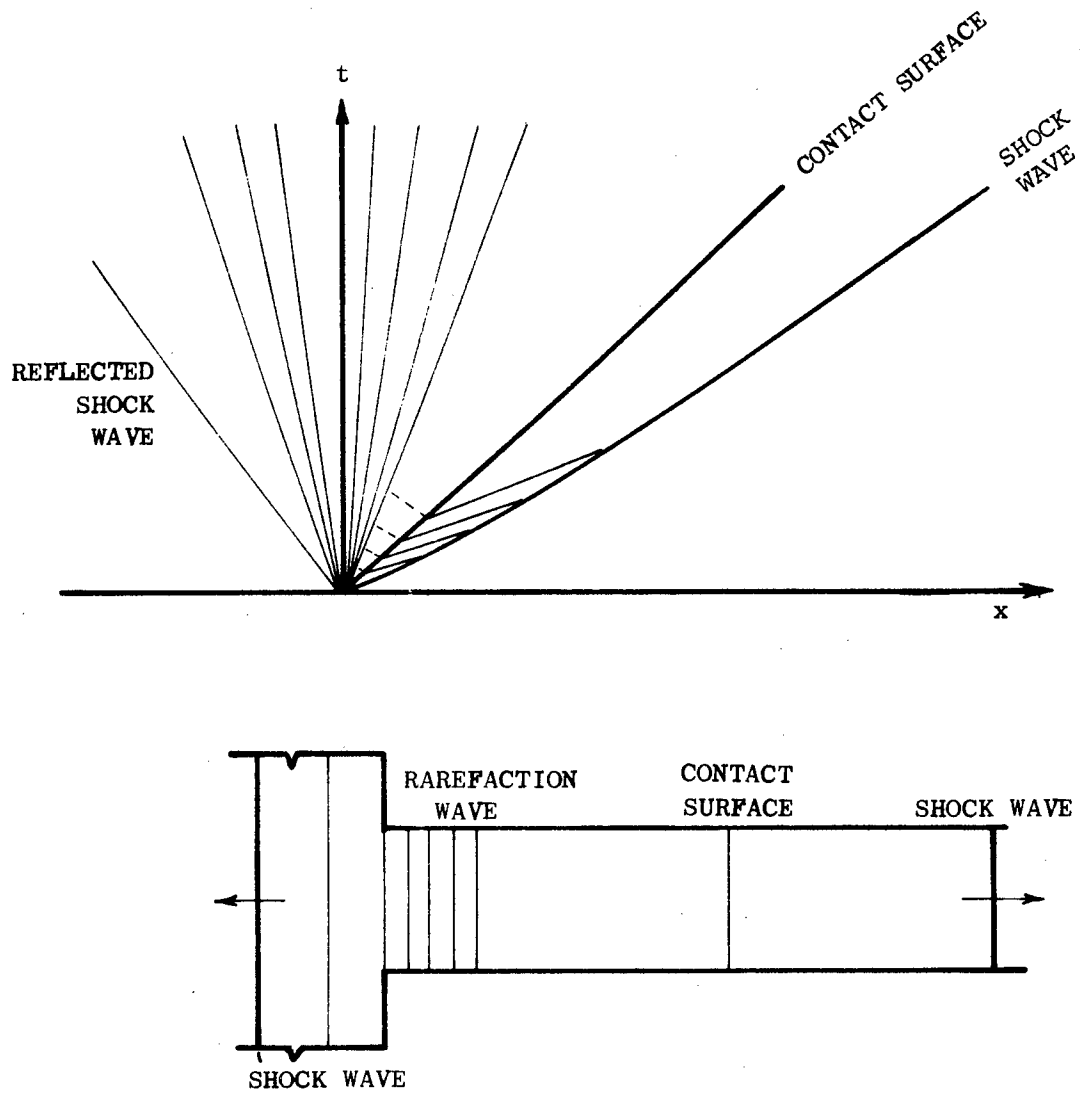


Fig. 31. A Simple Diagram of the Initiation of a Quasi-One-Dimensional Process

The expansion process during the transitory period creates an interesting anomaly. If a gas is expanded from the reservoir conditions to the pressure in the jet (or behind the shock front), a difference in velocities results. Since two masses cannot occupy the same space, the influent mass acts as a piston on the gas in the chamber (or brought in by the incident transmitted shock wave). The contact surface is then the boundary of the piston from which emanates a series of compression waves. As the piston is a gas and not a solid, a series of backward-facing rarefaction waves must also emanate from the contact surface.

In a steady flow these waves are absent as the shocked gas ahead of the contact surface has moved away and a steady expansion and flow condition has been reached. Under normal two-dimensional steady flow conditions, the fluid in the jet is a combination of influent gas and chamber gas, with the condition that at any cross-section the momentum is approximately constant. In the transient chamber-filling situation this condition is never precisely reached, and only at certain times in the filling process is it even approached.

The mathematical description of the inflow process is complicated by its nonlinearity. A quasi-steady approximation of the later portions of the inflow process was presented in Ref. 3 to provide some bounds on the process. The transiency of the flow, particularly at early times in the inflow, produces a wide variety of possible solutions depending upon the intermediate conditions. Several of these intermediate situations were approximated by quasi-steady flow analogies and were investigated in Ref. 2 and shown to provide valid local solutions.

To illustrate the process on a transient basis, the following example was selected. The incident wave impinges normally upon an infinite reflecting wall containing the chamber entrance. The wave will be assumed to be fully reflected in the reservoir region and the incident wave will be transmitted into the chamber without any attenuation (the most unfavorable condition for this argument). A pressure differential across the entry exists corresponding to the difference between incident and reflected conditions.

Rather than develop similar derivations as found in Ref. 2, the values presented therein will be used and are presented in Table 7 for the preceding conditions. For the most favorable, or lower bound, condition, the variation between inflow and shocked flow values range from multiples of 2 to 4. The upper bound flows, a full adiabatic expansion, have multiples ranging from approximately 3 to 7. The piston effect must exist if mass is to be conserved.

Table 7  
COMPARISON OF FLOW PARTICLE VELOCITIES

Overpressure (psi)		$u_2$ (fps)	$u_e^*$	$u_e^{**}$
Incident	Reflected			
1	2.06	53.4	362	195
2	4.23	104	502	333
3	6.51	152	610	416
4	8.90	198	730	468
5	11.4	242	831	503
6	14.0	284	921	528

$u_2$  = flow velocity behind incident wave, assumed to be the same as transmitted wave

$u_e$  = expanded velocity for a pressure differential between incident and reflected conditions

\* = pre-contraction, refers to flow value computed at the outer entrance of the chamber (Ref. 2)

\*\* = max-contraction, refers to the velocity obtained in a free adiabatic expansion (Refs. 2 and 3)

To illustrate the piston effect of the flow, we first consider a simplified case in the quasi-one-dimensional system. The inflow process must be modeled in the transformed one-dimensional coordinates for the more general case, hence the simplified case will use a start-up model, shown in Fig. 32.

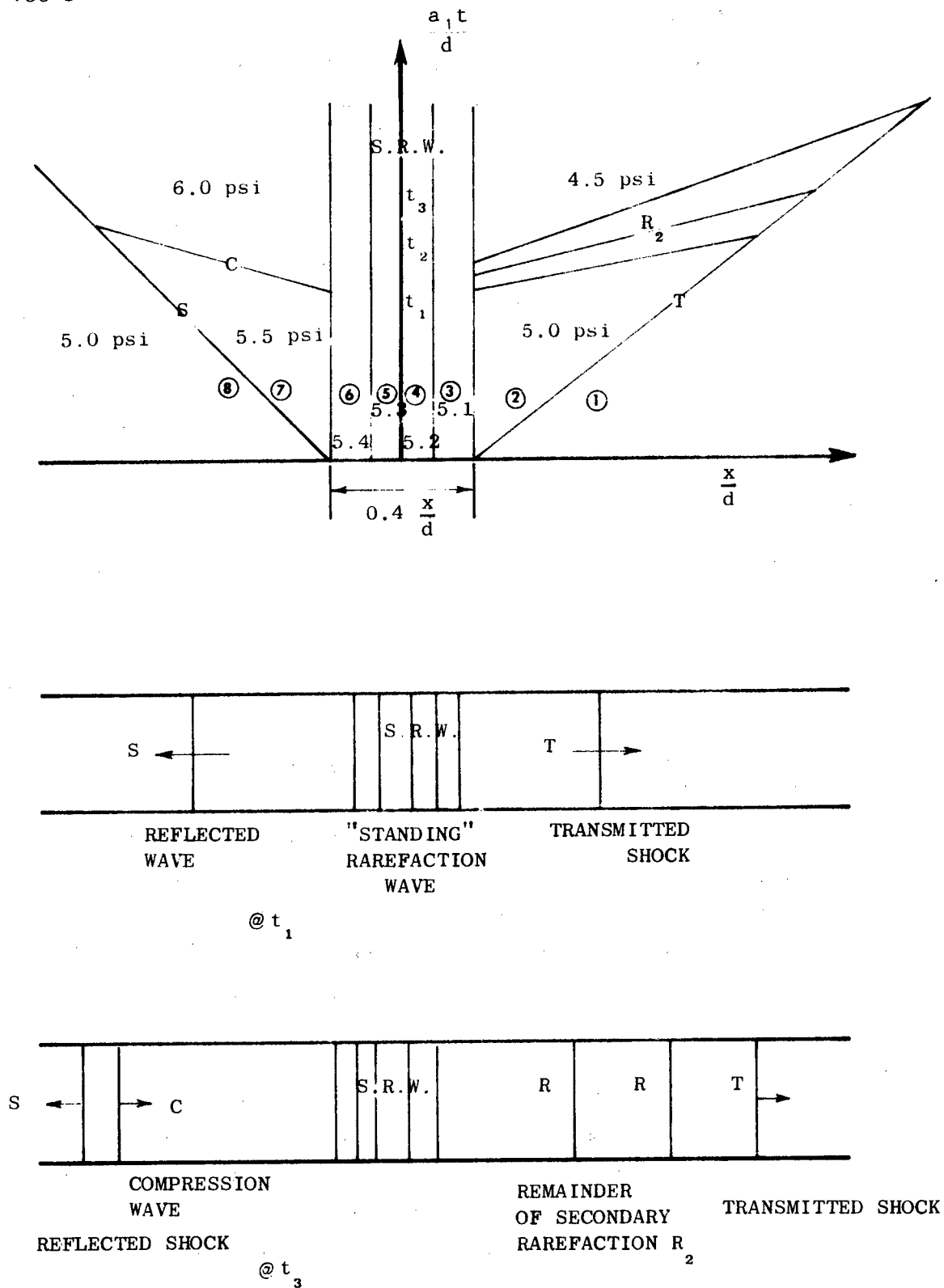


Fig. 32. Preliminary Wave Diagram of One-Dimensional Model

In the preliminary model (shown in Fig. 32) an artificial system is established. To account for the time span in originating the transmitted and reflected waves one dimensionally, in comparison to their two dimensional counterparts, a  $0.4 x/d$  spread was assumed (a close approximation to the closing model given in Ref. 2). As the flow begins, this standing wave remains and defines the expansion between the reservoir and the chamber. In the two-dimensional case, as the wave systems formed, the transmitted shock wave (T) was weakened by its expansion in the chamber and the hole in the reflected shock (S) closed. The compression wave (C) and the rarefaction wave ( $R_2$ ) are the conditions imposed to account for the beginning of the process. These would be impressed in steps, over a period  $t = 0$  to  $a_1 t/d = 1$ , such as the one shown at  $t_3$ .

If we review Fig. 32, during a period prior to  $t_2$  (such as  $t_1$ ) the following sequence is observed:

- An inflow corresponding to a 5.0 psi overpressure shock wave flows through the entrance and the reflected shock (S) is raised to an overpressure of 5.5 psi.
- The inflow is then expanded through the standing rarefaction wave to the 5 psi overpressure behind the transmitted wave.

Not shown in the wave diagram is the effect of the expansion on the flow behind the transmitted shock, i.e., the location of the contact surface. More specifically, if the expansion is adiabatic, does the expanded flow velocity equal the flow velocity behind the transmitted shock wave? This condition must be met if a contact surface is to exist (across which flow velocity and pressure are equal).

Using the above properties of the flow, the conditions behind the reflected shock can easily be determined by transforming the coordinate system so as to stop the wave in laboratory coordinates and then writing the continuity equation across the wave. For the weak waves being considered, adiabatic conditions can be assumed, and using  $a$  to represent sound speed,  $p$  pressure,  $u$  particle velocity,  $\rho$  density, and  $\gamma$  the adiabatic gas constant, the following equations can be written.

$$u_7 = u_8 - a_8 \left(1 - \frac{\rho_8}{\rho_7}\right) = u_8 - a_8 \left[1 - \left(\frac{a_8}{a_7}\right)^5\right] \quad (18)$$

$$\frac{p_7}{p_8} = \left(\frac{a_7}{a_8}\right)^7 = \left(\frac{\rho_7}{\rho_8}\right)^{1.4} \quad (19)$$

The expansion from condition 7 to 2 is adiabatic and hence not path-dependent. The energy equation for steady flow can be written as

$$\frac{u_7^2}{2} + \frac{p_7}{\rho_7} \left(\frac{\gamma}{\gamma-1}\right) = \frac{u_2^2}{2} + \left(\frac{\gamma}{\gamma-1}\right) \frac{p_2}{\rho_2} \quad (20)$$

and as  $p_8 = p_2$  then for a completely adiabatic process  $a_8 = a_2$ . Using the above relationships and combining them with the preceding equations, we can write

$$u_2^2 = \left\{ u_8 - a_8 \left[1 - \left(\frac{a_8}{a_7}\right)^5\right] \right\}^2 - 5 (a_7^2 - a_8^2) \quad (21)$$

Substituting values into Eq. (21) for the 5 psi incident overpressure condition, an expanded velocity of 313.5 fps is determined [the shocked flow velocity in region (2) is 241.5 fps]. The expanded flow is going faster than the shocked flow, hence it is acting like a piston.

To follow this line of reasoning a wave diagram will be constructed (Fig. 33) showing the initial sectors of the inflow formation process. The quasi-one-dimensional construct will again be used to provide a model for the process. The rapidly increasing complexity of the wave diagram precludes a full solution for the full period of inflow into the chamber. The preliminary phases of the wave diagram do, however, provide valuable insight into formation of the flow process.

A slight modification to the standing rarefaction wave has been made. As shown in the wave diagram, the standing rarefaction waves follow particle paths (zones 2', 3, 4, 5, and 6). An artificial separation of the variables occurs in zones 2', 2 and 12 and again between 13 and 16. A series of



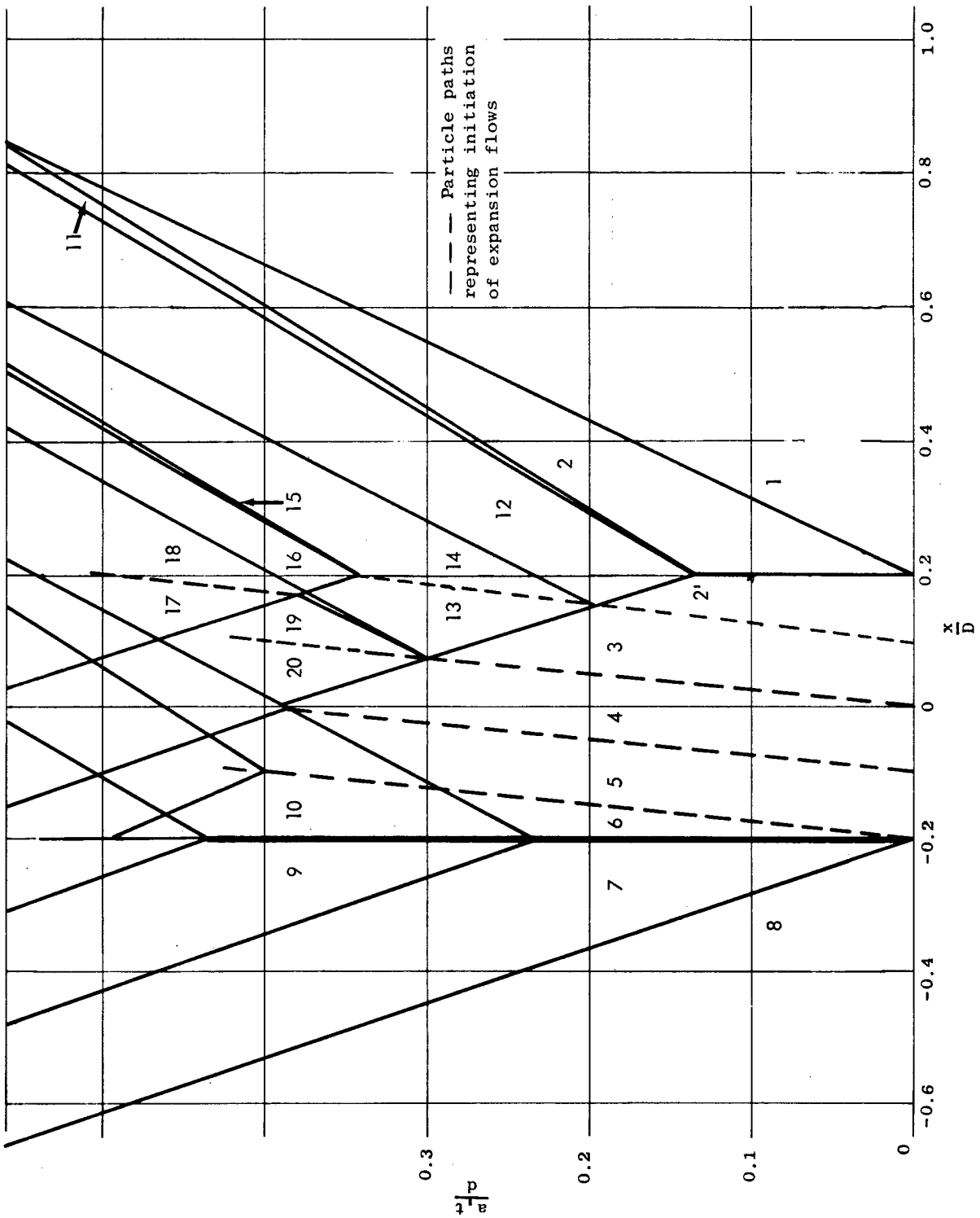


Fig. 33. Wave Diagram Approximation for Quasi-One-Dimensional Inflow Simulation

compression waves would emanate from gas particles expanding into zones 2 and 12 from 2' or 16 from 13. Rather than use a series of waves a single wave was used to represent these waves, hence an inconsistency occurs at the boundaries mentioned.

Tables 8 shows the values of the flow, state, and Reinman invariants for each zone. Adiabatic conditions were assumed across all waves, introducing a small error but simplifying the calculation procedure. In light of the assumptions made to form the quasi-one-dimensional process, the small error attributable to entropy increases is negligible. This is in keeping with the purpose of the exercise, that of providing insight into the flow process.

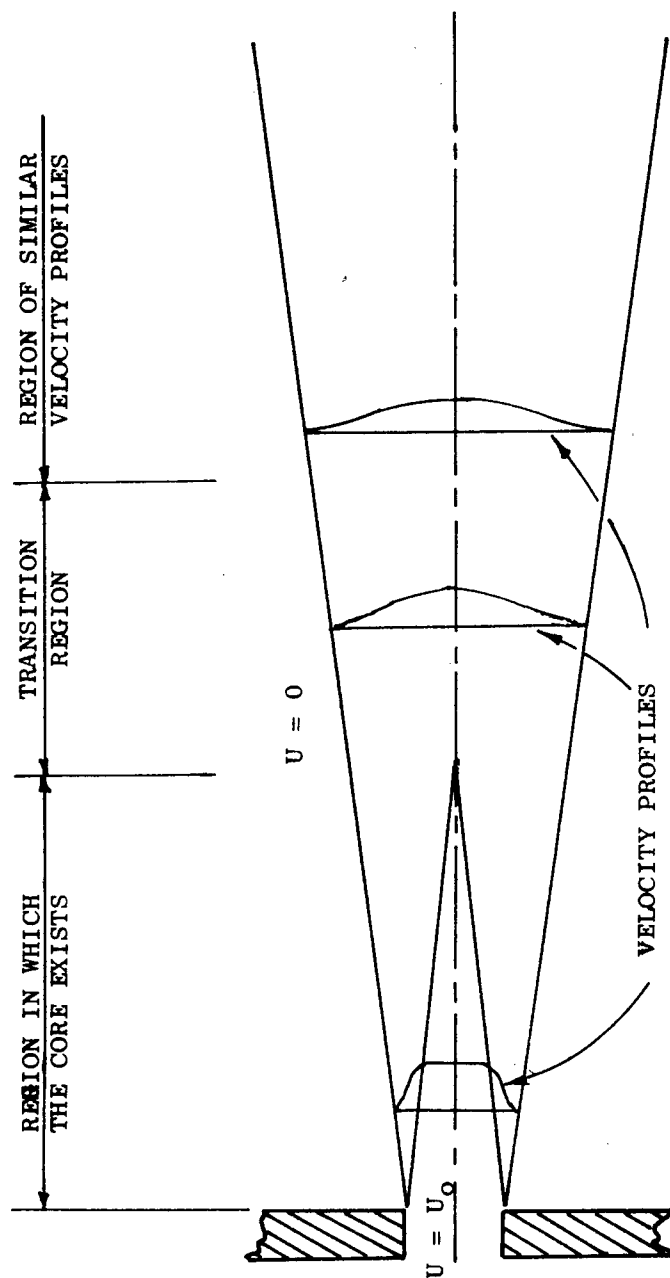
The flow ( $u$ ) across the expansion (regions 7, 6, 5, 4, 3, 2, 2') is seen to increase above the value for region 2 as was indicated by Eqs. (18) to (21). The result is a ~~so~~ compression wave moving into region 12. The pressure and velocity in regions 13 and 14 were matched by adjusting the value of the  $Q$  wave moving into regions 2' and 3. The expansion from 4 to 3 creates a velocity ( $u$ ) whose corresponding pressure is greater than the pressure in either region 3 or 13 and, therefore ~~P~~ and  $Q$  compression waves form.

The expansion of the shock wave in the chamber is simulated by the rarefaction waves between regions 2 and 12 and 14 and 16. The closure of the reflected shock wave by compression waves occurs between regions 7 and 8 and 9 and 10. In the investigation, the process discussed was varied by assuming different conditions at various interfaces. The results obtained from the other conceptualizations of the flow forming process did not vary appreciably.

Arguments can be produced to fault the assumptions of the preceding analysis. The results presented were for what appeared to be the most realistic of the wave diagrams constructed. Some similar diagrams for a duct exiting into free air can be found in Ref. 54. These wave diagrams carry out the computations to later times and show the pulsating nature of this form of flow

Table 8  
FLOW FIELD PARAMETERS FOR FIG. 33

Point	$\mathcal{P}$ (5a+u)	$a$ (5a-u)	u	a	u+a	u-a	P (psi)
1	5	5	0	1.0000	1.0000	-1.0000	0
2	5.42941	5.00179	0.213810	1.043120	1.25693	-0.82931	5.0
3	5.4829808	4.9563192	0.2633308	1.04393	1.3072608	-0.7805992	5.1
4	5.47140	4.975439	0.2479806	1.044684	1.29266	-0.796703	5.2
5	5.458826	4.995474	0.231676	1.04543	1.277106	-0.81375	5.3
6	5.44524	5.0164	0.21439	1.04617	1.26056	-0.83178	5.4
7	5.42983	5.03937	0.19523	1.04692	1.24215	-0.85169	5.5
8	5.42941	5.00179	0.213810	1.043120	1.25693	-0.82931	5.0
9	5.42983	5.075986	0.1769135	1.05058	1.227494	-0.873667	6.0
10	5.42941	5.061828	0.18379058	1.0491239	1.2329144	-0.8653333	5.8
11	5.410396	5.00179	0.2043028	1.0412186	1.2455214	-0.836916	4.75
12	5.391170	5.00179	0.194690	1.039296	1.233987	-0.844606	4.5
13	5.4829808	5.00179	0.240595	1.04847708	1.28907208	-0.807882	5.7
14	5.4829808	5.00179	0.240595	1.04847708	1.28907208	-0.807882	5.7
15	5.4638608	5.00179	0.2310354	1.0465651	1.27760048	-0.81552968	5.18
16	5.4447408	5.00179	0.2214754	1.04465308	1.26612848	-0.82317768	4.93
17	-						
18	-						
19	5.47140	5.00179	0.234805	1.047319	1.282124	-0.8125140	5.54
20	5.47140	5.00179	0.234805	1.047319	1.282124	-0.8125140	5.54



(REPRODUCED FROM REF. 3)

Fig. 34. Schematic of Jet Flow

velocity. The process changes the shape of the jet's velocity profile throughout a transition region which ends with the evolution of velocity profiles that will be maintained for the remainder of the flow. The balance of the acceleration of the outer gas and the deceleration of the inner gas can be considered to be a redistribution of momentum through a mixing process.

Variations of these properties of basic jet flow can be established, but they were not considered in Ref. 3. The jets were further categorized as incompressible, turbulent, free, viscous, subsonic, and submerged. In the present discussion only the plane two-dimensional jet will be considered. Well-documented and relatively simple solutions exist for incompressible jet flow with which also have all of the other characteristics listed above; hence the effect of incompressibility is of particular importance.

The magnitude of the effects of compressibility and heat transfer on the flow of subsonic jets were found to have been investigated by Abramovich (Ref. 55). The result of his investigations indicated that if heat transfer was low; i.e., the temperature difference between the core and the stationary gas was small, the effect on the flow's velocity profile was small. Similarly, he determined that the effects of compressibility were yet more limited for flows below Mach 1. The work in Ref. 2, showed these conditions are approximated by shelter flows.

The centerline velocity distribution for a plane jet is presented for several driving pressure differentials in Fig. 35. These centerline distributions were coupled to a full representation of the flow field in Fig. 36 for a pressure differential of 12 psi across the entranceway. A striking feature of these flows is the distance the jet flows before there is an appreciable decrease in the velocity; for example, the core extends into the chamber 5.5 diameters. The transverse growth of the jet is more restricted and the intense flows extend only 1.5 to 2.0 diameters from the centerline of the chamber.

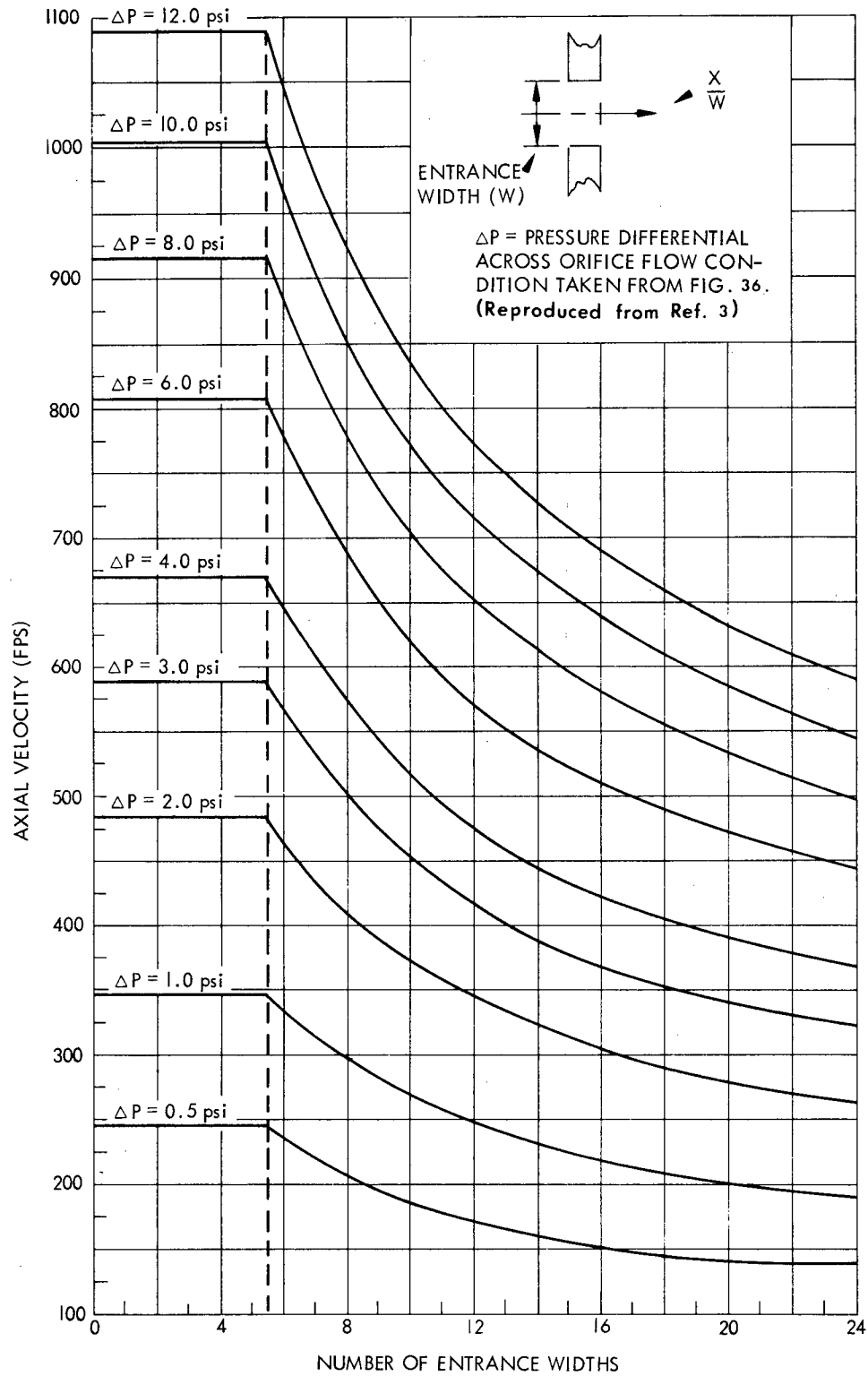


Fig. 35. Centerline Velocity Distribution

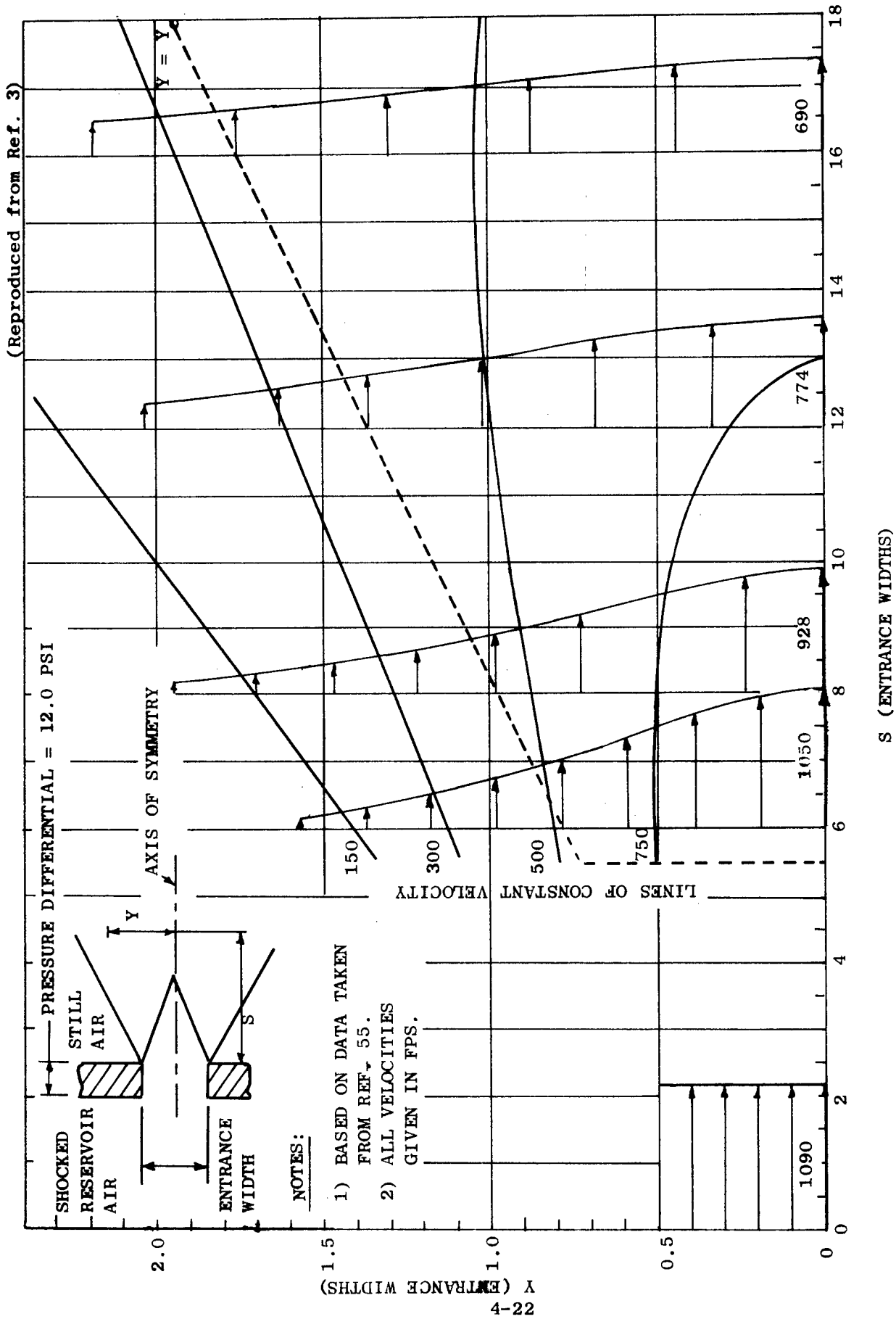


Fig. 36. The Velocity Profiles For A Plane Jet

Reference 3 also discussed some general characteristics of jets. Since the pressures in the free jet are relatively constant (Ref. 56) and the temperature variations small, the density of the jet flow does not vary greatly. Transverse flows occur only as perturbations in the flow field and present no lasting effect. A time period elapses between entrance of the shock wave into the chamber and the establishment of the fully developed jet as was discussed earlier in this report. Experimental evidence (Refs. 3 and 4) showed the penetration of the fully formed core into the chamber ranges from 3.5 to 5.5 effective entrance widths. The term "effective width" refers to the contraction of the inflow in the entrance corresponding to the formation of a vena contracta. The experimentally measured contraction ratios appear to correspond to values established by steady flows.

The preceding synopsis was a condensation of the initial estimate of the inflow process into a two-dimensional shelter space in the first of the present OCD study series (Ref. 3). Recent work has shown variations in the inflow process from the initial model of the flow do exist and warrant attention before considering an improved model of the inflow process. Earlier in this section, analytical models of the inflow process were discussed that showed the dynamics of the inflow process to play a stronger role than was assumed in the first work. The interaction of the gas ahead of the accelerating influent gas and the continuing interaction between the components of the flow field were shown to play a major role in the evolution of a steady flow jet.

Another variation from the quasi-steady characterization is that a flow field does exist within the chamber which reduces some of the transverse velocity discontinuities present in the steady flow free jet. The existence of the internal flow fields and their magnitudes are represented in the data discussed in Section 3 and in Appendix C. These flow fields are related to the piston effect (discussed earlier in this section) in which the motion of the gas ahead of the expanded inflow is driven by it; forming as one boundary condition on the inflow, the expanding shock wave in the chamber. The propagating shock wave will not terminate at the steady-state jet's shear flow



boundary, but rather will spread across the chamber with decreasing strength as documented in Refs. 3 and 4. Accordingly, the quiescent gas surrounding the inflow in the shelter situation does not exist in the pure form of a steady state free jet.

The preceding comments stress that the dynamics of the early portion of the inflow process play a significant role in forming the flow field. Curle's work provides an approximation of the form of the early inflow process. This description indicates the dynamics of the transient inflow may inhibit the spreading of the influent jet of gas. These analytic indications, when coupled with the results from the large scale experiments indicate that a further review of the spreading process should be undertaken. These conclusions are, however, contraindicated by the data from the scale model experiments which show a pronounced turbulent spreading of the inflow. The opposing results stress that a better understanding of the shelter flow process is needed.

To better understand the shelter inflow, a literature review was undertaken. Information was sought in several general areas:

- Characteristics of flows with the general character of shelter flows
- Shear flow
- Turbulence, mixing, and transition processes
- Impinging jets and wall jets

The literature review was then edited and the results presented in the bibliography in Section 7.

A review of the bibliography provides an insight into the complexity of the flow processes involved. Not only the volume of work, but also that it primarily represents quasi-steady or steady flows establishes the difficulty in gaining an understanding of the flow sufficient to develop a predictive model. Based on the literature review, several different approaches to studying the problems associated with the shelter flows were undertaken.

Due to the limitations and time constraints on the project, these investigations cannot be reported, but rather the combined overview gained will be presented and one very general approach to several major problem areas will be defined.

The basic hypothesis for the shelter inflow model is that a jet of gas flows into the shelter behind the expansion of the incident shock wave through the chamber. In the present argument, it is assumed that the surrounding air is stationary and that the jet is a potential core of laminar constant velocity flow. This situation creates a maximum velocity discontinuity which will be considered to be an infinitely thin line of separation, a laminar shear layer. The situation is then in the form of the classical "Helmholtz instability" problem.

For the divided flow, the shear layer can be considered to be an infinitely thin vortex sheet. The vortex sheet represents the introduction of an instability which caused the shear layer to grow to finite proportions. The rate of growth of the instability corresponds to a decrease in velocity in the potential flow and an increase in the velocity of the stationary gas. The conditions just described are similar to those described for the profile of a steady flow jet described earlier.

Of particular interest to the shelter flows is the growth rate of the instability, i.e., how rapidly does the momentum transfer from influent to stationary gas occur. The slower the spread the less the deceleration of the influent gas and the less the spread of the flow profile normal to the inflow axis. Several approaches to this problem were undertaken, the simplest and most general of these was to consider the shear line as a surface from which a boundary layer evolved in both directions. In this format the evolution of a boundary layer behind a shock wave on a flat plate can be used to approximate the flow processes.

The flow at any point on the flat plate begins with passage of the shock wave over that point. The flow can be turned into a steady-state problem by

considering the point to be the leading edge of a plate inserted into the flow stream, as shown in Fig. 37. For the initial purposes of this discussion, the flow field behind the shock wave will be considered to be that induced by a step shock wave. The following analysis was carried out in Ref. 57 for scaling effects on supersonic flows over antennas and will be reapplied and expanded for the present problem.

The displacement thickness of a boundary is given by the relationship

$$\delta^*(x) = \phi \sqrt{\frac{\nu x}{U}} \left( 1 + z \frac{\gamma-1}{2} M_2^2 \right) \quad (22)$$

$z$  is a temperature and viscosity dependent constant

$\nu$  is the dynamic viscosity

$u$  is the speed of the fluid

$x$  is the distance from the leading edge of the plate

$\delta^*$  is the displacement thickness of the boundary layer defined by the integral

$$\int_0^\infty \left( 1 - \frac{\rho u}{\rho_\infty U} \right) dy$$

$U$  is the free stream velocity

$\rho$  is the density

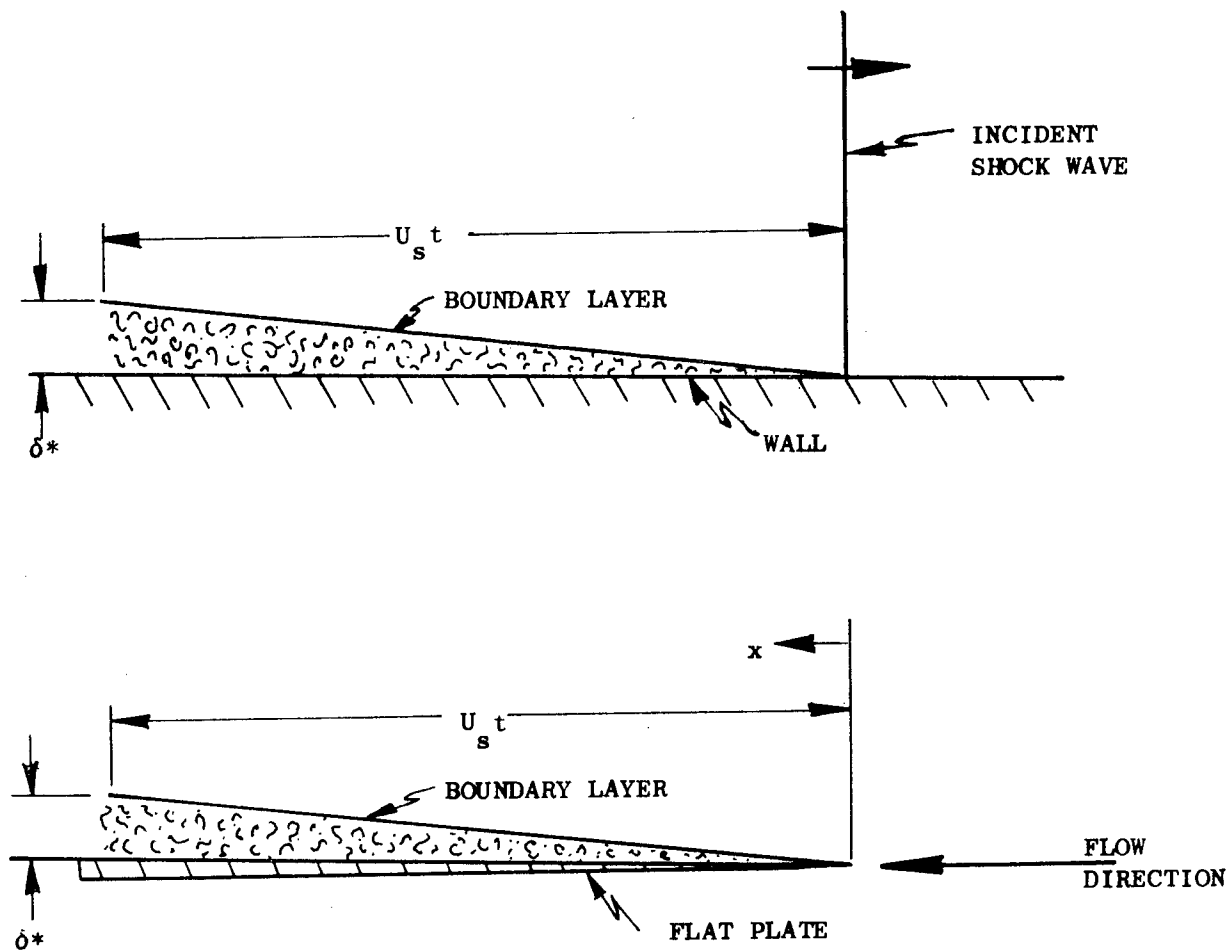
$\rho_\infty$  is the free stream density

$y$  is the coordinate perpendicular to the plate

$\phi$  is a constant

Using the nomenclature in Fig. 37, the dimension  $(x)$  can be replaced by  $U_s t$ , and the flow stream properties (subscripted by 2) by the Rankine-Hugoniot conditions behind the incident shock wave, or

$$\delta^*(t) = \phi \sqrt{\frac{\mu_2 U_s t}{\rho_2 U_2}} \left( 1 + z \frac{\gamma-1}{2} M_2^2 \right) \quad (23)$$



$t$  is measured from shock passage of point  
(Based on Ref. 57)

Fig. 37. Transient Boundary Layer Transformation to Steady Flow Analogy

The above expression can be rewritten in terms of the thermodynamic and aerodynamic parameter ratios across the shock front as

$$\delta^*(t) = \frac{\phi}{\rho_1} \sqrt{\frac{\mu_2 W_{11}}{\Gamma_{21} U_{21}}} \left( 1 + z \frac{\gamma-1}{2} M_2^2 \right) \sqrt{t} \quad (24)$$

where  $\Gamma_{21}$  is the density ratio,  $U_{21}$  the velocity ratio, and  $W_{11}$  the shock front Mach number. The rate of displacement thickness growth is given by

$$\frac{d \delta^*(t)}{dt} = \frac{\phi}{2\rho_1} \sqrt{\frac{\mu_2 W_{11}}{\Gamma_{21} U_{21}}} \left( 1 + z \frac{\gamma-1}{2} M_2^2 \right) t^{-1/2} \quad (25)$$

Both expressions show that the boundary layer profile does not scale linearly with time.

The work in Ref. 57 extended the preceding expression to consider the nonscaling character of the boundary layer in terms of a model and prototype situation. A linear scale factor ( $f_s$ ) was defined by the ratio  $t_m/t_p$ , time in the model ( $t_m$ ) and prototype ( $t_p$ ) reference frames, respectively. If the initial conditions and the shock strengths are equal, then

$$\frac{\delta^*(t)_m}{\delta^*(t)_p} = \sqrt{\frac{t_m}{t_p}} = \sqrt{f_s} \quad (26)$$

and

$$\frac{d \delta^*(t)_m / dt}{d \delta^*(t)_p / dt} = \frac{1}{\sqrt{f_s}} \quad (27)$$

To see what this would mean in terms of the boundary layer growth between a model and prototype situation, the BRL 4-in. shelter models (Fig. 2) were selected. The prototype room selected for comparison was 21.3 ft in

length. The linear geometric scale is 64 for this situation, which also is the factor for scaling time between model and prototype situations. Under these conditions the boundary layer in the modeled situation would grow eight times faster.

The above result helps to explain why the pronounced turbulent spread observed in the model data was not observed in the full-scale test results. The indications are then that the width of the mixing zone is reduced, but as the momentum cross-section must remain constant, the flow must be more intense. These results appeared to be reproduced by the preliminary work undertaken using the spread of a Helmholtz instability as the basis for the boundary layer growth. Preliminary work using the momentum transfer arguments, based on either Prantl's mixing length theory or Taylor's vorticity transport theorem, appeared to be yielding supportive results when this study ended.

The flows in the jet are quite intense, hence the boundary layer (which is being used to represent the jet's spread) will grow more quickly than for the flow conditions behind the shock wave. Since the disturbance is still initiated by a shock front, the shock front velocity will be retained, but the other properties will be taken from the conditions of an adiabatic expansion that forms the jet. Rather than use the complex expression described above, the following approximate formula can be applied (Ref. 58).

$$1.75 \cong \delta^* \sqrt{\frac{U}{\nu x}} \quad (28)$$

and if  $x = U_s t$ , then

$$\delta^*(t) \cong 1.75 \sqrt{\frac{\nu U_s t}{U_\infty}} \quad (29)$$

If we use the assumptions that the jet is formed by an adiabatic expansion to the initial chamber pressure, and that the shock front velocity is approximately equal for all shock strengths (selecting 1300 fps which has a maximum error of approximately  $\pm 15$  percent in the range of interest) then Eq. (29) can be written as

$$\delta^*(t) \cong 0.804 \sqrt{t/U_\infty} \quad (30)$$

The boundary layer thickness,  $\delta(t)$ , is approximately two and one-half times greater. Values for these parameters as a function of time and free-stream flow speed are presented in Fig. 38.

The curves in Fig. 38 support the indications of the nonscaling character of the flow. To ascertain the magnitude, the two sets of experimental data used earlier will be considered (the BRL  $4 \times 4 \times 4$ -in. model with a 1-in. opening and the URS shock tunnel test of a  $12 \times 15 \times 8$  ft room with a 2.7-ft opening). The last comparison time used with the BRL model was approximately 750  $\mu$ sec. On a linear time scaling basis, the comparable time in the large-scale model would have been 18 msec (using the shortest room dimension). In 750  $\mu$ sec the boundary layer thickness would have ranged between 0.02 and 0.07 in. in thickness. If we assume that this growth approximates the spread of the jet, then up to a 0.14 in. widening of the inflow for a 1-in. opening would occur. The full-scale room for an 18 msec fill time would show a maximum growth of 0.6 in. on a 27-in. door, i.e., the full-scale situation would exhibit a growth 1/6th less with respect to the opening width.

Linear scaling does not also apply to the filling of the chamber. The fill time ( $t_f$ ) in milliseconds can be approximated (Ref. 44) for a two-dimensional room by the expression

$$t_f = \frac{V_c}{2A_e} = \frac{A_f}{2W_e} \quad (31)$$

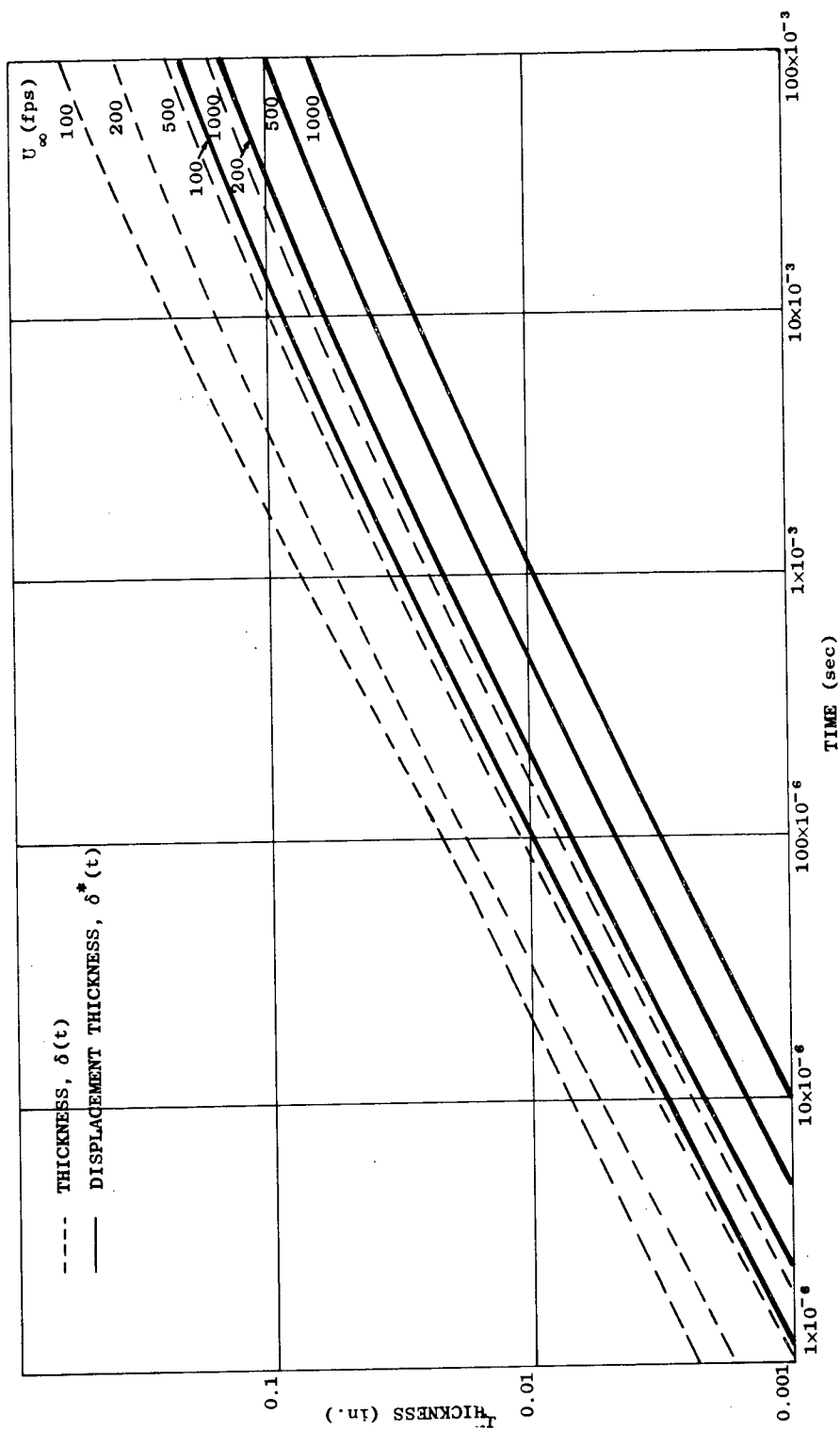


Fig. 38. Approximated Boundary Layer Thickness Parameters for a Free-Flow Jet



where  $V_c$  = volume of the chamber of floor area  $A_f$  and  $A_e$  = area of the entrance of width  $W_e$  (all dimensions are in feet). The fill time for the 4-in. model would then be 667  $\mu$ sec and 38 msec for the full-size room (linear scaling on the basis of opening size would give an 18 msec fill time). The argument of the nonscaling character of the flows in the models does not reduce their value in understanding the flow; it simply cautions against direct scaling and extrapolation to full-scale flows.

The boundary layer arguments presented apply equally well to the flows along the shelter walls, ceiling, and floor. The inflow is therefore not a free jet, but rather is more nearly a wall jet. In Fig. 38 the indication is that the effect of the walls in the form of the boundary layer build-up would be minimal for the large scale, but would have observable effects in the model flows. In the review of the data undertaken earlier, a decrease in the accuracy of the smoke grid experiments was noted with time as was a widening of the smoke grids. These occurrences are felt to be partially due to the boundary layer growth.

The growth of the boundary layer or the spread of the turbulence are energy dissipation and momentum transfer mechanisms in the flow. The jet flows into the shelter and to a pressure that is between the ambient and filled pressure values. The deceleration force, in terms of pressure gradients, is therefore not sufficient to reduce the flow in the chamber to zero. The momentum of the flow must therefore be transferred through mechanisms such as turbulence. The reduced spread of turbulence in the large scale rooms results in a long-term circulatory flow well past the filling period of the room (as documented by the URS shock tunnel tests).

There is a reduction in intensity as the inflow strikes an opposing wall and turns. The flow stream spreads and, since momentum must be conserved, a reduction in flow intensity occurs. The work unit ended as this portion of the flow was being reviewed. Some observations were noted from the preliminary work and will be briefly outlined.

The turning of the flow at an opposing wall and the long-term circulation appeared to be a function not only of the dynamics of the flow deflection but also of the wave dynamics within the chamber and the balance between kinetic and potential energy. The momentum generated by the influent air appeared to be retained with a large kinetic energy component well after the filling process was terminated.

The moving pictures taken in the large-scale room tests in the URS shock tunnel corroborated the preceding results. A circulatory flow was observed at 500 msec, more than an order of magnitude in time past the filling period. This long circulatory period was partially induced by the cyclic reflections in the closed tunnel, but the reflection process was not solely responsible. For example, circulatory flows were observed at two to three times the fill time well before the reflection process could have an effect.

Future studies interested in precisely defining shelter flow should investigate the circulatory flow phenomena. The investigation should include the dynamics of the flow process and the energy and momentum transition and dissipation processes. From these investigations, estimates of the damage potential of these flows should be possible.

#### GENERAL COMMENTS

In reviewing the literature, analyzing the numerical and experimental data, and in some of the preliminary analyses, some interesting observations on the shelter flow field were encountered. The first of these grew out of observations of early numerical simulations. As the percent opening (that is, the area of the entrance relative to the wall in which it exists) increases over 10 percent, a significant reduction in the reservoir pressure occurs. This decrease was documented experimentally as discussed in Appendix C and also in the numerical simulations as discussed in Section 3.

A preliminary investigation indicated that this corresponds to the difference between the free stream inflow into the reservoir and the high

velocity inflow into the chamber. The difference can be shown by simply considering a duct with an orifice. A 5 psi overpressure step shock will be assumed to propagate down the duct towards the orifice which has a 20 percent opening. To illustrate the difference between inflow and outflow, the mass rates can be estimated using the tables and graphs in Refs. 2 and 3.

On striking the orifice, the 5 psi wave would reflect to 11.4 psi overpressure. The reflected overpressure forms the reservoir for the inflow into the chamber. Under these conditions, the influx of mass into the reservoir can only be as great as the mass rate of the incident shock, while the efflux of mass into the chamber is a function of the expansion conditions. For the 20 percent opening, the ratio of influx to efflux mass rates would be 1.40. This ratio states that 0.4 of influent mass rate is available for the reservoir which is expanding at the reflected shock wave's propagation velocity (1091 fps). To maintain the reflected condition, the retention mass rate must equal 1, hence a decrease in the reservoir pressure must occur, reducing the influx into the chamber.

This result explains why the chamber-filling computer programs have an increasing error as the percent opening increases. The inclusion of the work term in the equations adjusts for the work that must be done on the gas internal to the chamber, but an allowance is not made for the effect of the inflow on the reservoir pressure. Similar results were noted for the transmission of shock waves into tunnels (Ref. 42). As the reflecting surface against which the incident shock wave impinged was reduced, the driven shock wave overpressure in the tunnel was reduced.

In terms of shelter flows, this result would indicate that the standard clearing time equation overestimates the driving pressure. The rarefaction waves generated by the inflow process contribute to the reduction in reflected pressure, hence a reservoir pressure value would most likely be between reflected and stagnation pressure in the early portion of the filling process. The later portions of the process would be "filled" from stagnation conditions

and perhaps a lower pressure depending on the mass rate flows into and through the shelter and shelter building.

Further work should be done in this area as the indications are that present techniques may overestimate the reservoir pressure. Since the reservoir is the driving force for the inflow, lower inflow velocities may actually occur. Based on the limited evaluations undertaken in this study, a value 20 to 50 percent of the difference between stagnation and reflected pressures greater than stagnation pressure would appear to be reasonable for estimating the reservoir pressure. The future work should relate the phenomena to the distribution of open area in buildings so as to be able to provide more definitive statements.

In the review of the literature, reference to swirl of flows in ducts after and in turns in the duct were found (Refs. 59, 60, 61). Turns in the entrances to shelters are to be expected, for example, stairwells. If the inflow does swirl, a stronger lift component may exist than for direct axial flows into the shelters. Although a low priority consideration, future work might ascertain the possibility or the extent of this type of flow.

A review of the recent OCD work units on structural failure and debris formation provided a different view on the potential for blast transmission through elevator shafts into shelters. The results of these studies indicated that the period for an elevator door to fail and move a significant distance might approach the filling time of the chamber. If this can be substantiated, then the filling of the shelter would be solely through the open entrances. The above comments do not include the situation in which the elevator may be between the aboveground floors and the shelter.

The last observation to be made on the shelter flows is the temperature of the gas within the chamber. An adiabatic expansion into the room and adiabatic conditions for the flow in the room are generally assumed. Under these conditions the temperature for the room after filling would then

correspond to an adiabatic compression to that pressure or approximately the temperature behind the incident shock wave. For a 15 psi overpressure shock wave, this temperature would be approximately 200°F. In terms of the long durations anticipated in the prototype situation, this temperature may be sufficiently high when coupled with the air movement in the shelter to warrant further consideration.

Some documentation of the occurrence of this potential hazard can be found in the summarization of "Non-Line-of-Site Thermal Problems" in Ref. 62. Temperature measurements taken in shelters away from the shelter entrances during the 1953 and 1955 test series at the Nevada Test Site did show significant temperature increases. Many animals exposed in these tests (including the 1957 test series) were also reported to have shown skin and fur burns. These burns were reported to have been intensified on the surfaces of the animals facing the inflow. As pointed out by Dr. White, these tests were not conclusive, but evidence does exist to warrant a further review of the hazard. The potential hazard in slanted shelters would be intensified as the expected durations would be considerably longer than the duration of the tests from which the data was collected.

## Section 5

### REVIEW OF NUMERICAL SIMULATIONS

A series of numerical simulations was prepared as a part of this work unit at the OCD computer facility at Olney, Maryland, and the computed results stored on magnetic tape. Selected parameters were printed out for review, and a yet smaller number were plotted in spatial contours for about four time intervals per computer run. Even with the selected output, the volume of data could not be presented within the economic constraints of this study.

The purpose of the simulations was to provide further insight into the flow process within a shelter to aid in the development of the conceptual model. Though the full set of data cannot be presented, a verbal description of the results will be provided in this section. The results stress interpretation of the calculated data as it pertains to understanding the flow in the shelters.

#### CHAMBER LENGTH VARIATION SIMULATIONS

The first series of simulations undertaken covered shelter spaces with 10 percent opening on a wall normal to the direction of propagation of the incident shock wave. The entries were located at one end of the upstream wall. The geometry of the three rooms involved was  $30 \times 30$ ,  $30 \times 60$ , and  $30 \times 180$  (width x length). The incident shock wave had a 4.9 psi overpressure in all three cases.

The expansion of the shock wave into and through the room generally followed the pressure distribution model described in Refs. 2 and 3. A strong decay in pressure across the chamber was observed behind the shock wave as the shock wave reached the rear wall of the chamber. At this time a low pressure area of zero psi overpressure was observed at about five entry widths from the front wall. The pressure contours at this time were approximately

perpendicular to the side walls of the chambers. This coincides with an observation that the shock wave first expands, and then is reinforced by the inflow into the chamber and retains its approximately normal position to the side walls.

The pressure distribution throughout the chamber varied spatially with time. Local high and low pressure areas formed and propagated through the chamber during the filling process. The chamber appeared to fill to about 75 percent of the exterior pressure in two transit times of a sound wave across the chamber (one filling cycle as defined in Ref. 2). The external or reservoir pressure was below reflected pressure (11.2 psi) and approached a steady value in the range of 9.5 psi. This result supports the argument for reduced reservoir pressures presented in Section 4.

The dynamic pressure contours for the chambers lagged behind the pressure contours. The dynamic pressure profiles were just beginning to approach their maximum intensities with their leading edge about 5 to 10 entrance diameters into the room as the expanding shock wave struck the rear wall. The profile continued to expand into the room as did the point of maximum intensity (about 7.5 psi). The dynamic pressure contours remained along the wall on the axis of the doorway throughout the entire flow period. Upon striking the rear wall, the flow turned and moved along it until it struck the next corner.

The flow, as it turned the corner, increased the local pressures corresponding to a stagnation zone. These local stagnation pressure zones and the flows causing them extended well past the filling time and were observed to continue past the point at which the pressure in the room had equalized. The flow intensity, as monitored by the dynamic pressures, was reduced after it turned each corner. The dynamic pressure contours were identical for each of the modeled rooms up to the point the rear wall was sensed.

#### ENTRANCE LOCATION EFFECTS

The next series of simulations was comprised of single rooms but their entrances were positioned other than in the center of the front or reflecting

surface. A free flow field was provided around the chamber. The chambers used in the simulations all were 40 ft long in the direction of incident flow and 20 ft wide in the transverse direction. All openings on the front and rear walls were 2 ft and on the side walls 4 ft. These openings were positioned in different combinations in each of the simulations.

The first simulation had the opening positioned on the side of the shelter at the upstream corner. The inflow into the chamber was initially similar to that observed in models filling from the front, but the flow was skewed toward the rear. The skewing of the flow corresponded to the component of the external flow past the entry. Both the flow and pressure distribution throughout the chamber were centered on the diagonal from the entry to the opposite corner.

Circulatory flows were not observed in any significant magnitudes. The reason for the absence of the circulatory flow correlated with the observation that the peak fill pressure monitored in the simulations was 1.5 psi, well below the incident shock wave's overpressure. The entry, located at the corner of the shelter, was below the separated free stream line in which area a low pressure zone exists. The pressure monitored in this region corresponded to the filled pressure.

The second simulation in this series had the entrance also located on the side wall, but at its mid-point. The chamber pressure at the "filled" condition was 4.0 psi, which corresponded to the side-on pressure at the exterior of the entrance. The maximum dynamic pressure monitored in the inflow was 1.5 psi. At the end of the simulation period the inflow had not yet reached the opposing wall of the chamber.

A chamber whose entry was on the rear wall was also simulated but problems in the plotting made it difficult to use the data. Since the limited results gained showed a similarity to the other fill processes reported in Ref. 2 and also in this section the simulation was not replotted. A fill pressure in the chamber of 5 psi was monitored, which corresponds to the free stream side-on pressure.



The next chamber simulated in this series had entrances both at the front and rear of the chamber. The main inflow occurred through the front entrance. Inflow from the rear opening was initiated, but it quickly subsided. The pressure in the chamber peaked at the 2.5 to 3.0 psi region as a through flow was evolved in the model. The pressure on the front of the model was approximately 5 psi. A peak dynamic pressure of 6 psi was monitored which steadied to a peak value in the through flow of 5 psi. These intensities are peak values and do not represent the average dynamic pressure of the flow. Due to the complex geometry of the dynamic pressure contours, good average values could not be determined.

The last configuration tested in this series had openings on the front wall and in the center of the side wall of the shelter. The inflow process through both openings was initiated separately. The flow in the front was accordingly much stronger as the reservoir pressure was greater. The inflow from the side was initially skewed to the rear of the chamber, but as the inflow from the front was sensed the side inflow began to skew towards the front of the chamber.

The side inflow did not contribute very much to the filling process as is evidenced by the peak dynamic pressures for the two flows - 6.5 psi early in the inflow from the front steadying to 4.5 at a later time, and a 0.5 psi maximum for the side inflow. The pressures in the chamber ranged between 4 and 6 psi overpressure which settled to a filled overpressure of 4.5 psi. This internal pressure corresponded to a pressure on the front of the chamber of 5 psi. Similar to other chambers with front entries, very low pressures were monitored during the early inflow process at a point just inside the front entrance along the front wall (a negative 1 psi was the lowest value shown in the plots).

#### MULTIPLE CHAMBER SIMULATIONS

The last series of simulations was undertaken for a two room configuration. The chamber was 30 by 90 ft with 3-ft openings positioned on the exterior and

the divider walls. The simulations were divided into two sets, the first set had the axis of the doors aligned and the upstream inflow occurring in the same cross-section as the chamber; the second set had the doors offset and the exterior of the chamber extended for 30 ft on either side of the entrance to approximate an infinite reflecting surface.

The simulations of the aligned-door set showed a pronounced through flow. The upstream chamber of the first simulation was 30-ft long and the downstream chamber was 60-ft long. The upstream room did not appear to fill quickly. The exterior pressure reached a steady value of 10 psi.

The second simulation of this set divided the chamber into two equal 45-ft rooms. The early flow and pressure histories observed corresponded to those of single room chamber. As the filling process continued, the pressure in the front chamber filled to 2.5 psi and leveled off while the flow continued on into the second room. Very little of the inflow appeared to remain in the first room. As the second room filled to about 4.5 psi, more of the inflow remained in the first room. The pressure in the second room increased to a peak of around 10 psi and then dropped back to about 8 psi.

The peak dynamic pressure monitored in the flow in both rooms ranged between 6.5 and 7.0 psi. Circulatory flow patterns were observed to occur in both rooms. The circulatory flows were more severe in the second room. The strength of the through flow can be envisioned by considering the stagnation regions that formed in the corners of the rooms with solid rear walls. In the case of the shelter with an entry to a second room at this location, the momentum is transferred into the second room rather than forming the stagnation zone.

In the second set of simulations, those with the offset doors, the same two floor plans were tested. The front room in the simulation of the 30 x 60 ft combination filled quickly to 3.5 to 4.0 psi. The second room began to fill from this pressure differential as the inflow from the front entry curled around the corner and moved along the partition wall. A well-developed flow is formed along the side and partition wall which is

largely shunted into the second room. Only a small portion of this flow remains in the front room to establish the circulatory flow pattern. The second room fills to its peak pressure at a much later time. At 200 msec (the end of the computation time) the rear room overpressure was 3.0 psi, the front chamber had an overpressure of 5.5 psi, and the exterior a 10.5 psi overpressure.

The last simulation undertaken in this series had two 45-ft chambers with offset doors. The flow pattern appeared to be similar to that for the 30 x 60 ft condition. The pressure in the front chamber increased to 4 to 4.5 psi, as the pressures in the second chamber rose to 2.5 psi at about midway in the computation of the fill period. The computation was ended at this point due to the long running time of this particular type of problem. The dynamic pressure monitored in the inflow in the second room had a peak value of 3 to 3.5 psi. The outside pressure again leveled off at 10.5 psi overpressure. The pressure monitored in the corner of the first chamber, near the offset entrance, was slightly reduced due to the flow into the second room, particularly during the early portion of the flow process.

#### COMMENTS

The preceding review described the relationship between the driving pressure and the peak dynamic pressure. The relationship developed in Ref. 2 is presented in Fig. 39 with the data points for peak values outlined in the discussion plotted over the curves. These peak conditions appear to follow the free flow vena contracta graph and generally fall near the upper portion of the bounded region developed in Ref. 2.

The values discussed are peak values and do not represent the space-time history of the inflow process. These representations are quite complex and at the conclusion of this work unit were not in suitable form for presentation. It is planned that a further attempt at a representation of the flow will be made in the companion work unit to this study (1154G).

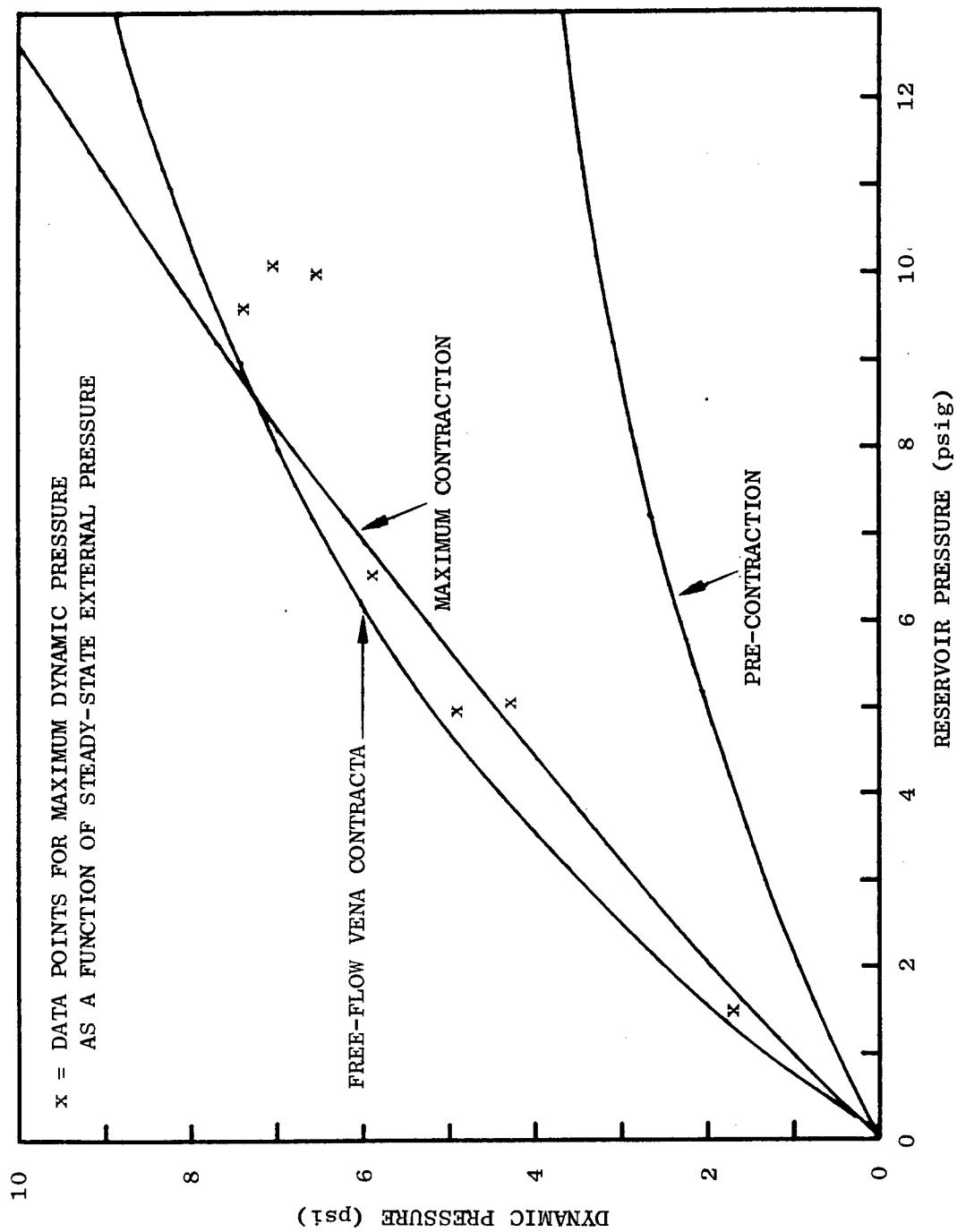


Fig. 39. Average Entry Dynamic Pressure

## Section 6

### DISCUSSION

One objective of this study was to develop a conceptual model of the air-blast-induced flow into basement shelters. The term conceptual model was not defined in the scope, other than to indicate it should be useful in defining engineering estimates of the flow. Before further considering the flow, some implications of the term conceptual model will be reviewed.

The first step in reviewing the term "conceptual model" was to graphically portray the flow field boundary conditions. The flow chart developed in Fig. 40 is often referred to as a system diagram, hence the process portrayed will be viewed as a system using the standard nomenclature of general systems theory. The purpose of this exercise was to graphically portray and explore the relational structure between the components of the flow-shelter interaction upon which any model must be built.

The system will be defined as the flow field into and within the chamber, its subsystems being the inflow and the flow internal to the chamber. The environment for the system is made up of the shelter area and reservoir conditions. The suprasystem includes the surroundings, the air blast environment, and the building in which the shelter is located.

If these designations are reviewed, the elements of the system components can be determined. For example, the shelter area (part of the environment) has two elements — entries and interior. These elements in turn have properties which were defined as location, size, and geometry. A hierarchical structure can thus be defined. The simplest prediction procedure would result if each of the levels in the structure hierarchy were independent and could be considered individually.

The condition of separable components is equivalent to the process of superposition of parts in a linear system. For these conditions to exist, each component of the overall system must be independent. An alternative

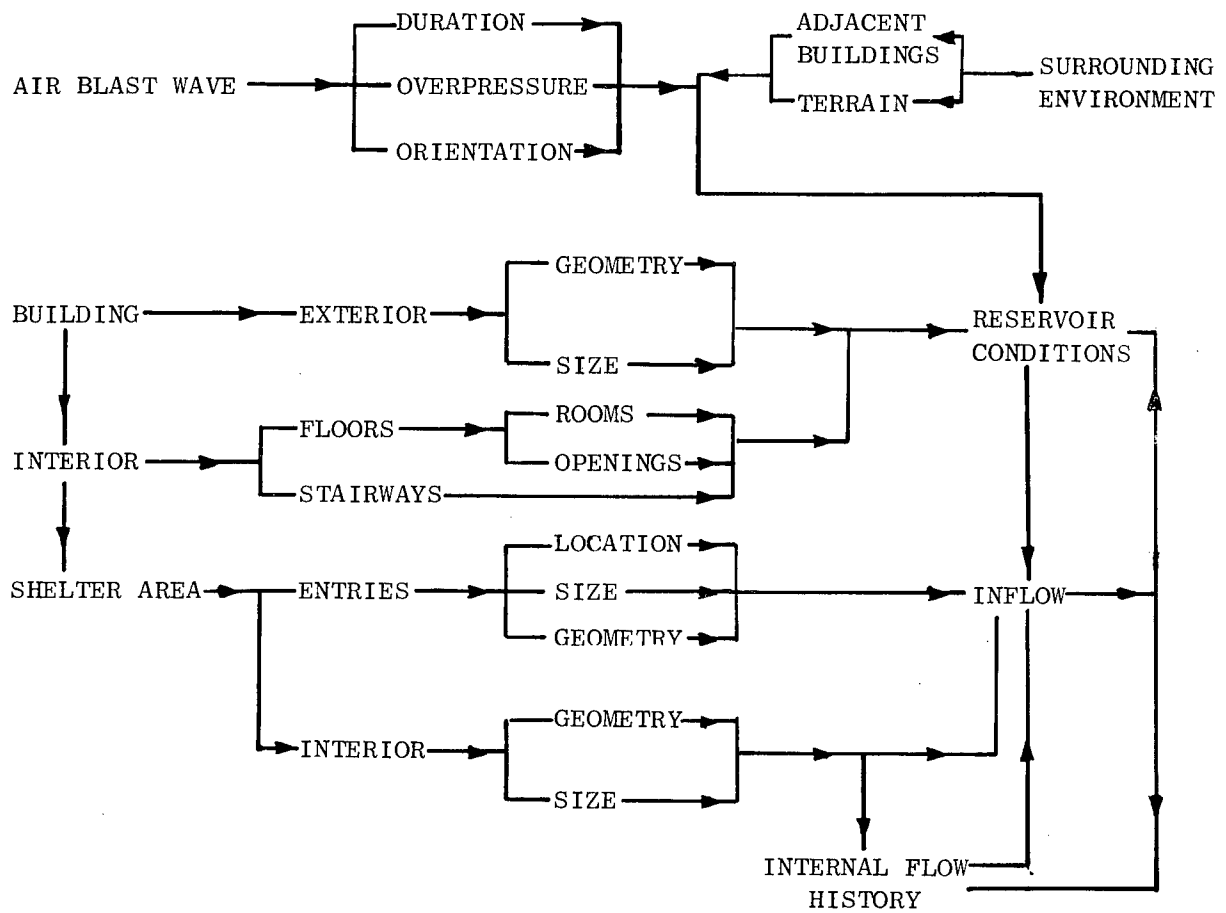


Fig. 40. A Simple Graphic Representation of Flow Field Boundary Conditions

view of the problem which provides some insight into the process would be to consider the systems diagram as a set  $S$  comprised of a group of subsets  $S_1, S_2, \dots, S_n$ . If an element  $\epsilon$  of  $S_1$  is also an element of  $S_2$ , then  $S_1$  and  $S_2$  have an intersection. The effect on element  $\epsilon$  by the properties of  $S_1$  must then affect set  $S_2$ , as element  $\epsilon$  is common to both. If this interaction occurs there is a relational structure between sets and they cannot be considered independently.

Two particularly strong interrelationships exist in the flow process in shelters which can be seen as feedback loops in the system diagram. These feedback loops occur between the inflow and the reservoir conditions and between the flow in the shelter and the inflow. The subsystems, as defined above, are therefore interrelated, as is the environment to the subsystems. These processes cannot, therefore, be considered to be independent with solutions that can be superpositioned on each to form a general solution.

An effective conceptual model must therefore not only define the individual subsets and environment components, but also their relational structure on the basis of a continuing interaction. To define the inflow into the shelter the details of the evolving internal flow fields must be established. These very technical concepts must then be interwoven to form the description of the total flow field. The complexity of this weaving process was stressed in Section 4, but more importantly it stresses the overall problem faced—i.e., too many potential variables for any explicit solution to be developed.

For the purpose of argument the flow field will be assumed to be definable in space-time-intensity parameters. The problem then simply reduces to defining the suprasystem and environment elements and their properties. The shelter area has a direct input into the flow system, therefore the definition should be precise if the conceptual model is to be meaningful. For example, two questions that must be answered are: 1) What specifically is a blast-slanted shelter? and 2) What properties does the shelter exhibit? Without specific answers to these questions it is difficult to describe a model of the flow, as the environment for the system has not been defined. For an open system this lack of definition means an undefined system exists.

The properties of the environment and suprasystem must also be defined. A preliminary review of previous work on the open shelter concept and of the RTI survey of new construction (Ref. 63) showed that a wide distribution in shelter geometry, size, and location within a building occurred. Based on this survey a blast-slanted shelter cannot be described explicitly, but rather can only be defined in terms of statistical distributions. Work on evolving more complete bounds on the definition process was begun, but time constraints precluded its continuation. The preliminary survey material was transferred to Work Unit 1154G in which a thorough analysis of the shelter data of the RTI survey is being made.

Another factor which stresses the problem of interaction between components is the orientation of the structure and the blast wave and the entry location in the interaction zone. In Sections 3, 4, and 5 observations and conclusions were discussed which stressed the strong role these interactions play on the inflow and internal flow processes. In developing a conceptual model the possible variations in the interaction zone must be defined, i.e., building-blast wave orientation, blast wave properties, building geometry, shelter location, and entry location. In the earlier review of the system it was noted that the inflow affects the reservoir conditions as do the above; hence an explicit definition again cannot be undertaken.

Rather than belabor the difficulties associated with the definition process, the positive aspects can be considered. Based on the preceding arguments a model can be defined, but only in general terms. These terms can verbally describe the processes, but do not, as such, provide a relational structure from which quantitative estimation procedures can be developed or applied.

A general model of the inflow can then be described only for a specific situation. The situation most commonly selected is for the incident shock wave to reflect normally from the shelter wall containing the entrance to the shelter. The process for the air-blast-induced filling of a chamber was discussed in Refs. 3 and 4 and then reviewed in Section 4. In Section 4



shortcomings in the early descriptions were noted and discussed. Rather than reproduce the material describing the inflow and the internal flow processes the summary will stress how these descriptions, when combined with the discussions of Sections 3 and 4 and Appendix C, can be used to provide an estimate of flows in the shelters, and to further illustrate the difficulty of developing a general conceptual model.

The first approach to defining the flows in the simple chamber is to define the reservoir conditions. The gross reservoir conditions are defined by the blast wave structure interaction. To refine the accuracy of these conditions the inflow into the shelter and into the structure must be evolved. The effect of the inflow can then be computed for each specific situation.

The predictions can be made either by analytical, experimental, or numerical procedures. The most likely procedure to be used would be the analytical approach. Using as a guide the requirement of engineering accuracy in predictions the following procedure is suggested. Assume the building in which the structure is situated is a solid block and calculate the reservoir pressure history for the shelter using standard procedures. If the openings on the upstream surface comprise less than 10 percent of that surface area use the calculated values.

If the openings on the building's exterior exceed 10 percent, the reservoir pressure should be adjusted. It is suggested that the adjustment use the methods outlined in Ref. 64. The following formula (which, based on observation, assumes a square power distribution) provides an approximation of decreases in reservoir pressure for long duration waves:

$$p_a(t) = p(t) + \left(1 - \frac{PO}{100}\right)^2 [p(t) - p_s(t)] \quad (32)$$

where  $p(t)$  is the calculated reservoir pressure,  $p_s(t)$  is the free stream stagnation pressure,  $p_a(t)$  is the adjusted reservoir pressure, and  $PO$  is the percent opening on the front surface of the building. The preceding assumes an equal distribution of openings on the surface. Even if this

condition is met, the above equation is an approximation, but it should provide estimates within a  $\pm 10$  percent variation.

Using the calculated reservoir conditions the inflow into the chamber can be determined from the graphs in Ref. 2. These graphs will provide the maximum inflow. An acceleration of the inflow from the flow velocity behind the incident shock to the peak velocity will occur in approximately five sound wave traverse times across the entrance. The location of the peak velocity will range between 2 to 6 diameters from the entry, depending on when in the inflow process it has occurred.

The peak velocity can be assumed to be constant for the fill time of the chamber. For estimation purposes the peak velocity can then be assumed to decay linearly to zero in another fill time. The preceding provides a guide for establishing the peak intensity history of the flow, but it does not provide the spatial intensity history. The difficulty of quantitatively modeling the flow in space-time terms, not only in the transitory stages but also in the long term flow patterns, was brought out in earlier discussions.

Based on recent work the basic character of the flow can be established. The intensity along the inflow axis decays exponentially with distance between the location of peak intensity and the rear wall. The location of the peak intensity moves inward with time. The increase or decay in intensity with time at a given location varies with the location. The intensity of the inflow also varies in a transverse direction. The combined effects make it difficult to undertake to predict the space-time-intensity of the full flow field.

The prediction of the turning process as the flow strikes the rear wall is dependent upon the ability to predict the conditions of the impinging jet. From the numerical simulations undertaken the dynamic pressure of the turned fluid appears to be one-half of the incident intensity. Part of the reduction was due to the accumulation of fluid in the forming stagnation zone and, in later times, to the general decay of the inflow process.

The above discussion was for a single chamber, with a simple geometry, without multiple openings, and for constant conditions in the reservoir. Inclusion of these variables make the description of the flow yet more complicated. These comments support the earlier conclusion as to the difficulty of establishing a generally valid conceptual model of the inflow. The inability to document the vast majority of information and observation on the flow process developed in this study, due to space limitations, further stresses the lack of an adequate description of the flow.

A general understanding of the overall scheme of blast-induced flow processes within blast-slanted shelters exists. An adequate though general understanding of the individual flow processes also exists, with some further study required in only a few specific technical areas. Based on the results of this study it appeared that further studies of technical areas should be in direct support to the specific needs of some facet of the shelter research program. The work undertaken in this study also indicated that a thorough all-inclusive and general conceptual model from which engineering estimates may be made for any situation is not a practical goal. To produce a model that would simulate flow fields and pressure distribution for any geometry with a 90 percent accuracy for the full blast profile would require inordinately high expenditures and amounts of technical effort.

The needs of the shelter research program do not appear to require this level of technical understanding. The flow as described, with some improvements in the understanding of a few specific technical areas, should be sufficiently accurate to answer specific questions. The specific regions of flow that do require additional understanding are the long term history of the jet in the chamber, and how it forms into the circulatory flow. The dissipative mechanisms and energy redistribution within the shelter should be included as part of this investigation.

Another flow area that should be investigated is the effect of the inflow into the shelter, and the interior of the shelter building, with respect to its effects on the reservoir pressure. Closely allied to the flow is the

effect of the building shock wave orientation, the geometry of the building, and the location of the shelter. In terms of the system diagram discussed earlier, the problem again translates to the definition of the environment components which form the inputs for the inflow processes.

Further arguments in support of considering these system constraints in more depth can be evolved from the descriptions of the flow in Section 5. The simulation discussed in Section 5 had the openings located at different points around the periphery of the shelter. The alterations in geometry were shown to drastically affect both the filled pressure and the peak inflow intensities. These effects could also be related to the reservoir conditions. The monitored velocities and pressures in these simulations were directly related to the reservoir conditions and were predictable from present adiabatic expansion theory once the reservoir conditions were defined.

The side and rear entrances of the multiple entrance configurations were seen to add very little to the inflow into the chamber. The rear entrance reduced the air circulation within the room as it formed a through flow across the shelter. The results of the simulation do indicate that the model of the inflow as described for the simple shelter does break down. The results described were for one angle of shock wave incidence relative to the shelter. Due to realities of construction and the inability to relate building orientation with the detonation point, the reservoir conditions cannot be defined — making a general inflow model harder to define.

The multiple room numerical simulations showed a strong dependence on internal geometry as well as reservoir conditions. The location of the divider wall determined the circulatory flow patterns, how quickly they form, and to what pressure level the first room fills. In the situations with aligned entries the shelter geometry with the small upstream room showed the strength of the through flow was sufficient to carry all the inflow through the first room. This situation was similar to the front-rear exit simulation of the single room.

The multiple room experiments again showed (Refs. 2, 3, 4, 5) that the upstream room does not completely act as a reservoir for the flow into the second room. In some cases the flow was seen to move completely through the upstream room and not add appreciable mass to the first room. The fill in most cases appears to be through the upstream room to the rear chamber and then back to the upstream chamber. Based on this model the downstream room will always fill to a higher pressure. Situations that were not investigated were: small downstream rooms, multiple openings to rooms, and varied incident shock wave to shelter orientations.

A question can be raised from the above results: why does the upstream room pressure increase if the flow is through the upstream room. The explanation appears to be related to a combination of the piston effect, discussed in Section 4, and the dynamics of the shock wave propagation through the room. The shock wave, as it expands through the room, moves gas from the vicinity of the entrance corridor. In a normal situation of an expanding shock wave, the rarefaction wave decreases the pressure behind the shock wave and the negative trough of the wave initiates a flow in the opposite direction. The reverse flow would be supported by reflected waves propagating back through the chamber.

The inflow, however, occurs behind expansion processes. The inflow, as discussed earlier, drives the shock wave and hence spreads the shock front velocity, or alternately, it strengthens the expanding shock wave. The reverse flow cannot, therefore, flow back into the area in and about the inflow corridor from which it flowed originally as the inflow is now occupying that space. It is felt that this simple process explains the early rises in pressure in the chamber before the influent mass can raise the pressure throughout the chamber.

The most important aspect of the flow review undertaken in the work unit was that it pointed some ways of planning future work in support of the OCD shelter research program. The work stressed a need for a more systematic

approach to the research. A thorough understanding of the flow can be gained with added effort, but the depth of this understanding can not be determined without a stronger emphasis on the practical aspects of the problems faced. Using the practical considerations as guides it may be possible to avoid some of the difficult technical questions.

The framework of understanding of the flow processes is in general sufficiently precise to predict flows with engineering accuracy if there is some idea of what the shelters might look like and what external conditions can be assumed. Assumptions of the worst conditions, although conservative, establishes a rather poor estimate of actual conditions. In the post-attack research area, the relational problem has begun to be considered (Refs. 65 and 66). Also, Ref. 67 stressed the importance of the geometric parameters in determining both flows and loading. The study undertaken by this work unit also indicated that a similar approach to the shelter problem might be taken in the immediate future. Under these guidelines, the term conceptual model would be used to include all the aspects of the air blast shelter interaction, not simply the flow processes.

From discussions held with other OCD engineers working in the shelter research area the above review might also include their specific areas of interest in the shelter research program. Different levels of understanding of the flow exist for each of these, but at present a good working outline or systematic representation is not available. The three working areas that appear to exist are:

- The pressure loading on structural elements
- The injury potential in the below-grade slanted basement shelter
- The above two problems with respect to above-grade building areas

Of the above, the evolvement of loading profiles on structural elements is a simpler procedure than providing general predictions for flow.

If the above reasoning is taken a step further, the question is raised as to whether the flow field is the item of interest, or if the damage potential is of interest. From the results of the investigation undertaken

in this work unit the definition of the damage potential appeared to be more influenced by the external parameters than by improved prediction techniques. The purpose of future studies may be to ascertain the damage potential and then suggest ways of limiting its causes. Based on the work undertaken a simple prediction procedure for providing flows for all possible geometries is not feasible, if the tenet of simplicity and small computer size is maintained.

The work on the code in Section 3 showed that for a simple two-dimensional geometry it might be possible to write a simple code. Three-dimensional effects and complex geometries would have to be excluded. The effort to provide this form of code would vary with the complexity of the output desired and the number of output variables. For the prediction of pressures in shelters it might, however, be an economic feasibility.

The use of the above code, if developed, would appear to be an oversophistication relative to the real-world environment. The aim of this work unit was to consider the concept of the flows, and it brought out some of the oversophistication of approaches that have been used to generate data and develop theories. The reality of the prototype situation produces variables and stochastic distributions that far outweigh many of the minor fluctuations observed and then researched. This problem is not unique to the aerodynamic portion of the shelter research program. A pronounced tendency to get involved in technical detail, rather than the broad general overview was observed (for example, a review of this report will underscore this tendency).

Based on the work undertaken in this work unit the following suggestions are made for future studies:

- The first priority of future studies in this area should be to develop a system for describing an overview of the processes involved.
- Further studies should work towards the final objectives of the shelter research program area using the system model as a guide. The use of this approach should significantly increase the effectiveness of further studies.

- Experiment should be used to corroborate analytical work, the systems model, or to provide answers to specific problems. Rather than increased experimental effort, more effort should be placed into interpreting the results to provide empirical insights and knowledge of the air blast shelter interaction.
- A freer use of analytical and numerical simulations should be undertaken to aid in the evolvment of understanding, but under the same constraints as with the experimental simulations. More emphasis should be placed on full-scale simulation by both of the simulation techniques.

The following specific recommendations on technical areas for further study of the flow are made:

- A brief review of the arguments on the spread of turbulence and the growth of boundary layers via different procedures should be undertaken to ascertain if the implications derived in this work unit will bear the weight of further scrutiny.
- A further expansion of the piston effect analysis should be made, particularly relating the spread of the inflow and the definition of the inflow movements and distribution of mass and energy.
- A better understanding of the transition of the inflow energy and its distribution, in conjunction with the evolvment of the circulatory flows should be developed. A combination of experimental and numerical simulations appears to be needed to develop a better intuitive insight so as to shorten further analysis.
- The problems of interactions between internal rooms within shelters should be studied.
- A better understanding of the effect on the reservoir conditions of the flow into the shelter or shelter building should be developed.

A closing suggestion is that the work in this area be closely tied into operational concepts as defined in Ref. 68 to ascertain what effect these will have on the work area being studied. The system model discussed earlier would fit into this framework.



Section 7  
REFERENCES

1. Shea, J.T., Blast Casualty Prediction-Past, Present, and Future, Report No. 127, Cosmic Inc., Apr 1968 (AD 668 342)
2. Melichar, J.F., Air Blast Induced Aerodynamic Effects in Blast-Slanted Shelters, URS 692-3, URS Research Co., Burlingame, Calif., Jan 1969
3. Melichar, J.F., The Propagation of Blast Waves Into Chambers, BRL-MR-1920, Ballistic Research Laboratories, Mar 1968
4. Coulter, G.A., Air Shock Filling of Model Rooms, BRL-MR-1916, Ballistic Research Laboratories, Mar 1968
5. Coulter, G.A., Air Shock and Flow in Model Rooms, BRL-MR (Draft) Ballistic Research Laboratories, Feb 1969
6. Vansant, C.A., et al., Open Shelter Feasibility Study, TR-68-1, Vertex Corp., Oct 1968
7. Gentry, R.A., R.E. Martin, and B.J. Daly, "An Eulerian Differencing Method for Unsteady Compressible Flow Problems," J. Comp. Phys., Vol. 1, 1966, pp. 87-118
8. VonNeuman, J. and R.D. Richtmyer, "A Method for the Numerical Calculation of Hydrodynamic Shocks," J. Appl. Phys., Vol. 21, Mar 1950, pp. 232-237
9. Richtmyer, R.D., Difference Methods for Initial-Value Problems, Interscience, New York, 1957
10. Streeter, V.L., Fluid Dynamics, McGraw-Hill, New York, 1948
11. Stanyukovich, K.P., Unsteady Flow of Continuous Media, Pergamon Press, New York, 1960
12. Owczarek, J., Fundamentals of Gas Dynamics, International Textbook Co., Scranton, Pa., 1964
13. Rich, M., A Method for Eulerian Fluid Dynamics, LAMS-2826, Los Alamos Scientific Laboratory, Los Alamos, N. M., 1963

14. Harlow, F.H., The Particle-In-Cell Computing Method for Fluid Dynamics, Vol. 3: Methods in Computational Physics, Academic Press, New York, 1964
15. Landshoff, R., A Numerical Method for Treating Fluid Flow in the Presence of Shocks, LA-1930, Los Alamos Scientific Laboratory, Los Alamos, N. M., Jan 1955
16. Ames, W.F., Non-Linear Partial Differential Equations, Academic Press, New York, 1965
17. Schulz, W.D., Two-Dimensional Lagrangian Hydrodynamic Difference Equations, Vol. 3: Methods in Computational Physics, Academic Press, New York, 1964, pp. 1-45
18. Emery, A.E., "Evaluation of Several Differencing Methods for Inviscid Flow," J. Comp. Phys., Vol. 2, 1968, pp. 306-331
19. Amsden, A.A., "The Particle-In-Cell Method for the Calculation of the Dynamics of Compressible Fluids," LA-3466, Los Alamos Scientific Laboratory, Los Alamos, N. M., Jun 1966
20. Daly, B., F. Harlow and J. Welch, Numerical Fluid Dynamics Using the Particle-and-Force Method, LA-3144, Los Alamos Scientific Laboratory, Los Alamos, N. M., 1965
21. Harlow, F.H., etal, Two-Dimensional Hydrodynamic Calculations, LA-2301, Los Alamos Scientific Laboratory, Los Alamos, N. M., Apr 1959
22. Harlow, F.H., Dynamics of Compressible Fluids, LA-2412, Los Alamos Scientific Laboratory, Los Alamos, N. M., Apr 1960
23. Evans, M.W. and F.H. Harlow, The Particle-In-Cell Method for Hydrodynamic Calculations, LA-2139, Los Alamos Scientific Laboratory, Los Alamos, N. M., Jul 1960
24. Frank, R.M., Mixed Eulerian-Lagrangian Method, Vol. 3: Methods in Computational Physics, Academic Press, New York, 1964, pp. 47-66
25. Noh, W.F., CEL: A Time Dependent, Two-Space-Dimensional, Coupled Eulerian-Lagrange Code, Vol. 3: Methods in Computational Physics, Academic Press, New York, 1964, pp. 117-179

26. Lax, P., Communications on Pure and Applied Mathematics, Vol. 7, Institute for Mathematic Sciences, New York University, Interscience Publishers, Inc., 1954, pp. 159-193
27. Longley, H.J., Methods of Differencing in Eulerian Hydrodynamics, LAMS-2379, Los Alamos Scientific Laboratory, Los Alamos, N. M., 1960
28. Lax, P. and B. Wendroff, Communications on Pure and Applied Mathematics, Vol. 13, Institute for Mathematic Sciences, New York University, Interscience Publishers, Inc., 1960, pp. 217-237
29. Rusanov, V., Calculation of Interaction of Non-Steady Shock Waves With Obstacles, Translation No. 1027, National Research Council of Canada, 1962
30. Burnstein, S.Z., Finite Difference Calculations for Hydrodynamic Flows Containing Discontinuities, NYO-1480-33, New York University, Sep 1965
31. Richtmyer, R.D., A Survey of Difference Methods for Non-Steady Fluid Dynamics, NCAR-TN-63-2, National Center for Atmospheric Research, 1962
32. Burnstein, S.Z., Numerical Calculations of Multidimensional Shocked Flows, NYO-10,433, New York University, Nov 1963
33. Harlow, F., Stability of Difference Equations Selected Topics, LAMS-2452, Los Alamos Scientific Laboratory, Los Alamos, N. M., Sep 1960
34. Kaplan, M.A. and R.A. Papetti, An Analysis of the Two-Dimensional Particle-In-Cell Method, RM-4876-PR, Rand Corp., Sep 1966 (AD 641 655)
35. Daly, B.J., The Bounding Instabilities of the PIC Difference Equations, LA-2414, Los Alamos Scientific Laboratory, Los Alamos, N. M., Mar 1963
36. Ahlers, E.B., Trajectory Analysis for Structural Fragments, OCD Work Unit 3322A, SRM-65-1, IIT Research Institute, Aug 1965
37. Hoerner, S.F., Fluid-Dynamic Drag, Published by the Author, Midland Park, N. J., 1958
38. System/360 Scientific Subroutine Package, Programmer's Manual, H20-0205-3, International Business Machines Corp., White Plains, N. Y., 1968

39. Buck, R.C., Advanced Calculus, 2nd Ed., McGraw-Hill, New York, 1965
40. Crandall, S.H., Engineering Analysis, A Survey of Numerical Procedures, McGraw-Hill, New York, 1956
41. Hamming, R.W., Numerical Methods for Scientists and Engineers, McGraw-Hill, New York, 1962
42. Shock Tube Facility Staff, Information Summary of Blast Patterns in Tunnels and Chambers, BRL-MR-1390, Ballistic Research Laboratories, Mar 1962
43. Muirhead, J.C., Model Studies of Blast Effects, VII: Entry of Blast Into the Household Basement Fallout Shelter, STP No. 215, Suffield Experimental Station, Jan 1961 (AD 252 137)
44. Rempel, J.R., Room Filling From Air Blast, OCD Work Unit 1125B, Stanford Research Institute, Menlo Park, Calif., Jul 1969
45. Gurevich, M.I., The Theory of Jets in an Ideal Fluid, Pergamon Press, New York, 1966
46. Streeter, V.L., Fluid Dynamics, McGraw-Hill, New York, 1948
47. Rouse, H.L., Advanced Mechanics of Fluids, J. Wiley, New York, 1959
48. Sedov, L.I., Two-Dimensional Problems in Hydrodynamics and Aerodynamics, Interscience Publishers, New York, 1965
49. Churchill, R.V., Introduction to Complex Variables and Applications, McGraw-Hill, New York, 1948
50. Chaplygin, S., Gas Jets (Scientific Memoirs, Moscow University, 1902) NACA TM No. 1063, Aug 1944 (ADI No. 19993)
51. Lamb, H., Hydrodynamics, MacMillan, London, 1932
52. Curle, N., Unsteady Two-Dimensional Flows With Free Boundaries, I: General Theory, Proc. Roy. Soc. (London), Vol. 235, Series A, Mathematical and Physical Sciences, Jun 1956

53. Curle, N., Unsteady Two-Dimensional Flows With Free Boundaries, II: The Incompressible Viscous Jet, Proc. Roy. Soc. (London), Vol. 235, Series A. Mathematical and Physical Sciences, Jun 1956
54. Rudinger, G., Nonsteady Duct Flow: Wave Diagram Analysis, Dover Publications, Inc., 1969
55. Abramovich, G.N., The Theory of Turbulent Jets, M.I.T. Press, Cambridge, Mass., 1963
56. Pai, Sheh-I, Fluid Dynamics of Jets, D. Van Nostrand, New York, 1959
57. Melichar, J.F., Diffractioned Air Shock Pressure Loading on a Low Profile Three-Dimensional Model, BRL-M-1557, Ballistic Research Laboratories, Mar, 1964
58. Schlichting, H., Boundary Layer Theory, 4th Ed., McGraw-Hill, New York, 1960
59. Kreith, F. and OK. Sonju, "The Decay of a Turbulent Swirl in a Pipe," J. Fluid Mech., (Great Britain), Vol. 22, Part 2, Jun 1965, pp. 257-271
60. Wilks, Graham, "Swirling Flow Through a Convergent Funnel," J. Fluid Mech., (Great Britain), Vol. 34, Part 3, 2 Dec 1968, pp. 575-593
61. Tunstall, M. J. and J.K. Harvey, "On the Effect of a Sharp Bend in a Fully Developed Turbulent Pipe-flow," J. Fluid Mech., (Great Britain), Vol. 34, Part 3, 2 Dec 1968, pp. 595-608
62. White, C.S. et al, Biological Tolerance To Air Blast and Related Biomedical Criteria, CEX-65.4, Lovelace Foundation, April 1965
63. Documentation for Selected NFSS Buildings, Report R-OU-393, Research Triangle Institute, North Carolina, Nov 1968 (prepared for OCD through SRI)
64. Glass-tone, S., editor, The Effects of Nuclear Weapons, U.S. Government Printing Office, Washington 25, D.C., April 1962
65. Melichar, J.F., Personal Notes, Dec 1967, and communications to M. Pachuta, Post Attack Research - OCD, URS Research Company, Burlingame, California, 1968-1969

66. Melichar, J.F., Notes OCD Work Unit 3341B, Post Attack Research, URS Research Company, Burlingame, California
67. Melichar, J.F., Internal Loading of Structures by Blast Waves, Shock and Vibration Bulletin, Bulletin 37, Part 4, Naval Research Laboratory, Jan 1968
68. Miller, C.F., Civil Defense Operational Concepts, URS-757-1, URS Research Company, Burlingame, California, May 1969

## BIBLIOGRAPHY

Subjects Related to the General Flow Field

- Arie, M. and H. Rouse, "Experiments on Two-Dimensional Flow Over a Normal Wall," J. Fluid Mech., Vol. 1, Jul 1956, pp. 129-141
- Becker, H.A. and T.A. Massaro, "Vortex Evolution in a Round Jet," J. Fluid Mech., Vol. 31, Part 3, 26 Feb 1968, pp. 435-448
- Benjamin, T.B., "On the Flow in Channels When Rigid Obstacles are Placed in the Stream," J. Fluid Mech., Vol. 1, Jul 1956, pp. 227-248
- Benjamin, T.B., "Theory of the Vortex Breakdown Phenomenon," J. Fluid Mech., Vol. 14, Dec 1962, pp. 593-629
- Bradshaw, P., D.H. Ferriss, and N.P. Atwell, "Calculation of Boundary Layer Development Using the Turbulent Energy Equation," J. Fluid Mech., Vol. 28, Part 3, 1967, pp. 593-616
- Corcoran, W.H., et. al., Momentum Transfer In Fluids, Academic Press, New York, 1956
- Deckker, B.E.L. and Y.F. Chang, "Transient Effects in the Discharge of Compressed Air from a Cylinder Through an Orifice," Paper No. 68-FE-27, The American Society of Mechanical Engineers, New York, 1968
- Djojodihardjo, R.H. and J.F. Thorpe, "Fully Developed Laminar Flow in a Stepped Rectangular Channel," J. App. Mech., Jun 1966, pp. 438-440
- Finely, P.J., "The Flow of a Jet from a Body Opposing a Supersonic Free Stream," J. Fluid Mech., Vol. 26, Part 2, Oct 1966, pp. 337-368
- Grant, H.L., "The Large Eddies of Turbulent Motion," J. Fluid Mech., Vol. 4, Part 2, Jun 1958, pp. 149-190
- Gundersen, R., "The Flow of a Compressible Fluid With Weak Entropy Changes," J. Fluid Mech., Vol. 3, Mar 1958, pp. 553-581
- Harvey, J.K., "Some Observations of the Vortex Breakdown Phenomenon," J. Fluid Mech., Vol. 14, Part 4, Dec 1962, pp. 585-592
- Hinze, J.O., Turbulence, An Introduction to Its Mechanism and Theory, McGraw-Hill, New York, 1959

- Jonsson, V.K. and E.M. Sparrow, "Experiments on Turbulent-Flow Phenomena in Eccentric Annular Ducts," J. Fluid Mech., Vol. 25, Part 1, May 1966, pp. 65-86
- King, J.L., P. Boyle, and J.B. Ogle, "Instability in Slotted Wall Tunnels," J. Fluid Mech., Vol. 4, Jul 1958, pp. 283-305
- Lamb, H., Hydrodynamics, 6th Ed., Dover, N.Y., 1945
- Liu, C.Y., "Boundary Effects in Wake Flow," Paper No. 68-APM-P, J. App. Mech., 1968
- McDonald, H., "The Effect of Pressure Gradient on the Law of the Wall in Turbulent Flow," J. Fluid Mech., (Great Britain), Vol. 35, Part 2, 3 Feb 1969, pp. 311-336
- Mellor, G.L. and D.M. Gibson, "Equilibrium Turbulent Boundary Layers," J. Fluid Mech., Vol. 24, Part 2, 1966, pp. 225-253
- Neilson, J.H. and A. Gilchrist, "An Analytical and Experimental Investigation of the Velocities of Particles Entrained by the Gas Flow in Nozzles," J. Fluid Mech., (Great Britain), Vol. 33, Part 1, 12 Jul 1968, pp. 131-149
- Rudinger, G., "The Reflection of Pressure Waves of Finite Amplitude from an Open End of a Duct," J. Fluid Mech., Vol. 3, Oct 1957, pp. 48-66
- Rudinger, G., "Nonsteady Supercritical Discharge Through an Orifice," Project Squid, Technical Report CAL-82-P, James Forrestal Research Center, Princeton, N.J., Dec 1960
- Shercliff, J.A., "Some Generalizations in Steady One-Dimensional Gas Dynamics," J. Fluid Mech., Vol. 3, Mar 1958, pp. 645-657
- Stewart, R.W., "Irrotational Motion Associated With Free Turbulent Flows," J. Fluid Mech., Vol. 1, Part 6, Dec 1956, pp. 593-606
- Walker, W.F., G.W. Zumwalt, and L.J. Fila, "Numerical Solution for the Interaction of a Moving Shock Wave With a Turbulent Mixing Region," Paper No. 68-APM-M, J. App. Mech., 1968
- Williams, F.A., "Linearized Analysis of Constant-Property Duct Flows," J. Fluid Mech., Vol. 34, Part 3, Nov 1968, pp. 241-261
- Ximenez, D., "A Study of Viscous Effects in Separated Compressible Flow," Accession-No. N6831224, Clearinghouse (a Dissertation), University of Alabama, 1968



Properties of Jets

- Abramovich, G.N., The Theory of Turbulent Jets, M.I.T. Press, Cambridge, Mass., 1963
- Ackerberg, R.C. and A. Pal, "On the Interaction of a Two-Dimensional Jet With a Parallel Flow," U.S. Army Aviation Materiel Laboratories, Polytechnic Institute of Brooklyn, Aug 1966 (44p.)
- Ackerberg, R.C., "On a Non-Linear Theory of Thin Jets, Part I, J. Fluid Mech., Vol. 31, Part 3, 26 Feb 1968, pp. 583-601
- Ackerberg, R.C., "On a Non-Linear Theory of Thin Jets, Part II: A Linear Theory for Small Injection Angles," J. Fluid Mech., (Great Britain) Vol. 33, Part 2, 12 Aug 1968, pp. 261-272
- Adamson, T.C., Jr. and J.G. Nickolls, "On the Structure of Jets From Highly Underexpanded Nozzles Into Still Air," 2397-5-F, University of Michigan, Feb 1958
- Albini, F.A., "Approximate Computation of Underexpanded Jet Structure," AIAA J., Vol. 3, No. 8, Aug 1965, pp. 1535-1537
- Atvars, et. al., Refraction of Sound By Jet Flow or Jet Temperature, UTIAS, TN No. 109, May 1965
- Bradbury, L.J.S., "The Structure of a Self-Preserving Turbulent Plane Jet," J. Fluid Mech., Vol. 23, Part 1, 1965, pp. 31-64
- Chaplygin, S., Gas Jets, NACA TM 106-3, 1944
- Chu, W.T., "Velocity Profile in the Half-Jet Mixing Region of Turbulent Jets," AIAA J., Vol. 3, No. 4, Apr 1965, pp. 789-790
- Crane, L.J. and D.C. Pack, "The Laminar and Turbulent Mixing of Jets of Compressible Fluid, Part I: Flow Far From the Orifice," J. Fluid Mech., Vol. 2, Jul 1957, pp. 449-455
- D'Attorre, L. and F.C. Harshbarger, "Parameters Affecting the Normal Shock Location in Underexpanded Gas Jets," AIAA J., Vol. 3, No. 3, Mar 1965, pp. 530-531
- Fitzpatrick, H.M. and R. Lee, Measurement of Noise Radiated by Subsonic Air Jets, Navy Dept., David Taylor Model Basin, Report 835, NS-715-102, NR-062-094, Nov 1952

- Glass, D.R., "Effects of Acoustic Feedback on the Spread and Decay of Supersonic Jets," AIAA J., Vol. 6, No. 10, Oct 1968, pp. 1890-1897
- Grande, E., Refraction of Sound By Jet Flow and Jet Temperature, II, UTIAS, TN No. 110, Dec 1966
- Heskestad, G., "Hot-Wire Measurements in a Radial Turbulent Jet," J. App. Mech., Jun 1966, pp. 417-424
- Heskestad, G., "Hot-Wire Measurements in a Plane Turbulent Jet," J. App. Mech., Dec 1965, pp. 721-734
- Hill, P.G., "Turbulent Jets in Ducted Streams," J. Fluid Mech., Vol. 22, May 1965, pp. 161-186 (Part I)
- Hubbard, E.W., "Approximate Calculation of Highly Underexpanded Jets," AIAA J., Vol. 4, No. 10, Oct 1966, pp. 1877-1879
- Ilizarova, L.I., "Some Results of Velocity Fluctuation Measurements in the Initial Section of an Axisymmetric Jet," Industrial Aerodynamics, No. 27, 1966, pp. 111-120
- Johannesen, N.H., The Mixing of Free Axially Symmetrical Jets of Mach Number 1.40, F.M. 2490, Aeronautical Research Council, Jan 1957
- Kleinstien, G., An Approximate Solution For the Axisymmetric Jet of a Laminar Compressible Fluid, ARL 51, Apr 1961
- Kolpin, M.O., Velocity Correlation Measurement In the Mixing Region of a Jet, MIT/ASRL, TR-1008, Mar 1963 (also AGARD. R-452, Apr 1963)
- Ladenburg, R., C.C. Van Voorhis, and J. Winckler, Interferometric Study of Supersonic Phenomena, Part I: A Supersonic Air Jet at 60 psi Tank Pressure, NAVORD Report 69-46, Apr 1946
- Larock, B.E., "Jets from Two-Dimensional Symmetric Nozzles of Arbitrary Shape," J. Fluid Mech., Vol. 37, Part 3, 1969, pp. 479-489
- Launder, B.E., "A Note on Jets and Wakes With Small Shear Velocities," Trans. ASME, J. App. Mech., Vol. 3, Dec 1967, p. 1042
- Lennox, S.C. and D.C. Pack, "The Flow in Compound Jets," J. Fluid Mech., Vol. 15, Apr 1963, pp. 513-526
- Lindow, B. and I. Greber, "Similarity Solution for a Laminar, Incompressible Jet Flowing Along a Curved Surface," AIAA J., Vol. 6, No. 7, Jul 1968, pp. 1331-1335

- Marrone, P.V., "Temperature and Density Measurements in Free Jets and Shock Waves," Phys. of Fluids (USA), Vol. 10, No. 3, Mar 1967, p. 521
- McNaughton, K.J. and C.G. Sinclair, "Submerged Jets in Short Cylindrical Flow Vessels," J. Fluid Mech., Vol. 25, Part 2, Jun 1966, pp. 367-375
- Mellor, G.E., "Linear Jet and Wake Solutions With Pressure Gradients," AIAA J., Vol. 3, No. 5, May 1965, pp. 975-977
- Miles, J.B. and J-S. Shih, "Similarity Parameter for Two-Stream Turbulent Jet-Mixing Region," AIAA J., Vol. 6, No. 7, Jul 1968, pp. 1429-1430
- Mollo-Christensen, E., Measurement of Near Field Pressure of Subsonic Jets, AGARD Report 449, Apr 1963
- Napalitoni, L.G. and F. Manzo, "Cross Flow Effects in the Plane Wall Jet," AIAA J., Vol. 3, No. 9, Sep 1965, pp. 1746-1747
- Pack, D.C., "The Hodograph Method Applied to Flow Past Profiles and in Jets," ARDC/EO TR-60-61, Roy. Col. of Sci. and Tech., Glasgow, Apr 1960
- Pavlovskiy, V.V., The Main Section of Axisymmetrical Jets of an Incompressible Fluid Flowing From the Aperture of Finite Size Into a Coaxial Uniform Flow of the Same Fluid, Redstone Arsenal, RSA RSIC-612, Nov 1966
- Pai, S.I., Viscous Flow Theory, Part I: Laminar Flow, Van Nostrand, New York, 1956
- Pai, S.I., Fluid Dynamics of Jets, Van Nostrand, New York, 1954
- Rom, J., "Study of Similarity of High-Temperature, Turbulent Jets," AIAA J., Vol. 6, No. 7, Jul 1968, pp. 1368-1370
- Rotem, Z., "Axisymmetrical Turbulent Jet - Tollmien's Problem Extended," AIAA J., Vol. 1, No. 11, Nov 1963, pp. 2633-2635
- Rubin, S.G. and R. Falco, "Plane Laminar Jet," AIAA J., Vol. 6, No. 1, Jan 1968, pp. 186-187
- Sami, S., "Balance of Turbulence Energy in the Region of Jet-Flow Establishment," J. Fluid Mech., Vol. 29, Part 1, Jul 1967, pp. 81-92
- Schetz, J.A., P.F. Hawkins, and H. Lehman, "Structure of Highly Under-Expanded Transverse Jets in a Supersonic Stream," AIAA J., Vol. 5, No. 5, May 1967, pp. 882-884
- Shuran and Dosanjh, Observations on Jet Flows From a 2-D, Underexpanded, Sonic Nozzle, AIAA-TN, Vol. 6, No. 3, Mar 1968, p. 540

- Sutton, G.W., "Fluctuation Intensity of Passive Species in a Turbulent Subsonic Jet," AIAA J., Vol. 7, No. 1, Jan 1969, pp. 90-95
- Tatsumi, T. and T. Kakutani, "The Stability of a Two-Dimensional Laminar Jet," J. Fluid Mech., Vol. 4, Jul 1958, pp. 261-275
- Tempelmeyer, K.E., An Analytical Study of Hot Jet Simulation With a Cold Gas Mixture, AEDC-TN-58-54, Sep 1958
- Thompson, P.A., "A One-Dimensional Treatment of Inviscid Jet or Duct Flow," AIAA J., Vol. 3, No. 2, Feb 1965, pp. 212-215
- Trentacoste, N. and P.M. Sforza, "Some Remarks on Three-Dimensional Wakes and Jets," AIAA J., Vol. 6, No. 12, Dec 1968, pp. 2454-2456
- Trentacoste, N. and P.M. Sforza, "Further Experimental Results for Three-Dimensional Free Jets," AIAA J., Vol. 5, No. 5, May 1967, pp. 885-891
- Uchida, S. and T. Suzuki, "On a Similar Solution for a Turbulent Half Jet Along a Curved Streamline," J. Fluid Mech., (Great Britain), Vol. 33, Part 2, 12 Aug 1968, pp. 379-395
- Vick, A.R., et al., Comparisons of Experimental Free-Jet Boundaries With Theoretical Results Obtained With the Method of Characteristics, NASA Tech. Note, NASA TN D-2327, Jun 1964
- Wang, T.C., Turbulence Measurements Relevant to Jet Noise, UTIAS Report 119, Nov 1966
- Weeks, T.M. and D.S. Dosanjh, "Interaction Between an Advancing Shock Wave and Opposing Jet Flow," AIAA J., Vol. 1, No. 7, Jul 1963, p. 1527
- Wynnanski, I., "Two-Dimensional Turbulent Jet in a Uniform, Parallel Stream," AIAA J., Vol. 7, No. 1, Jan 1969, pp. 86-89
- Wynnanski, I. and H.E. Fiedler, "Jets and Wakes in Tailored Pressure Gradient," Phys. Fluids, Vol. 11, No. 12, Dec 1968, pp. 2513-2523

Shear Flow

- Baker, R.L., et al., Stability of Shear Flow With Density Gradients and Viscosity, NASA-CR-958, Feb 1968
- Batchelor, G.K., "Diffusion in Free Turbulent Shear Flows," J. Fluid Mech., Vol. 3, Oct 1957, pp. 67-80
- Bradshaw, P., "The Effect of Initial Conditions on the Development of a Free Shear Layer," J. Fluid Mech., Vol. 26, Part 2, Oct 1966, pp. 225-236
- Browand, F.K., "An Experimental Investigation of the Instability of an Incompressible, Separated Shear Layer," J. Fluid Mech., Vol. 26, Part 2, Oct 1966, pp. 281-307
- Chen, C.F. and B.J. Mangione, "Effect of Flow Shear on Induced Drag," AIAA J., Vol. 5, No. 11, Nov 1967, p. 2056
- Crow, S., "Turbulent Rayleigh Shear Flow," J. Fluid Mech., Vol. 32, Part 1, Apr 1968, pp. 113-130
- Davies, P.O.A.L., "Turbulence Structure in Free Shear Layers," AIAA J., Vol. 4, No. 11, Nov 1966, pp. 1971-1978
- Devan, L., "Similar Flow Boundary Layer on Bodies in the Presence of Shear Flow," AIAA J., Vol. 3, No. 9, Sep 1965, pp. 1747-1749
- Esch, R.E., "The Instability of a Shear Layer Between Two Parallel Streams," J. Fluid Mech., Vol. 3, Part 3, Dec 1957, pp. 289-303
- Goren, S.L., "Development of the Boundary Layer at a Free Surface From a Uniform Shear Flow," J. Fluid Mech., Vol. 25, Part 1, May 1966, pp. 87-95
- Halskinen, R.J. and N. Rott, "Similar Solutions for Merging Shear Flows, II," AIAA J., Vol. 3, No. 8, Aug 1965, pp. 1553-1554
- Hanson, F.B., S.H. Kozak, and P.D. Richardson, "Velocity Spikes in Separated Flows," J. Fluid Mech., Vol. 25, Part 1, May 1966, pp. 43-50
- Hasen, E.M., "A Non-Linear Theory of Turbulence Onset in a Shear Flow," J. Fluid Mech., Vol. 29, Part 4, Sep 1967, pp. 721-729
- Heskestad, G., "A Generalized Taylor Hypothesis With Applications for High Reynolds Number Turbulent Shear Flows," J. App. Mech., Dec 1965, pp. 735-739

- Inger, G.R., "A Simple Model Shear Flow With Blowing," AIAA J., Vol. 4, No. 10, Oct 1966, pp. 1834-1836
- Johansson, B., Lifting-Line Theory for Subsonic Shear Flow, The Aeronautical Research Institute of Sweden, FFA Report 114, Stockholm, 1967
- Kotansky, D.R., "The Use of Honeycomb for Shear Flow Generation," AIAA J., Vol. 4, No. 8, Aug 1966, pp. 1490-1491
- Mark, R.M., "On Shear Flow Past Flat Plates," J. Fluid Mech., Vol. 14, Nov 1962, pp. 452-462
- Menkes, J., "An Estimate of the Decay of Turbulent Intensity in a Shear Flow," AIAA J., Vol. 3, No. 6, Jun 1965, pp. 1182-1184
- Menkes, J., "On the Stability of a Shear Layer," J. Fluid Mech., Vol. 6, Nov 1959, pp. 518-522
- Mills, R.D., "Numerical and Experimental Investigations of the Shear Layer Between Two Parallel Streams," J. Fluid Mech., (Great Britain), Vol. 33, Part 3, 2 Sep 1968, pp. 591-616
- Nee, Victor Wai-Tsu, A Phenomenological Theory of Quasi-Parallel Turbulent Shear Flow, 67-13,818 University Microfilms, Inc., Ann Arbor, Mich. 1968

#### Turbulence, Mixing, and Transition Processes

- Batchelor, G.K. and A.E. Gill, "Analysis of the Stability of Axisymmetric Jets," J. Fluid Mech., Vol. 14, Dec 1962, pp. 529-551
- Cohen, N.S., "A Correlation of the Spread and Decay of Turbulent Free Jets," AIAA J., Vol. 4, No. 5, May 1966, pp. 929-930
- Crane, L.J., "The Laminar and Turbulent Mixing of Jets of Compressible Fluid. Part II: The Mixing of Two Semi-Infinite Streams," J. Fluid Mech., Vol. 3, Oct 1957, pp. 81-92
- Csanady, G.T., "On the Energy Balance of a Turbulent Mixing Layer," J. Fluid Mech., Vol. 15, Apr 1963, pp. 545-559

- Escudier, M.P. and W.B. Nicoll, "The Entrainment Function in Turbulent Boundary-Layer and Wall-Jet Calculations," J. Fluid Mech., Vol. 25, Part 2, Jun 1966, pp. 337-366
- Gill, A.E. and P.G. Drazin, "Note on Instability of Compressible Jets and Waves to Long-Wave Disturbances," J. Fluid Mech., Vol. 22, Part 2, Jun 1965, p. 415
- Greenspan, H.P. and D.J. Benney, "On Shear-Layer Instability, Breakdown and Transition," J. Fluid Mech., Vol. 15, Jan 1963, pp. 133-153
- Kireyev, V.T., On the Effecting of a Steady Mixing in Jets, FTD-MT-67-54, prepared by Translation Division, Foreign Technology Division, Wright-Patterson AFB, Ohio, 24 Aug 1967
- Leith, C.E., "Numerical Treatment of Turbulent Flows," AIAA J., Vol. 3, No. 7, Jul 1965, pp. 1364-1365
- Lessen, M., J.A. Fox, and H.M. Zien, "The Instability of Inviscid Jets and Wakes in Compressible Fluid," J. Fluid Mech., Vol. 21, Jan 1965, pp. 129-143
- Miles, J.B. and J. Shih, "Similarity Parameter for Two-Stream Turbulent Jet-Mixing Region," AIAA J., Vol. 6, No. 7, Jul 1968, pp. 1429-1430
- O'Connor, T.J., E.H. Comfort, and L.A. Cass, "Turbulent Mixing of an Axisymmetric Jet of Partially Dissociated Nitrogen with Ambient Air," AIAA J., Vol. 4, No. 11, Nov 1966, pp. 2026-2032
- Page, R.H. and W.G. Hill, "Location of Transition in a Free Jet Region," AIAA J., Vol. 4, No. 5, May 1966, p. 444
- Patel, V.C. and M.R. Head, "Reversion of Turbulent to Laminar Flow," J. Fluid Mech., Vol. 34, Part 2, Nov 1968, pp. 371-392
- Ricou, F.P. and D.B. Spalding, "Measurements of Entrainment by Axisymmetrical Turbulent Jets," J. Fluid Mech., Vol. 11, Part 1, Aug 1961, pp. 21-32
- Rom, J., "Study of Similarity of High-Temperature, Turbulent Jets," AIAA J., Vol. 6, No. 7, Jul 1968, pp. 1368-1370
- Sato, H., "The Stability and Transition of a Two-Dimensional Jet," J. Fluid Mech., Vol. 7, Part 1, Jan 1960, pp. 53-80
- Schetz, J.A., "Turbulent Mixing of a Jet in a Coflowing Stream," AIAA J., Vol. 6, No. 10, Oct 1968, pp. 2008-2010

- Sforza, P.J., H.H. Stiger, and N. Trentacoste, "Studies on 3D Viscous Jets," AIAA J., Vol. 4, No. 5, May 1966, pp. 800-806
- Wang, D.P., "Finite Amplitude Effect on the Stability of a Jet of Circular Cross-Section," J. Fluid Mech., Vol. 34, Part 2, Nov 1968, pp. 299-313
- Wynanski, I. and O. Hawaleshka, "Effect of Upstream Velocity Profile on the Free Mixing of Jets With Ambient Fluid," AIAA J., Vol. 5, No. 6, Jun 1967, pp. 1057-1062
- Zawacki, T.S., Turbulence in the Mixing Region Between Coaxial Streams, University Microfilms, Inc., Ann Arbor, Mich., 1968
- Zawacki, T.S. and H. Weinstein, Experimental Investigation of Turbulence in the Mixing Region Between Coaxial Streams, NASA CR-959, I.I.T., Feb 1968

#### Impinging and Wall Jets

- Bakke, P., "An Experimental Investigation of a Wall Jet," J. Fluid Mech., Vol. 2, Jul 1957, pp. 467-472
- Bloom, M.H. and M.H. Steiger, Perturbed Boundary Layer Solutions Applied to the Wall Jet and the Blasius Profile, AFOSR TN-60-1340, PIBAL Rpt No. 471, Oct 1960
- Bloom, M.H. and M.H. Steiger, Some Compressibility and Heat Transfer Characteristics of the Wall Jet, Proc. 3rd U.S. National Congress of Applied Mechanics, Brown University, ASME, Jun 1958
- Fox, H. and M.H. Steiger, "Some Mass Transfer Effects on the Wall Jet," J. Fluid Mech., Vol. 15, Part 4, Apr 1963, pp. 597-609
- Glauert, M.B., "The Wall Jet," J. Fluid Mech., Vol. 1, 1956, p. 625
- Kacker, S.C. and J.H. Whitelaw, "Some Properties of the Two-Dimensional Turbulent Wall Jet in a Moving Stream," J. App. Mech., Dec 1968, pp. 641-651



- Kim, Tong Soo, Analysis of Flow Characteristics in Circular, Submerged, Impinging Jets, 67-12,504, University Microfilms, Inc., Ann Arbor, Mich., 1968
- Kruka, V. and Eskinaza, "The Wall-Jet in a Moving Stream," J. Fluid Mech., Vol. 20 Part 4, 1964, pp. 555-579
- Lindow, B. and I. Greber, "Similarity Solution for a Laminar, Incompressible Jet Flowing Along a Curved Surface," AIAA J., Vol. No. 7, Jul 1968, pp. 1331-1335
- Mallonee, R.C., II and S.L.S. Jacoby, "Plane, Turbulent Compressible Wall Jet With and Without Parallel Free Stream," 68-FE-40, Am. Soc. of Mech. Eng., New York, 1968
- Miller, D.R. and E.W. Comings, "Static Pressure Distribution in the Free Turbulent Jet," J. Fluid Mech., Vol. 3, Part 1, Oct 1957, pp. 1-16
- Riley, N., "Effects of Compressibility on a Laminar Wall Jet," J. Fluid Mech., Vol. 4, Nov 1958, pp. 615-628
- Sarpkaya, T., The Deflection of Plane Turbulent Jets by Convex Walls, NPS-59SL8061A, Naval Postgraduate School, Monterey, Calif., 27 Jun 1968
- Schubert, G. and G.M. Corcos, "The Dynamics of Turbulence Near a Wall According to a Linear Model," J. Fluid Mech., Vol. 29, Part 1, Jul 1967, pp. 113-135
- Schwartz, W.H. and W.P. Cosart, "The Two-Dimensional Turbulent Wall Jet," J. Fluid Mech., Vol. 10, Part 4, Jun 1961, pp. 481-495
- Starr, J.B. and E.M. Sparrow, "Experiments on a Turbulent Cylindrical Wall Jet," J. Fluid Mech., Vol. 29, Part 3, Sep 1967, pp. 495-512
- Steinheuer, J., "Similar Solutions for the Laminar Wall Jet in a Decelerating Outer Flow," AIAA J., Vol. 6, No. 11, Nov 1968, pp. 2198-2200
- Wyganski, I.J. and F.H. Champagne, "The Laminar Wall-Jet Over a Curved Surface," J. Fluid Mech., Vol. 31, Part 3, 26 Feb 1968, pp. 459-465

# Appendix A REPRESENTATIVE FINITE-DIFFERENCE EQUATIONS

The following finite-difference equations developed by Rich are presented in this appendix (as Rich developed them in Ref. 13) to provide the reader a representative set of Eulerian finite-difference equations and calculation procedures. In this presentation, the center of each cell, (i,j) is labeled by its row (i) and column (j) location in the mesh. Time is differenced in multiples (n) of constant time increment ( $\Delta t$ ). The values of density  $\left[ \rho_{i,j}^{(n)} \right]$ , velocity  $\left[ u_{i,j}^{(n)}, v_{i,j}^{(n)} \right]$ , and specific energy  $\left[ E_{i,j}^{(n)} \right]$  are constant within each cell for each time increment n as defined by the superscript (n).

The equations will be given in the computational sequence described in the text. This computational sequence had three phases: (I) the calculation of intermediate values of velocity and specific energy in each cell with the boundary condition of no mass flow out of the cell; (II) mass transport across the boundaries based on the intermediate values; and (III) the computation of the resultant conditions in the cell.

The difference equation for the conservation of momentum and energy during Phase I is given by:

$$\begin{aligned} \rho_{i,j}^{(n)} \left( \frac{\partial u}{\partial t} \right)_{i,j}^{(n)} \Delta x \Delta y &= - \left[ p_{i+\frac{1}{2},j}^{(n)} - p_{i-\frac{1}{2},j}^{(n)} \right] \Delta y \\ \rho_{i,j}^{(n)} \left( \frac{\partial v}{\partial t} \right)_{i,j}^{(n)} \Delta x \Delta y &= - \left[ p_{i,j+\frac{1}{2}}^{(n)} - p_{i,j-\frac{1}{2}}^{(n)} \right] \Delta x \\ \rho_{i,j}^{(n)} \left( \frac{\partial E}{\partial t} \right)_{i,j}^{(n)} \Delta x \Delta y &= - \left\{ \left[ p_{i+\frac{1}{2},j}^{(n)} u_{i+\frac{1}{2},j}^{(n)} - p_{i-\frac{1}{2},j}^{(n)} u_{i-\frac{1}{2},j}^{(n)} \right] \Delta y \right. \\ &\quad \left. + \left[ p_{i,j+\frac{1}{2}}^{(n)} v_{i,j+\frac{1}{2}}^{(n)} - p_{i,j-\frac{1}{2}}^{(n)} v_{i,j-\frac{1}{2}}^{(n)} \right] \Delta x \right\} \end{aligned}$$

Where the pressure and velocity at the cell boundaries are given by linear interpolation as in the following examples,

$$p_{i+\frac{1}{2},j}^{(n)} = \frac{1}{2} \left[ p_{i,j}^{(n)} + p_{i+1,j}^{(n)} \right]$$

$$u_{i+\frac{1}{2},j}^{(n)} = \frac{1}{2} \left[ u_{i,j}^{(n)} + u_{i+1,j}^{(n)} \right]$$

$$v_{i,j+\frac{1}{2}}^{(n)} = \frac{1}{2} \left[ v_{i,j}^{(n)} + v_{i,j+1}^{(n)} \right]$$

and the time derivatives are defined by

$$\left( \frac{\partial u}{\partial t} \right)_{i,j}^{(n)} = \frac{\tilde{u}_{i,j}^{(n)} - u_{i,j}^{(n)}}{\Delta t}$$

$$\left( \frac{\partial v}{\partial t} \right)_{i,j}^{(n)} = \frac{\tilde{v}_{i,j}^{(n)} - v_{i,j}^{(n)}}{\Delta t}$$

$$\left( \frac{\partial E}{\partial t} \right)_{i,j}^{(n)} = \frac{\tilde{E}_{i,j}^{(n)} - E_{i,j}^{(n)}}{\Delta t}$$

Substitution of the above equations in the original difference equations establishes the following equations for the intermediate velocities and specific energy (denoted by the tilde) in any cell (i,j):

$$\tilde{u}_{i,j}^{(n)} = u_{i,j}^{(n)} - \frac{p_{i+\frac{1}{2},j}^{(n)} - p_{i-\frac{1}{2},j}^{(n)}}{\Delta x} \frac{\Delta t}{\rho_{i,j}^{(n)}}$$

$$\tilde{v}_{i,j}^{(n)} = v_{i,j}^{(n)} - \frac{p_{i,j+\frac{1}{2}}^{(n)} - p_{i,j-\frac{1}{2}}^{(n)}}{\Delta y} \frac{\Delta t}{\rho_{i,j}^{(n)}}$$

$$\begin{aligned} \tilde{E}_{i,j}^{(n)} = E_{i,j}^{(n)} - & \left[ \frac{p_{i+\frac{1}{2},j}^{(n)} u_{i+\frac{1}{2},j}^{(n)} - p_{i-\frac{1}{2},j}^{(n)} u_{i-\frac{1}{2},j}^{(n)}}{\Delta x} \right. \\ & \left. + \frac{p_{i,j+\frac{1}{2}}^{(n)} v_{i,j+\frac{1}{2}}^{(n)} - p_{i,j-\frac{1}{2}}^{(n)} v_{i,j-\frac{1}{2}}^{(n)}}{\Delta y} \right] \frac{\Delta t}{\rho_{i,j}^{(n)}} \end{aligned}$$

The tilde values represent the change in momentum and energy due to the surface forces acting on the control volume, i.e., any cell (i,j). These values are used to compute the mass transport effects in the following Phase II equations. The mass transport across a cell boundary is proportional to the fluid density and the normal component of velocity at the interface. The exchange must conserve mass, hence the Eulerian expression for this condition must be satisfied and is expressed in the difference format as

$$\rho_{i,j}^{(n+1)} \Delta x \Delta y = \rho_{i,j}^{(n)} \Delta x \Delta y - \Delta M_{i+\frac{1}{2},j}^{(n)} + \Delta M_{i-\frac{1}{2},j}^{(n)} - \Delta M_{i,j+\frac{1}{2}}^{(n)} + \Delta M_{i,j-\frac{1}{2}}^{(n)}$$

where

$$\Delta M_{i+\frac{1}{2},j}^{(n)} = \rho_{i+\frac{1}{2},j}^{(n)} \tilde{u}_{i+\frac{1}{2},j}^{(n)} \Delta y \Delta t$$

$$\Delta M_{i,j+\frac{1}{2}}^{(n)} = \rho_{i,j+\frac{1}{2}}^{(n)} \tilde{v}_{i,j+\frac{1}{2}}^{(n)} \Delta x \Delta t$$

Similarly for the cell boundaries (i-1/2,j) and (i,j-1/2).

In the above expressions, the cell boundaries across which the mass is exchanged are indicated by the subscripts.

The tilde values in the preceding equation are those at the cell boundaries, not at the center of the cell. Rich (Ref. 13) and other investigators have shown the use of simple averages for the densities and velocities at the cell boundaries leads to minor, but noticeable, instabilities in the solution of the difference equations. Rich's technique avoids the instability by preferentially weighting the density and velocity in favor of the cell out of which the fluid flows, and to take advantage of the differencing property which limits the center of the fluid element (located at the center of the cell of the Eulerian mesh) from leaving the cell during the computational time step. A better representation for the values of the boundary quantities ( $\tilde{u}$ ,  $\tilde{v}$ ,  $\tilde{\rho}$ ), particularly in the mass flow calculations, were shown to be obtained from the first two terms of a Taylor expansion about the center of the emptying cell. The use of simple averages for the density terms was shown by Rich (Ref. 13) to be sufficient in most instances.

The Taylor series expansion is about the center of the emptying cell, thus the equations for the boundary quantities are dependent upon the direction of flow at the cell interface. The selection of direction can be best accomplished by using the quantity  $\left[ \tilde{u}_{i,j}^{(n)} + \tilde{u}_{i+1,j}^{(n)} \right]$  - in essence the average value - as the test condition for direction. The average insures the same condition is used as a test irrespective of the direction at which the computation is approached, i.e., either from  $i$  or  $i+1$  the result is the same. The mass flow  $\Delta m_{i+1/2,j}^{(n)}$  would be calculated for the right-hand boundary of cell  $(i,j)$ , i.e.,  $(i+2,j)$ , as follows:

If  $\tilde{u}_{i,j}^{(n)} + \tilde{u}_{i+1,j}^{(n)} > 0$  and

$$\tilde{u}_{i+1/2,j}^{(n)} = \tilde{u}_{i,j}^{(n)} + \left( \frac{\partial \tilde{u}}{\partial x} \right)_{i,j}^{(n)} \frac{\Delta x}{2} = \tilde{u}_{i,j}^{(n)} + \frac{\tilde{u}_{i+1,j}^{(n)} - \tilde{u}_{i-1,j}^{(n)}}{4} > 0$$

then

$$\Delta M_{i+\frac{1}{2},j}^{(n)} = \left[ \tilde{u}_{i,j}^{(n)} + \frac{\tilde{u}_{i+1,j}^{(n)} - \tilde{u}_{i-1,j}^{(n)}}{4} \right] \left[ \rho_{i,j}^{(n)} + \frac{\rho_{i+1,j}^{(n)} - \rho_{i-1,j}^{(n)}}{4} \right] \Delta y \Delta t$$

If  $\tilde{u}_{i,j}^{(n)} + \tilde{u}_{i+1,j}^{(n)} < 0$  and

$$\tilde{u}_{i+\frac{1}{2},j}^{(n)} \equiv \tilde{u}_{i+1,j}^{(n)} - \left( \frac{\partial \tilde{u}}{\partial x} \right)_{i+1,j}^{(n)} \frac{\Delta x}{2} = \tilde{u}_{i+1,j}^{(n)} - \frac{\tilde{u}_{i+2,j}^{(n)} - \tilde{u}_{i,j}^{(n)}}{4} < 0$$

then

$$\Delta M_{i+\frac{1}{2},j}^{(n)} = \left[ \tilde{u}_{i+1,j}^{(n)} - \frac{\tilde{u}_{i+2,j}^{(n)} - \tilde{u}_{i,j}^{(n)}}{4} \right] \left[ \rho_{i+1,j}^{(n)} - \frac{\rho_{i+2,j}^{(n)} - \rho_{i,j}^{(n)}}{4} \right] \Delta y \Delta t$$

Otherwise  $\Delta M_{i+\frac{1}{2},j}^{(n)} = 0$ .

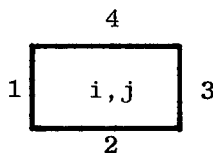
The flows across the other three sides of cell (i,j) are obtained in a similar manner.

In the Eulerian calculation scheme, the mass flowing from one cell to another carries with it the tilde velocity and specific energy of the cell from which it came. At the completion of the mass transport of Phase II, the composition of a given cell may be represented as a summation of all the mass and energy flows across its boundaries. The determination of final values is the third phase of the computational sequence. By combining the laws of conservation of momentum and energy with the mass transport quantities, the terminal value of velocity and specific energy for each cell can be obtained:

$$\vec{v}_{\text{final}} = \frac{\sum_k M_k \vec{v}_k}{\sum_k M_k}$$

$$E_{\text{final}} = \frac{\sum_k M_k E_k}{\sum_k M_k}$$

To simplify the computational scheme, Rich numbered the four sides of cell (i,j)  $k = 1, 2, 3$ , and  $4$ , as shown below.



A function  $C_{i,j}(k)$  for any cell (i,j) and its side  $k$  was defined such that

$$\begin{aligned} C_{i,j}(k) &= 1 \text{ if fluid flows into cell (i,j) across side } k \\ &= 0 \text{ if fluid flows out of cell (i,j) across side } k \end{aligned}$$

Rich then presented the following difference equations for the final velocity and energy,

$$\begin{aligned} u_{i,j}^{(n+1)} &= \left( C_{i,j}(1) \tilde{u}_{i-1,j}^{(n)} \Delta M_{i-\frac{1}{2},j}^{(n)} + C_{i,j}(2) \tilde{u}_{i,j-1}^{(n)} \Delta M_{i,j-\frac{1}{2}}^{(n)} \right. \\ &\quad \left. + C_{i,j}(3) \tilde{u}_{i+1,j}^{(n)} \Delta M_{i+\frac{1}{2},j}^{(n)} \right. \\ &\quad \left. + C_{i,j}(4) \tilde{u}_{i,j+1}^{(n)} \Delta M_{i,j+\frac{1}{2}}^{(n)} + \tilde{u}_{i,j}^{(n)} \left[ \rho_{i,j}^{(n)} \Delta x \Delta y - [1 - C_{i,j}(1)] \right. \right. \\ &\quad \left. \left. \times \Delta M_{i-\frac{1}{2},j}^{(n)} - [1 - C_{i,j}(2)] \Delta M_{i,j-\frac{1}{2}}^{(n)} \right. \right. \\ &\quad \left. \left. - [1 - C_{i,j}(3)] \Delta M_{i+\frac{1}{2},j}^{(n)} - [1 - C_{i,j}(4)] \Delta M_{i,j+\frac{1}{2}}^{(n)} \right] \right) / \left[ \rho_{i,j}^{(n+1)} \Delta x \Delta y \right] \\ v_{i,j}^{(n+1)} &= \left( C_{i,j}(1) \tilde{v}_{i-1,j}^{(n)} \Delta M_{i-\frac{1}{2},j}^{(n)} + C_{i,j}(2) \tilde{v}_{i,j-1}^{(n)} \Delta M_{i,j-\frac{1}{2}}^{(n)} \right. \\ &\quad \left. + C_{i,j}(3) \tilde{v}_{i+1,j}^{(n)} \Delta M_{i+\frac{1}{2},j}^{(n)} + \right. \end{aligned}$$

(Equation continued)

$$\begin{aligned}
& + c_{i,j}^{(4)} \tilde{v}_{i,j+1}^{(n)} \Delta M_{i,j+\frac{1}{2}}^{(n)} + \tilde{v}_{i,j}^{(n)} \left\{ \rho_{i,j}^{(n)} \Delta x \Delta y - [1 - c_{i,j}^{(1)}] \right. \\
& \quad \times \Delta M_{i-\frac{1}{2},j}^{(n)} - [1 - c_{i,j}^{(2)}] \Delta M_{i,j-\frac{1}{2}}^{(n)} \\
& \quad \left. - [1 - c_{i,j}^{(3)}] \Delta M_{i+\frac{1}{2},j}^{(n)} - [1 - c_{i,j}^{(4)}] \Delta M_{i,j+\frac{1}{2}}^{(n)} \right\} \Big/ \left[ \rho_{i,j}^{(n+1)} \Delta x \Delta y \right] \\
E_{i,j}^{(n+1)} = & \left( c_{i,j}^{(1)} \tilde{E}_{i-1,j} \Delta M_{i-\frac{1}{2},j}^{(n)} + c_{i,j}^{(2)} \tilde{E}_{i,j-1} \Delta M_{i,j-\frac{1}{2}}^{(n)} \right. \\
& + c_{i,j}^{(3)} \tilde{E}_{i+1,j} \Delta M_{i+\frac{1}{2},j}^{(n)} \\
& + c_{i,j}^{(4)} \tilde{E}_{i,j+1} \Delta M_{i,j+\frac{1}{2}}^{(n)} + \tilde{E}_{i,j}^{(n)} \left\{ \rho_{i,j}^{(n)} \Delta x \Delta y - [1 - c_{i,j}^{(1)}] \right. \\
& \quad \times \Delta M_{i-\frac{1}{2},j}^{(n)} - [1 - c_{i,j}^{(2)}] \Delta M_{i,j-\frac{1}{2}}^{(n)} \\
& \quad \left. - [1 - c_{i,j}^{(3)}] \Delta M_{i+\frac{1}{2},j}^{(n)} - [1 - c_{i,j}^{(4)}] \Delta M_{i,j+\frac{1}{2}}^{(n)} \right\} \Big/ \left[ \rho_{i,j}^{(n+1)} \Delta x \Delta y \right]
\end{aligned}$$

These equations complete Rich's computational cycle for the transition of the fluid configuration from time  $n$  to time  $(n+1)$ .



## Appendix B

## A DISCUSSION OF THE GEOMETRIC ASPECTS OF PRESSURE MEASUREMENT

The wide use of pressure-time measurements from scaled experiments in the Office of Civil Defense (OCD) shelter program requires some knowledge of the characteristics of the mapped pressure histories. The following discussion considers some aspects of the pressure-mapping process which have not been widely discussed in other sources. The material is based on an unpublished draft technical note the author prepared while employed at the Ballistic Research Laboratories (BRL). The gages and data referred to in the discussion are those of the BRL. Since the main body of available data on flow within OCD shelters has resulted from scale model studies done by the BRL, it seemed in the best interest of the OCD shelter program to leave it in that format.

## INTRODUCTION

The aerodynamic effects on a prototype object that are created by its interaction with an air blast wave can be experimentally determined by testing linearly scaled models in shock tubes. One measureable aerodynamic property of the interaction field surrounding the object is its overpressure as a function of time. To obtain pressure histories related to points within the field, pressure transducers are mounted on and about the modeled object. A number of these localized histories can be combined to establish the overall aerodynamic loading on and about the object.

The developed loading on the model can be related to the prototype situation by the use of scaling laws. In this appendix, linear scaling will be used, i.e., there will be a one-to-one relationship in aerodynamic properties. Flow velocities are then equal, model-to-prototype situation; and, therefore, time and distance scale linearly. The scale factor of the system is the ratio of the dimensions of the prototype to those of the model.

As the scale factor increases, i.e., the dimensions of the model decrease, the fixed size of the gage's sensing element becomes larger in relation to the model's surface. In linear scaling, corresponding to the decreased dimensions, there is a decrease in the time scale of the aerodynamic events being measured. These factors make the gage response, the average of the pressure acting on its surface, more the history of an area than of a point. The shift is due to the larger relative area of the gage, in comparison to the modeled surface, as well as to the shortened time scale of the aerodynamic occurrences. Measurement error is introduced due to the fixed velocities having to cross longer scaled distances, while the properties of the field vary more rapidly with both distance and time.

One such condition occurs with the beginning of the mapping of the pressure upon incidence of the pressure wave at the leading edge of the transducer element. As the wave traverses the gage, an increasing area is exposed to the pressure until the pressure wave has completely crossed the gage element. At any given moment, the pressure mapped by the transducer is the average of the pressure then acting on the sensing element. If the wave changes its amplitude before crossing the gage, as occurs with sharply decaying exponential waves, then the true maximum pressure is never mapped.

In the following discussion, this form of measurement will be considered for the linearly and exponentially decaying shock waves, such as those which are formed in the interaction of shock waves with scaled shelter models. The interaction forms a complex wave system, which can be considered to consist of a series of waves, as shown in Fig. B-1. For this investigation the shortest duration of any component wave will be 50  $\mu$ sec for a linearly decaying wave, and 100  $\mu$ sec for an exponentially decaying wave. These durations are compatible with the test conditions of experimental model shelter studies made at the Ballistic Research Laboratories for OCD.

The decay of the amplitude of the pressure pulse begins at each point on the gage at a rate that is measured in time from incidence of the wave at that point. For a rapidly decaying wave, the time delay due to the transit time of

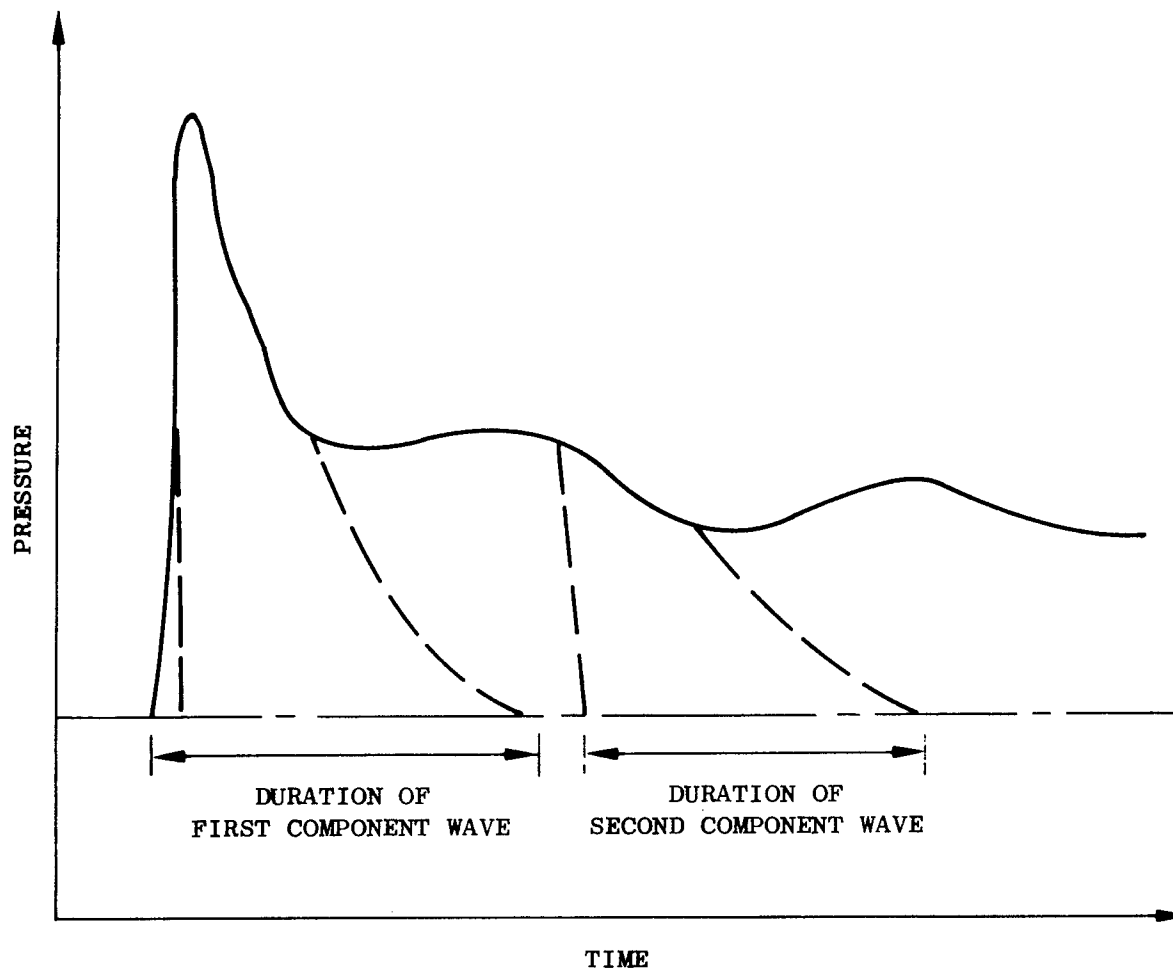


Fig. B-1. Component Wave Definition

the wave over the gage would result in a measureable nonuniformity in pressure. This nonuniformity would be absorbed in the averaging process and would result in the following: an inability to measure the wave's peak pressure, a phase shift in the mapped profile with respect to time measured from the wave incidence on the leading edge of the gage, and an undetermined line of action of the average pressure.

These three areas will be considered within the bounds of the conditions that have been set. A mathematical model of the physical situation will be established. This model will then be used to show how the mapped pressure-time profile is affected by the mapping process. A corrective procedure will then be postulated.

#### DISCUSSION

A mathematical model of the gage sensing area's interaction with the pressure wave will be used to represent the mapping of the applied pressure. Let a function  $p(t)$  be the overpressure-time profile of a shock wave that traverses the gage's circular element of radius  $R$  at a velocity  $U$ . The function  $p(t)$  is assumed to vary only in time in the direction of the wave propagation, as illustrated by Fig. B-2.

The distance  $x$  is measured across the gage element from the leading edge of the sensing surface, and time  $t$  is measured from the wave's incidence at that edge. The time delay between incidence of the wave front at the leading edge and its reaching any point is then  $x/U$ . In this coordinate system, the pressure at the leading edge begins its decay at  $t = 0$ ; but for any other point  $x_i$ , the decay begins at  $t_i = x_i/U$ , as illustrated by Fig. B-3. The different starting point in time for the decay of pressure (phase shift) is the reason the transducer cannot precisely map the incident peak overpressure. The valid time range for this mathematical model will begin when the incident wave completely crosses the element and will end when the range of  $p(t)$  ("the positive duration") is terminated at the leading edge. The mathematical model presented has the advantage of being spatially and temporally continuous in the defined ranges.

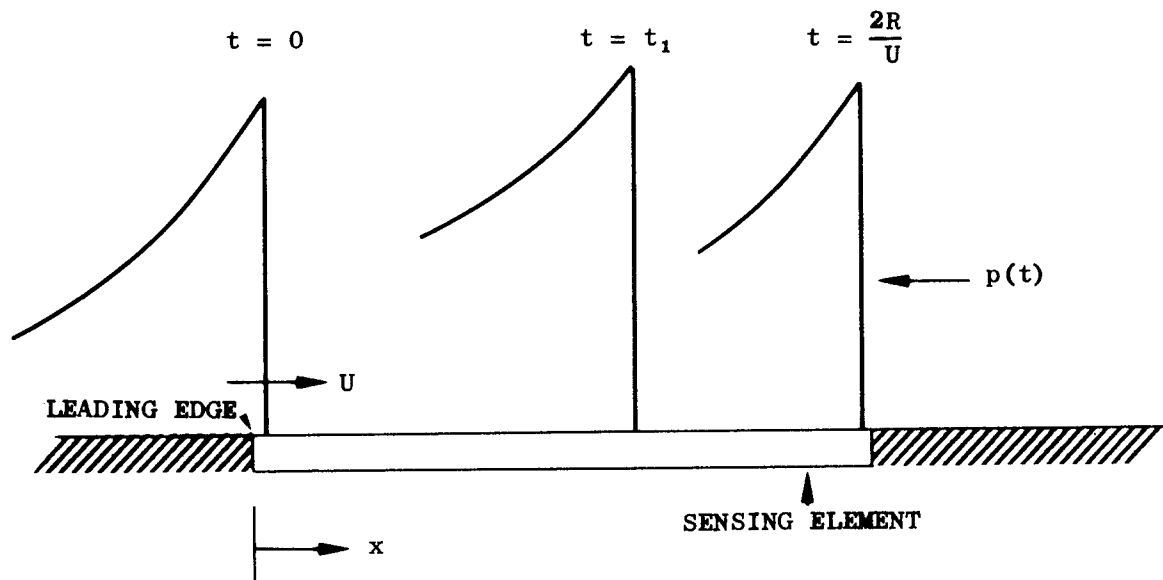


Fig. B-2. Incident Wave Crossing Gage Element

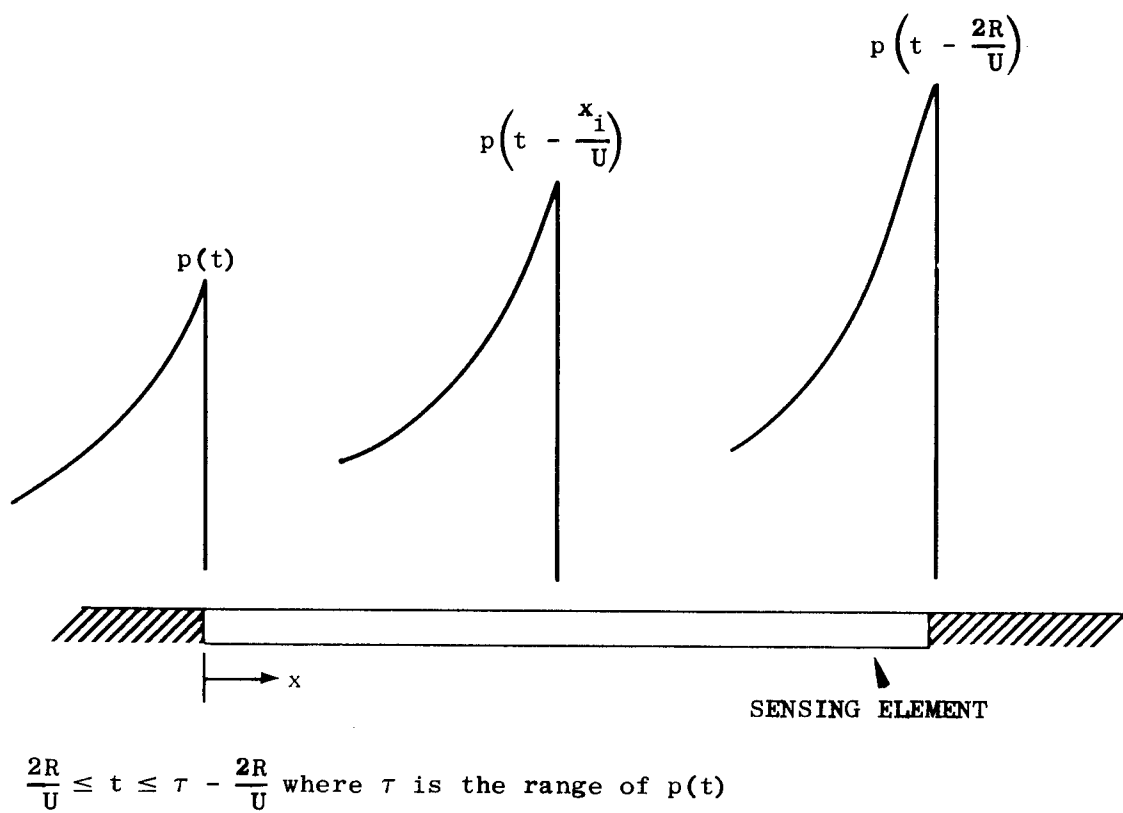


Fig. B-3. Schematic of the Adjusted Time Scale

As discussed, the mapped pressure at any time  $t_1$  is the average of the pressure acting over the surface of the sensing element. The average, or transduced signal, can be described by the integral of the applied pressure over the area of the sensing surface. The integral is that of a force volume (the depth dimension being pressure), with the property that when the volume is divided by the area of the sensing element, the measured average pressure is acquired. Figure B-4 presents the force volume  $V_f$  as a truncated circular cylinder in Cartesian coordinates. Integral calculus (Refs. 1, 2)\* defines the force volume by,

$$V_f = 2 \int_0^R \int_{x_1(y)}^{x_2(y)} f(x,y) dx dy \quad (B.1)$$

where

$$f(x,y) = P \left( t - \frac{x}{U} \right) \quad (B.2)$$

and

$$x_2(y) = R + \sqrt{R^2 - y^2} \quad (B.3)$$

$$x_1(y) = R - \sqrt{R^2 - y^2} \quad (B.4)$$

This integration was carried out for several exponential decaying waves and for a linearly decaying wave. A general solution was determined of the form

$$\bar{p}(t) = p(t - R/U) \cdot f(wR) \quad (B.5)$$

where  $wR = cR/U$  and  $\bar{p}(t)$  is the measured pressure. The term  $cR/U$  is the ratio of one-half of the sensing-area crossing-time\*\* to the duration of the wave.

---

\*References for this Appendix are presented at the end of the body of the Appendix.

\*\*Defined as the time interval  $2R/U$ .

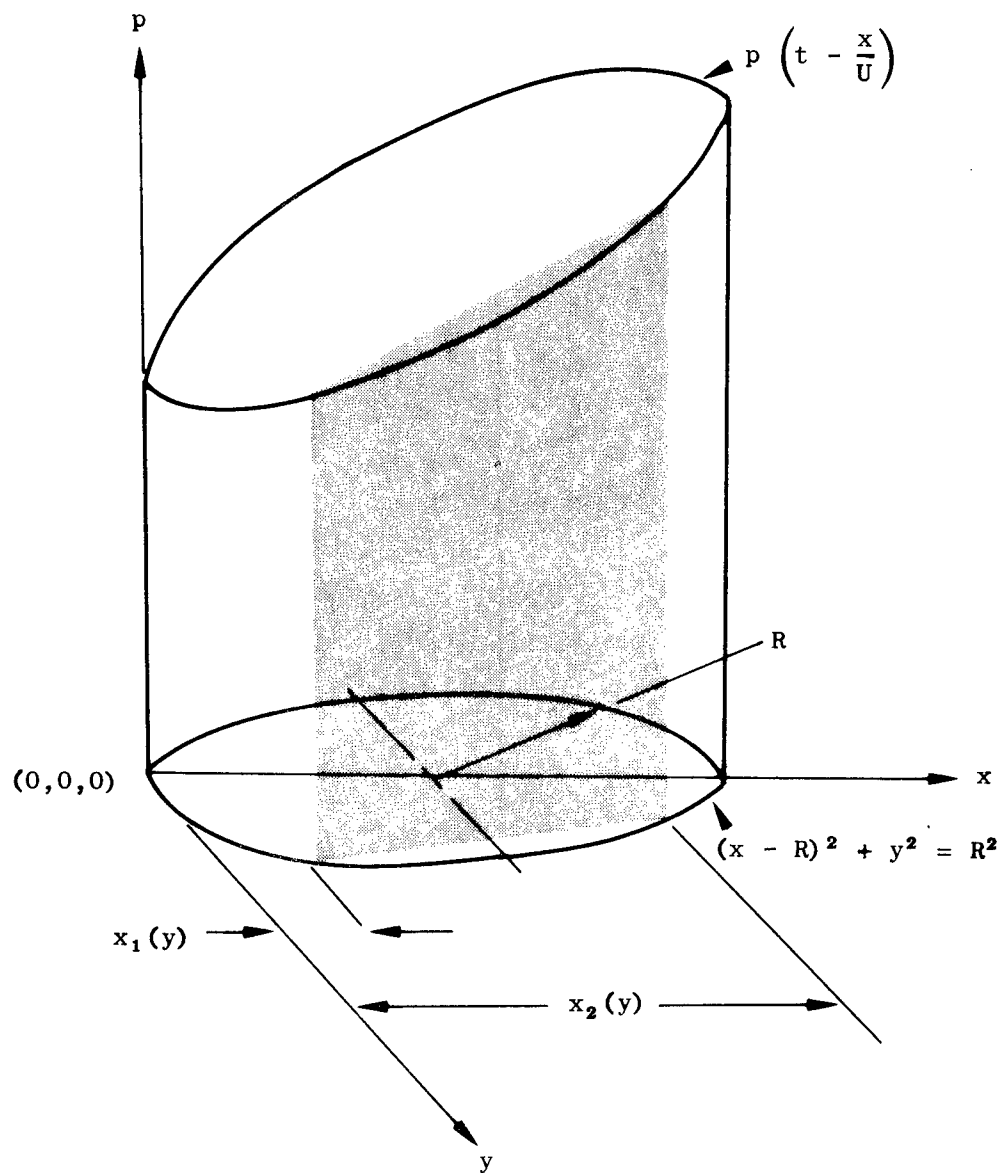


Fig. B-4. Force Volume



The term  $f(wR)$  was found to be a series with a first term of unity and the second term of order two in  $wR$ . The integration for one type of exponentially decaying wave is carried out in Exhibit I. In the development of the analysis in Exhibit II, it was determined, for the range of experimental values being considered, that terms of order two in  $wR$  are negligible. With this conclusion, Eq. (B.5) can be rewritten as

$$\bar{p}(t) = p(t - R/U) \quad (B.6)$$

The line of action of the average pressure would be through the centroid of the force volume. Exhibit II determines the location of the centroid for a triangularly decaying wave through the use of a triple integral. The table in Fig. B-5 tabulates the deviation of the centroid from the centerline for a ratio of crossing-time to duration of 10. It can be seen that except for times past 0.9 of the duration, the deviation is small, with a maximum of 11.1% at the end of the integration range of time.

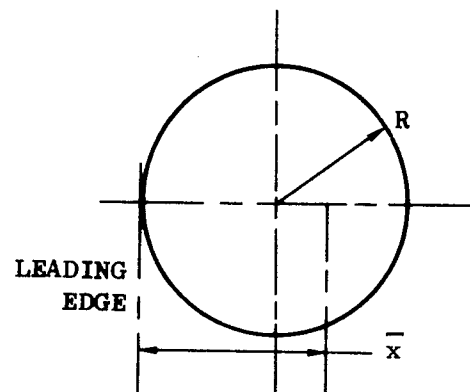
The results gained in Exhibit II can be generalized by consideration of the "force volume" as a composite volume. Consider the force volume to consist of a cylindrical volume and a wedge-shaped volume (Figs. B-4 or B-6). The centroid of the force volume is the resultant of the composite volumes. As the ratio of crossing time to duration increases, the portion of the total volume occupied by the wedge-shaped volume decreases. With the decrease, the effect of its centroid on the centroid of the composite force volume diminishes. In the limit, the force volume centroid is that of the cylindrical portion.

The analysis for the general case by use of centroids of composite volumes is carried out in Exhibit III. It is shown that the centroid  $\bar{x}$  of the force volume can be given by

$$\bar{x} = R \left( \frac{2p_1}{p_1 + p_2} \right) = R \left( \frac{2}{1 + \frac{p_2}{p_1}} \right) \quad (B.7)$$

$$\frac{CR}{U} = \frac{1/2 \text{ CROSSING-TIME}}{\text{WAVE DURATION}} = 0.1$$

$1 - ct$	$\bar{x}$
0.05	1.111R
0.10	1.083R
0.20	1.056R
0.50	1.028R
0.80	1.019R
0.95	1.007R



INCIDENT WAVE GIVEN BY:  $p(t) = \bar{p}(1 - ct)$

Fig. B-5. Effect of Wave Decay on (x) Centroid

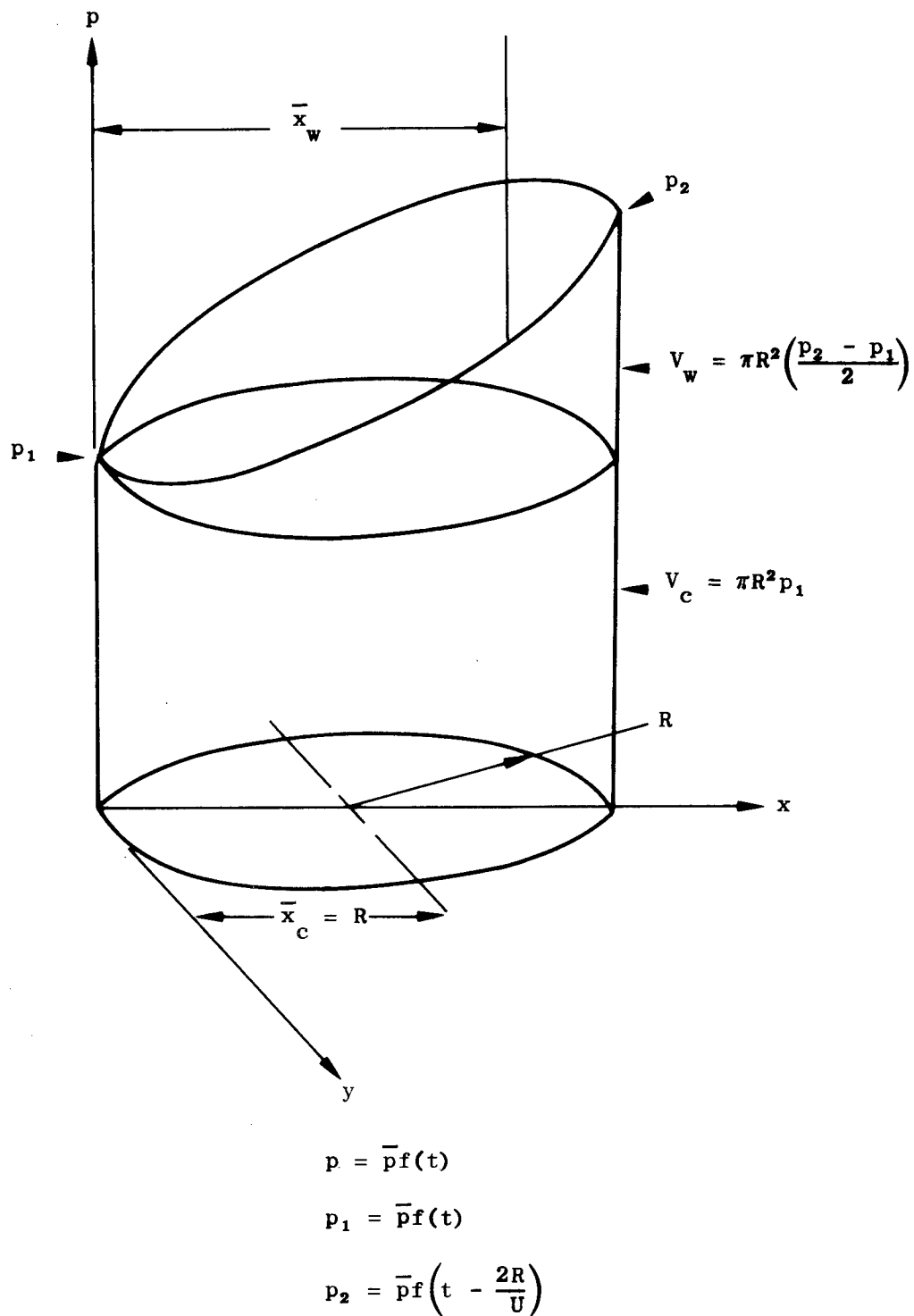


Fig. B-6. Nomenclature for Generalized Computation of the Centroids of the Force Volume

where  $p_1$  and  $p_2$  are the pressures at the lead and aft edges respectively at any time  $t$ . This result was based on a linear pressure gradient across the transducer with the centroid of the wedge at its worst location,  $2R$ . The use of the "worst condition" will provide a maximum value of  $\bar{x}$  irrespective of the probable wave shapes to be encountered.

By this technique an estimate of the location of the centroid may be acquired. To use it, one could use the crossing-time and then select a time and measure the pressure differential. From this value the ratio  $p_2/p_1$  can be acquired and hence the centroid. Within the bounds being considered, the decay of pressure does not affect the centroid of the force volume significantly. The line of action of the average pressure mapped by the transducer is then the geometric center of the sensing area.

Combining the results of the two analyses, it is found that the pressure record is shifted one-half of the gage crossing-time and acts through the centerline of the gage. Correspondingly the correct record would be represented if the record were to be read from one-half the crossing time instead of from the first rise of pressure. This record would be valid for that profile sensed at the centerline of the gage.

The peak pressure is not mapped. This, however, can be inferred by extrapolation of the pressure profile back in time to a point equal to one-half the crossing-time. If a small flat top wave were included on the top of the wave, as shown in Fig. B-7, or if the wave were a compression wave, such an extrapolation would be erroneous. The flat top wave is most often formed in the regular reflection process or from the compression waves in the shock wave formation process. Both these situations are predictable and caution can be exercised for these cases.

Three methods of extrapolation are commonly used: use of the initial slope, mathematical curve fitting, and graphical methods. The use of the initial slope is treated in Ref. 4, and some inherent mathematical errors

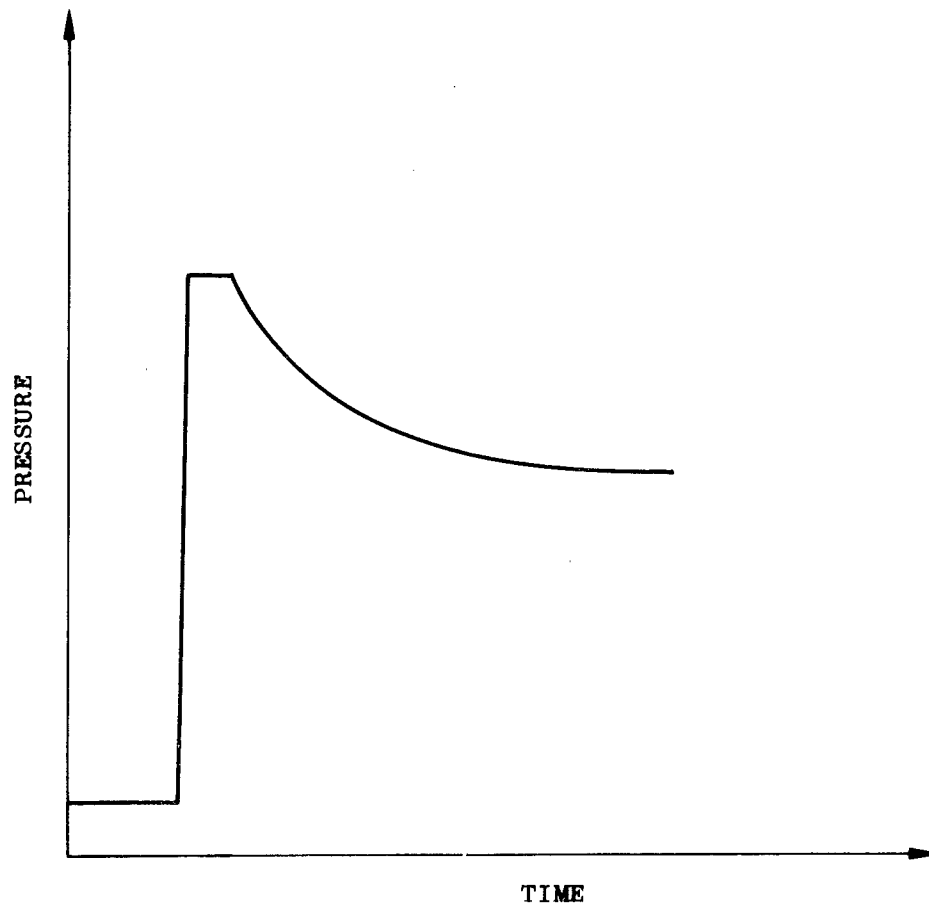


Fig. B-7. Pressure-Time Profile of a Regularly Reflected Shock Wave

are pointed out. A more pronounced problem is created by distortion in the mapped waveform attributable to transducer or the electronic monitoring/recording system characteristics. Since the initial slope method relies on tangency at a point, any minor variations can act as levers for producing a large error in the extrapolation.

An example of this is shown in Fig. B-8. The gages were exposed to identical waves and were monitored with the same electronic system. The differences were the element diameters and the frequency response characteristics of the gage. The BRL-Bar gage is a 2-MHz gage, while the BRL-3 is a 400-kHz gage. The extrapolated peak pressure varies 6.0%.

A better extrapolation method would make use of a longer baseline. Both of the last two methods described are based on this principle. For simplicity's sake, the graphical approach was used in the example shown in Fig. B-9. In this figure the same gage records shown in Fig. B-8 were used, but the wave forms were extrapolated (by means of a French curve) back in time to a point equal to one-half of the crossing-time. The peak pressures agree within 1.8%. The dashed curve represents a shift of the upper curve to compensate for the difference in time scales, since time was measured from the leading edges of the gages. The time shift was determined from the equation

$$\text{Time Shift} = \frac{R_l - R_s}{U} \quad (\text{B.8})$$

or the difference of one-half of the individual crossing times. The remaining deviation between the curves is well within the limits of experimental accuracy.

In the preceding discussion, the incident pressure wave was assumed not to decay in crossing the sensing element. To ascertain the validity of the assumption, an analysis was considered using a wave of constant duration, with a variation only in the peak pressure. Based on these conditions, the mapped

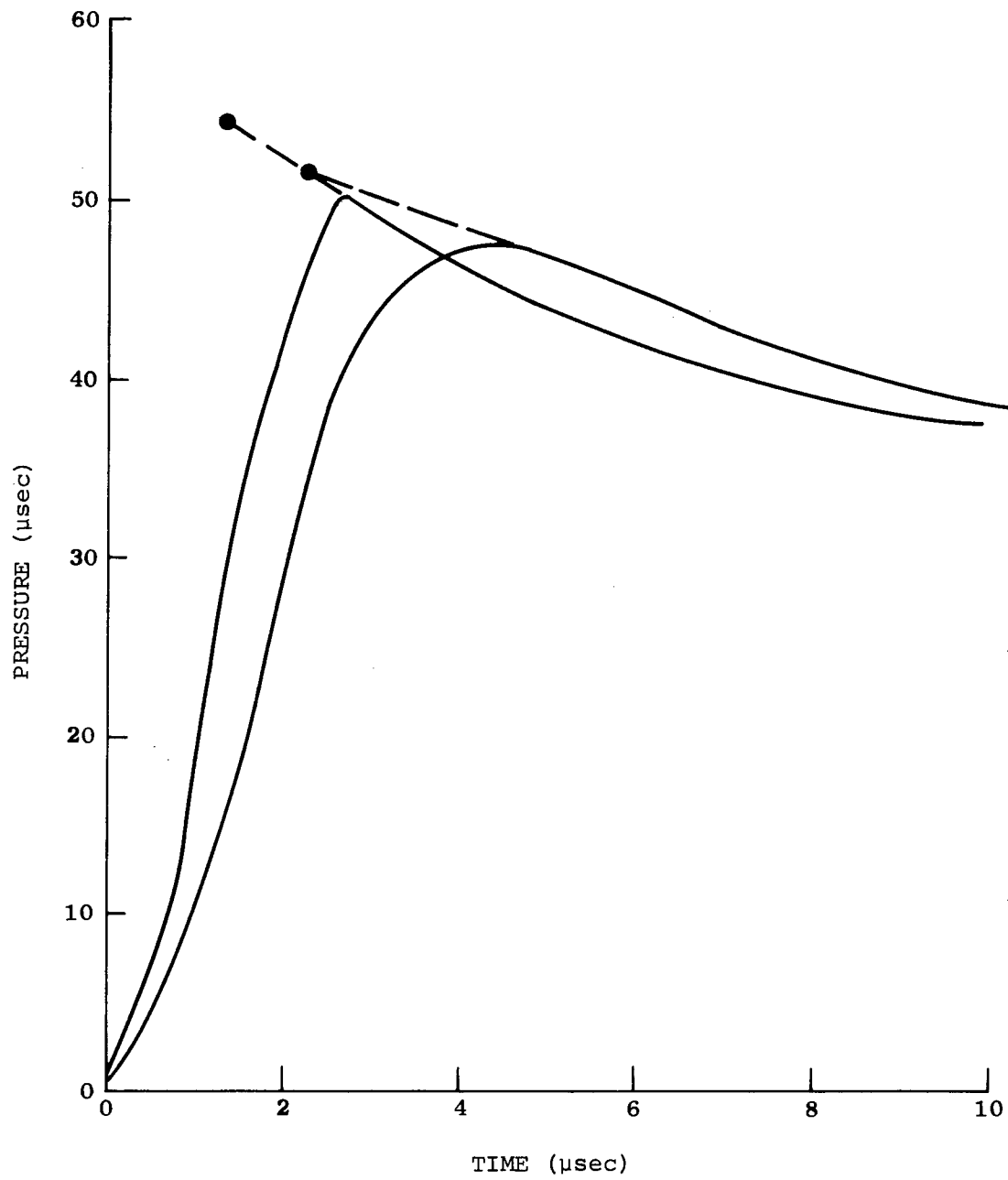


Fig. B-8. Initial Slope Extrapolation

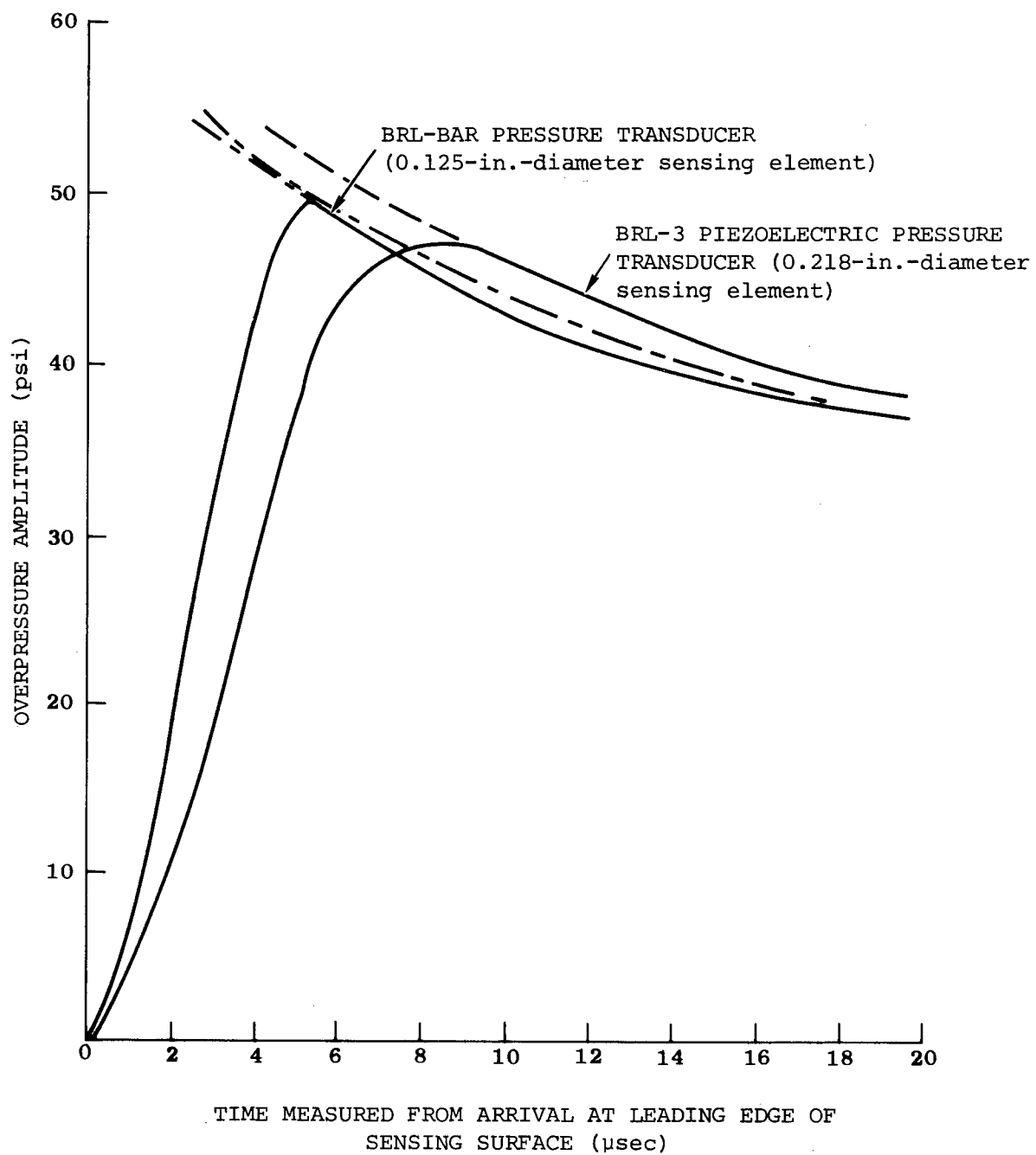


Fig. B-9. Effect of Sensing Element Size on Mapping Profile



pressure profile of a triangularly shaped pressure pulse would be given by

$$p(t) = \bar{p} \left\{ 1 - c \left[ t - \left( 1 - \frac{\alpha}{8} \right) \frac{R}{U} \right] \right\} \quad (\text{B.9})$$

as developed in Exhibit IV, where  $(\alpha)$  is the fractional decay of the peak pressure across the gage. For up to a 10% decay in pressure, there is an approximate 1% change in  $R/U$ , which is not significant to the overall pressure-mapping accuracy. If  $\alpha/8$  is taken as very small, Eq. (B.9) becomes

$$p(t) = \bar{p} \left[ 1 - c \left( t - \frac{R}{U} \right) \right] \quad (\text{B.10})$$

This is the equation for the mapped profile of a triangularly decaying wave. Based on this result, within the range of interest being discussed, any small decay encountered in crossing the element does not significantly affect the mapping of the pressure pulse.

In the discussion to this point, the pressure-time profile has been assumed to be symmetrical about the gage diameter in the direction of the shock wave propagation. If, at a later time, a second rarefaction wave system crosses the gage from another direction and interacts with the initial wave system, then that assumption is in error. The line of action of the pressure would have to be considered in both the  $x$  and  $y$  directions. The volume of the wedge (Figs. B-4 and B-6) and its effect on the composite  $x$  centroid has been shown not to affect the line of action of the average pressure. By the same method it can be reasoned that the  $y$  centroid would not be significantly affected by the incidence of a second rarefaction wave system.

The rate of decay caused by the second rarefaction will not shorten the duration of the incident wave. The averaging process described is then not appreciably affected. Secondly, the slow rates of decay caused by rarefaction systems lend themselves to averaging by the small gage diameters. For these reasons it is concluded that in mapping, only insignificant alteration of the

pressure profile will be created by the incidence of a second rarefaction wave system. If the second wave system were a shock wave, then the technique discussed in the earlier portions of this section would have to be reapplied.

One example of how this analysis can be applied is illustrated by Fig. B-10. The finite crossing-time produces the averaging process in the mapping with a corresponding error in the peak pressure measured. The graph of Fig. B-10 plots this error for a family of wave durations for a linearly decaying pressure as a function of the time required for the shock wave to cross the gage's sensing area.

## CONCLUSIONS

The conclusions to be drawn are based on the following considerations:

1. The sensing element is circular with a diameter between 1/8 and 1/4 in.
2. The duration of any component wave is greater than 50  $\mu\text{sec}$  for a triangular decay and 100  $\mu\text{sec}$  for an exponential decay

These conditions are not particularly restrictive and are met by the average modeled case encountered in the BRL experimental data. Based on these considerations, the following conclusions are made about the mapping of an incident pressure profile given as  $p(t)$ :

- The mapped pressure profile can be described by the relation  $p(t - R/U)$  and acts through the centerline of sensing area
- If the mapped pressure profile is measured from the leading edge of the gage sensing surface, then it is in error  $R/U$  in time in relation to a fixed point on the model
- The peak pressure can best be estimated by extrapolating the mapped pressure-time curve back in time  $R/U$
- The extrapolation of the curve provides a better estimate than use of the initial slope as the extrapolation model

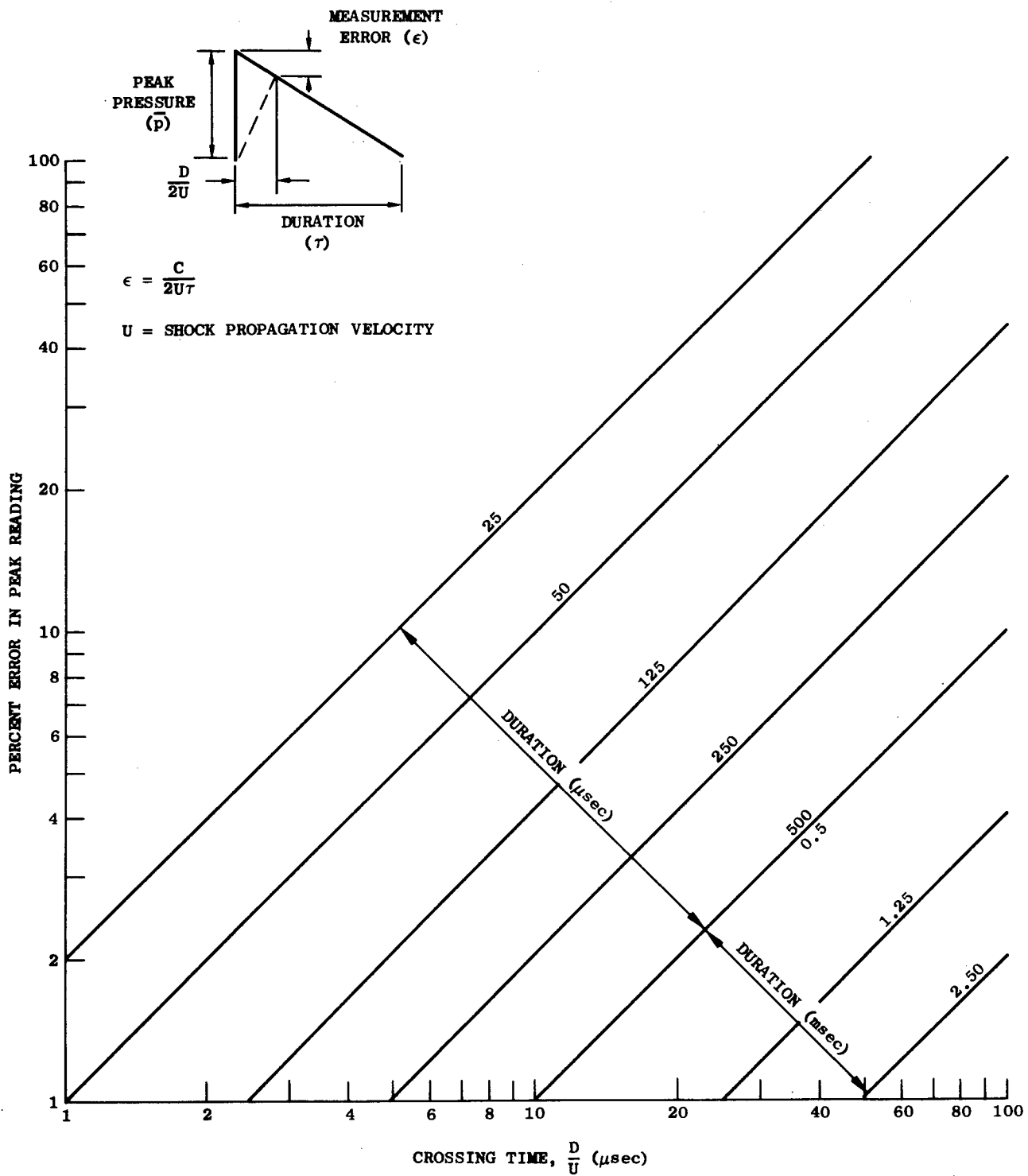


Fig. B-10. Error in Peak Pressure Reading Due to Gage Crossing-Time

- The error introduced by less than a 10% decay in the peak pressure across the gage element is not significant
- The decay in the pressure profile created by the incidence of two rarefaction wave systems from different directions does not alter the previous conclusions.

REFERENCES

1. Kells, L., Analytic Geometry and Calculus, Prentice-Hall, Inc., N.Y., N.Y., 1950
2. Taylor, A., Advanced Calculus, Ginn and Company, N.Y., N.Y., 1955
3. Dwight, H.B., Tables of Integrals and Other Mathematical Functions, Fourth Edition, The MacMillan Company, N.Y., N.Y., 1961
4. Armendt, B.F., et al., The Initial Decay of Pressure Behind a Shock Front: Comparison of Experimental and Calculated Results, BRL-MR-997, Ballistic Research Laboratories, Aberdeen Proving Ground, Md., April 1956
5. Fine, H.G., Calculus, MacMillan Company, N.Y., N.Y., 1932

Exhibit I  
FORCE VOLUME INTEGRATION OF A GENERAL WAVEFORM

For the integration, the general waveform

$$p(t) = \bar{p} \left[ 1 - c \left( t - \frac{x}{U} \right) \right] \exp \left[ -ac \left( t - \frac{x}{U} \right) \right] \quad (I.1)$$

has been selected. The terms are defined as:

- $\bar{p}$  peak overpressure
- $c$  inverse of the duration
- $t$  time
- $x$  distance
- $U$  shock front velocity
- $a$  Friedlander-type constant

All definitions and nomenclature are consistent with the system described in the body of Appendix B.

Substituting Eq. (I.1) into the force volume integral defined in the body of Appendix B gives

$$V_f = 2\bar{p} \exp(-act) \int_0^2 \int_{x_1(y)}^{x_2(y)} \left[ (1 - ct) \exp\left(\frac{acx}{U}\right) + \frac{c}{U} x \exp\left(\frac{acx}{U}\right) \right] dx dy \quad (I.2)$$

If we define

$$z = \frac{V_f}{2\bar{p} \exp(-act)} , \quad w = \frac{ac}{U} , \quad k = \frac{c}{U}$$

and

$$\phi = 1 - ct$$

then Eq. (I.2) can be written as

$$z = \int_0^R \int_{x_1(y)}^{x_2(y)} \left[ \phi \exp(w x) + k x \exp(w x) \right] dx dy \quad (I.3)$$

Integrating with respect to (x) and rearranging gives

$$z = \int_0^R \left[ \left( \frac{\phi}{w} - \frac{k}{w^2} \right) \exp(w x) + \frac{k}{w} x \exp(w x) \right]_{x_1(y)}^{x_2(y)} dy \quad (I.4)$$

and if  $\frac{\phi}{w} - \frac{k}{w^2} = A_1$  and  $\frac{k}{w} = A_2$ , then

$$z = \int_0^R \left[ A_1 \exp(w x) + A_2 x \exp(w x) \right]_{x_1(y)}^{x_2(y)} dy \quad (I.5)$$

Evaluating the bracketed terms,

$$\begin{aligned} A_1 \exp(w x) \Big|_{x_1(y)}^{x_2(y)} &= A_1 \exp(w R) \left[ \exp\left(w \sqrt{R^2 - y^2}\right) - \exp\left(-w \sqrt{R^2 - y^2}\right) \right] \\ &= 2A_1 \exp(w R) \sinh w \sqrt{R^2 - y^2} \end{aligned} \quad (I.6)$$

and

$$\begin{aligned} A_2 x \exp(w x) \Big|_{x_1(y)}^{x_2(y)} &= A_2 \exp(w R) \left\{ R \left[ \exp\left(w \sqrt{R^2 - y^2}\right) - \exp\left(-w \sqrt{R^2 - y^2}\right) \right] \right. \\ &\quad \left. + \sqrt{R^2 - y^2} \left[ \exp\left(w \sqrt{R^2 - y^2}\right) + \exp\left(-w \sqrt{R^2 - y^2}\right) \right] \right\} \\ &= 2A_2 \exp(w R) \left( R \sinh w \sqrt{R^2 - y^2} + \sqrt{R^2 - y^2} \cosh w \sqrt{R^2 - y^2} \right) \end{aligned} \quad (I.7)$$

Equations (I.6) and (I.7) can be substituted into (I.5) to provide

$$z = 2 \exp(wR) \int_0^R \left[ (A_1 + A_2 R) \sinh(w\sqrt{R^2 - y^2}) + A_2 \sqrt{R^2 - y^2} \cosh(w\sqrt{R^2 - y^2}) \right] dy \quad (I.8)$$

Hyperbolic functions can be expanded in series (Ref. 3) as

$$\sinh x = x + \frac{x^3}{3!} + \frac{x^5}{5!} + \frac{x^7}{7!} + \dots$$

and

$$\cosh x = 1 + \frac{x^2}{2!} + \frac{x^4}{4!} + \frac{x^6}{6!} + \dots$$

Combining these expansions with Eq. (I.8) and consolidating terms and letting

$$A_1 + A_2 R = A_3$$

$$z = 2 \exp(wR) \int_0^R \left[ (A_3 w + A_2) (R^2 - y^2)^{1/2} + \left( \frac{A_3 w^3 + 3A_2 w^2}{3!} \right) (R^2 - y^2)^{3/2} \right. \\ \left. + \left( \frac{A_3 w^5 + 5A_2 w^4}{5!} \right) (R^2 - y^2)^{5/2} + \left( \frac{A_3 w^7 + 7A_2 w^6}{7!} \right) (R^2 - y^2)^{7/2} + \dots \right] dy \quad (I.9)$$

Integrating Eq. (I.9), evaluating at the limits, and rearranging terms provides

$$p(t) = \bar{p} \exp \left[ -ac \left( t - \frac{R}{U} \right) \right] \left[ (A_3 w + A_2) + \left( \frac{A_3 w^3 + 3w^2 A_2}{2! 2^2} \right) R^2 + \left( \frac{A_3 w^5 + 5w^4 A_2}{4! 2^3} \right) R^4 \right. \\ \left. + \left( \frac{A_3 w^7 + 7w^6 A_2}{6! 2^4} \right) R^6 + \dots \right] \quad (I.10)$$



which can be shown to equal

$$p(t) = \bar{p} \exp \left[ -ac \left( t - \frac{R}{U} \right) \right] \left\{ 1 - c \left( t - \frac{R}{U} \right) + R^2 \left[ \frac{w[\phi + k(wR + 3)] - k}{8} \right. \right. \\ \left. \left. + \frac{R^2[w^3(\phi + wR + 5)] - k}{192} + \dots \right] \right\} \quad (I.11)$$

Approximate maximum values of the constants would be

$$c = 10^4 \text{ sec}^{-1}$$

$$U = 10^3 \text{ feet per second}$$

$$R = 10^{-2} \text{ feet}$$

and assuming a value of  $a$  equal to 1, then

$$k = w = 1$$

For these values, the terms in the series of Eq. (I.11) after the first term are seen to add a negligible amount, and Eq. (I.11) can be written as

$$p(t) = \bar{p} \exp \left[ -ac \left( t - \frac{R}{U} \right) \right] \left[ 1 - c \left( t - \frac{R}{U} \right) \right] \quad (I.12)$$

Exhibit II  
CENTROID LOCATION

The centroid of the force volume  $V_f$  for a triangularly decaying wave can be defined by use of a triple integral (Ref. 2). The centroid is needed to be known in the  $x, y$  plane. Since the  $y = 0$  plane is a plane of symmetry, it contains the centroid (Ref. 5), thus the problem is to find the  $x$  coordinate  $\bar{x}$ . The centroid  $\bar{x}$  is defined by

$$V_f \bar{x} = 2 \int_0^R dy \int_{x_1(y)}^{x_2(y)} dx \int_0^{\bar{p} \left[ 1 - c \left( t - \frac{x}{U} \right) \right]} x dz \quad (II.1)$$

The parameters used are consistent with those outlined in Exhibit I. The integration yields

$$\bar{x} = \frac{\bar{p} \pi R^3 \left[ (\phi + kR) + \frac{kR}{6} \right]}{V_f} \quad (II.2)$$

where  $\phi = 1 - ct$ , and  $k = c/U$ .

The force volume  $V_f$  is described by

$$\pi R^2 \left[ p_1 + \frac{1}{2} (p_2 - p_1) \right] = \frac{\pi R^2}{2} (p_1 + p_2) \quad (II.3)$$

and

$$\bar{x} = \frac{2\bar{p}R \left( \phi + \frac{7}{6} kR \right)}{p_1 + p_2} \quad (II.4)$$

where

$$p_1 = \bar{p}(1 - ct) \quad \text{and} \quad p_2 = \bar{p} \left[ 1 - c \left( t - \frac{2R}{U} \right) \right]$$

Algebraically this reduces to

$$\bar{x} = \frac{R \left[ (1 - ct) + \frac{7}{6} \frac{cR}{U} \right]}{\left[ (1 - ct) + \frac{cR}{U} \right]} \quad (\text{II.5})$$

## Exhibit III

## GENERAL CASE OF CENTROID OF FORCE VOLUME

The centroid of the force volume (Figs. B-4 and B-6) in the x,y plane will determine the line of action in the z direction of the average pressure mapped by the transducer. If a plane of symmetry exists, then the centroid must lie on it (Ref. 5). For the cases being considered, the x,y plane for  $y = 0$  is a plane of symmetry; thus one coordinate of the centroid is  $x, y = 0$ . The x coordinate of the centroid  $\bar{x}$  can be given by

$$\bar{x} = \frac{\bar{x}_w V_w + R V_c}{V_f} \quad (\text{III.1})$$

as defined in Fig. B-8. Substituting in the values for  $V_w$ ,  $V_c$ , and  $V_f$  in Eq. (III.1) gives

$$\bar{x} = \frac{x_w \left( \frac{p_2 - p_1}{2} \right) + R p_1}{\frac{p_2 - p_1}{2} + p_1} \quad (\text{III.2})$$

The worst possible case has  $\bar{x}_w = 2R$  which reduces Eq. (III.2) to

$$\bar{x} = R \left[ \frac{p_1 + (p_2 - p_1)}{p_1 + \left( \frac{p_2 - p_1}{2} \right)} \right] \quad (\text{III.3})$$

or

$$\bar{x} = R \left( \frac{2p_2}{p_1 + p_2} \right) \quad (\text{III.4})$$

## Exhibit IV

## DECAY OF STRENGTH ACROSS THE SENSING ELEMENT

Assume the peak pressure  $p_K$  varies with distance  $x$  across an element's width of radius  $R$  according to the relation

$$p_K = \bar{p} \left( 1 - \frac{\alpha x}{2R} \right) \quad (\text{IV.1})$$

where  $\bar{p}$  is the peak incident pressure. Let  $\alpha$  be the fractional spatial decay observed, and further assume no change in wave duration. A triangularly decaying wave would then be given by

$$p(t) = \bar{p} \left( 1 - \frac{\alpha x}{2R} \right) \left[ 1 - c \left( t - \frac{x}{U} \right) \right] \quad (\text{IV.2})$$

If we use the force-volume integral described in the discussion of the body of this report, then

$$V_f = 2 \int_0^R \int_{x_1(y)}^{x_2(y)} \bar{p} \left[ 1 - c \left( t - \frac{x}{U} \right) \right] dx dy - 2 \int_0^R \int_{x_1(y)}^{x_2(y)} \frac{\alpha \bar{p} x}{2R} \left[ 1 - c \left( t - \frac{x}{U} \right) \right] dx dy \quad (\text{IV.3})$$

By the techniques applied in Exhibit I the expression for  $p(t)$ , the average sensed pressure, can be shown to be

$$p(t) = \bar{p} \left\{ 1 - c \left[ t - \left( 1 - \frac{\alpha}{8} \right) \frac{R}{U} \right] \right\} \quad (\text{IV.4})$$

## Appendix C

## PRESENTATION OF PRELIMINARY URS SHOCK TUNNEL TEST DATA

The data on the air-blast-induced flows in full-scale rooms to be discussed in this appendix were collected from tests in the URS shock tunnel. The aim of these tests was to evaluate the potential of the shock tunnel for aerodynamic testing and to recommend changes for more closely meeting future OCD test requirements. The findings reported herein are oriented toward the evaluative task of this study. An evaluation of the tunnel and of the subsequent improvements to the test procedures is being considered in another work unit and will not be included in this discussion.

The room geometry of the two-dimensional test (the only one to be considered herein) is shown in Fig. C-1. The geometry and wave form monitored at Station 1 were reproduced in the FLIC code as boundary and initial conditions. A direct comparison between full-scale experiment and numerical simulation could then be made.

The first section of data to be presented is the pressure-time histories monitored in the room, the second section will consist of flow data. Variations between the experimentally and the numerically derived data will be pointed out and then will be explained individually. It should be noted that the tests were run for tunnel evaluation purposes and, hence, the data are not representative of the results gained in present test series. Since limited full-scale data exist, and those data are not well documented generally, it was decided to make use of the available preliminary data from the tunnel.

Data from two tests were used. The first test was the room shown in Fig. C-1, and the second was the same situation without a rear wall. The data presented for the downstream side of the front wall were taken from tests with no rear wall. The data for the front wall cannot be directly compared with the numerical simulations for the full time range recorded. The

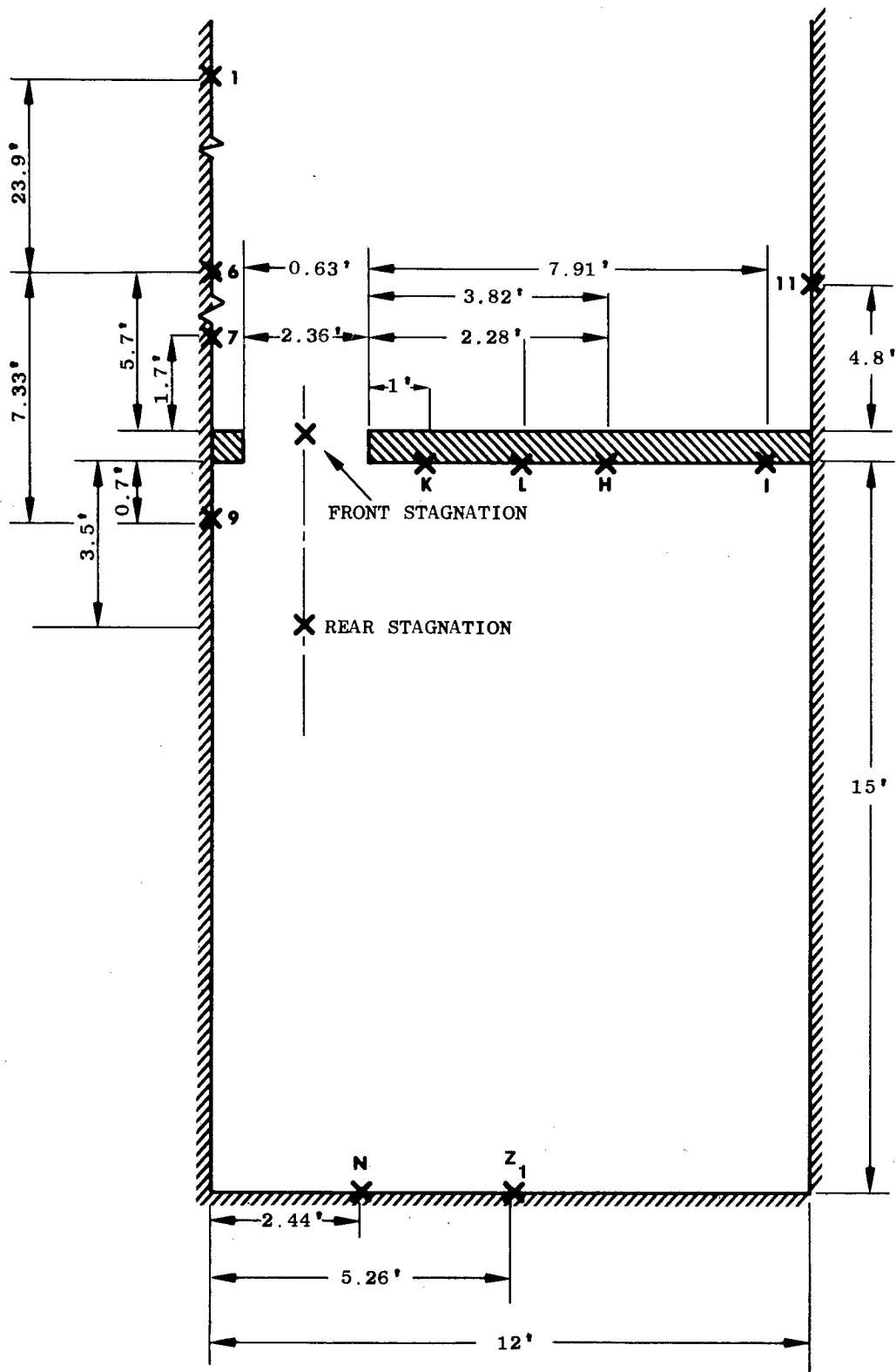


Fig. C-1. Layout of Shock Tunnel Test

comparison becomes invalid at that point in time when the rear of the front wall senses the presence of the rear wall (approximately 2 traverse times of a sound wave across the chamber).

In the second test, the input wave overpressure was lower, although a similar charge of primacord\* was used in the compression chamber. The pressure-time records presented were adjusted accordingly by linear extrapolation. The normalizing factor used was the ratio of shock front overpressures monitored at Station 6. There is some error involved in using this simple adjustment to the same input condition; but, considering the accuracy of the data, it did not seem cost-effective to be any more elaborate.

A moderately good agreement between numerical and experimentally produced pressure-histories can be noted at the input Stations 6, 7, and 11 (Figs. C-2 and C-3). Variations later in the histories can be noted which correspond to a 10 to 20 percent lower experimentally determined pressure at fixed times. Excellent agreement was reached for the first 20 msec of each trace, though the values monitored were also lower in this range (generally about 10 percent). The absolute experimental accuracy was 10 to 15 percent; hence it is difficult to fully ascribe the cause of the variations to the code.

Station 9, just inside the doorway, also showed good agreement between experiment and numerical simulation for about 20 msec. At about 30 msec the increase in pressure monitored in the experimental trace tapered off to a 3 psi plateau. This measurement is not considered valid since an external overpressure in excess of 6.5 psi was monitored up to about 60 msec. Filling

---

\* Primacord is manufactured for wave-propagation characteristics; hence the primary manufacturing controls are not for equal charge weights per unit length. The resulting pressures developed by two different lots vary. Since the tests were 6 months apart, the primacord differed; hence equal quantities did not produce driven shock waves of equal strength.



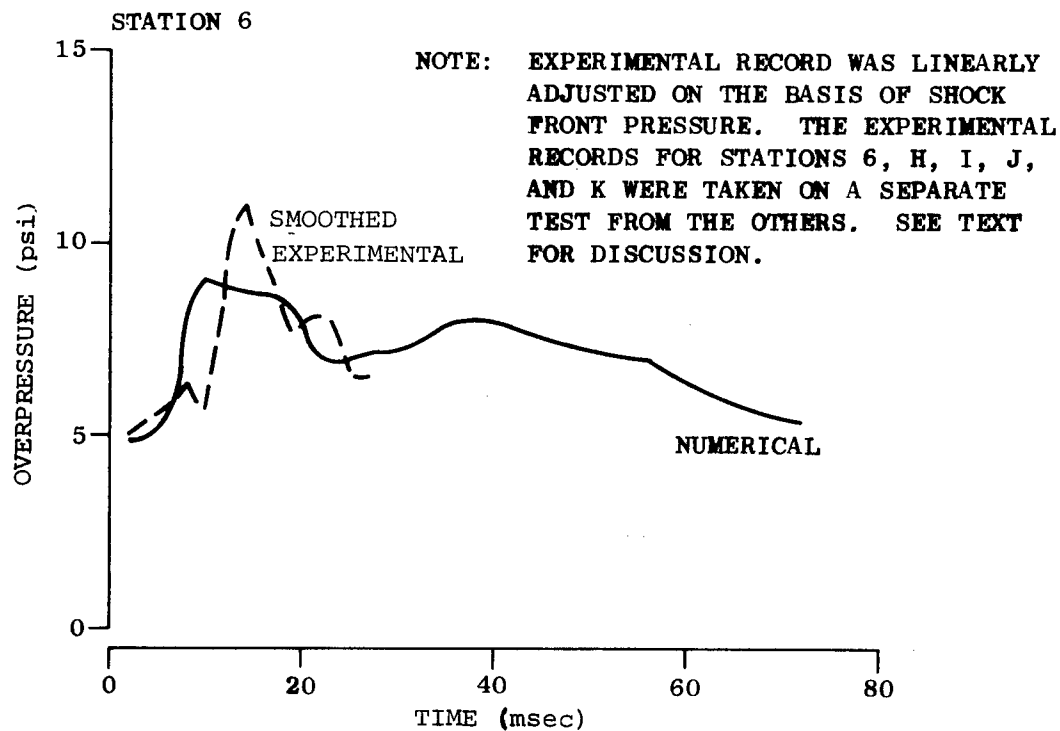
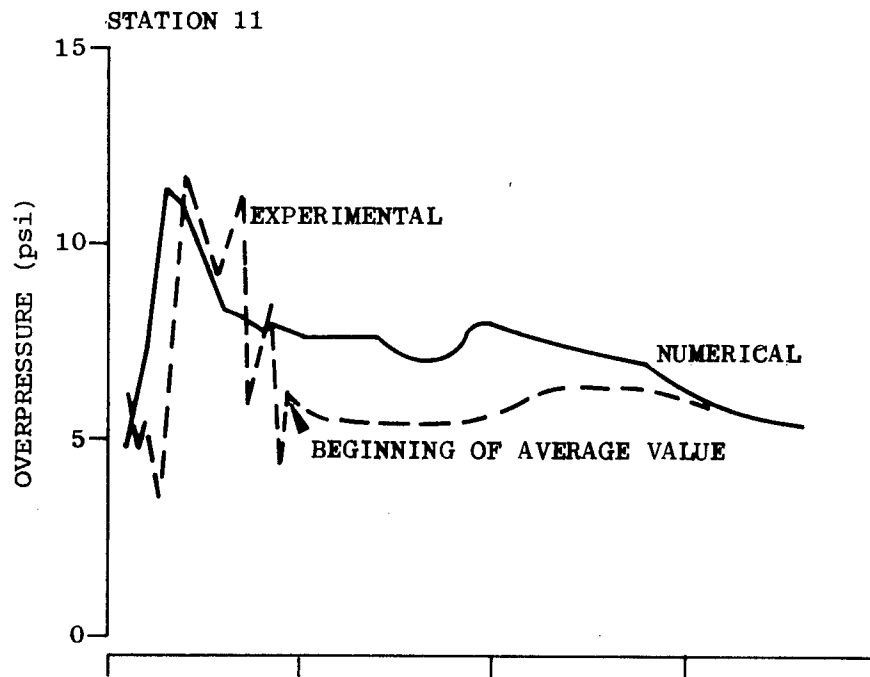


Fig. C-2. Pressure-Time Histories, Stations 6 and 11

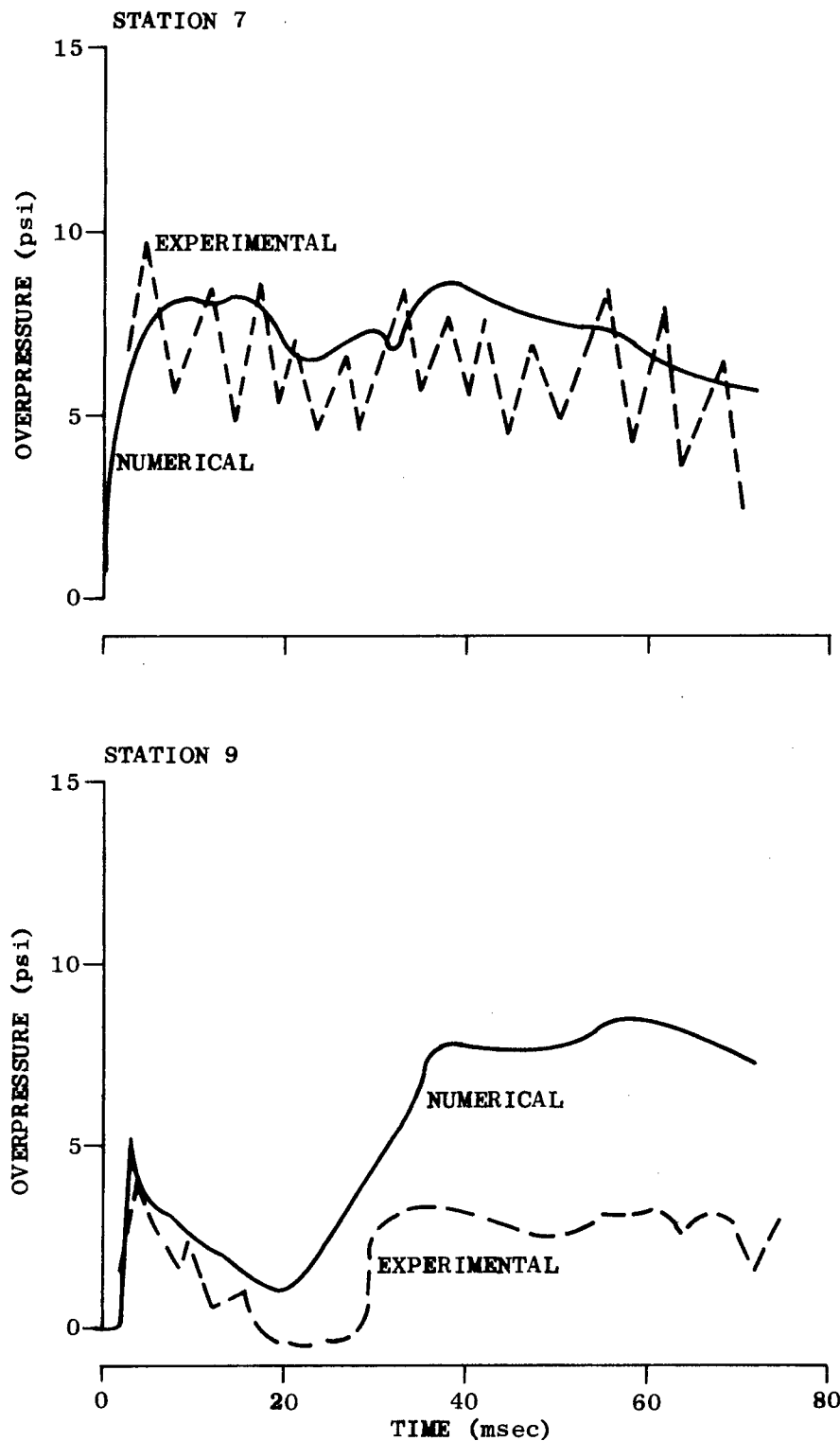


Fig. C-3. Pressure-Time Histories, Stations 7 and 9

of the chamber should have continued and the internal pressure should have increased to the external value. Otherwise a 3.5-psi discontinuity would have to exist between Stations 7 and 9 (a distance of 3.4 feet) and this is a physical impossibility.

A similar problem was noted for Station Z on the rear wall. The monitored pressure stayed at about 4 psi after 35 msec. A break in the monitoring history can be noted at about 35 msec, which indicates a recording or monitoring system malfunction may have occurred at that time.

Station N showed a much better agreement over the full range than did Station Z (Fig. C-4). The rarefaction trough in the 40-msec range was not reproduced as faithfully, and the characteristically lower experimental value again occurred. Also, the disparities in the pressure values yielded by the two methods are in the range of experimental error. If the input pressure history was lower (after 30 msec) in the experimental case, as indicated, the internal pressures must be accordingly reduced.

The break in the monitored history, similar to that seen at Station N on the rear wall, was also seen in Stations H, I, K, and L on the rear of the front wall (Figs. C-5 and C-6). Stations H and K do show good agreement for about 30 msec, however. The disruption of recording was traced to cable-noise problems although the conditions previously noted also contributed.

The two stagnation probes recorded for about 20 msec before being destroyed as illustrated in their pressure-time histories presented in Fig. C-7. The stagnation values recorded (essentially the sum of dynamic and "side-on" pressures) compared well with the code for this period, an indication that the code was predicting the flow as well as the pressure within at least a 15 percent value (assuming the experiment was correct).

One major variation between the simulation and the experiment was the loss of the door jamb in the experiment. The high-intensity flows tore the wooden jamb from the steel frame, which caused a partial disruption of the

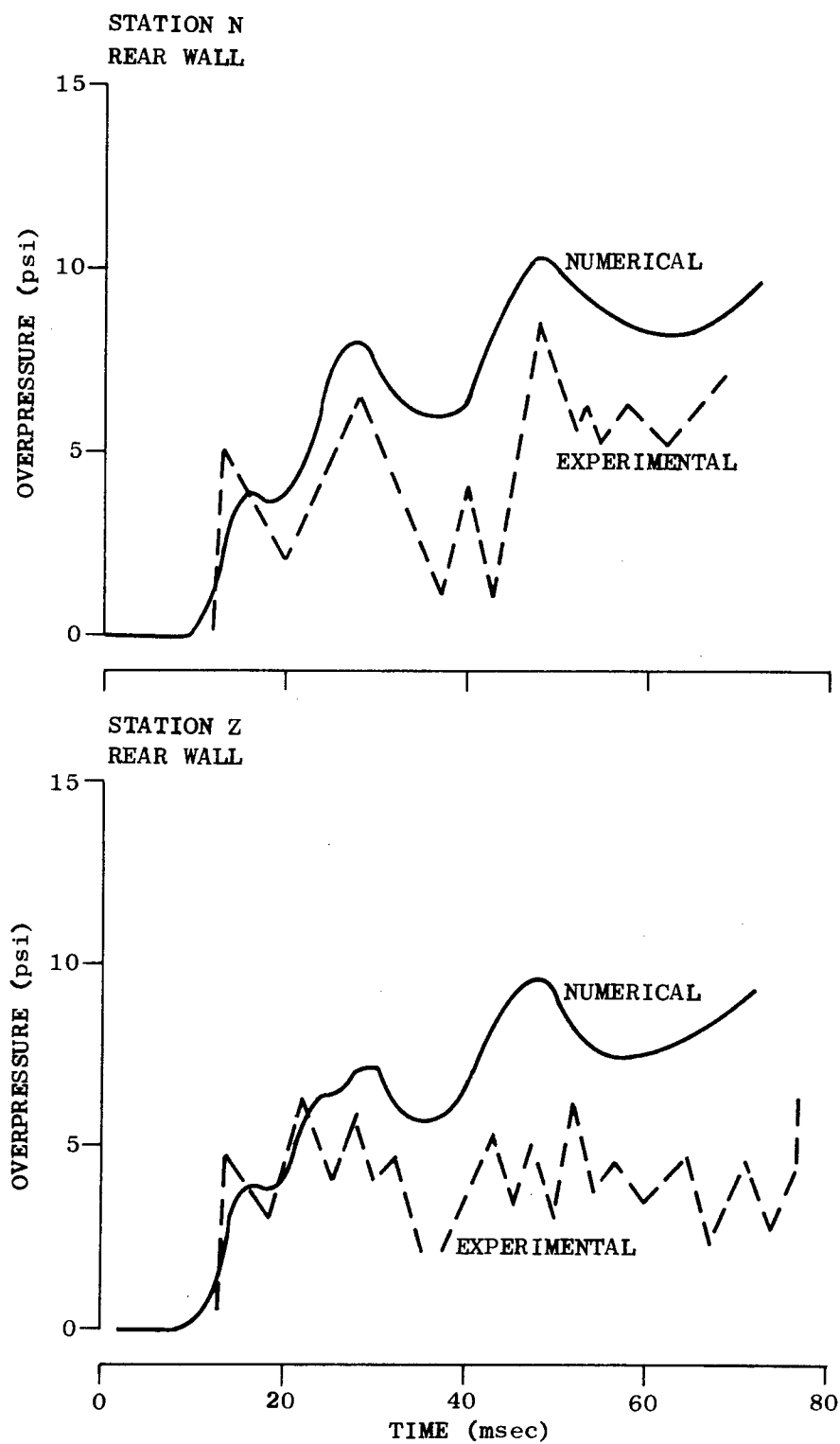


Fig. C-4. Pressure-Time Histories, Stations N and Z

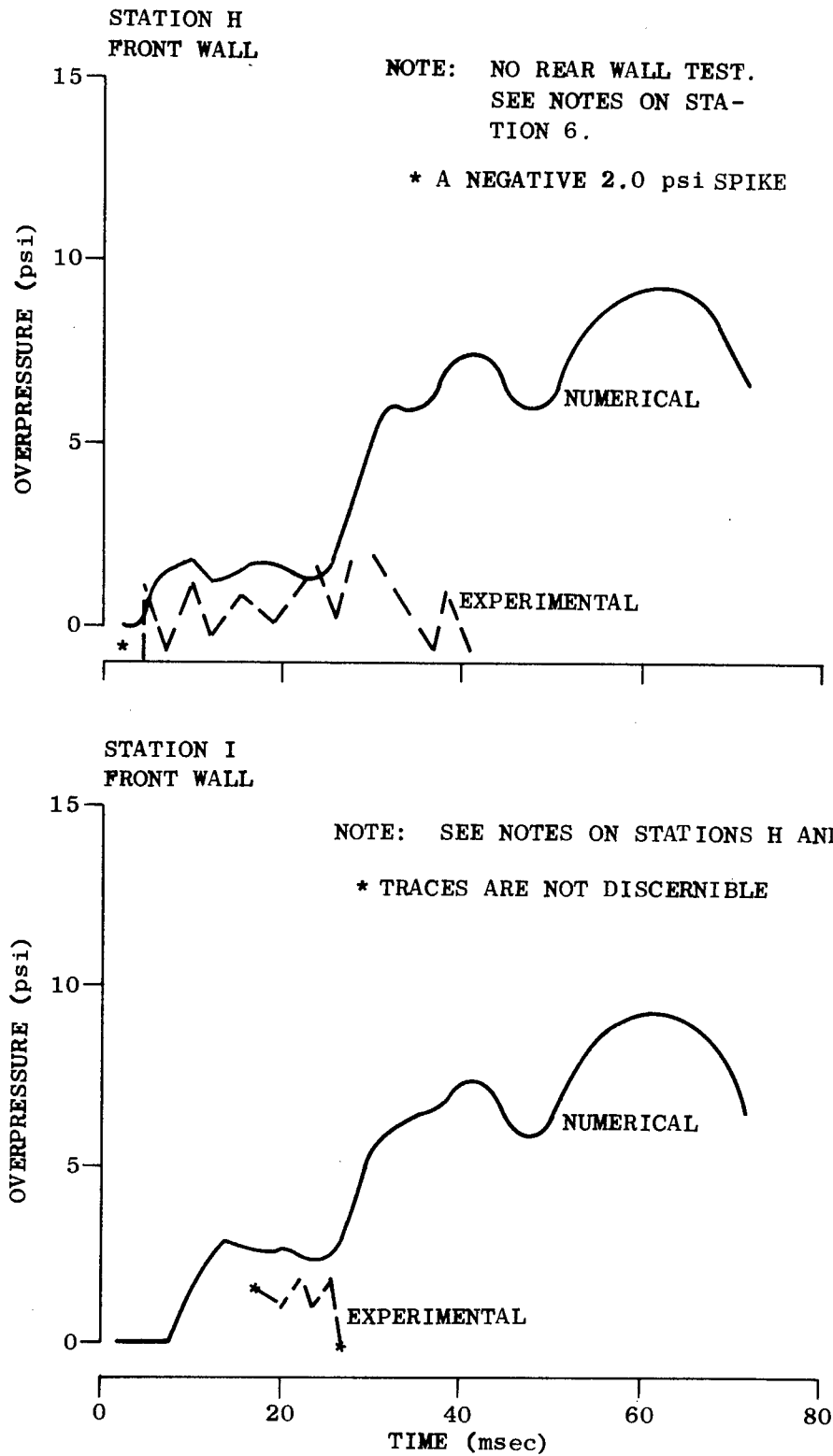


Fig. C-5. Pressure-Time Histories, Stations H and I

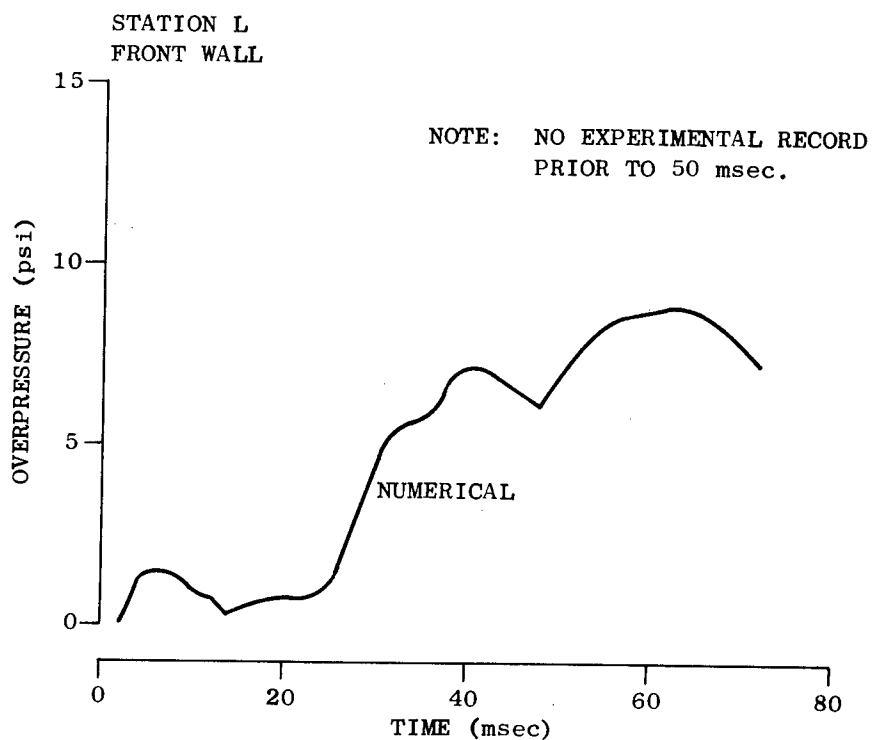
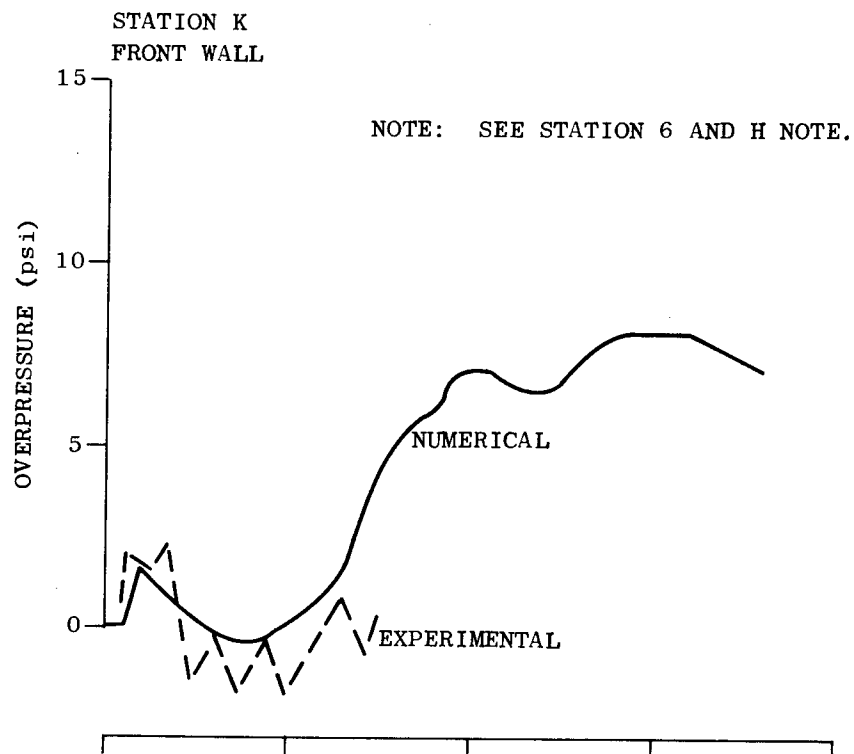


Fig. C-6. Pressure-Time Histories, Stations L and K

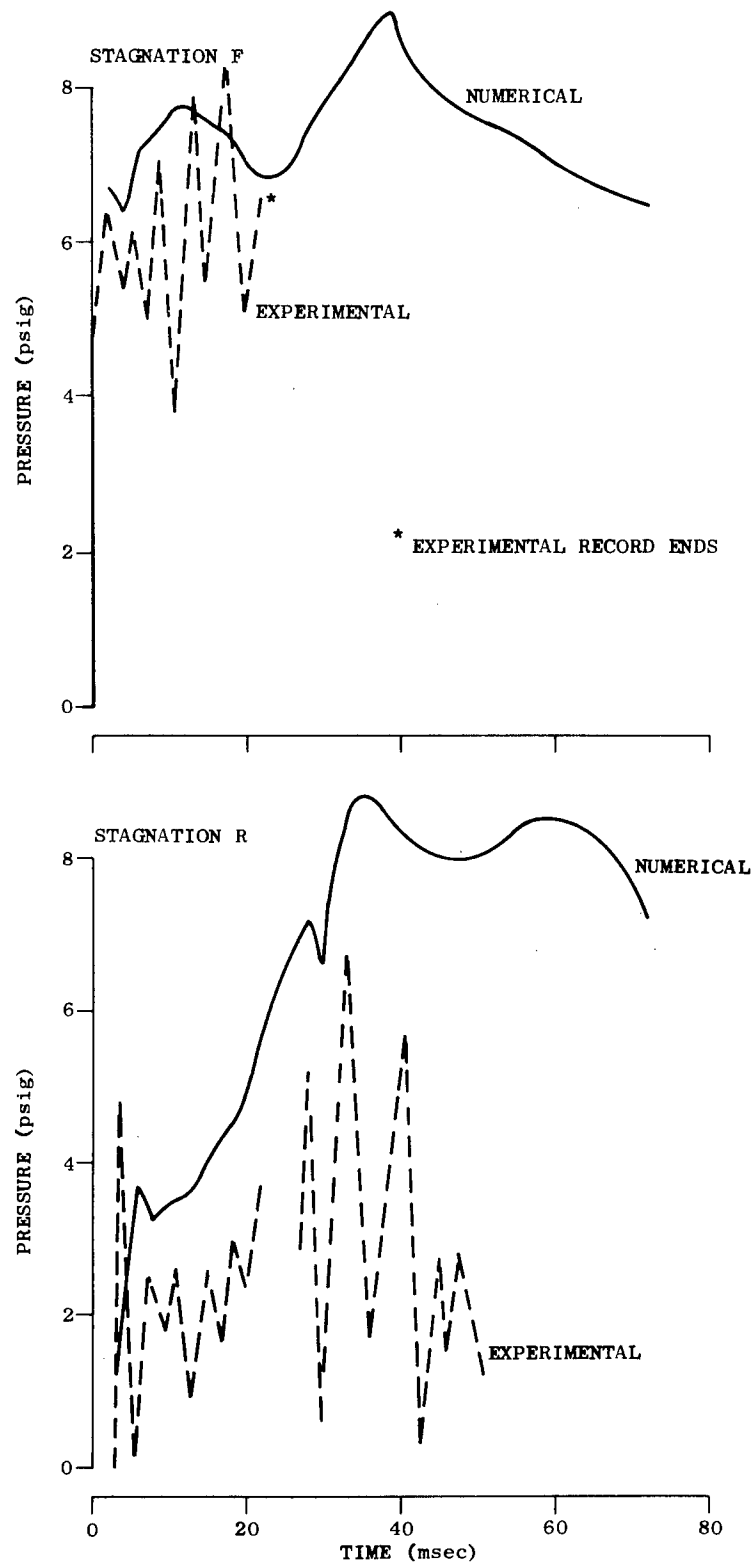


Fig. C-7. Stagnation Pressure-Time Histories, Stations Rear (R) and Front (F)

flow and may have been responsible for some of the deviations in the presented histories. The exact value of the error was not estimated because of the complexity of such a procedure and because, in the time frame used in the comparison, the perturbations produced by the error were relatively small.

Flow visualization in the two-dimensional room was accomplished by means of ping pong balls and cloth flags placed throughout the room. A three-dimensional room in which a window replaced the door was also tested, but the data from it will not be discussed here. The data from the three-dimensional room were superior to those from the two-dimensional case and were used in establishing the data reduction procedures. They were also used in the data reduction process to check for errors, because similar flows occurred in both situations.

The raw data were in the form of a series of pictures taken with two cameras. The location of the cameras and the ping pong balls are shown in Fig. C-8. The arrival of the shock wave was monitored by the movement of cloth flags along the roof of the room. Distances were measured by means of vertical and horizontal grids on each wall. In the film plane, the balls appear against the background of the grids. The true spatial positions of the balls were established from the geometry of the two camera projections (congruent triangles).

The tests were originally planned as preliminary trials for another OCD work unit, as previously discussed. The data of use to the computer evaluation effort of this work unit were removed and adapted for present use. The data reduction and evaluation techniques being developed for that work unit were used in their preliminary form with some adaptations.

The first test was the two-dimensional configuration. Lighting difficulties were encountered and were corrected for the second test, the three-dimensional window configuration. Since the numerical simulation evaluations needed two-dimensional data, the poorer test had to be used. The motion of only three balls could be continuously followed for a sufficient



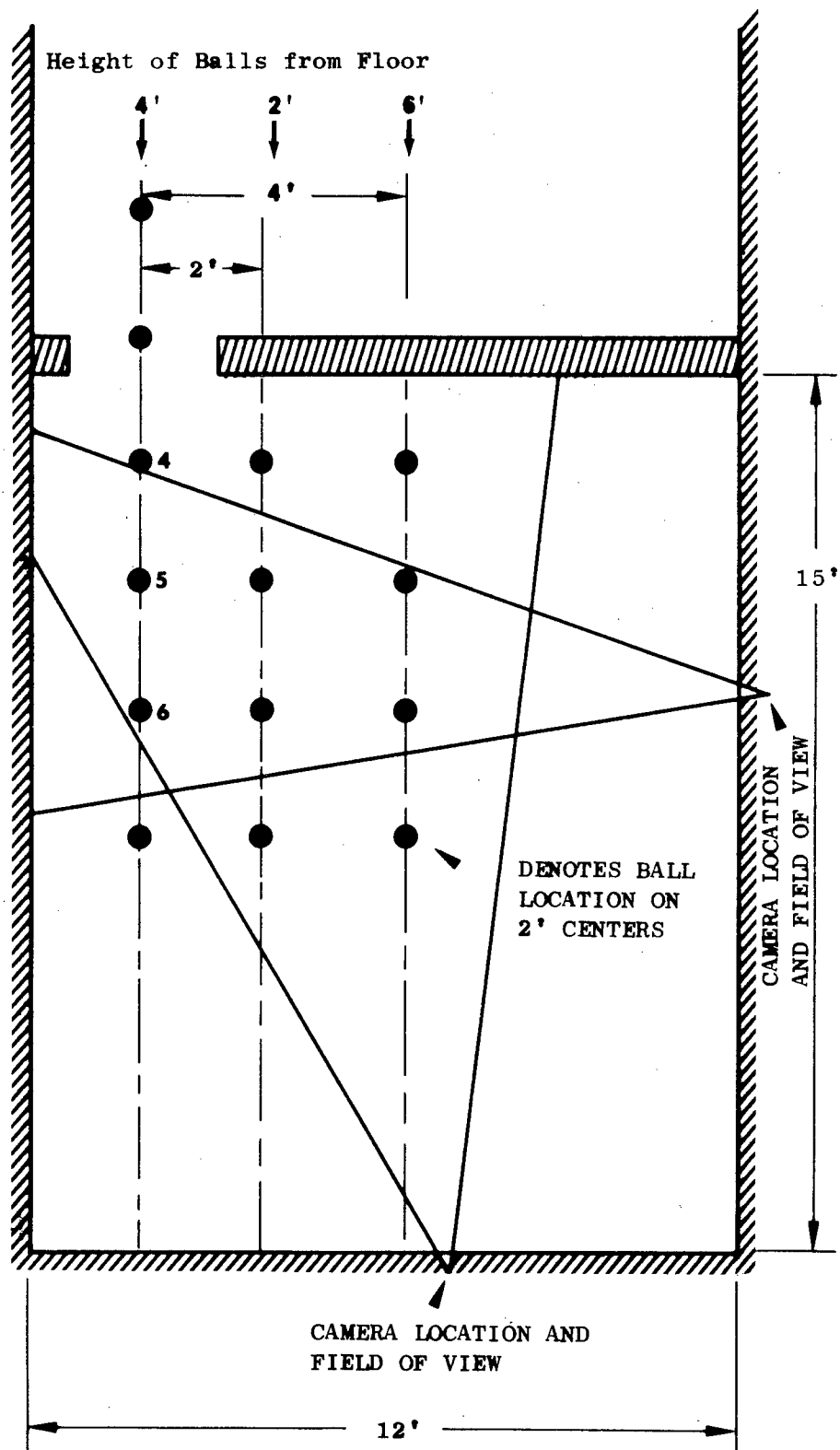


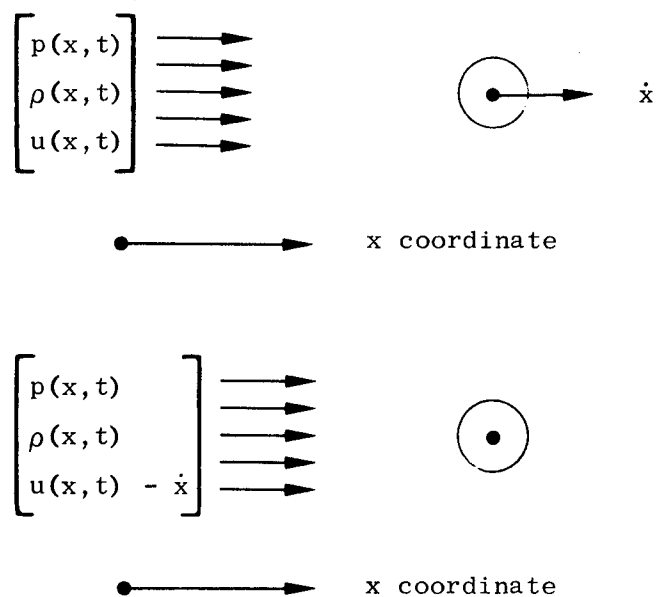
Fig. C-8. Layout of Shock Tunnel for Flow Visualization Tests

period to provide the raw data to establish their trajectories. Additional qualitative data were, however, evolved for short time spans during the flow history. Though useful in developing the conceptual model of the flow, the short-time-span data will not be used to develop quantitative information on the flow.

The trajectories of ping pong balls, though indicating the flow direction and magnitude, are not a direct measure of the flow velocity. As a guide to understanding the underlying process, the question of how rapidly a ping pong ball can be accelerated by the "jet" flows was considered. The acceleration determines what fraction of the particle velocity of the flow the ball will attain as a function of time. These acceleration curves will provide some insight into what the magnitude of the driving flows must be in order to obtain the monitored ball translation velocities.

The physical model of the acceleration process is simply a Newtonian force balance on the target ball. The force is provided by the drag of the flow field surrounding the ball, i.e., the flow velocity experienced by the ball is relative to itself, not to laboratory coordinates. The entire system can be transformed to the fixed laboratory coordinates simply by defining the driving flow in terms of the velocity differential between the flow and the sphere. The system is presented in Fig. C-9.

Equation (C.3) is nonlinear both in  $x$  and  $t$  (see Fig. C-9). For illustrative purpose, assume a step wave is incident on a target ball.



$$F = \left\{ \frac{1}{2} \rho(x, t) [u(x, t) - \dot{x}]^2 \right\} C_D A \quad (C.1)$$

$$F = m \frac{d\dot{x}}{dt} \quad (C.2)$$

$$\frac{d\dot{x}}{dt} = \frac{1}{2} \rho(x, t) [u(x, t) - \dot{x}]^2 \frac{C_D A}{m} \quad (C.3)$$

Fig. C-9. A Schematic of the Sphere Flow Field Interaction

For this case, Eq. (C.3) can be written (for all  $t \geq 0$ ) as

$$\frac{d(\dot{x})}{dt} = \frac{1}{2} \rho [u - \dot{x}]^2 \left( \frac{C_D A}{m} \right) \quad (C.4)$$

assuming  $C_D$  is a constant. Ahlers (Ref. 36) considered Eq. (C.4) to be of the Ricatti type and solved it by a transformation of coordinates. For the

step conditions assumed, Eq. (C.4) can be directly integrated without any substitutions. Using either method, the solution to Eq. (C.4) can be shown to be (using Ahler's nomenclature)

$$\dot{x} = u + \frac{C_3 \beta}{1 + C_3 t} \quad (C.5)$$

and

$$x = C_4 + ut + \beta \ell_n (1 + C_3 t) \quad (C.6)$$

where  $C_3$  and  $C_4$  are constants of integration and

$$\beta = \frac{-2}{r \left( \frac{AC_D}{m} \right) \rho} \quad (C.7)$$

The value of  $r$  equals  $-1$  if  $\dot{x} \geq u$  and equals  $+1$  if  $\dot{x} \leq u$ .

In his work, Ahlers further considered the case in which  $\rho$ ,  $u$ , and  $p$  were not invariant with  $x$  and  $t$ . The previous solution is invalid for spatial and temporal variations in thermodynamic and flow properties. Ahlers' approach was to represent the above solution in a difference format. The differencing steps in this format could be selected so that average values of  $\rho$  and  $u$  over the time step could be used without introducing significant errors. The following equations present Ahlers' difference equations with errors in the original work corrected.

$$\dot{x}_{m+1} = u_m + \frac{(\dot{x}_m - u_m) \beta_m}{\beta_m + (\dot{x}_m - u_m) \Delta t} \quad (C.8)$$

$$x_{m+1} = x_m + u_m \Delta t + \beta_m \ell_n \left( 1 + \frac{\dot{x}_m - u_m}{\beta_m} \Delta t \right) \quad (C.9)$$

One added variable, which is part of the term  $\beta_m$ , is the drag coefficient. The values of the drag coefficient for a sphere are presented in Fig. C-10 as a function of flow Mach number. As the space-time variations in the flow occur, the corresponding corrections in the drag coefficient must be made.

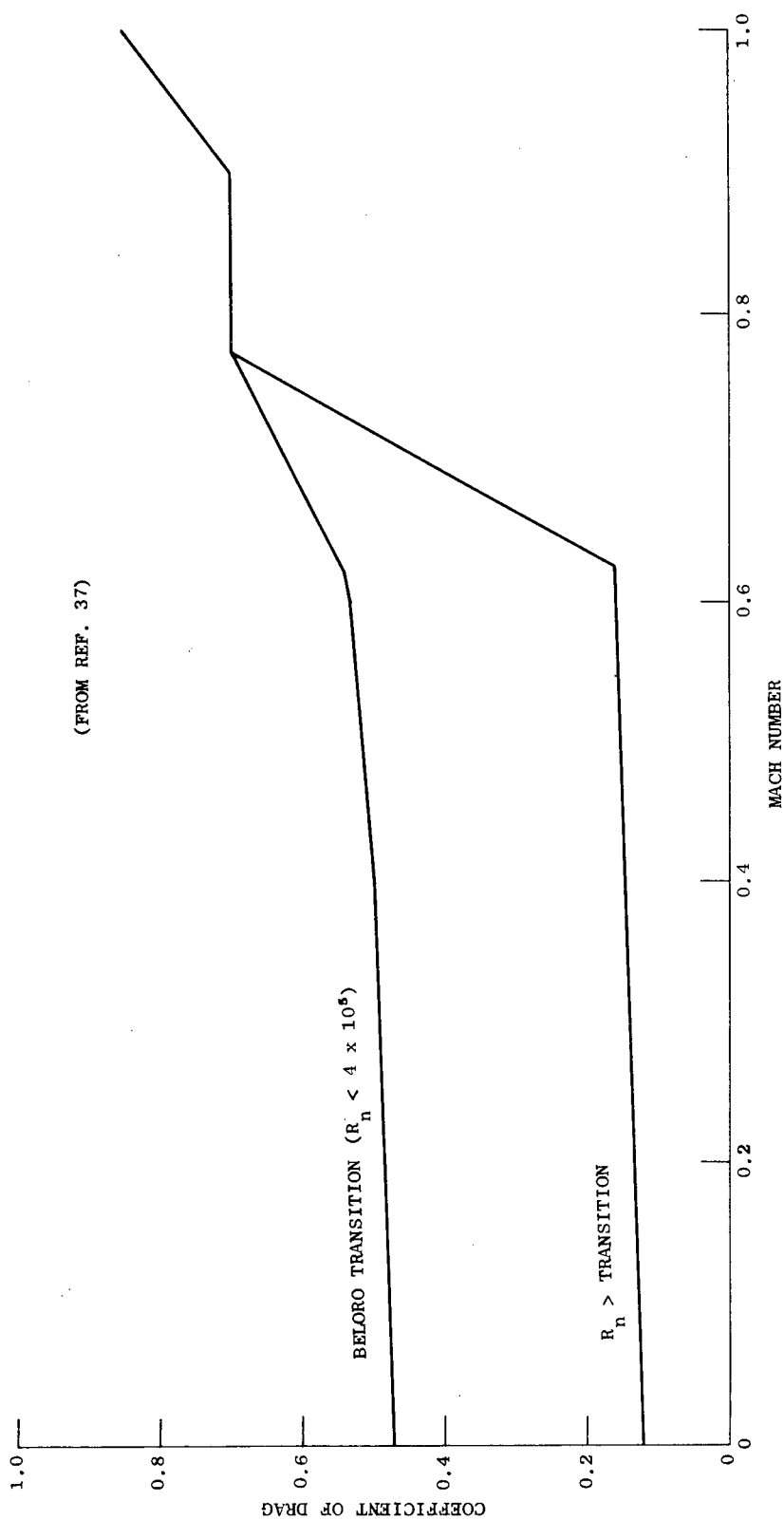


Fig. C-10. Drag Coefficient for a Sphere

A branch in the curve can be noted at a Mach number of approximately 0.775. The branching is dependent upon whether turbulent or laminar flow occurs. The transition Reynolds number is  $4 \times 10^5$ . If the inflow velocities range from 100 to 1000 fps at standard sea level densities and temperatures, then  $R_n$  would vary from  $7.8 \times 10^4$  to  $7.8 \times 10^5$ , which includes the transition between laminar and turbulent flow.

Before making the comparison of numerical and experimental simulations, the original consideration of the acceleration time of the ping pong balls to a step drag profile will be discussed. The profile selected will be for a jet of fluid with the conditions described in Ref. 2 for free-flow jets initiated by a shock wave impinging on a chamber. From these values, the time it takes a ping pong ball to reach a percentage of the flow speed (U) can be calculated using Eq. (C.9) and the drag coefficients presented in Fig. C-10. A constant density and viscosity were assumed corresponding to a fully expanded flow. The drag coefficients were based on calculated values of Reynolds and Mach numbers for the flow in each time step. The computations were made using a short computer program which selected the proper drag coefficient based on Mach and Reynolds numbers and then used these values to calculate velocity data. The results are presented in the curves in Fig. C-11.

These curves provide some interesting insights into the motion of the balls. The rather long acceleration times and the asymptotic behavior of the balls' velocity-time profile reflects the decreasing driving force as the balls approach flow velocity. At 10 msec, the balls are at 25 to 40 percent of the free-stream particle velocity; at 100 msec, the balls are 75 to 85 percent of the particle velocity; and at 1 sec about 97 percent of the particle velocity. The crossing of the curves for  $\Delta P = 9$  and 12 psi and some of the inflections in the curves correspond to changes in the drag coefficient created by transitions from laminar to turbulent flow as defined by the flow Mach number and Reynolds number. Though not a precise prediction procedure, the test for the drag conditions is considered sufficiently accurate for the exploratory and explanatory purposes of this study.

In reviewing the equations and the curves for the drag coefficient, the question arises: If the trajectory of the target object is known, can the

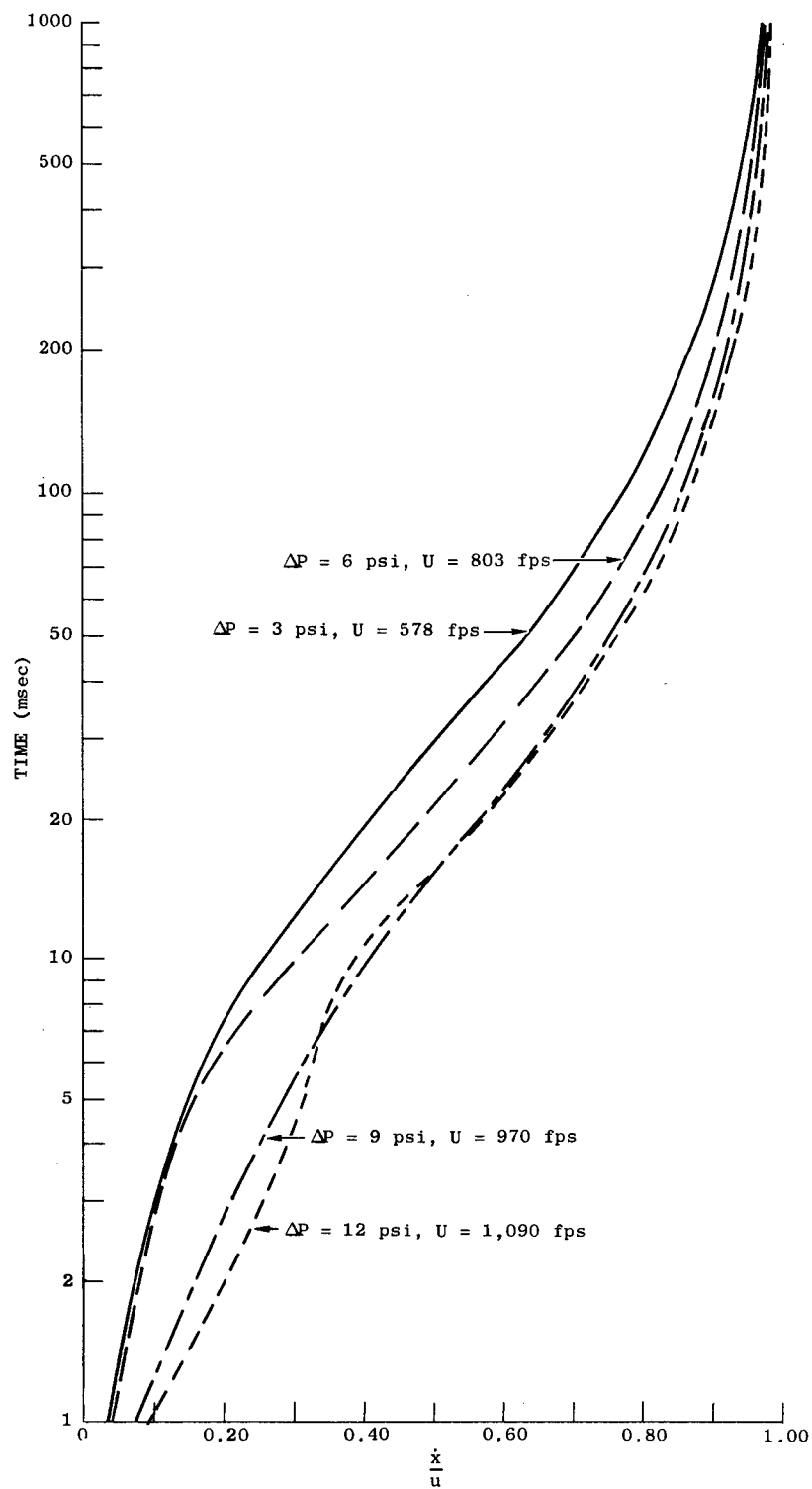


Fig. C-11. Acceleration of Ping-Pong Balls to Various Strength Jets

flow field be inferred from it? The drag coefficient, as presented in Fig. C-10, is a function of Mach number and Reynolds number. The Mach and Reynolds numbers are, in turn, functions of the velocity differences between the flow and the object, the viscosity and density of the gas, and the object's diameter. The experimental data provides  $\dot{x}_{m+1}$ ,  $\dot{x}_m$ , and  $\Delta t$  from the ball's trajectory.

More explicitly, an expression for  $u_m$ , the flow velocity during the period  $\Delta t$ , can be derived from Eq. (C.8) in the form

$$\dot{x}_{m+1} - \dot{x}_m - (\dot{x}_{m+1} - u_m)(\dot{x}_m - u_m) \frac{\Delta t}{\beta_m} = 0 \quad (C.10)$$

which reduces to

$$u_m^2 - C_1 u_m + C_2 \beta_m = C_3 \quad (C.11)$$

where  $C_1$ ,  $C_2$ , and  $C_3$  are constants determined from the initial conditions.  $\beta_m$  is determined from these conditions and  $C_D$ , the drag coefficient, which can be expressed in functional form as

$$C_D = f(u_m, a_m, \rho_m, \mu_m) \quad (C.12)$$

If the flow conditions at one point in the flow field are known and a single condition is known at another point of interest then Expression (C.10) could be solved by iteration. To visualize this, consider a one-dimensional, constant-area, homentropic flow field. For these conditions, the isentropic relationship and the conservation of energy and mass are given by

$$\frac{p_m}{\rho_m^\gamma} = \text{constant} = D_1 \frac{\gamma - 1}{\gamma} \quad (C.13)$$

$$\frac{1}{2} u_m^2 + \frac{\gamma}{\gamma - 1} \frac{p_m}{\rho_m} = \text{constant} = D_2 \quad (C.14)$$

$$\rho_m u_m = \text{constant} = \sqrt{2} D_3 \quad (C.15)$$



These equations can be combined to yield the expression

$$\rho_m^2 - \frac{D_1}{D_2} \rho_m^{\gamma-1} = \frac{D_3^2}{D_2} \quad (C.16)$$

which cannot be solved explicitly.

Assume  $\rho_m$  is known. Then the conditions needed to determine sound speed and viscosity can be derived from Eq. (C.13) and the equation of state. Under these conditions Eq. (C.11) could be rewritten as

$$u_m^2 - C_1 u_m + C_4 f(u_m) = C_3 \quad (C.17)$$

where  $C_4$  is a constant and  $C_D = f(u_m)$ . Even with these "most favorable conditions", an iterative solution is required since  $u_m$  must be known to determine  $f(u_m)$ . The conclusion to be reached is that the procedure is somewhat less than an optimum method of directly developing flow speed measurements. In reality, it is an approximation if only experimental data are used. Further complicating the process is the fact that arguments can be posed as to the true values of transient drag coefficients and the effects of lift and spin on the trajectories of the balls.

In the present effort some of the above problems were avoided by putting the target objects into the flow field simulated by the FLIC code. The flow properties are precisely known in the computer simulation; hence if we assume steady-state drag coefficients apply and that no lift or spin effects occur, the trajectories of objects in the simulation can be determined. The calculated trajectories can then be compared to the experimental trajectories.

In the calculation procedure the thermodynamic and aerodynamic parameters of the flow field were established via interpolations for the space-time points in the flow. The calculation procedure was simplified by taking very small difference steps and using constant values across it for all parameters. The simplified Newtonian equations were placed in a computer program that

also included subroutines for calculating the drag coefficient, viscosity, Reynolds number, sound speed, and Mach number each as a function of the input variables. The program was checked against the more complex one used to calculate the acceleration data. The agreement between the data evolved from both programs was found to be consistent within a 1% error.

The results of the computations are presented in Figs. C-12 through C-14. Fig. C-12 presents the trajectory data. The variation between numerical and experimentally determined trajectories ranges from 1 to 3 msec for fixed points on the trajectory curves. This variation corresponds to one-half to two frames of the film, and also corresponds to about the best zero-time measurement (shock arrival) for the method used. The agreement was surprisingly good. If, for example, a 1- to 2-msec error in shock arrival time did occur, as is indicated by the velocity curves of Figs. C-13 and C-14, then on the adjusted time scale the numerical and experimental trajectories superimpose.

The errors in the translational velocity histories shown in Figs. C-13 and C-14 were larger. The velocities of the experimental objects were initially low. They were then subject to some unrealistically large accelerations and became slightly greater than the numerically calculated values. The variation in the slope between experimental points caused these errors, as will be shown in succeeding paragraphs. Before discussing the errors, the effect of smoothing the data will be reviewed.

The smoothing technique used was a five-point Lagrangian interpolation which was based on methods presented in Ref. 38. The interpolation routine was a subroutine of the program being developed to reduce data from object translation for Work Unit 1154G. Of the available data, only ball No. 4 had sufficient points to warrant applying the smoothing techniques. The results are presented in Fig. C-15.

The experimental curve drawn from the smoothed data has a noticeably different profile than the curve for the unsmoothed data. The inflections correspond to some of the rarefaction wave motions, but appear to have an

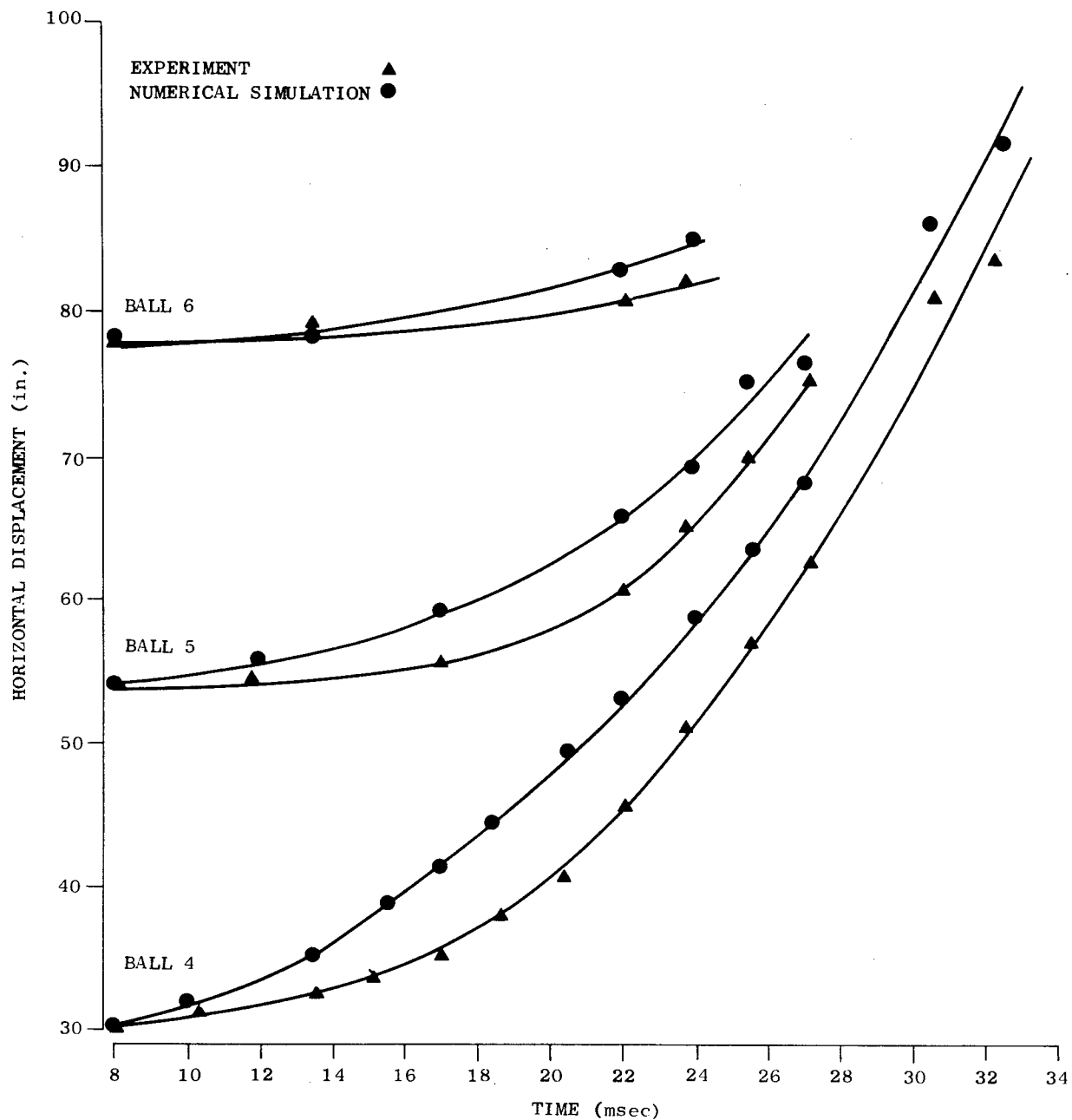


Fig. C-12. Comparison of Displacement Time Histories of Balls in Shock Tunnel Tests to Numerical Simulations

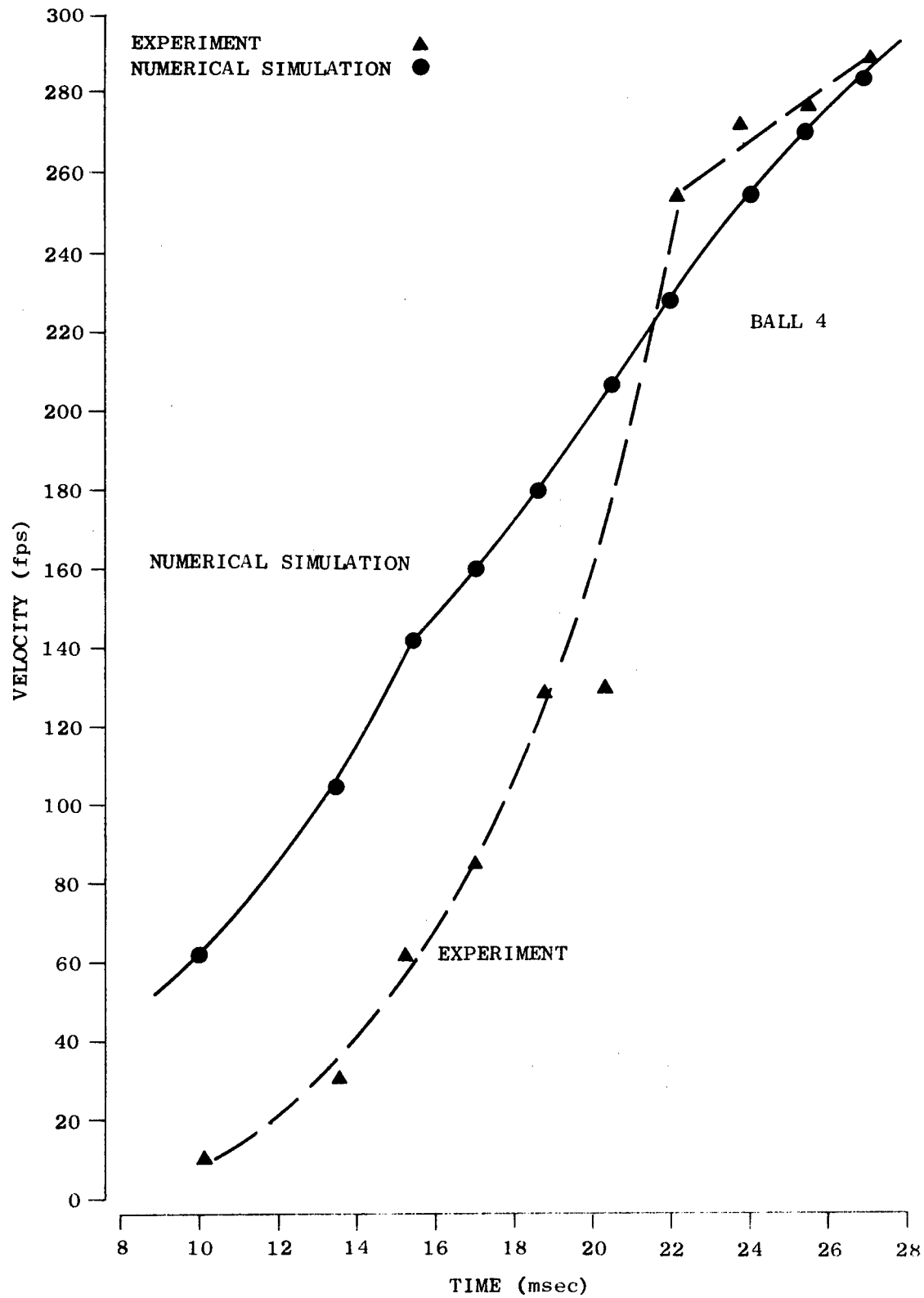


Fig. C-13. Comparison of Velocity Time Histories of a Ball in Shock Tunnel Tests to Numerical Simulations

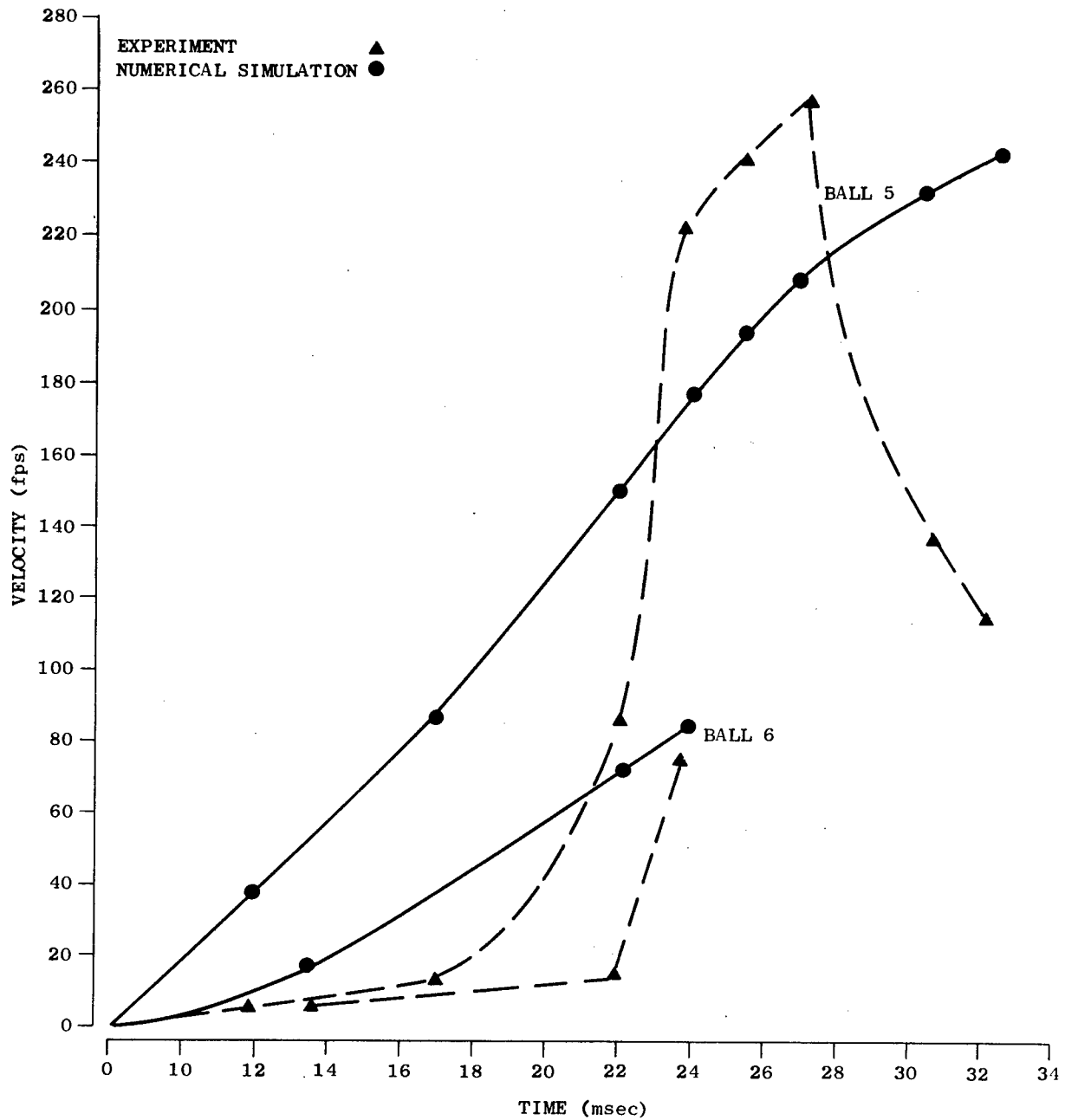


Fig. C-14. Comparison of Velocity-Time History of Balls in Shock Tunnel Tests to Numerical Simulation

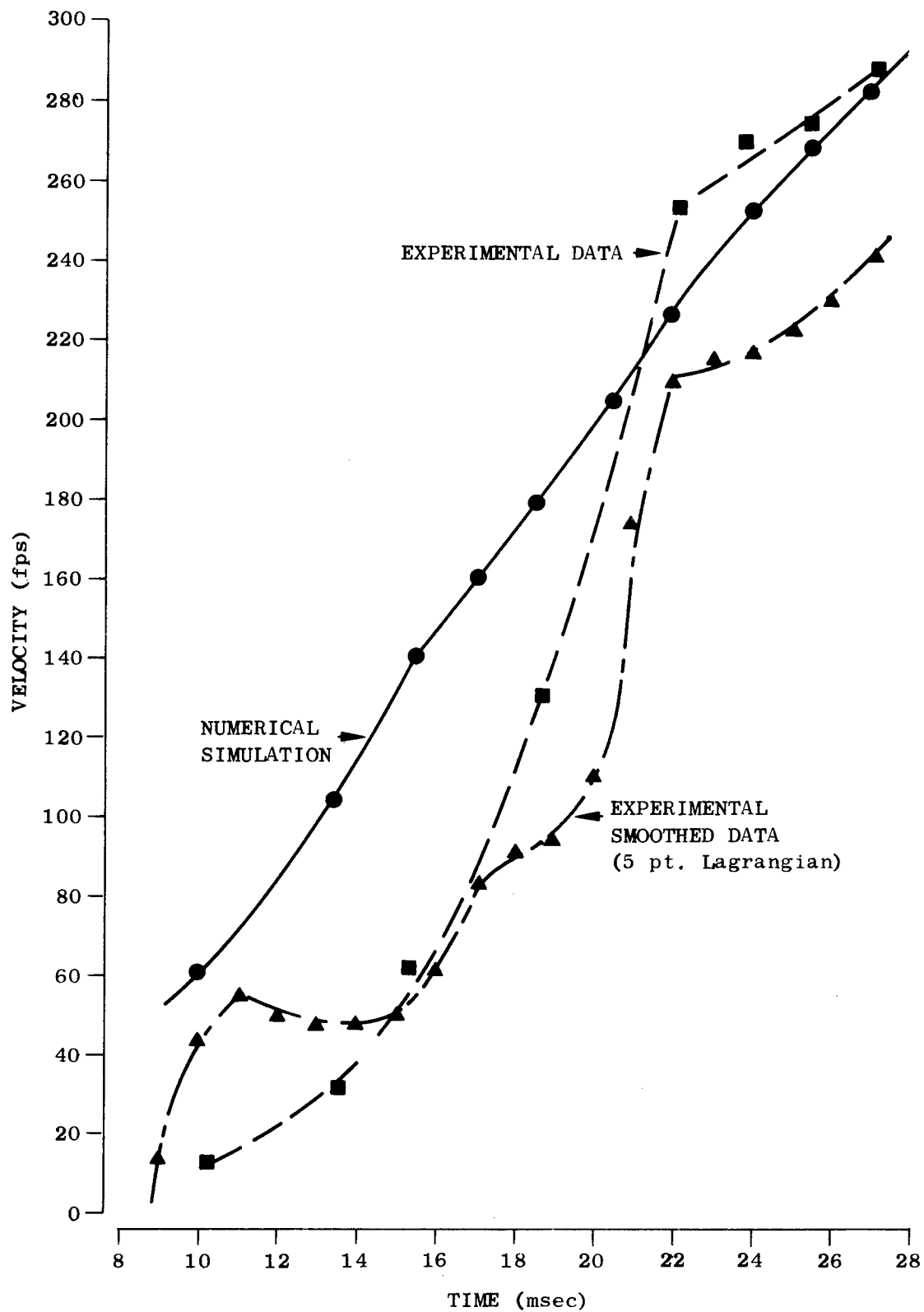


Fig. C-15. Comparison of Smooth and Unsmoothed Velocity Time Data in Shock Tunnel Tests

overly strong effect. The numerical simulations do not show the same pronounced decrease in acceleration, which would indicate that the simulation spread the steep rarefaction behind the shock wave due to the limited number of cells in the entry area. Although this may occur, the smoothed data appeared to have an inconsistency sufficiently serious to question their validity. The smoothed curve shows the ball decelerating, indicating a flow under 45 fps, well below those observed in either the numerical simulations or the BRL experiments (Refs. 4 and 5).

The accelerations in some sections of the smoothed curve appear to be too great in view of the acceleration curves presented earlier. For example, at 110 fps, the smoothed curve showed the ball accelerated to 210 fps in 2 msec. This acceleration can only be approached in one small section of the  $\Delta P = 9$  psi curve in Fig. C-11. This result would presume an instantaneous change in flow properties at 20 msec. These arguments indicate that the smoothing improved the presentation, but did not eliminate all the experimental variation. The conclusions drawn are that the smoothed data leveraged actual changes in the flow and that a more extensive analysis is warranted in future work to determine what smoothing techniques should be used.

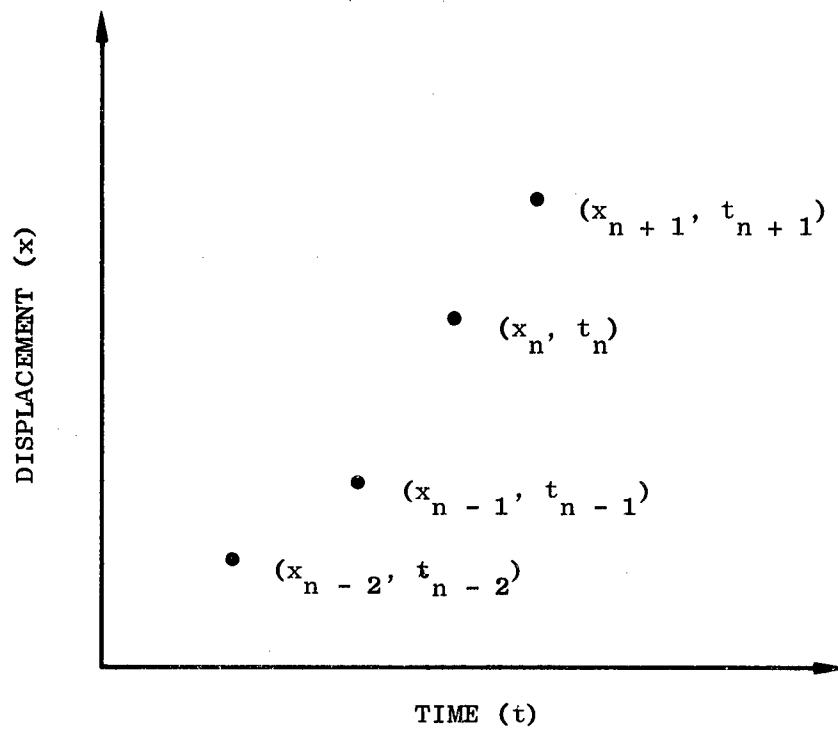
Even with this variation, the final velocities were within 10 percent of each other. Part of this is attributable to the effect of experimental error. A review of the equations will yield the presence of a second effect which will partly explain why deviations would tend not to be maintained. The driving force is directly proportional to the square of the object-to-flow field velocity differential. A slower object speed relative to a fixed flow speed will result in the object being accelerated faster. The more rapid acceleration will reduce the velocity difference between objects and the flow stream. If the same object is subjected to identical flows in two simulations but has a slower initial velocity in one simulation, then for the above reason the slower object will accelerate more rapidly reducing the object velocity differential between simulations.

In a sense errors are somewhat self-limiting, unless the spatial-temporal relationships between simulations have a large variance. The trajectories result from different driving forces which, in turn, increase the error, as was the situation for smoke particles in the BRL experiments. The velocities of the balls did not become very large (about 200 fps in the time frame of interest). The spatial variation for the smaller displacements and the accompanying errors were much smaller. The shifts noted in the scale model comparisons would have occurred on a reduced scale. In that the spatial variation between experimental and numerical simulations did not occur, i.e., the object trajectories compared reasonably well, it is concluded that the variations in velocities were basically attributable to experimental errors. On this basis the code-to-experiment dynamic pressure correlations would be judged to be within 10 percent.

To develop a better understanding of the experimental data and the meaning of the experimental errors a brief error analysis will be undertaken. Fig. C-16 presents the nomenclature for the  $x, t$  data to be considered. Each  $x, t$  set corresponds to a data point reduced from the films taken during the experiments.

The data sets correspond to the discrete points in monotonically increasing time from which the position-time curves presented earlier were drawn. The mean value theorem states (Ref. 30), "Let  $f$  be continuous on  $[a, b]$  and let  $f'(t)$  exist for  $a < t < b$ . Then, a point  $t_0$  can be found, with  $a < t_0 < b$ , such that  $f(b) = f(a) + (b-a)f'(t_0)$ ." If the position time curve is defined as  $f$ , and if the displacement in a time interval  $\Delta t$  (given by  $b-a$ ) is  $f(b) - f(a)$  then a velocity exists at some time in the interval  $\Delta t$  which corresponds to  $[f(b)-f(a)]/(b-a)$ ." The velocity so defined is simply the change in displacement ( $\Delta x$ ) divided by the time increment ( $\Delta t$ ). This argument states that it occurs at some time  $t_0$  in the interval  $\Delta t$ , but this does not mean that it must be the average velocity in that interval, nor does it locate the time  $t_0$ .



Fig. C-16. Presentation of  $(x, t)$  Sets

In taking this "average" value and ascribing it to the mid-point of the interval  $\Delta t$  an error results. An exact estimate of the error involved in this procedure is dependent upon the function  $f$  in the interval  $\Delta t$ . Crandall (Ref. 40) provides several methods of analyzing the error for parabolic curves through three adjacent points. Similar arguments are presented by Hamming (Ref. 41). Both presentations show the error to be a function of smoothness of the curve and the step size, i.e., the closer the segment of the curve is to being linear the smaller the error and the nearer the average value falls to the mid point of the interval  $\Delta t$ .

The trajectory curves shown in Fig. C-12 can be quite accurately represented by straight line segments for the intervals shown. The indication is that this is not the major source of error contributing to the observed deviation in the velocity-time profiles. The source of error can, however, be shown to be related to small measurement errors in the  $x$ - $t$  sets of the trajectory data.

By using either the law of the mean or the definition of a derivative we can define\* the velocity under the above conditions as

$$\frac{dx}{dt} \equiv \frac{\Delta x}{\Delta t} \equiv \frac{f(a) - f(b)}{a - b} \quad (C.18)$$

which can be rewritten for the nomenclature in Fig. C-16 as

$$\left(\frac{\Delta x}{\Delta t}\right)_n = \frac{x_{n+1} - x_{n-1}}{t_{n+1} - t_{n-1}} \quad (C.19)$$

For convenience sake the set of points  $x_n, t_n$  is considered to be between the two experimental data sets  $n + 1$  and  $n - 1$ . If we assume displacement

---

\*This is by definition only, for in reality

$$\frac{dx}{dt} = \lim_{\substack{\Delta x \rightarrow 0 \\ \Delta t \rightarrow 0}} \frac{\Delta x}{\Delta t} = \lim_{(a-b) \rightarrow 0} \frac{f(a) - f(b)}{a - b}; \text{ If } x = f(t)$$

measurement errors ( $\epsilon_x$ ) occur, then the true value of  $(\Delta x / \Delta t)_n$  can be given as

$$\left( \overline{\frac{\Delta x}{\Delta t}} \right)_n = \frac{(x_{n+1} - x_{n-1}) \pm \epsilon_x}{t_{n+1} - t_{n-1}} \quad (\text{C.20})$$

An experimental measurement error of  $\pm 0.5$  inches will be assumed which is not completely unrealistic. The data had a  $\Delta t$  value of 1.7 msec and corresponding  $\Delta x$ 's in the range of 3 to 6 inches ( $\Delta t$  and  $\Delta x$  correspond to  $n$ ). The error in the computed velocity would be given by the relationship

$$\left( \overline{\frac{\Delta x}{\Delta t}} \right)_n - \left( \frac{\Delta x}{\Delta t} \right)_n = \pm \frac{\epsilon_x}{\Delta t} \quad (\text{C.21})$$

The percent error ( $\epsilon_{vp}$ ) would be given by

$$\epsilon_{vp} = \frac{\left( \overline{\frac{\Delta x}{\Delta t}} \right)_n - \left( \frac{\Delta x}{\Delta t} \right)_n}{\left( \overline{\frac{\Delta x}{\Delta t}} \right)_n} \quad (100) \quad (\text{C.22})$$

$$= \frac{\left( \frac{\Delta x}{\Delta t} \right)_n \pm \frac{\epsilon_x}{\Delta t} - \left( \frac{\Delta x}{\Delta t} \right)_n}{\left( \frac{\Delta x}{\Delta t} \right)_n \pm \frac{\epsilon_x}{\Delta t}} \quad (100) \quad (\text{C.23})$$

$$= \frac{1}{\pm \Delta x / \epsilon_x + 1} \quad (100) \quad (\text{C.24})$$

For the conditions  $\Delta x = 5$  in. and  $\epsilon_x = 0.5$  in., the error would be  $\pm 9.9$  percent. The geometry involved in the reduction process of the projections includes measurements up to 20 ft; therefore, a 0.5 in. error corresponds to a 0.2 percent error. The ping pong balls also move during each frame and estimates of their centers must be made from blurred images. Errors of 1/8 to 1/2 in. are not therefore unreasonable. A more thorough analysis of these errors is being presently undertaken in Work Unit 1154G.

A second source of error could be the variations in the framing speed. These would be slower variations and most likely would follow a cyclic or smooth curve. The smoothed data in Fig. C-15 showed this form of variation. An approximate sinusoid with about a 7-msec natural period (150 Hz) appeared. This frequency is approximately the frequency of a harmonic which appears in the electrical power at the experimental facility.

The true value including errors in both timing and displacement measurements would be given by the following relationships.

$$\left(\frac{\Delta x}{\Delta t}\right)_n = \frac{\Delta x \pm \epsilon_x}{\Delta t \pm \epsilon_t} = \frac{\Delta x}{\Delta t \pm \epsilon_t} \pm \frac{\epsilon_x}{\Delta t \pm \epsilon_t} \quad (C.25)$$

The percent error in the measurement would be given by

$$\epsilon_{vpt} = \frac{(\Delta x / \Delta t \pm \epsilon_t) \pm (\epsilon_x / \Delta t \pm \epsilon_t) - (\Delta x / \Delta t)}{(\Delta x / \Delta t \pm \epsilon_t) \pm (\epsilon_x / \Delta t \pm \epsilon_t)} \quad (100) \quad (C.26)$$

$$= \frac{1 \pm (\epsilon_t / \epsilon_x) (\Delta x / \Delta t)_n}{1 \pm (\Delta x / \epsilon_x)} \quad (100) \quad (C.27)$$

If  $\epsilon_t \rightarrow 0$ , then Eq. (C.27) reduces to Eq. (C.24). For the same conditions as previously discussed ( $\Delta x / \epsilon_x = 10$ ), and with  $\epsilon_t / \Delta t = +0.1$ , the maximum total error would be 22.2 percent. For  $\epsilon_t / \Delta t = +0.02$ , the maximum total error would be 13.3 percent. The timing error could therefore significantly contribute to the total measurement error.

The preceding analysis shows how small measurement errors in trajectory data can be compounded by the conversion of the data to velocities. For this reason, the spatial trajectory data was used in the comparison of numerical to experimental simulations. The disadvantages and problems of computing translations, discussed earlier in this appendix, would cause smaller errors than differentiating the trajectory curve. Using the trajectory comparison, an estimate of the correlation between numerical and experimental dynamic pressure data would appear to be better than 90 percent. A more precise estimate of variation would require a more thorough error analysis of the experimental data.

## Copies

## DISTRIBUTION LIST

45 Office of Civil Defense, Office of the Secretary of the Army, Attn: Research Administration Office, Pentagon, Washington, D.C. 20310  
1 Army Library, 1A 518, Pentagon, Washington, D.C. 20310  
1 Assistant Secretary of the Army (R&D) Attn: Assistant for Research, Washington, D.C. 20310  
1 Chief of Naval Research, Department of the Navy, Washington, D.C. 20360  
1 Commander, Naval Supply Systems Command (Code 0611C1), Department of the Navy, Washington, D.C. 20360  
1 Commander, Naval Facilities Engineering Command, Research and Development (Code 0322C), Department of the Navy, Washington, D.C. 20390  
1 Mr. Richard Park, Advisory Committee on Civil Defense, National Academy of Sciences, 2101 Constitution Avenue, N.W., Washington, D.C. 20418  
20 Defense Documentation Center, Cameron Station, Alexandria, Virginia 22314  
1 Mrs. Joanne S. Gailar, Civil Defense Research Project, Oak Ridge National Laboratory, P. O. Box X, Oak Ridge, Tennessee 37830  
1 Mr. Norward A. Meador, Shelter Research Division, Office of Civil Defense, Dept. of the Army - OSA, Washington, D.C. 20310  
1 Chief of Naval Personnel, (Code Pers M 12), Department of the Navy, Washington, D.C. 20360  
1 U. S. Naval Civil Engineering Laboratory, Port Hueneme, California 93041  
1 Director, Disaster and Defense Services Staff, Agricultural Stabilization and Conservation Service, U.S. Dept. of Agriculture, Washington, D.C. 20250  
1 Mr. Bill Miller, Department of Civil Engineering, 307 More Hall, University of Washington, Seattle, Washington 98105  
1 Mr. Carl Koontz, Department of Civil Engineering, Worcester Polytechnic Institute, Worcester, Massachusetts, 01609  
1 Mr. Robert Bailey, School of Civil Engineering, Civil Engineering Building, Purdue University, Lafayette, Indiana 47907  
1 Mr. John A. Samuel, Department of Mechanical Engineering, University of Florida, Gainesville, Florida 32601  
1 Mr. G.K. Vetter, School of Architecture, University of Colorado, Boulder, Colorado 80302  
1 Miss Nancy K. Barberis, OCD Professional Advisory Service Center, University of Arizona, Tucson, Arizona 85721  
1 Mr. Dick Kummer, 101 Eng. A, Pennsylvania State University, University Park, Pennsylvania 16802  
1 Director, Defense Atomic Support Agency, Attn: Jack R. Kelso, Washington, D.C. 20301  
1 Director of Research and Development, Office of Emergency Preparedness, Washington, D.C. 20504  
1 Director, Civil Effects Branch, Division of Biology and Medicine, Atomic Energy Commission, Attn: Mr. L.J. Deal, Washington, D.C. 20545  
1 Mr. George N. Sisson, Director, Shelter Research Division, Office of Civil Defense, Dept. of the Army - OSA, Washington, D.C. 20310  
2 Air Force Special Weapons Laboratory, Attn: Technical Library, Kirtland Air Force Base, New Mexico 87117  
1 Los Alamos Scientific Laboratory, Attn: Document Library, Los Alamos, New Mexico 87544  
1 Chief of Engineers, Department of the Army, Attn: ENGME-RD, Washington, D.C. 20315  
1 Chief, Joint Civil Defense Support Group, Office, Chief of Engineers, Department of the Army, Gravelly Point, Washington, D.C. 20315  
1 Director, Army Materials and Mechanics Research Center, Attn: Technical Library, Watertown, Massachusetts 02172  
1 Director, U.S. Army Ballistic Research Laboratory, Attn: Document Library, Aberdeen Proving Ground, Maryland 21005  
1 Director, U.S. Army Ballistic Research Laboratory, Attn: Mr. William Taylor, G. Coulter, Aberdeen Proving Ground, Maryland 21005  
1 Director, Defense Atomic Support Agency, Attn: Technical Library, Washington, D.C. 20301  
1 Director, U.S. Army Engineer Waterways Experiment Station P. O. Box 631, Attn: Nuclear Weapons Effects Branch, Vicksburg, Mississippi, 39180  
1 Director, U.S. Army Engineer Waterways Experiment Station P.O. Box 631, Attn: Document Library, Vicksburg, Mississippi 39180  
1 District Engineer, U.S. Army Engineer District, Omaha, Attn: Chief, Engineering Division, 6012 U.S. Post Office and Courthouse, Omaha, Nebraska 68101  
1 Mr. Carl K. Wiehle, Civil Defense Technical Office, Stanford Research Institute, Menlo Park, California 94025  
5 Mr. William L. White, Civil Defense Technical Office, Stanford Research Institute, Menlo Park, California 94025  
1 Mr. Werner Weber, Director, New York State Civil Defense Commission, Public Security Bldg., State Office Bldg. Campus, Albany, New York, 12226  
1 Agbabin-Jacobsen Associates, 8943 South Sepulveda Boulevard, Los Angeles, California 90045  
1 Amman and Whitney, 111 Eighth Avenue, New York, New York 10011  
1 Mr. Arthur D. Caster, Chairman, Coordinating Committee on Civil Defense, American Society of Engineers, 2864 McFarlan Park Dr., Cincinnati, Ohio 45211  
1 The Dikewood Corporation, 1009 Bardbury Drive, S.E., University Research Park, Albuquerque, New Mexico 87106  
1 General American Transportation Corporation, General American Research Division, 7449 North Natchez Avenue, Niles, Illinois 60648  
1 Hudson Institute, Quaker Ridge Road, Croton-on-Hudson, New York 10520  
1 Bell Telephone Laboratories, Inc., Attn: Mr. R. W. Mayo, Whippany Road, Whippany, New Jersey 07981  
1 Dr. Eugene Sevin, IIT Research Institute, 10 West 35th Street, Chicago, Illinois 60616  
1 Dr. Harold Brode, The RAND Corporation, 1700 Main Street, Santa Monica, California 90401  
1 Research Triangle Institute, P.O. Box 12194, Research Triangle Park, North Carolina 27709  
1 Mr. Luke J. Vortman, Division 5412, Sandia Corporation, Box 5800, Sandia Base, Albuquerque, New Mexico 87115  
1 URS Research Company, 1811 Trousdale Drive, Burlingame, California 94011  
1 Massachusetts Institute of Technology, Department of Civil and Sanitary Engineering, Cambridge, Massachusetts 02138  
1 Dr. Nathan M. Newmark, University of Illinois, 111 Talbot Laboratory, Urbana, Illinois 61801  
1 Dr. William Hall, University of Illinois, 111 Talbot Laboratory, Urbana, Illinois 61801  
1 Dr. Merit P. White, University of Massachusetts, School of Engineering, Amherst, Massachusetts 01002  
1 Dr. Abner Sachs, Institute for Defense Analyses, 400 Army-Navy Drive, Arlington, Virginia 22202  
1 The Vertex Corporation, 10400 Connecticut Avenue, Kensington, Maryland 20795  
1 Chief of Engineers, Department of the Army, Attn: ENGMC-EM, Washington, D.C. 20315  
1 Dr. C. S. White, President-Director, Lovelace Foundation, 5200 Gibson Boulevard, S.E. Albuquerque, New Mexico 87108  
1 Dr. Charles Osterberg, Acting Chief, Environmental Sciences Branch, Division of Biology and Medicine, U.S. Atomic Energy Commission, Washington, D.C. 20545  
1 Mr. J. J. Davis, Effects Evaluation Division, Nevada Operations Office, U.S. Atomic Energy Commission, Las Vegas, Nevada 89101  
1 Mr. Eugene F. Witt, Bell Telephone Laboratories, Inc., Whippany Road, Whippany, New Jersey 07981  
1 Mr. Paul Zigman, Environmental Science Associates, 770 Airport Boulevard, Burlingame, California 94010

Unclassified  
Security Classification

**DOCUMENT CONTROL DATA - R & D**

*(Security classification of title, body of abstract and indexing annotation must be entered when the overall report is classified)*

1. ORIGINATING ACTIVITY (Corporate author)  URS Research Company 1811 Trousdale Drive Burlingame, California 94010		2a. REPORT SECURITY CLASSIFICATION  Unclassified	
		2b. GROUP	
3. REPORT TITLE  The Air-Blast-Induced Environment Within Civil Defense Blast-Slanted Shelters			
4. DESCRIPTIVE NOTES (Type of report and inclusive dates)			
5. AUTHOR(S) (First name, middle initial, last name)  Joseph F. Melichar			
6. REPORT DATE  November 1969		7a. TOTAL NO. OF PAGES  236	7b. NO. OF REFS  68
8a. CONTRACT OR GRANT NO.  DAHC20-67-C-0136		9a. ORIGINATOR'S REPORT NUMBER(S)  URS 755-3	
b. PROJECT NO.  c. OCD Work Unit 1123F  d.		9b. OTHER REPORT NO(S) (Any other numbers that may be assigned this report)	
10. DISTRIBUTION STATEMENT  This document has been approved for public release and sale; its distribution is unlimited.			
11. SUPPLEMENTARY NOTES		12. SPONSORING MILITARY ACTIVITY  Office of Civil Defense	
13. ABSTRACT  The study evaluated the potential usefulness of two dimensional hydrodynamic computer codes to the civil defense shelter research program, and also continued work on evolving a conceptual model of air blast-induced flows in "blast-slanted" basement shelters. The review of the numerical simulation techniques included the theoretical aspects of the code usage as well as questions of practical usefulness. The numerical simulations were compared against experimental simulations and it was concluded that they were less expensive and more flexible. It was also included that a blend of both simulation techniques is necessary to the shelter research program and that the blend between the two techniques and analysis is directly related to specific research goals. The numerical simulations, experimental simulations, and analytical techniques were used to extend the understanding of basic flow process of the air blast transmission process into the shelter. These results, coupled with past work, were used to show the economic infeasibility of developing a generalized conceptual model of the flow into blast-slanted basement shelters. Questions were raised as to the need for such a model and recommendations as to future research needs were made.			

Unclassified

Security Classification

14. KEY WORDS	LINK A		LINK B		LINK C	
	ROLE	WT	ROLE	WT	ROLE	WT
civil defense shelter research program air blast-induced flows blast-slanted basement shelters numerical simulation						

Unclassified

Security Classification

THE AIR-BLAST-INDUCED ENVIRONMENT WITHIN CIVIL DEFENSE BLAST SLANTED-SHELTERS

URS 755-3

URS Research Company, Burlingame, California

November 1969 219 pp. Contract No. DAHC20-67-C-0136

Work Unit 1123F

UNCLASSIFIED

The study evaluated the potential usefulness of two dimensional hydrodynamic computer codes to the civil defense shelter research program, and also continued work on evolving a conceptual model of air blast-induced flows in "blast-slanted" basement shelters. The review of the numerical simulation techniques included the theoretical aspects of the code usage as well as questions of practical usefulness. The numerical simulations were compared against experimental simulations and it was concluded that they were less expensive and more flexible. It was also included that a blend of both simulation techniques is necessary to the shelter research program and that the blend between the two techniques and analysis is directly related to specific research goals. The numerical simulations, experimental simulations, and analytical techniques were used to extend the understanding of basic flow process of the air blast transmission process into the shelter. These results, coupled with past work, were used to show the economic infeasibility of developing a generalized conceptual model of the flow into blast-slanted basement shelters. Questions were raised as to the need for such a model and recommendations as to future research needs were made.

THE AIR-BLAST-INDUCED ENVIRONMENT WITHIN CIVIL DEFENSE BLAST-SLANTED SHELTERS

URS 755-3

URS Research Company, Burlingame, California

November 1969 219 pp. Contract No. DAHC20-67-C-0136

Work Unit 1123F

UNCLASSIFIED

The study evaluated the potential usefulness of two dimensional hydrodynamic computer codes to the civil defense shelter research program, and also continued work on evolving a conceptual model of air blast-induced flows in "blast-slanted" basement shelters. The review of the numerical simulation techniques included the theoretical aspects of the code usage as well as questions of practical usefulness. The numerical simulations were compared against experimental simulations and it was concluded that they were less expensive and more flexible. It was also included that a blend of both simulation techniques is necessary to the shelter research program and that the blend between the two techniques and analysis is directly related to specific research goals. The numerical simulations, experimental simulations, and analytical techniques were used to extend the understanding of basic flow process of the air blast transmission process into the shelter. These results, coupled with past work, were used to show the economic infeasibility of developing a generalized conceptual model of the flow into blast-slanted basement shelters. Questions were raised as to the need for such a model and recommendations as to future research needs were made.

THE AIR-BLAST-INDUCED ENVIRONMENT WITHIN CIVIL DEFENSE BLAST-SLANTED SHELTERS

URS 755-3

URS Research Company, Burlingame, California

November 1969 219 pp. Contract No. DAHC20-67-C-0136

Work Unit 1123F

UNCLASSIFIED

The study evaluated the potential usefulness of two dimensional hydrodynamic computer codes to the civil defense shelter research program, and also continued work on evolving a conceptual model of air blast-induced flows in "blast-slanted" basement shelters. The review of the numerical simulation techniques included the theoretical aspects of the code usage as well as questions of practical usefulness. The numerical simulations were compared against experimental simulations and it was concluded that they were less expensive and more flexible. It was also included that a blend of both simulation techniques is necessary to the shelter research program and that the blend between the two techniques and analysis is directly related to specific research goals. The numerical simulations, experimental simulations, and analytical techniques were used to extend the understanding of basic flow process of the air blast transmission process into the shelter. These results, coupled with past work, were used to show the economic infeasibility of developing a generalized conceptual model of the flow into blast-slanted basement shelters. Questions were raised as to the need for such a model and recommendations as to future research needs were made.

THE AIR-BLAST-INDUCED ENVIRONMENT WITHIN CIVIL DEFENSE BLAST-SLANTED SHELTERS

URS 755-3

URS Research Company, Burlingame, California

November 1969 219 pp. Contract No. DAHC20-67-C-0136

Work Unit 1123F

UNCLASSIFIED

The study evaluated the potential usefulness of two dimensional hydrodynamic computer codes to the civil defense shelter research program, and also continued work on evolving a conceptual model of air blast-induced flows in "blast-slanted" basement shelters. The review of the numerical simulation techniques included the theoretical aspects of the code usage as well as questions of practical usefulness. The numerical simulations were compared against experimental simulations and it was concluded that they were less expensive and more flexible. It was also included that a blend of both simulation techniques is necessary to the shelter research program and that the blend between the two techniques and analysis is directly related to specific research goals. The numerical simulations, experimental simulations, and analytical techniques were used to extend the understanding of basic flow process of the air blast transmission process into the shelter. These results, coupled with past work, were used to show the economic infeasibility of developing a generalized conceptual model of the flow into blast-slanted basement shelters. Questions were raised as to the need for such a model and recommendations as to future research needs were made.